Title
Intermolecular Interactions and Surface Properties of Self-Assembled Monolayers of Functional Boron Clusters

Author
Goronzy, Dominic Pascal

Publication Date
2019

Peer reviewed|Thesis/dissertation

UNIVERSITY OF CALIFORNIA

Los Angeles

Intermolecular Interactions and Surface Properties of Self-Assembled Monolayers of Functional Boron Clusters

A dissertation submitted in partial satisfaction of the requirements for the degree of Doctor of Philosophy in Chemistry

by

Dominic Pascal Goronzy

2019

ABSTRACT OF THE DISSERTATION

Intermolecular Interactions and Surface Properties of

Self-Assembled Monolayers of Functional Boron Clusters

by

Dominic Pascal Goronzy

Doctor of Philosophy in Chemistry

University of California, Los Angeles, 2019

Professor Paul S. Weiss, Chair

Self-assembled monolayers (SAMs) are an advantageous platform for probing the fundamental interactions that dictate the spontaneous formation of nanostructures and supramolecular assemblies and directly affect macroscale properties. As such, SAMs provide an avenue for creating surfaces with defined chemical and physical properties. The assembly of these nanoscale constructs is driven by three primary factors: the interface between the substrate and the monolayer, the interactions between the adsorbate molecules, and the interface between the monolayer and the environment. I studied an icosahedral cage boron cluster, the carborane, as a building block for SAMs with properties that we can tune to advantage. Carboranes have several favorable traits, including providing a scaffold for a variety of functional groups. A chalcogenide group, typically a thiol, is used for surface attachment; moreover, bifunctional carboranes also

enable control of the valency during assembly and greater reactivity at the environmental interface of the SAM. Additionally, isomers of carboranethiol have distinct dipole moments in terms of orientation and magnitude. The dipoles can lead to the formation of long-range dipole-dipole networks within the SAM, which can stabilize the SAM and also modify the surface properties of the material. The rigid, symmetric backbone of the carborane cage results in SAMs that are relatively pristine and defect free. Due to these advantageous traits, carboranes enable the creation of monolayers with tunable interactions at the SAM interfaces. This system not only enables myself and others to study the molecular forces of assembly but also facilitates the simultaneous modification of both chemical and physical properties of surfaces and interfaces.

This thesis describes several carborane-based surface assemblies and the variable interactions they have within the SAM interfaces. The introduction of a second thiol group to the carborane cage can be used to modulate the interaction of the SAM with the substrate. Carboranedithiol SAMs exhibit two binding modes, a monovalent state and a divalent state. The presence of these two modes enables tuning of valency using acid-base chemistry and thus the ratio of singly bound to dual bound surface molecules can be modified during deposition.

Another avenue to alter the interactions at the substrate-monolayer interface is to use an alternative functional group for surface attachment. A chalcogenide group similar to thiol is selenol, however carboraneselenolate SAMs have a distinct surface morphology compared to carboranethiolate SAMs. Carboraneselenolate SAMs exhibit a dynamic double lattice where surface molecules appear to switch between high- and low-conductance binding modes. This morphology is consistent with other cage molecule selenolate SAMs and is typically associated with substrate-mediated interactions. In contrast, the carboraneselenolate SAMs are resistant to thermal rearrangement and desorption due to the dipole-dipole interactions within the monolayer.

Carboranethiols can be modified by adding a carboxylic acid functional group that both alter the interactions within the monolayer and provide a platform for further reactions at the environmental interface. The introduction of a laterally positioned carboxyl functional group increases the steric demands of the molecule, thereby decreasing the packing density, but also enables hydrogen-bonding interactions within the monolayer. The pK_a of the surface bound carboxylic acid is shifted such that it is approximately two pH units less acidic than in solution. This shift is driven by the dielectric of the environment that the carboxyl group experiences on the surface, which is determined by the intermolecular interactions within the monolayer, partial desolvation, and the proximity to the substrate surface.

The carboxyl group also remains available for further chemistry on the surface and can coordinate with a variety of metal ions or be used as an attachment point for performing chemical lift-off lithography (CLL). This lithographic technique was performed successfully on several types of carboxyl carboranethiolate SAMs. The use of these SAMs also enabled the characterization of the post CLL substrate surface *via* scanning tunneling microscopy. This analysis revealed the molecules left behind during the CLL process are either in small molecular islands or sparsely packed, highly mobile molecules.

There remain many opportunities for further chemistry to be performed with these carboxyl terminated SAMs or with carboranethiol SAMs with other additional functional groups. Carborane-based SAMs are a versatile system that provides a high degree of tunability at all three interfaces of a SAM. The work presented lays the foundation for further application in lithography, like CLL, as well as the use of these SAMs in organic electronics and devices and as interfacial materials.

This dissertation of Dominic Pascal Goronzy is approved.

Anastassia N. Alexandrova

Stanley J. Osher

Paul S. Weiss, Committee Chair

University of California, Los Angeles

2019

For my family, for my friends, and for my mentors

Table of Contents

List of Abbreviations

Acronyms and Symbols

1ATC9	3-mercapto-*N*-nonylpropionamide
1O2	1,2-carboranedithiol
9O12	9,12-carboranedithiol
AFM	atomic force microscopy
Ag	silver
Ag/AgCl	silver/silver chloride
Au	gold
B	boron
Ba	barium
BE	bonding energy
n-BuLi	n-butyllithium
C	carbon
Ca	calcium
Cl	chloride
CLL	chemical lift-off lithography
Co	cobalt
COOH	carboxylic acid
Cu	copper
DFT	density functional theory
E_F	Fermi energy
ESI	electrospray ionization
Et_2O	ethyl ether
F	fluoride
Fcc	face-centered cubic
Fe	iron
FTIR	Fourier transform infrared spectroscopy

FWHM	full width at half maximum
Ge	germanium
H	hydrogen
HCl	hydrochloric acid
Hcp	hexagonal close-packed
I_t	tunneling current
I_{tunnel}	tunneling current
IR	infrared spectroscopy
KE	kinetic energy
LBH	local barrier height spectroscopy
La	lanthanum
M1	*m*-1-carboranethiol
M9	*m*-9-carboranethiol
M1-COOH	carboxylic acid functionalized *m*-1-carboranethiol
M9-COOH	carboxylic acid functionalized *m*-9-carboranethiol
M1Sel	*m*-1-carboraneselenol
M9Sel	*m*-9-carboraneselenol
Mg	magnesium
Na	sodium
NaOH	sodium hydroxide
Ni	nickel
NMR	nuclear magnetic resonance
P1	*p*-carboranethiol
P1-COOH	carboxylic acid functionalized *p*-carboranethiol
P	phosphorus
Pb	lead
Pd	palladium
PDMS	polydimethylsiloxane
PDOS	predicted density of states

PE	photoelectron
Ppm	parts per million
Pt	platinum
S	sulfur
S-	thiolate
SAM	self-assembled monolayer
SH	thiol
Si	silicon
Sm	samarium
SO_4	sulfate
Sr	strontium
STM	scanning tunneling microscopy
STS	scanning tunneling spectroscopy
T	temperature
Tb	terbium
Tl	thallium
UPS	ultraviolet photoelectron spectroscopy
UV	ultraviolet
V_s	sample voltage bias
V_{sample}	sample voltage bias
XPS	X-ray photoelectron spectroscopy
Zn	zinc

Units

Å	Ångstroms
a.u.	arbitrary units
°C	degrees Celsius
cm^{-1}	inverse centimeters
D	Debye

deg	degree
eV	electron volt
g	gram
h	hour
Hz	Hertz
K	Kelvin
kcal	kilocalorie
kHz	kilohertz
kJ	kilojoule
kV	kilovolt
m	meter
mA	milliampere
min	minutes
mL	milliliter
mM	millimolarity
mmol	millimole
mol	mole
ms	milliseconds
mV	millivolt
N	Newton
nm	nanometer
nN	nanonewton
pA	picoampere
sec	second
μm	micrometer
V	volt

Acknowledgments

I would like to first thank Prof. Paul S. Weiss, my thesis advisor, without whom none of this would have been possible. Not only did he support and encourage me throughout my graduate career, he also gave me the freedom to grow as an independent investigator. In his group, I not only increased my understanding of scientific principles, but also learned how to write about and communicate my research to a broader audience and how to manage an academic research lab. I would also like to acknowledge the other members of my thesis committee, Prof. Anastassia N. Alexandrova, Prof. James K. Gimzewski, and Prof. Stanley J. Osher, for their continued support and feedback throughout my graduate career.

Prof. Alexandrova has not only been a critical influence on me as a member of my thesis committee, but also as a collaborator, who always asks the important questions that push a research project forward. I hope to be able to continue to work with her in the future. One other influential collaborator has been Prof. Tomáš Baše, whom it has been my pleasure to work with over the years and whose expertise was critical to the success of the research described in this thesis.

I also would like to thank the members of the Weiss group not only for their contributions to projects and scientific discussions but also for their friendship. Dr. John Thomas gave me my start in the group, showed me the ropes, and helped lay the foundation for my graduate career. My successor in the group, Erin Avery, has been a wonderful mentee and I know I can trust her to take over the work that stems from my research. One of the first people I would always turn to when I was trying to work through a new puzzle is Kevin Cheung, and I am so pleased we had the chance to work on a project together in the end. Logan Stewart has been a good office mate and a good friend, always willing to help no matter what the issue. Diana Yugay allowed me to join her project

and gave me a little scientific variety that was much appreciated. Furthermore, the group as a whole, throughout my time in graduate school, has aided my success in immeasurable ways.

I gratefully acknowledge the funding sources that supported this work, the Department of Energy (grant #DE-SC-0005025) for support of instrumentation and methods and (grant #DE-SC-0005161) for work on buried interfaces, the W. M. Keck Foundation for support of image and data analysis methods through the Keck Center for Leveraging Sparsity, the Czech Academy of Sciences (grant #M200321201) for support of the synthetic aspects of this work, the Scientific and Technological Research Council of Turkey (grant #116F174) and the NSF-CAREER award (grant #CHE-1351968) for support of the computational modeling and analyses, and the National Science Foundation (grant #CMMI-1636136) for support of the chemical lift-off lithography experiments. I would also personally like to acknowledge the support of the UCLA Dissertation Year Fellowship.

On a more personal note, I want to thank my parents for their continued love and support. Not only did they introduce me to science from the very beginning but also taught me the ins and outs of academia and research and continue to be a source of guidance and inspiration to this day. Lastly, I want to thank Liz for putting up with me all this time and for always being there for me. I cannot imagine the last few years without her and I do not know if I would have succeeded without her support.

Vita

I received my Bachelor of Science in Chemistry from the College of Chemistry at the University of California, Berkeley with a minor in Public Policy in 2013. During my undergraduate tenure, I pursued research in the lab of Prof. Michael Fayer at Stanford University and the lab of Prof. Charles Harris at UC Berkeley. In Prof. Fayer's lab, I applied time-correlated single photon counting spectroscopy for fluorescent anisotropy measurements. Using this technique, I worked to investigate the molecular structure of lithium-room temperature ionic liquid complexes as a function of metal ion concentration and the proton transfer dynamics in polyfluoronated sulfonic membranes as a function of membrane hydration. In the lab of Prof. Harris I worked to set up a system to perform thermal programmed desorption experiments and also investigated vibrational stretching modes of organometallic compounds using time-dependent IR spectroscopy.

I started my graduate studies at the University of California, Los Angeles in 2013 and joined the group of Professor Paul S. Weiss in the Department of Chemistry and Biochemistry, transitioning away from ultrafast laser spectroscopy and towards surface science. Under his mentorship, I studied self-assembled monolayers and supramolecular assemblies at buried and exposed interfaces, primarily using scanning tunneling microscopy and scanning tunneling spectroscopy at both ambient and ultrahigh vacuum, cryogenic conditions. These techniques were used to map hydrogen-bonding networks in amide-containing monolayers, study the assembly and material properties of carborane-based monolayers, including dithiol isomers, carboxylic acid isomers, and selenol isomers, and probe bimolecular assemblies for the effects of metal ions/organic modulators. In 2018, I was a finalist for the American Vacuum Society's Nano

Science and Technology Division Award. Also in 2018, I was a recipient of UCLA's Dissertation Year Fellowship.

List of Publications

1. Thomas, J. C.; Goronzy, D. P.; Dragomiretskiy, K.; Zosso, D.; Gilles, J.; Osher, S. J.; Bertozzi, A. L.; Weiss, P. S. Mapping Buried Hydrogen-Bonding Networks. *ACS Nano* **2016**, *10*, 5446-5451. DOI: 10.1021/acsnano.6b01717

2. Yugay, D.; Goronzy, D. P.; Kawakami, L. M.; Claridge, S. A.; Song, T.-B.; Yan, Z.; Xie, Y.-H.; Gilles, J.; Yang, Y.; Weiss, P. S. Copper Ion Binding Site in β-Amyloid Peptide. *Nano Lett.* **2016**, *16*, 6282-6289. DOI: 10.1021/acs.nanolett.6b02590

3. Thomas, J. C.; Goronzy, D. P.; Serino, A. C.; Auluck, H. S.; Irving, O. R.; Jimenez-Izal, E.; Deirmenjian, J. M.; Macháček, J.; Sautet, P.; Alexandrova, A. N.; Base, T.; Weiss, P. S. Acid–Base Control of Valency within Carboranedithiol Self-Assembled Monolayers: Molecules Do the Can-Can. *ACS Nano* **2018**, *12*, 2211–2221. DOI: 10.1021/acsnano.7b09011

4. Goronzy, D. P.; Ebrahimi, M.; Rosei, F.; Arramel; Fang, Y.; De Feyter, S.; Tait, S. L.; Wang, C.; Beton, P. H.; Wee, A. T. S.; Weiss, P. S.; Perepichka, D. F. Supramolecular Assemblies on Surfaces: Nanopatterning, Functionality, and Reactivity. *ACS Nano* **2018**, *12*, 7445-7481. DOI: 10.1021/acsnano.8b03513

5. Wang, S.; Goronzy, D. P.; Young, T. D.; Wattanatorn, N.; Stewart, L.; Base, T.; Weiss, P. S. Formation of Highly Ordered Terminal Alkyne Self-Assembled Monolayers on the Au{111} Surface through Substitution of 1-Decaboranethiolate. *J. Phys. Chem. C* **123**, 1348-1353. DOI: 10.1021/acs.jpcc.8b11033

6. Bui, K.; Fauman, J.; Kes, D.; Mandiola, L. T.; Ciomaga, A.; Salazar, R.; Bertozzi, A. L.; Gilles, J.; Goronzy, D. P.; Guttentag, A. I.; Weiss, P. S. Segmentation of Scanning Tunneling Microscopy Images Using Variational Methods and Empirical Wavelets. *Pattern Anal. Applic.* DOI: 10.1007/s10044-019-00824-0

Chapter 1: Characterization of Carborane-Based Self-Assembled Monolayers

1.1 Nanostructured Materials

Nanoscale materials have become ubiquitous components of everyday life in the 21st Century. The processing chips that our electronics rely on are all nanopatterned devices, and nanoparticles are used for a variety of applications in consumer goods, from UV absorption in sunscreen to anti-microbial effects in food packaging. Nanotechnology continues to advance further into new fields, such as green technology and nanomedicine. Nanostructured materials are so incredibly useful due to their size, their capacity to be fabricated by both top-down and bottom-up assembly methods, and since they often have enhanced or unique properties relative to macroscopic bulk materials. These altered properties are often the result of quantum phenomena or increased interfacial interactions. The latter characteristic is perhaps the most distinguishing feature of nanoscale structures; as the size of an object decreases, it loses volume much more rapidly than surface area; at the extreme end, these materials can be thought to be completely interfacial and dominated by surface properties. Thus, from a fundamental perspective, understanding atomistic and molecular interactions at surfaces and interfaces is required for developing new nanoscale constructs with defined chemical and physical properties.

1.2 Formation and Properties of Self-Assembled Monolayers

A primary instance of a nanoscale construct dominated by surface interactions is the self-assembled monolayer (SAM), which is typically only 1-3 nm thick.[1] These SAMs provide a facile and flexible avenue to modify the surface properties of a substrate. These monolayers can act as barriers or as pathways for further chemical and physical reactions or interfacial transport. Furthermore, monolayers can be patterned or heterogeneous monolayers can be formed by two or more constituent molecules. Self-assembled monolayers form spontaneously into ordered thin

films, the structures and characteristics of which are determined primarily by three interactions: the interface between the substrate and the monolayer, the interactions between adsorbate molecules, and the environmental interface of the monolayer (Figure 1.1).[2] The most studied class of SAMs is that of *n*-alkanethiols adsorbed on a metal surface, where the thiolate head group readily binds to the metal. The interactions between the alkyl backbones results in a hexagonally close-packed monolayer. This system is prone to a variety of defects, like tilt domain boundaries, gauche defects, and substrate vacancy islands, which offer both drawbacks and opportunities.

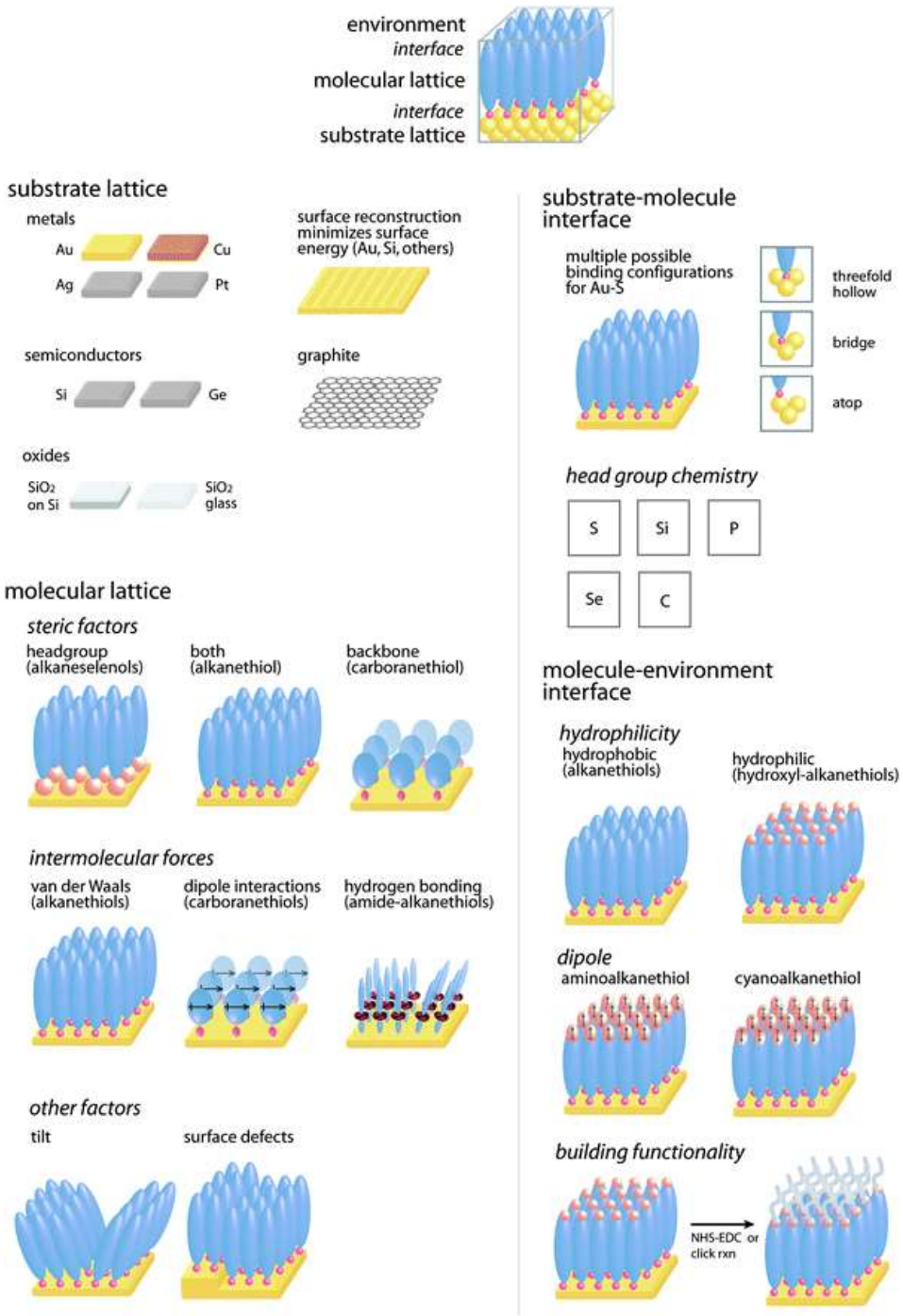

Figure 1.1: A schematic overview of the interactions that drive the formation of self-assembled monolayers and determine their resulting properties. The substrate-monolayer interface is defined by interactions of the atomic and electronic configurations of the substrate and the chemical nature of the head group of the adsorbate molecule. The morphology of the molecular lattice is determined by steric forces and intermolecular interactions between neighboring adsorbates. The exposed terminal groups of the monolayer molecules can not only influence monolayer structure but also defines the characteristics at the environmental interface. Figure reproduced with permission from Reference 2. Copyright 2013 Royal Society of Chemistry.

1.2.1 The Substrate-Monolayer Interface

The spontaneous assembly of SAMs is a result of the high affinity between the head group and the substrate; in the case of the prototypical alkanthiolate monolayer, the gold-sulfur bond has an enthalpy of formation of ~45 kcal mol^{-1}.[3] Early SAMs were formed by depositing disulfides on Au surfaces,[4] but since then, monolayers have been assembled on Au,[1,3,5] Ag,[6-9] Cu,[7,8,10] Pt,[8] and Pd,[11,12] as well as on semiconductor surfaces,[13,14] such as Si and Ge. Self-assembled molecular networks, while not covalently bound to the surface but rather through physisorption, have also been formed on such surfaces as graphite.[15] Of these, the Au surface is frequently used and well-studied due to its ease of preparation as a substrate, its stability in ambient conditions, and its high affinity and selectivity for binding with thiols.[4] At the other side of the interface, the identity of the binding head group also has great variability. Besides sulfur, cyanide and isocyanide[16,17] have been used, as well as, Se,[6,18-20] Si,[21,22] P,[23,24] amine,[25,26] and carboxylic acid groups.[27,28]

The interactions at the substrate-monolayer interface go beyond just the constituent binding substrate and binding head group. There exist multiple potential binding sites in the substrate lattice that each engage different sets of atoms. Additionally, surface reconstruction may occur to minimize the surface energy. In the case of the bare Au{111} surface, this reconstruction is referred to as the herringbone reconstruction and arises from alternating face-centered-cubic structures and hexagonally closed-packed structures. The binding of thiols to this surface removes the reconstruction due to the S-Au bond being stronger than the Au-Au bond.[9] Furthermore, it is thought that this strong interaction with the thiol results in the lifting of some gold atoms from the surface to sit on top of the substrate lattice, referred to as Au adatoms.[29] It is also known that molecules move on the surface as mobile thiolate-Au adatom complexes.[30] Computational

analyses have shown that there are multiple stable binding configurations with similar energies: one sulfur bound in a three-fold hollow site, one sulfur bound in a two-fold bridge site, one sulfur atop a Au adatom, and two sulfur atoms bound to a single Au adatom.[31-36] In juxtaposition, selenols bind to Au{111} surfaces with greater mobility and promiscuity and create observable moiré patterns.[19] The differences between thiol binding and selenol binding will be expanded upon further in Chapter 3 of this thesis.

1.2.2 Intermolecular Interactions within the Monolayer

While the interactions of the head group and the surface are the primary driver of assembly and differences in these interactions can result in significantly different monolayers, the interactions between molecular adsorbates can play substantial roles in terms of stability and morphology of the resulting monolayers. The interactions within the monolayer can vary in strength and complexity. In the case of the prototypical alkanethiol system, van der Waals interactions are the dominating intermolecular force; but systems can have stronger interactions in the form of dipole-dipole interactions and even stronger forces in the form of hydrogen bonding. With an alkyl chain, each methylene unit contributes approximately 1 kcal/mol of interaction energy and thus, with longer chain length there is increased stability.[30,37] The molecular backbone can also be functionalized further to alter these van der Waals interactions or to introduce new interactions. Examples of these functional groups include alkenes, alkynes, amides, aryl groups, diacetylene, oligo(phenylene ethynylene), oligo(ethylene glycol), sulfones, and azobenzene.[38-41] Cage molecules are a class of SAMs where the molecular backbone is a rigid cage structure as opposed to a linear chain; these include adamantanes, decaboranes, carboranes, and fullerenes.[42-

[46] Due to their much bulkier and sterically demanding backbone, these assemblies have lower packing densities than *n*-alkanethiolate monolayers, making them more prone to displacement.[43]

As is the case with some functionalized alkanethiol systems, the backbones of carboranethiols possess the dipole moment, which can increase the intermolecular interactions within the monolayer.[47] The characteristics of carborane-based monolayers and implications of strong dipole-dipole networks within the monolayers will be discussed extensively in Section 4 of this chapter. Another avenue for increasing the intermolecular interactions with the monolayer is through hydrogen bonding as is the case with 3-mercapto-*N*-nonylpropionamide (1ATC9). 1ATC9 is chemically similar to decanethiol with the addition of an amide functional group in the backbone, near the headgroup. The inclusion of the amide group enables hydrogen bonding within the monolayer and increases the interaction energy by approximately 6 kcal/mol.[48,49] The 1ATC9 monolayer is bicomponent with one tilted phase and one phase normal to the surface.[50] The tilted phase enables a higher degree of hydrogen bonding and thus is thermodynamically favorable upon annealing.[40] A detailed mapping of the hydrogen-bonding networks in the 1ATC9 system found that these networks are continuous across traditional domain boundaries.[51]

1.2.3 The Monolayer-Environment Interface

The nature of the terminal group can both contribute to the interactions that dictate the morphology of the monolayer and determine the physical surface properties at the environmental interface. A wide array of monolayer terminations has been studied, including methyl termination, amines, alcohols, carboxylic acids, nitriles, fullerenes, and biomolecules.[1,46,52-55] Intermolecular interactions between the terminal groups are prevalent: in the case of carboxylic-acid-terminated monolayers the degree of hydrogen bonding between neighboring molecules can vary significantly

depending on the protonation/deprotonation of the terminal group.[56] Another instance of the terminal carboxylic acids influencing monolayer stability is that the monolayer becomes disordered upon esterification of the acid on the surface.[57] This *in-situ* esterification is also an example of the ability to use the monolayer terminus as a platform for additional reactions. Again in the case of carboxylic-acid-terminated monolayers, the acid group can be dimerized resulting in surface-bound polymerization initiators.[58] Carboxylic-acid-terminated monolayers are a versatile system to probe the properties of surface-bound molecules, and this strategy will be explored further in Chapter 4 of this thesis. The surface can also act as a platform for photoreactions. Surface-bound, tethered azobenzene can act as a reversible photo-switch, isomerizing between the trans and cis configurations upon exposure to UV light and blue light, respectively.[59,60] Anthracene-terminated phenylethynylthiolates within alkanethiolate monolayers can undergo photo-induced cycloaddition reactions.[61]

The terminal group of the monolayer is often the primary factor in determining the physical properties of these surfaces. In the case of the prototypical *n*-alkanethiolate monolayer, the hydrophobic terminal methyl group results in a hydrophobic monolayer; conversely, in the case of a terminal hydroxyl group on the alkane chain, the monolayer is hydrophilic, despite the majority of the molecular backbone having a hydrophobic nature. The dipole moment of a monolayer can be reversed by using either an electron-rich amine terminal group or an electron-poor nitrile terminal group.[54] Thus, the identity of the monolayer terminal group can be facile knob to tune, causing significant changes in surface properties. Furthermore, the environmental interface is the platform on which additional chemistry can occur.

1.2.4 Structure and Defects

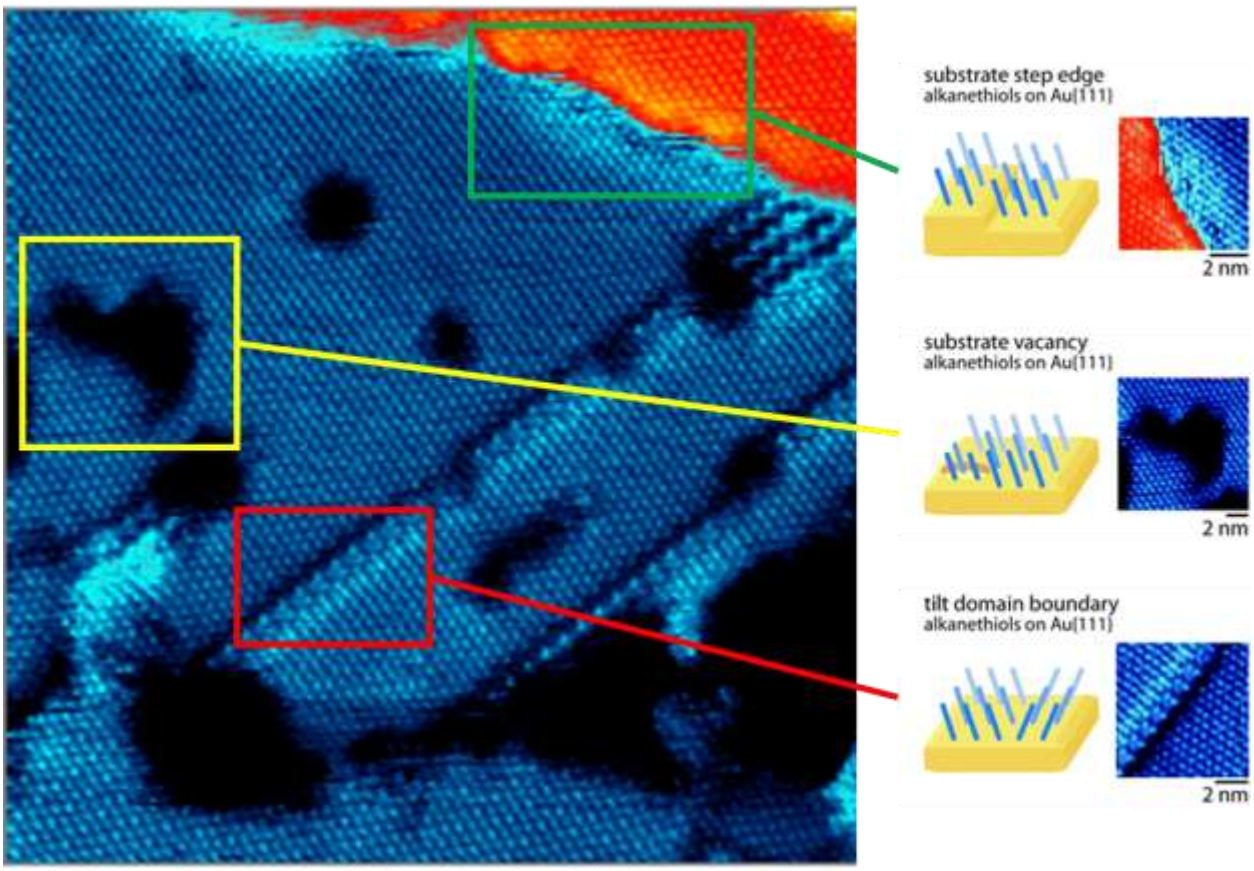

Figure 1.2 A scanning tunneling microscopy image of a dodecanethiolate self-assembled monolayer of a Au{111} substrate, V_s = -1.0 V and I_t = 1.0 pA. Seen in this image are some common monolayer defects including a substrate step edge (green), a substrate vacancy (yellow), and a tilt domain boundary (red). Adapted with permission from References 2 and 5. Copyrights 2013 Royal Society of Chemistry and 2008 American Chemical Society.

Defects in the assembled monolayers can provide insight into the mechanisms of assembly and the behavior of the monolayer and also provide a point of interaction with and manipulation of the monolayer.[5] Some defects are a result of the nature of the substrate such as the offset produced by an atomic step edge.[62] Others result from the interactions between the substrate and the absorbate molecules, such as the thiol lifting off gold atoms to produce substrate vacancies or orientational offsets in the gold attachment.[42,62] Yet others are a result of the interactions within the molecular lattice; the linear chains within *n*-alkanethiolate monolayers are titled with respect

to the surface normal and thus domain boundaries appear between regions of differing molecular azimuthal orientation and surface registry.[62] Figure 1.2 shows how these defects are observed in SAMs. These types of defects can be minimized or eliminated through subsequent monolayer processing or through the targeted choice of monolayer precursors.[63] In the case of 1-adamantanethiolate and carboranethiolate monolayers, the bulky cage backbone results in relatively no molecular tilt and as such tilt domain boundaries do not occur within these systems.[43,47] On the other hand, defects have been used to advantage for the insertion and study of isolated molecules.[59,64-66] Understanding and controlling the nature and distribution of defects in a monolayer are critical towards expanding the applications of SAMs for organic electronics, bottom-up assembly, and interfacial materials.

1.3 Characterization of Surface Properties

A variety of microscopic and spectroscopic methods are used to interrogate the properties of SAMs. Predominant among these is scanning tunneling microscopy (STM), which can gain real-space sub-Ångstrom structural information about a surface assembly. Scanning tunneling microscopy was developed by Binnig and Rohrer for which they received the Nobel Prize in 1986 and relies on the principle of quantum tunneling.[67,68] An atomically sharp tip is brought within tunneling distance of the sample surface, and a voltage is applied across this junction to produce a tunneling current. In constant-current mode, as used in the studies described here, the tip is rastered across the surface and the distance between the tip and sample is adjusted *via* a feedback loop to maintain a constant tunneling current. This change in tip height produces the STM image, which is a convulsion of both the physical typography of the surface and the electronic density of states. STM has resolution on the molecular and atomic level, but so do other techniques like X-ray

crystallography. One key advantage that STM has is that images are recorded in real space and are not ensemble averages and thus can observe unique, non-periodic features that are averaged out in other methods. As such, STM, often in combination with spectroscopic methods, can be a powerful tool for investigating the morphology of surface assemblies and their electronic properties.

Often STM cannot provide information about the chemical nature of SAMs and other techniques are required. Fourier transform infrared spectroscopy (FTIR) can be used to track the chemical fingerprints of surface species. This complementary technique can aid in determining the chemical functionalization of a monolayer, differentiate between isomeric species, and determine compositions of heterogeneous SAMs. Another powerful surface-sensitive technique is X-ray photoelectron spectroscopy (XPS), which provides elemental and oxidative state information. Using XPS, SAM stability can be tested; furthermore, elemental binding energies can provide further information on monolayer interactions, and in some cases, XPS can provide quantitative compositional information. Additional techniques are used to assess the surface and interfacial properties of SAMs. As mentioned above, one of the malleable properties of SAMs is their hydrophobicity/hydrophilicity, which can be assessed through contact angle measurements. This technique can be expanded further to perform contact angle titrations, a method that probes the reactivity of functional groups on the surface.[69] The acid-base interactions of surface-bound molecules will be elaborated further in Chapter 4. Another property of interest is the surface work function and how it is affected by the SAM interface. To probe this feature, ultraviolet photoelectron spectroscopy (UPS) is used. Through the use of these techniques, the physical and chemical properties of SAMs can be adeptly characterized.

1.4 Carboranethiol-Based Self-Assembled Monolayers

Beyond self-assembly in general, this thesis focuses on SAMs composed of carborane derivatives. Dicarba-*closo*-dodecaboranes, or carboranes, have a molecular formula of $C_2B_{10}H_{12}$ where the central structure is an icosahedral cage composed of the two carbon atoms and ten boron atoms. First synthesized in 1963, they are a widely studied boron cluster.[70-72] They have several advantageous features that make them useful as SAM precursors. First, as mentioned above, due to their rigid and symmetric cage molecule structure they tend to create SAMs that are more pristine and defect free compared to traditional *n*-alkanethiolate SAMs.[42] Since the carboranethiol molecule has relatively no tilt on the surface, these monolayers exhibit no tilt domain boundaries; even other surface registration-based defects are minimized such as rotational domain boundaries, which appear much more subtle.[47] The second advantage of the carboranethiol system is that there are wide variety of isomers, each with a unique dipole moment, as shown in Figure 1.3.[73] The dipole moment is determined by the position of the carbon atoms in the cage; thus, by using a different isomer with a different arrangement of carbon atoms, the dipole-dipole interactions within the monolayer can be tuned. However, since the general structure of the cage remains unchanged between isomers, other chemical and physical properties remain the same. The dipole-dipole interactions within these monolayers are quite pronounced, as evidenced by the fact that at cryogenic temperatures these molecules will spontaneously orient their dipoles in the same direction; this behavior is even observed across traditional domain boundaries and substrate step edges.[74] Furthermore, these dipole-dipole networks can be used to tune surface properties such as the work function; this modification has been accomplished on both metal surfaces, such as Au and Ag, as well as semiconductor surfaces, such as Ge.[28,75] Additionally, these networks can also control the alignment of self-assembled molecular networks assembled on top of the SAM.[73]

Lastly, a noteworthy advantage of carboranes is that they serve as scaffolds for additional functional groups. This feature has already been applied to facilitate the functionalization of the thiol group which is used for surface attachment. Additional functional groups are available in the carborane cage that can be multifunctional.[28,76]

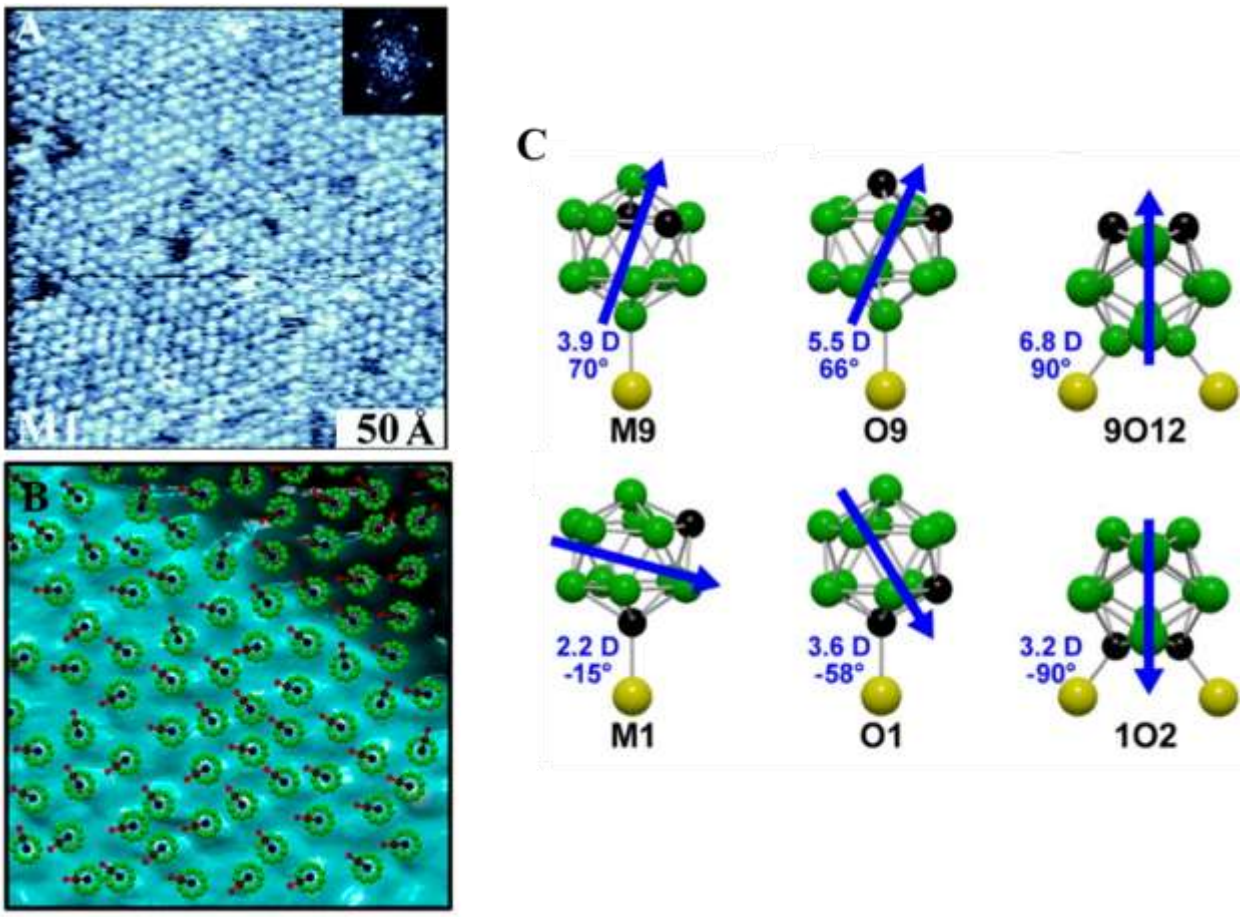

Figure 1.3 (A) A scanning tunneling microscopy image of a *m*-1-carboranethiolate monolayer. (B) A schematic overlay on a scanning tunneling microscopy image showing the spontaneous dipole alignment at cryogenic temperatures. (C) Models of six different carboranethiol and carboranedithiols isomers, each denoted with the orientation and magnitude of their dipole moment. Adapted with permission from References 47, 73, and 74. Copyrights 2009 American Chemical Society, 2016 American Chemical Society, and 2015 American Chemical Society.

1.5 Perspectives

Self-assembled monolayers have become a facile and reliable method to pattern surfaces with specific morphologies and material properties. Further understanding of intermolecular interactions, assembly kinetics, and changes in chemical behavior of surface bound molecules is still required to access the full potential applications of SAMs for organic electronics, bottom-up assembly, and interfacial materials. Advances in surface science hold the promise of finding avenues to create designer materials with predetermined chemical and physical properties.

1.6 Thesis Overview

This chapter has provided an overview of self-assembly, characterization of surface assemblies, and carboranethiol-based systems, which will be a focus of this thesis. Chapter 2 will describe our group's published work on carboranedithiolate monolayers and how the morphology of these monolayers can be easily tuned with simple acid-base chemistry. Chapter 2 has been modified with permission from the following manuscript: Thomas, J. C.; Goronzy, D. P.; Serino, A. C.; Auluck, H. S.; Irving, O. R.; Jimenez-Izal, E.; Deirmenjian, J. M.; Macháček, J.; Sautet, P.; Alexandrova, A. N.; Baše, T.; Weiss, P. S. Acid–Base Control of Valency within Carboranedithiol Self-Assembled Monolayers: Molecules Do the Can-Can. *ACS Nano* **2018,** *12*, 2211-2221. Copyright 2018 American Chemical Society. Chapter 3 will discuss carboraneselenolate monolayers and how they deviate in characteristics both from carboranethiolate monolayers and other selenolate-based system; the chapter has been modified from a manuscript in preparation entitled: Dipole-Induced Stabilization in Carboraneselenolate Self-Assembled Monolayers. Chapter 4 will describe the characterization of bifunctional carboxylic acid carboranethiolate monolayers. Not only is the difference in monolayer morphology of interest, but also the changes

in chemical behavior of the carboxylic acid when surface-bound in a monolayer. The chapter has been modified from a manuscript in preparation entitled: Influence of Terminal Carboxyl Group on Structure and Reactivity of Functionalized *m*-Carboranethiolate Self-Assembled Monolayers. Chapter 5 will examine the lithographic application of carboxylic acid carboranethiolate monolayers in combination with chemical lift-off lithography; the chapter has been modified from a manuscript in preparation entitled: Characterization of Bifunctional Boron Cluster Assemblies Modified *via* Chemical Lift-Off Lithography. Chapter 6 will cover my conclusions and perspectives on future directions of carborane-based monolayers.

1.7 References

(1) Love, J. C.; Estroff, L. A.; Kriebel, J. K.; Nuzzo, R. G.; Whitesides, G. M. Self-Assembled Monolayers of Thiolates on Metals as a Form of Nanotechnology. *Chem. Rev.* **2005,** *105*, 1103-1170.

(2) Claridge, S. A.; Liao, W.-S.; Thomas, J. C.; Zhao, Y.; Cao, H. H.; Cheunkar, S.; Serino, A. C.; Andrews, A. M.; Weiss, P. S. From the Bottom Up: Dimensional Control and Characterization in Molecular Monolayers. *Chem. Soc. Rev.* **2013,** *42*, 2725-2745.

(3) Nuzzo, R. G.; Zegarski, B. R.; Dubois, L. H. Fundamental Studies of the Chemisorption of Organosulfur Compounds on Gold(111). Implications for Molecular Self-Assembly on Gold Surfaces. *J. Am. Chem. Soc.* **1987,** *109*, 733-740.

(4) Nuzzo, R. G.; Allara, D. L. Adsorption of Bifunctional Organic Disulfides on Gold Surfaces. *J. Am. Chem. Soc.* **1983,** *105*, 4481-4483.

(5) Weiss, P. S. Functional Molecules and Assemblies in Controlled Environments: Formation and Measurements. *Acc. Chem. Res.* **2008,** *41*, 1772-1781.

(6) Shaporenko, A.; Ulman, A.; Terfort, A.; Zharnikov, M. Self-Assembled Monolayers of Alkaneselenolates on (111) Gold and Silver. *J. Phys. Chem. B* **2005,** *109*, 3898-3906.

(7) Laibinis, P. E.; Whitesides, G. M.; Allara, D. L.; Tao, Y. T.; Parikh, A. N.; Nuzzo, R. G. Comparison of the Structures and Wetting Properties of Self-Assembled Monolayers of N-Alkanethiols on the Coinage Metal Surfaces, Copper, Silver, and Gold. *J. Am. Chem. Soc.* **1991,** *113*, 7152-7167.

(8) Zangmeister, C. D.; Picraux, L. B.; van Zee, R. D.; Yao, Y.; Tour, J. M. Energy-Level Alignment and Work Function Shifts for Thiol-Bound Monolayers of Conjugated Molecules Self-Assembled on Ag, Cu, Au, and Pt. *Chem. Phys. Lett.* **2007,** *442*, 390-393.

(9) Ulman, A. Formation and Structure of Self-Assembled Monolayers. *Chem. Rev.* **1996,** *96*, 1533-1554.

(10) Azzaroni, O.; Vela, M. E.; Fonticelli, M.; Benítez, G.; Carro, P.; Blum, B.; Salvarezza, R. C. Electrodesorption Potentials of Self-Assembled Alkanethiolate Monolayers on Copper Electrodes. An Experimental and Theoretical Study. *J. Phys. Chem. B* **2003,** *107*, 13446-13454.

(11) Love, J. C.; Wolfe, D. B.; Chabinyc, M. L.; Paul, K. E.; Whitesides, G. M. Self-Assembled Monolayers of Alkanethiolates on Palladium Are Good Etch Resists. *J. Am. Chem. Soc.* **2002,** *124*, 1576-1577.

(12) Carvalho, A.; Geissler, M.; Schmid, H.; Michel, B.; Delamarche, E. Self-Assembled Monolayers of Eicosanethiol on Palladium and Their Use in Microcontact Printing. *Langmuir* **2002,** *18*, 2406-2412.

(13) Bent, S. F. Organic Functionalization of Group Iv Semiconductor Surfaces: Principles, Examples, Applications, and Prospects. *Surf. Sci.* **2002,** *500*, 879-903.

(14) Buriak, J. M. Organometallic Chemistry on Silicon and Germanium Surfaces. *Chem. Rev.* **2002,** *102*, 1271-1308.

(15) Goronzy, D. P.; Ebrahimi, M.; Rosei, F.; Arramel; Fang, Y.; De Feyter, S.; Tait, S. L.; Wang, C.; Beton, P. H.; Wee, A. T. S.; Weiss, P. S.; Perepichka, D. F. Supramolecular Assemblies on Surfaces: Nanopatterning, Functionality, and Reactivity. *ACS Nano* **2018,** *12*, 7445-7481.

(16) Guttentag, A. I.; Barr, K. K.; Song, T.-B.; Bui, K. V.; Fauman, J. N.; Torres, L. F.; Kes, D. D.; Ciomaga, A.; Gilles, J.; Sullivan, N. F.; Yang, Y.; Allara, D. L.; Zharnikov, M.; Weiss, P. S. Hexagons to Ribbons: Flipping Cyanide on Au{111}. *J. Am. Chem. Soc.* **2016,** *138*, 15580-15586.

(17) Murphy, K. L.; Tysoe, W. T.; Bennett, D. W. A Comparative Investigation of Aryl Isocyanides Chemisorbed to Palladium and Gold: An ATR-IR Spectroscopic Study. *Langmuir* **2004,** *20*, 1732-1738.

(18) Huang, F. K.; Horton, R. C.; Myles, D. C.; Garrell, R. L. Selenolates as Alternatives to Thiolates for Self-Assembled Monolayers: A Sers Study. *Langmuir* **1998,** *14*, 4802-4808.

(19) Monnell, J. D.; Stapleton, J. J.; Jackiw, J. J.; Dunbar, T.; Reinerth, W. A.; Dirk, S. M.; Tour, J. M.; Allara, D. L.; Weiss, P. S. Ordered Local Domain Structures of Decaneselenolate and Dodecaneselenolate Monolayers on Au{111}. *J. Phys. Chem. B* **2004,** *108*, 9834-9841.

(20) Hohman, J. N.; Kim, M.; Schüpbach, B.; Kind, M.; Thomas, J. C.; Terfort, A.; Weiss, P. S. Dynamic Double Lattice of 1-Adamantaneselenolate Self-Assembled Monolayers on Au{111}. *J. Am. Chem. Soc.* **2011,** *133*, 19422-19431.

(21) Allara, D. L.; Parikh, A. N.; Rondelez, F. Evidence for a Unique Chain Organization in Long Chain Silane Monolayers Deposited on Two Widely Different Solid Substrates. *Langmuir* **1995,** *11*, 2357-2360.

(22) Lio, A.; Charych, D. H.; Salmeron, M. Comparative Atomic Force Microscopy Study of the Chain Length Dependence of Frictional Properties of Alkanethiols on Gold and Alkylsilanes on Mica. *J. Phys. Chem. B* **1997,** *101*, 3800-3805.

(23) Jewell, A. D.; Kyran, S. J.; Rabinovich, D.; Sykes, E. C. H. Effect of Head-Group Chemistry on Surface-Mediated Molecular Self-Assembly. *Chemistry – A European Journal* **2012,** *18*, 7169-7178.

(24) Gouzman, I.; Dubey, M.; Carolus, M. D.; Schwartz, J.; Bernasek, S. L. Monolayer *Vs.* Multilayer Self-Assembled Alkylphosphonate Films: X-Ray Photoelectron Spectroscopy Studies. *Surf. Sci.* **2006,** *600*, 773-781.

(25) Kamenetska, M.; Dell'Angela, M.; Widawsky, J. R.; Kladnik, G.; Verdini, A.; Cossaro, A.; Cvetko, D.; Morgante, A.; Venkataraman, L. Structure and Energy Level Alignment of Tetramethyl Benzenediamine on Au(111). *J. Phys. Chem. C* **2011,** *115*, 12625-12630.

(26) Venkataraman, L.; Klare, J. E.; Tam, I. W.; Nuckolls, C.; Hybertsen, M. S.; Steigerwald, M. L. Single-Molecule Circuits with Well-Defined Molecular Conductance. *Nano Lett.* **2006,** *6*, 458-62.

(27) Lim, M. S.; Feng, K.; Chen, X.; Wu, N.; Raman, A.; Nightingale, J.; Gawalt, E. S.; Korakakis, D.; Hornak, L. A.; Timperman, A. T. Adsorption and Desorption of Stearic Acid Self-Assembled Monolayers on Aluminum Oxide. *Langmuir* **2007,** *23*, 2444-2452.

(28) Serino, A. C.; Anderson, M. E.; Saleh, L. M. A.; Dziedzic, R. M.; Mills, H.; Heidenreich, L. K.; Spokoyny, A. M.; Weiss, P. S. Work Function Control of Germanium through Carborane-Carboxylic Acid Surface Passivation. *ACS Appl. Mater. Interfaces* **2017,** *9*, 34592-34596.

(29) Yu, M.; Bovet, N.; Satterley, C. J.; Bengió, S.; Lovelock, K. R. J.; Milligan, P. K.; Jones, R. G.; Woodruff, D. P.; Dhanak, V. True Nature of an Archetypal Self-Assembly System: Mobile Au-Thiolate Species on Au(111). *Phys. Rev. Lett.* **2006,** *97*, 166102.

(30) Stranick, S. J.; Parikh, A. N.; Allara, D. L.; Weiss, P. S. A New Mechanism for Surface Diffusion: Motion of a Substrate-Adsorbate Complex. *J. Phys. Chem.* **1994,** *98*, 11136-11142.

(31) Häkkinen, H. The Gold–Sulfur Interface at the Nanoscale. *Nat. Chem.* **2012,** *4*, 443.

(32) Maksymovych, P.; Voznyy, O.; Dougherty, D. B.; Sorescu, D. C.; Yates, J. T. Gold Adatom as a Key Structural Component in Self-Assembled Monolayers of Organosulfur Molecules on Au(111). *Prog. Surf. Sci.* **2010,** *85*, 206-240.

(33) Cossaro, A.; Mazzarello, R.; Rousseau, R.; Casalis, L.; Verdini, A.; Kohlmeyer, A.; Floreano, L.; Scandolo, S.; Morgante, A.; Klein, M. L.; Scoles, G. X-Ray Diffraction and Computation Yield the Structure of Alkanethiols on Gold(111). *Science* **2008,** *321*, 943.

(34) Mazzarello, R.; Cossaro, A.; Verdini, A.; Rousseau, R.; Casalis, L.; Danisman, M. F.; Floreano, L.; Scandolo, S.; Morgante, A.; Scoles, G. Structure of a CH_3S Monolayer on Au(111) Solved by the Interplay between Molecular Dynamics Calculations and Diffraction Measurements. *Phys. Rev. Lett.* **2007,** *98*, 016102.

(35) Chaudhuri, A.; Lerotholi, T. J.; Jackson, D. C.; Woodruff, D. P.; Dhanak, V. R. The Local Adsorption Structure of Methylthiolate and Butylthiolate on Au(111): A Photoemission Core-Level Shift Investigation. *Surf. Sci.* **2010,** *604*, 227-234.

(36) Otálvaro, D.; Veening, T.; Brocks, G. Self-Assembled Monolayer Induced Au(111) and Ag(111) Reconstructions: Work Functions and Interface Dipole Formation. *J. Phys. Chem. C* **2012,** *116*, 7826-7837.

(37) Vericat, C.; Vela, M. E.; Benitez, G.; Carro, P.; Salvarezza, R. C. Self-Assembled Monolayers of Thiols and Dithiols on Gold: New Challenges for a Well-Known System. *Chem. Soc. Rev.* **2010,** *39*, 1805-1834.

(38) Zheng, Y. B.; Payton, J. L.; Chung, C.-H.; Liu, R.; Cheunkar, S.; Pathem, B. K.; Yang, Y.; Jensen, L.; Weiss, P. S. Surface-Enhanced Raman Spectroscopy to Probe Reversibly Photoswitchable Azobenzene in Controlled Nanoscale Environments. *Nano Lett.* **2011,** *11*, 3447-3452.

(39) Smith, R. K.; Lewis, P. A.; Weiss, P. S. Patterning Self-Assembled Monolayers. *Prog. Surf. Sci.* **2004,** *75*, 1-68.

(40) Kim, M.; Hohman, J. N.; Serino, A. C.; Weiss, P. S. Structural Manipulation of Hydrogen-Bonding Networks in Amide-Containing Alkanethiolate Monolayers via Electrochemical Processing. *J. Phys. Chem. C* **2010,** *114*, 19744-19751.

(41) Grave, C.; Risko, C.; Shaporenko, A.; Wang, Y.; Nuckolls, C.; Ratner, M. A.; Rampi, M. A.; Zharnikov, M. Charge Transport through Oligoarylene Self-Assembled Monolayers: Interplay of Molecular Organization, Metal–Molecule Interactions, and Electronic Structure. *Adv. Funct. Mater.* **2007,** *17*, 3816-3828.

(42) Hohman, J. N.; Claridge, S. A.; Kim, M.; Weiss, P. S. Cage Molecules for Self-Assembly. *Mater. Sci. Eng. R Rep.* **2010,** *70*, 188-208.

(43) Kim, M.; Hohman, J. N.; Morin, E. I.; Daniel, T. A.; Weiss, P. S. Self-Assembled Monolayers of 2-Adamantanethiol on Au{111}: Control of Structure and Displacement. *The Journal of Physical Chemistry A* **2009,** *113*, 3895-3903.

(44) Wang, S.; Goronzy, D. P.; Young, T. D.; Wattanatorn, N.; Stewart, L.; Baše, T.; Weiss, P. S. Formation of Highly Ordered Terminal Alkyne Self-Assembled Monolayers on the Au{111} Surface through Substitution of 1-Decaboranethiolate. *J. Phys. Chem. C* **2019,** *123*, 1348-1353.

(45) Bould, J.; Macháček, J.; Londesborough, M. G. S.; Macías, R.; Kennedy, J. D.; Bastl, Z.; Rupper, P.; Baše, T. Decaborane Thiols as Building Blocks for Self-Assembled Monolayers on Metal Surfaces. *Inorg. Chem.* **2012,** *51*, 1685-1694.

(46) Patnaik, A.; Setoyama, H.; Ueno, N. Surface/Interface Electronic Structure in C_{60} Anchored Aminothiolate Self-Assembled Monolayer: An Approach to Molecular Electronics. *J. Chem. Phys.* **2004,** *120*, 6214-6221.

(47) Hohman, J. N.; Zhang, P.; Morin, E. I.; Han, P.; Kim, M.; Kurland, A. R.; McClanahan, P. D.; Balema, V. P.; Weiss, P. S. Self-Assembly of Carboranethiol Isomers on Au{111}: Intermolecular Interactions Determined by Molecular Dipole Orientations. *ACS Nano* **2009,** *3*, 527-536.

(48) Clegg, R. S.; Reed, S. M.; Hutchison, J. E. Self-Assembled Monolayers Stabilized by Three-Dimensional Networks of Hydrogen Bonds. *J. Am. Chem. Soc.* **1998,** *120*, 2486-2487.

(49) Clegg, R. S.; Hutchison, J. E. Control of Monolayer Assembly Structure by Hydrogen Bonding Rather Than by Adsorbate−Substrate Templating. *J. Am. Chem. Soc.* **1999,** *121*, 5319-5327.

(50) Moore, A. M.; Yeganeh, S.; Yao, Y.; Claridge, S. A.; Tour, J. M.; Ratner, M. A.; Weiss, P. S. Polarizabilities of Adsorbed and Assembled Molecules: Measuring the Conductance through Buried Contacts. *ACS Nano* **2010,** *4*, 7630-7636.

(51) Thomas, J. C.; Goronzy, D. P.; Dragomiretskiy, K.; Zosso, D.; Gilles, J.; Osher, S. J.; Bertozzi, A. L.; Weiss, P. S. Mapping Buried Hydrogen-Bonding Networks. *ACS Nano* **2016,** *10*, 5446-5451.

(52) Lee, S.-H.; Lin, W.-C.; Chang, C.-J.; Huang, C.-C.; Liu, C.-P.; Kuo, C.-H.; Chang, H.-Y.; You, Y.-W.; Kao, W.-L.; Yen, G.-J.; Kuo, D.-Y.; Kuo, Y.-T.; Tsai, M.-H.; Shyue, J.-J. Effect of the Chemical Composition on the Work Function of Gold Substrates Modified by Binary Self-Assembled Monolayers. *Phys. Chem. Chem. Phys.* **2011,** *13*, 4335-4339.

(53) Carot, M. L.; Macagno, V. A.; Paredes-Olivera, P.; Patrito, E. M. Structure of Mixed Carboxylic Acid Terminated Self-Assembled Monolayers: Experimental and Theoretical Investigation. *J. Phys. Chem. C* **2007,** *111*, 4294-4304.

(54) Romaner, L.; Heimel, G.; Zojer, E. Electronic Structure of Thiol-Bonded Self-Assembled Monolayers: Impact of Coverage. *Phys. Rev. B* **2008,** *77*, 045113.

(55) Vaish, A.; Shuster, M. J.; Cheunkar, S.; Singh, Y. S.; Weiss, P. S.; Andrews, A. M. Native Serotonin Membrane Receptors Recognize 5-Hydroxytryptophan-Functionalized Substrates: Enabling Small-Molecule Recognition. *ACS Chemical Neuroscience* **2010,** *1*, 495-504.

(56) Osnis, A.; Sukenik, C. N.; Major, D. T. Structure of Carboxyl-Acid-Terminated Self-Assembled Monolayers from Molecular Dynamics Simulations and Hybrid Quantum Mechanics–Molecular Mechanics Vibrational Normal-Mode Analysis. *J. Phys. Chem. C* **2012,** *116*, 770-782.

(57) Saavedra, H. M.; Thompson, C. M.; Hohman, J. N.; Crespi, V. H.; Weiss, P. S. Reversible Lability by in Situ Reaction of Self-Assembled Monolayers. *J. Am. Chem. Soc.* **2009,** *131*, 2252-2259.

(58) Cohen, R.; Mazuz, Y.; Tikhonov, M.; Sukenik, C. N. Carboxylic Acid Decorated Self-Assembled Monolayer Films: New Acid Synthesis Chemistry and Reaction Chemistry Including Bridged Diacyl Peroxide Preparation. *Langmuir* **2015,** *31*, 3049-3058.

(59) Kumar, A. S.; Ye, T.; Takami, T.; Yu, B.-C.; Flatt, A. K.; Tour, J. M.; Weiss, P. S. Reversible Photo-Switching of Single Azobenzene Molecules in Controlled Nanoscale Environments. *Nano Lett.* **2008,** *8*, 1644-1648.

(60) Cho, J.; Berbil-Bautista, L.; Levy, N.; Poulsen, D.; Fréchet, J. M. J.; Crommie, M. F. Functionalization, Self-Assembly, and Photoswitching Quenching for Azobenzene Derivatives Adsorbed on Au(111). *J. Chem. Phys.* **2010,** *133*, 234707.

(61) Kim, M.; Hohman, J. N.; Cao, Y.; Houk, K. N.; Ma, H.; Jen, A. K. Y.; Weiss, P. S. Creating Favorable Geometries for Directing Organic Photoreactions in Alkanethiolate Monolayers. *Science* **2011,** *331*, 1312.

(62) Poirier, G. E. Characterization of Organosulfur Molecular Monolayers on Au(111) Using Scanning Tunneling Microscopy. *Chem. Rev.* **1997,** *97*, 1117-1128.

(63) Bumm, L. A.; Arnold, J. J.; Charles, L. F.; Dunbar, T. D.; Allara, D. L.; Weiss, P. S. Directed Self-Assembly to Create Molecular Terraces with Molecularly Sharp Boundaries in Organic Monolayers. *J. Am. Chem. Soc.* **1999,** *121*, 8017-8021.

(64) Moore, A. M.; Dameron, A. A.; Mantooth, B. A.; Smith, R. K.; Fuchs, D. J.; Ciszek, J. W.; Maya, F.; Yao, Y.; Tour, J. M.; Weiss, P. S. Molecular Engineering and Measurements to Test Hypothesized Mechanisms in Single Molecule Conductance Switching. *J. Am. Chem. Soc.* **2006,** *128*, 1959-1967.

(65) Lewis, P. A.; Inman, C. E.; Maya, F.; Tour, J. M.; Hutchison, J. E.; Weiss, P. S. Molecular Engineering of the Polarity and Interactions of Molecular Electronic Switches. *J. Am. Chem. Soc.* **2005,** *127*, 17421-17426.

(66) Dameron, A. A.; Hampton, J. R.; Smith, R. K.; Mullen, T. J.; Gillmor, S. D.; Weiss, P. S. Microdisplacement Printing. *Nano Lett.* **2005,** *5*, 1834-1837.

(67) Binnig, G.; Rohrer, H. Scanning Tunneling Microscopy-from Birth to Adolescence. *Rev. Mod. Phys.* **1987,** *59*, 615-625.

(68) Binnig, G.; Rohrer, H.; Gerber, C.; Weibel, E. Surface Studies by Scanning Tunneling Microscopy. *Phys. Rev. Lett.* **1982,** *49*, 57-61.

(69) Bain, C. D.; Whitesides, G. M. A Study by Contact Angle of the Acid-Base Behavior of Monolayers Containing .Omega.-Mercaptocarboxylic Acids Adsorbed on Gold: An Example of Reactive Spreading. *Langmuir* **1989,** *5*, 1370-1378.

(70) Grimes, R. N. *Carboranes*. Academic Press: New York, 1970.

(71) Heying, T. L.; Ager, J. W.; Clark, S. L.; Mangold, D. J.; Goldstein, H. L.; Hillman, M.; Polak, R. J.; Szymanski, J. W. A New Series of Organoboranes. I. Carboranes from the Reaction of Decaborane with Acetylenic Compounds. *Inorg. Chem.* **1963,** *2*, 1089-1092.

(72) Spokoyny, A. M.; Machan, C. W.; Clingerman, D. J.; Rosen, M. S.; Wiester, M. J.; Kennedy, R. D.; Stern, C. L.; Sarjeant, A. A.; Mirkin, C. A. A Coordination Chemistry Dichotomy for Icosahedral Carborane-Based Ligands. *Nat. Chem.* **2011,** *3,* 590.

(73) Schwartz, J. J.; Mendoza, A. M.; Wattanatorn, N.; Zhao, Y.; Nguyen, V. T.; Spokoyny, A. M.; Mirkin, C. A.; Baše, T.; Weiss, P. S. Surface Dipole Control of Liquid Crystal Alignment. *J. Am. Chem. Soc.* **2016,** *138,* 5957-5967.

(74) Thomas, J. C.; Schwartz, J. J.; Hohman, J. N.; Claridge, S. A.; Auluck, H. S.; Serino, A. C.; Spokoyny, A. M.; Tran, G.; Kelly, K. F.; Mirkin, C. A.; Gilles, J.; Osher, S. J.; Weiss, P. S. Defect-Tolerant Aligned Dipoles within Two-Dimensional Plastic Lattices. *ACS Nano* **2015,** *9,* 4734-4742.

(75) Kim, J.; Rim, Y. S.; Liu, Y.; Serino, A. C.; Thomas, J. C.; Chen, H.; Yang, Y.; Weiss, P. S. Interface Control in Organic Electronics Using Mixed Monolayers of Carboranethiol Isomers. *Nano Lett.* **2014,** *14,* 2946-2951.

(76) Thomas, J. C.; Boldog, I.; Auluck, H. S.; Bereciartua, P. J.; Dušek, M.; Macháček, J.; Bastl, Z.; Weiss, P. S.; Baše, T. Self-Assembled *p*-Carborane Analogue of *p*-Mercaptobenzoic Acid on Au{111}. *Chem. Mater.* **2015,** *27,* 5425-5435.

Chapter 2: Acid-Base Control of Valency within Carboranedithiol Self-Assembled Monolayers: Molecules Do the Can-Can

2.1 Introduction

Self-assembled monolayer (SAM) formation is driven by a combination of substrate-molecule interactions, molecule-molecule interactions, and molecule-environment interactions.[1-3] The most commonly studied SAMs, *n*-alkanethiolates on Au{111}, contain a single thiol group available for substrate binding as thiolates and have linear backbones, resulting in numerous defects that originate from gauche defects in the alkyl chains, different alkyl tilt orientations, translational and rotational lattice registry offsets, and reconstruction of the underlying substrate.[1,4-9] Monolayers formed from dialkyl disulfides on Au{111} yield identical assemblies as the Au surface cleaves the S-S bond.[10-12] In contrast, in unfunctionalized carboranethiol SAMs, the molecules do *not* tilt nor can they change their conformation; thus, there are fewer and simpler defects in comparison to SAMs composed of *n*-alkanethiols.[2-17] Interactions between carboranethiol molecules at both exposed and buried interfaces have been observed. Carboranethiol isomers with nonzero components of their dipoles parallel to the surface exhibit long-range attractive interactions due to dipole alignment.[18] This phenomenon was previously inferred from the results of competitive adsorption experiments, where carboranethiol isomers with larger in-plane dipole components outcompeted those with greater out-of-plane components.[19] Mixed assemblies of carboranethiol isomers can be used to tailor the effective metal work functions of noble metal surfaces while not changing the wetting properties of the overlying polymers and thus not changing their morphologies.[15,20] These interactions have been observed with submolecular resolution, where correlations between simultaneously acquired scanning tunneling microscopy (STM) topographic and local barrier height (LBH) images enabled the observation of single-molecule orientations within SAM matrices and demonstrated defect-tolerant dipole alignment.[16] The surfactants 9,12-carboranedithiol (9O12)

and 1,2-carboranedithiol (1O2) have been shown to be stable isomers, to functionalize noble metal surfaces, and to modify effective metal work functions due to oppositely oriented dipoles originating from the carborane backbone.[21-26] Carboranethiol SAMs can also be used to align overlying liquid crystal orientations.[27] Here, both isomers of carboranedithiol studied (1O2 and 9O12) promote formations with higher sulfur surface coverage and fewer defects due to rigid, nearly spherical backbones.

Typical SAM formation from thiols is governed by simple acid-base reactions, where an acidic thiol group (SH) is deprotonated to a thiolate (S-) on reactive surfaces.[4,28] As noted above, disulfides can form SAMs by cleaving the disulfide bonds, again leading to adsorbed thiolates.[10-12] Adsorbed thiolates form stable bonds to Au surfaces (~45 kcal/mol), stronger than typical Au-Au bonds.[3,29-31] The S-Au bond is partially ionic and partially covalent; the effective charge transfer depends on the backbone attached to the S.[32] Adsorbed, but relatively labile, thiols (i.e., with protons still in place) have also been observed within SAMs, such as *p*-carboranethiol, on Au{111} at low conentrations.[17] The ease of formation coupled with tunable defect formations contributes toward thin films with controllable intermolecular interactions and modifiable surface-mediated effects that can be used to place and to direct single molecules and supramolecular assemblies into controlled environments.[2,3,12,13,33] Acid-base chemistry, at the exposed interface, has shown broad importance in surface wettability, colloid and emulsion stability, biological signal transduction and membrane assembly, and catalysis.[34-37] We sought to manipulate and to control the valency, the molecule-substrate bond density, and subsequent monolayer formation using two different isomers of carboranedithiol on Au surfaces, both of which have the potential for one or two bonds to the substrate per molecule. Both 1O2 and 9O12 are stable in their respective dithiol and dianion states, where 1O2 is a stronger acid

compared to 9O12.[26] The acid-base properties intrinsic to homogeneous monolayers composed of either 1O2 or 9O12 can be used as a means of control.

Kitagawa and co-workers assembled adamantanetrithiol on Au{111} and found trivalent interactions that resulted in small chiral cluster structures on the surface.[38] In earlier unpublished work, we found that it is important to take into account both bond angles and substrate access in forming multivalent molecule-substrate interactions.[39,40] The lessons learned from those studies resulted in the inclusion of flexible linkers in attaching caltrops and other molecules to surfaces.[41-44]

Control of thin-film properties of both exposed and buried interfaces has broad implications, for example, for molecular devices and lithographic patterning.[3,29,33,35,45,46] These isomers of *o*-carboranedithiols serve as ideal test candidates for binding, valency, and surface bond density, where singly bound (monovalent) modes produce monolayers with lower thiolate-Au bond densities in comparison to doubly bound (divalent) modes. We demonstrate, with a variety of surface-sensitive techniques and with density functional theory (DFT) calculations, that homogeneous monolayers composed of either 1O2 or 9O12 show two distinct binding states, which are susceptible to manipulation by controlling pH, in solution, prior to deposition, as well as during deposition via exposure to acidic or basic solution; identical nearest-neighbor spacings and lattices are maintained throughout processing, independent of valency. We also show that the differences between the monovalent and divalent modes of these carboranes are not simple geometric effects, but also critically depend on electronic effects.

Scanning tunneling microscopy is able to probe the topographic landscape of surfaces with sub-Ångström precision.[7,47-50] We have previously used spectroscopic imaging modalities of STM to probe buried interfaces and layers in molecular monolayers of other systems.[7,16,32,51-55]

2.2 Results and Discussion

We assembled and measured monolayers composed of either 1O2 or 9O12 carboranedithiols on Au{111}/mica, where, upon imaging, two distinct binding states differing in apparent height in each homogeneous SAM are recorded (Figure 2.1). Both isomers form hexagonally close-packed (hcp) monolayers with nearest-neighbor spacings of 7.6 ± 0.5 Å. This formation is best explained by a $(\sqrt{7} \times \sqrt{7})R19.12°$ superstructure that is found for several carboranethiols on Au{111}.[19,56] We measured a bimodal distribution, with tunable coverages, which we attribute to both singly bound (monovalent) and doubly bound (divalent) states. Self-assembled monolayers formed of 1O2 from a neutral solution show 21 ± 8% coverage of the singly bound (greater apparent height in STM images) binding structure and, correspondingly, 79 ± 8% coverage of the doubly bound (lower apparent height) structure. These modes are differentiated as described below. Measurements over monolayers composed of 9O12 show a strong preference (98 ± 1%) for monovalent binding (less protruding, counterintuitively, as explained below) in comparison to divalent (2 ± 1%, more protruding). Images can be segmented by apparent height in topographic images by applying a gray scale threshold value that is used to compute binding concentrations in image binaries (Figure 2.9, Section 2.5). Monovalent structures in 1O2 monolayers have greater apparent heights (1.5 ± 0.3 Å with the tunneling conditions and tip used to record the data in Figure 2.1) than the divalent structures under the conditions measured; conversely, the monovalent structures in 9O12 SAMs have lower apparent heights (0.4 ± 0.2 Å with the tunneling conditions and probe tip used to record the data in Figure 2.1) than the divalent structures. The DFT calculations help explain this apparent inverted contrast for monovalent/divalent modes for 9O12.

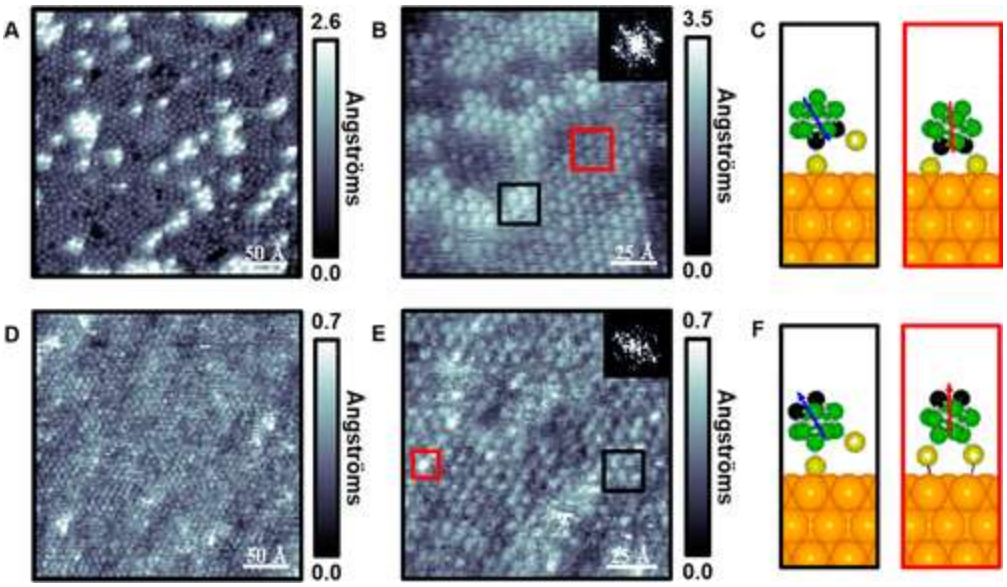

Figure 2.1 Scanning tunneling microscope images of (A, B) 1,2-$(HS)_2$-1,2-$C_2B_{10}H_{10}$ (1O2) on Au{111}/mica at two different resolutions (V_{sample} = −0.1 V, $I_{tunneling}$ = 100 pA, T = 298 K). Insets depict fast Fourier transforms (FFTs) that indicate hexagonally close-packed arrangements with nearest-neighbor spacings of 7.6 ± 0.5 Å. Two distinct binding states are highlighted in red and black. (C) Binding modes are shown schematically, where 1O2 assembles into both monovalent (black box) and divalent (red box) modes. (D, E) Scanning tunneling microscope images (Vsample = −0.1 V, Itunneling = 100 pA, T = 298 K) of 9,12-$(HS)_2$-1,2-$C_2B_{10}H_{10}$ (9O12) on Au{111}/mica at different resolutions. The inset depicts a FFT showing a hexagonally close-packed arrangement with the same spacing as 1O2. The two binding states are highlighted schematically in red and black boxes. (F) Binding modes for 9O12 are depicted schematically, where both monovalent (black box) and divalent (red box) modes are present.

We performed DFT calculations to gain a detailed understanding of molecular chemisorption modes and their related appearances in STM images and to help identify the adsorbed species. With this aim, we explored all the possible binding sites of singly and doubly dehydrogenated (i.e., monovalent and divalent, respectively) carboranedithiols on the Au{111}: face-centered cubic (fcc), hcp, over a bridge, and over a single atom (atop). The most stable species that are most closely correlated with the experimental results are shown in Figure 2.2. The geometric features of 1O2 and 9O12 are almost identical. The preferred binding site for the monovalent molecules is a fcc hollow site, which allows them to maximize the number of Au–S

bonds. Divalent species adsorb preferentially on one fcc and one hcp hollow site, although somewhat off center toward the bridge site. Overall, S–Au bond lengths are calculated to be between 2.37 and 3.06 Å. The natural bond orbital analysis shows that these are predominantly covalent bonds. For the most stable monovalent chemisorption mode, the S–C or S–B bond is simply normal to the surface. If one defines the molecular axis as connecting the center of the cage and the point halfway from one S atom to another, this line then is 28–30° from the surface normal in the monovalent binding mode. The z (surface normal) coordinates of the uppermost atoms (excluding H), also shown in Figure 2.2, reveal that the monovalent structures in both 1O2 and 9O12 extend further from the surface than their corresponding divalent species, each with a physical height difference of ca. 0.4 Å.

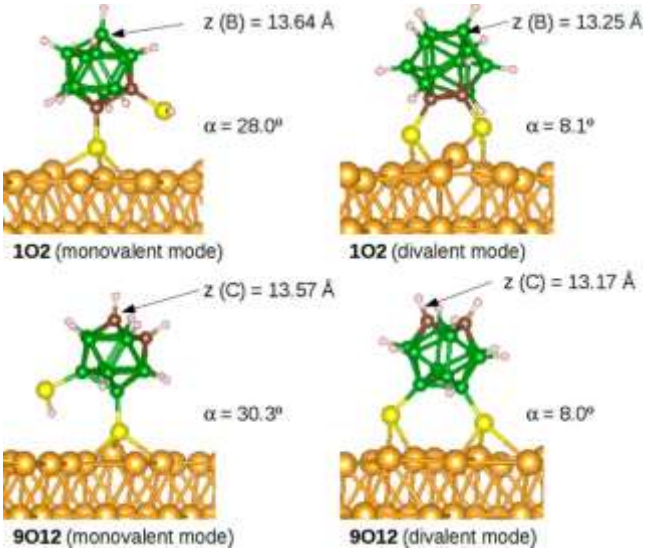

Figure 2.2 Preferred structures/binding sites for 1O2 and 9O12 in their respective monovalent and divalent binding modes. The z coordinate of the uppermost atom (without considering H atoms) and the tilt angles of the molecules with respect to the surface normal (α) are shown for each case.

The simulated STM images for these four structures are shown in Figure 2.3. In agreement with experiments and in line with the geometry, monovalent 1O2 appears more

protruding in STM images than divalent 1O2. The calculated apparent height difference in the simulated STM images is 0.6 Å. For STM images of 9O12, however, the situation is different: the monovalent mode appears less protruding, while the divalent structure appears more protruding. The height difference in the simulated images is 0.3 Å. As mentioned above, the z coordinates of the topmost atoms are higher in the monovalent than in the divalent 9O12. These results indicate that electronic effects play important roles in these systems and are critical to explain the differences between images of monovalent and divalent 1O2 and 9O12 on Au{111}.

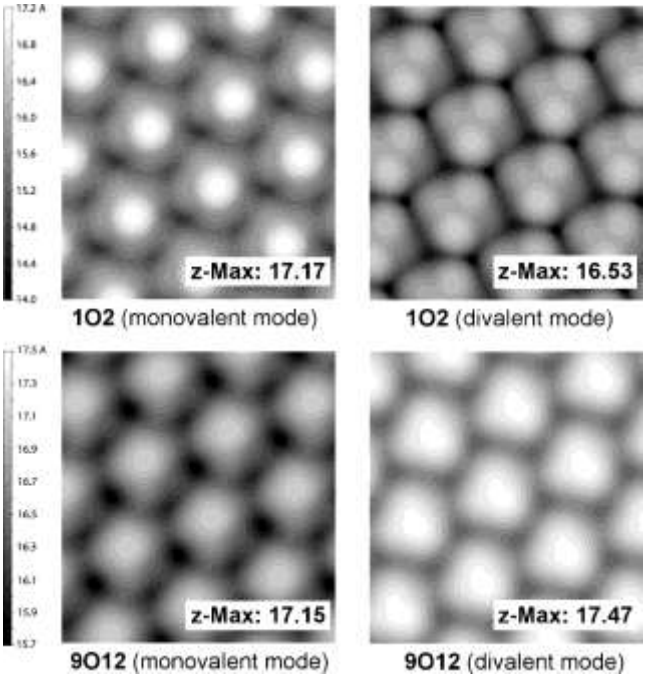

Figure 2.3 Simulated scanning tunneling microscope images for 1O2 and 9O12 in their respective monovalent and divalent binding modes, with the maximum height shown in the insets (in Å). The 10^{-4} isovalue for the charge density was used.

In order to understand this "inverted contrast" in the STM images for 9O12, we additionally plotted the charge densities within the same energy window captured by the STM (from the Fermi energy (E_F) to (E_F - 0.1 eV). From the images in Figure 2.4, we observe that the contributions of C and B in these states are quite similar for monovalent and divalent 1O2

structures. Indeed, the relative apparent heights and the relative geometrical heights correlate well. For 9O12, the charge density plots for monovalent and divalent modes are significantly different. In the case of the monovalent structure, the contributions of the carborane cage atoms in the proximity of the Fermi level are significantly smaller, which gives rise to the calculated "inverted contrast". The density plots in Figure 2.4 reflect the collective contributions of all electronic states that fall within the experimentally measured energy window (E_F - 0.1 eV). Examination of the electronic states and their energies across the entire Brillouin zone reveals that there are only a few (1–3) of these states for each species. Furthermore, for the monovalent 9O12, there is essentially only a single experimentally accessible state, the least among all considered adsorbed molecules. The projected density of states (PDOS) plots (reported in the Supporting Information) are consistent with this finding. Since carboranes, in general, have similar delocalized chemical bonding, described by Lipscomb via three-center, two-electron bonds, and obey Wade's electron-counting rules,[57] it is expected that the molecular orbitals on all the studied species are similar in structure and only shift in energy from one species to another. Thus, we suggest that the small number of electronic states detected by STM for the monovalent 9O12 simply has to do with the energies of those states relative to the experimentally probed energy window of (E_F - 0.1 eV).

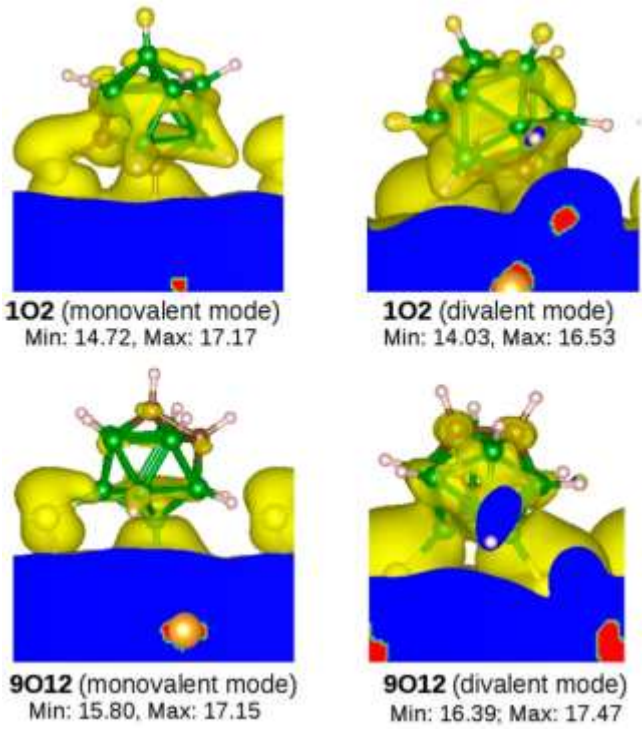

Figure 2.4 Charge density plots from the Fermi energy to E_F - 0.1 eV for (top) 1O2 and (bottom) 9O12 in their respective (left) monovalent and (right) divalent binding modes. The images are plotted with an isodensity value of 0.00002, because most of the charge density is located on the gold surface. "Min" and "Max" stand for the minimum and maximum topographic ranges (in Å), taken from the simulated STM images.

The aggregation of domains in SAMs composed of 1O2 suggests intermolecular interactions between monovalent molecules, which possess larger in-plane dipole components due to binding geometry. The reported dipoles for 1O2 and 9O12 are 3.7 and 5.5 D, respectively,[24] where this component is close to the surface normal (8°) if both S atoms are surface bound (as thiolates), however, the singly bound state is tilted ~30° (*vide supra*), yielding a parallel component (~1.8 D for 1O2 and ~2.8 D for 9O12). This dipole component results in increased intermolecular interactions between neighboring singly bound adsorbates[16] and apparently leads to phase separation. This result is confirmed in samples of each monolayer and further enables binding assignments; SAMs composed of 1O2 demonstrate aggregation between

higher protrusions, and, in SAMs composed of 9O12, higher intensity protrusions are localized and not phase aggregated. Both isomers form hcp monolayers with nearest-neighbor spacings of 7.6 ± 0.5 Å. This formation is best explained by a $(\sqrt{7} \times \sqrt{7})R19.12°$ superstructure that is found for several carboranethiols on Au{111}.[56] One of the advantages of working with carboranethiol SAMs is the conservation of surface structure among isomers so that the effects of different interactions can be tested independently of structural variations.[13,19] Both isomers form monolayers with the same spacings and surface structures; however, each contains different concentrations of monovalent and divalent modes.

Next, we tested each binding state by coupling STM with scanning tunneling spectroscopy (STS) to monitor both the exposed and buried interfaces.[7,16,54] Multimodal STM, which can simultaneously record the topographic landscape and the dipolar interface, can be used to extract molecular orientations within monolayers.[7,16,32,54,58-60] Topographic and LBH extrema are computed within a defined radial vector (the size of one molecule), and correlations are computed via block-matching,[61,62] to associate symmetric molecular apexes with dipolar extrema.[7,16] Here, local maxima (inverted minima) within SAMs composed of 9O12 can be locally attributed to carbons at the 1- and 2-positions within the cage. Conversely, local maxima within SAMs composed of 1O2 can be attributed to the local dipolar offsets within the boron cage. Correlated topographic maxima to LBH extrema values, shown in Rose plots (Figure 2.5), indicate that greater apparent protrusions in SAMs composed of 1O2 have larger offsets (3.8 ± 1.0 Å) than lesser protrusions (2.2 ± 0.6 Å). In SAMs composed of 9O12, greater protrusions show slightly smaller offsets (1.9 ± 0.3 Å) in comparison to lesser protrusions (2.6 ± 0.6 Å). For the small areas in the data shown, orientations in each homogeneous monolayer (283 ± 39° in 1O2 SAMs, 150 ± 33° in 9O12 SAMs with respect to the fast-scan direction, shown as

horizontal, left to right, in these displayed images) suggest charge-separation stabilization and relative dipolar alignment across each two-dimensional landscape. Other orientations are found in other areas of the surfaces. These observations are consistent with our binding model (monovalent and divalent modes) in each homogeneous monolayer. Since each binding state maintains the same nearest-neighbor spacing, the fraction of sulfur bound to the Au substrate can be tailored by up to a factor of 2 if binding can be manipulated. Motivated by the fact that each isomer is stable in both their dithiol and dithiolate states,[24] we modified the pH to deposit either the dithiol or the dithiolate selectively. In chemical lift-off lithography,[29-31] the amount of sulfur bound to Au may affect the amount and structure of lifted-off Au from the surface. Controlling the sulfur-surface density would enable tunable amounts of surface-bound Au available for patterning.[63]

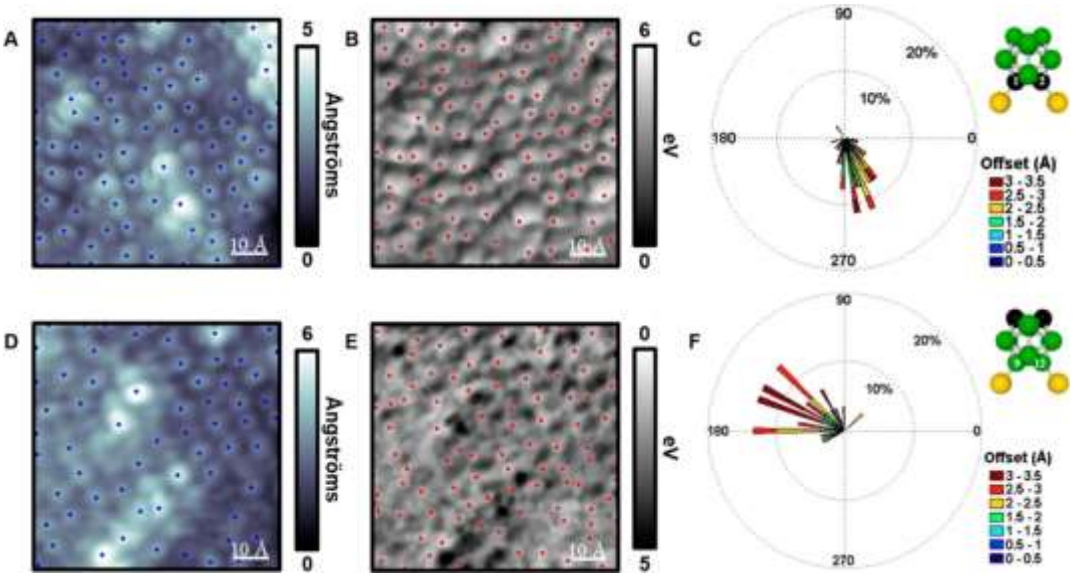

Figure 2.5 (A) Scanning tunneling microscope images, recorded at low temperature (V_{sample} = −0.5 V, $I_{tunneling}$ = 15 pA, T = 4 K) of 1,2-$(HS)_2$-1,2-$C_2B_{10}H_{10}$ (1O2) on Au{111} with local maxima (blue) highlighted. (B) Simultaneously acquired local barrier height (LBH) image, with LBH maxima (red) highlighted. (C) Rose plot (depicting correlated dipole offsets) that is binned by both magnitude (0.5 Å bins) and orientation (4° bins), and a ball-and-stick model of 1O2 showing thiol positions. (D) Scanning tunneling microscope image, recorded at low temperature (V_{sample} = −0.5 V, $I_{tunneling}$ = 15 pA, T = 4 K) of 9,12-$(HS)_2$-1,2-$C_2B_{10}H_{10}$ (9O12) on Au{111} with local maxima (blue) highlighted. (E) Simultaneously acquired LBH map, with inverted LBH maxima (red) highlighted. (F) Rose plot (depicting correlated dipole offsets) that is binned by both magnitude (0.5 Å bins) and orientation (4° bins), and a ball-and-stick model of 9O12.

We tested the resulting assemblies of each carboranedithiol in both basic (2:1 NaOH:carboranedithiol) and acidic conditions (1:1 HCl:carboranedithiol) with STM. Upon deposition under basic conditions, majority divalent binding is achieved that is attributed to deposition of the molecular dianion (dithiolate) state. Scanning tunneling microscope images depict a concentration change of each phase and show predominance of the divalent mode in monolayers fabricated under basic conditions (Figure 2.6). Images are segmented by apparent height to compute percent coverage (Figure 2.10, Section 2.5). The divalent mode is dominant in each single-component monolayer (98 ± 2% for 1O2, 99 ± 1% for 9O12) under basic conditions. The small fractions of the monovalent mode should appear more protruding for 1O2 but less

protruding for 9O12. The possible small fractions of monovalent species after deposition from basic solution may be difficult to distinguish from defects, and the monolayers, in any case, are within experimental error of being completely divalent.

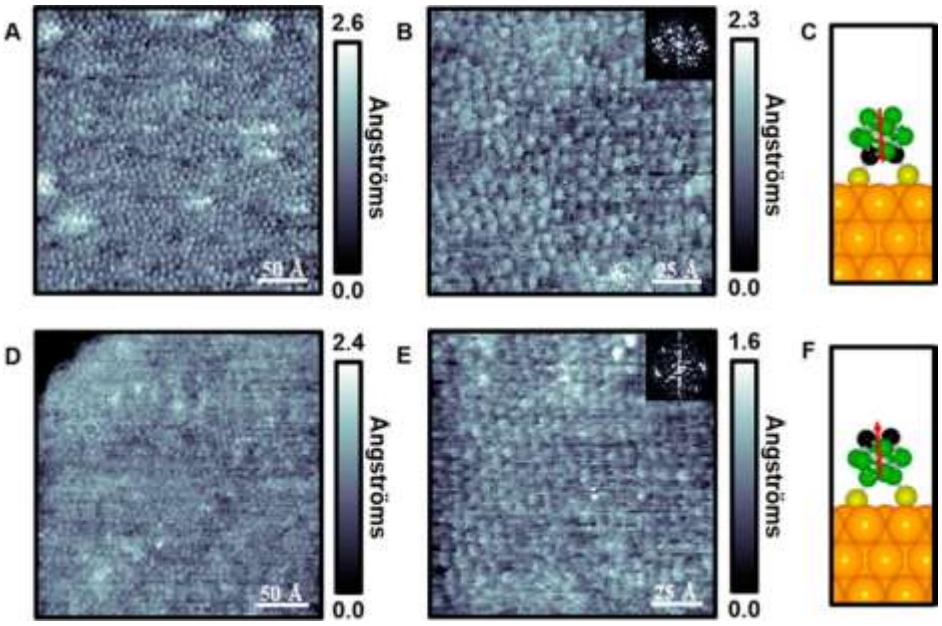

Figure 2.6 (A,B) Scanning tunneling microscope images (V_{sample} = −0.1 V, $I_{tunneling}$ = 100 pA, T = 298 K) of 1,2-$(HS)_2$-1,2-$C_2B_{10}H_{10}$ (1O2) on Au{111}/mica at two different resolutions after basic deposition conditions (2:1, NaOH:1O2). Insets depict fast Fourier transforms (FFTs) that show hexagonally close-packed arrangements with the same nearest-neighbor spacings as in Figure 2.1. (C) A majority of the 1O2 molecules have divalent surface attachment, depicted schematically. (D,E) Scanning tunneling topographs (V_{sample} = −0.1 V, $I_{tunneling}$ = 100 pA, T = 298 K) of 9,12-$(HS)_2$-1,2-$C_2B_{10}H_{10}$ (9O12) on Au{111}/mica at different resolutions after basic deposition (2:1, NaOH:9O12). Inset depicts a FFT showing the same arrangement and spacing as 1O2. (F) A divalently bound 9O12 molecule is shown schematically.

We also performed deposition experiments under acidic conditions and measured the resulting monolayers. Saturating carboranedithiol solutions with excess protons, prior to deposition, enabled somewhat higher concentrations of monovalent (thiol/thiolate) molecules, in comparison to their counterparts deposited from neutral solutions. Figure 2.7 depicts the topographic environment after acidic deposition, where an increase in (greater apparent protrusions) SAMs composed of 1O2 indicates higher concentrations (31 ± 3%) of monovalent

(thiol/thiolate) species; SAMs composed of 9O12 already show an almost total monovalent mode (lesser protrusions) at neutral pH and hence do not show any change in a proton-rich deposition environment (98 ± 1%). In summary, SAMs composed of divalent 1O2 or 9O12 (basic conditions) enable high dithiolate surface attachment, where SAMs composed of monovalent 9O12 (neutral or acidic conditions) permit low sulfur-surface attachment simply due to the controllable binding within structurally equivalent isomeric monolayers.

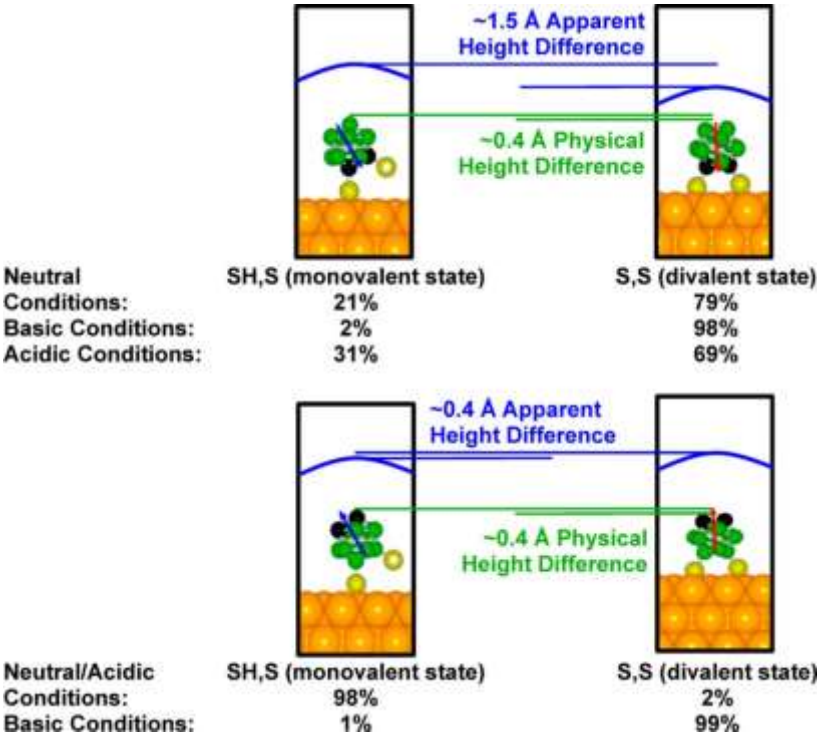

Figure 2.7 Binding assignments measured by scanning tunneling microscopy and scanning tunneling spectroscopy (STS). (Top) Self-assembled monolayers composed of 1,2-$(HS)_2$-1,2-$C_2B_{10}H_{10}$ (1O2) form into (left) a thiol/thiolate state (monovalent form) and (right) a dithiolate state (divalent form) that differ in apparent height in scanning tunneling microscope images. (Bottom) Monolayers composed of 9,12-$(HS)_2$-1,2-$C_2B_{10}H_{10}$ (9O12) form into (left) an adsorbed monothiol/monothiolate (monovalent) state, under acidic and neutral conditions, and (right) a dithiolate (divalent) state that differ in measured apparent height, as shown for the conditions in Figure 2.1. Upon deposition under basic conditions, majority dithiolate binding is observed for both isomers, as determined by STM imaging.

In order to monitor the results of SAM formation in each environment at the ensemble scale and to complement the STM measurements, we used both X-ray photoelectron spectroscopy (XPS) and Fourier transform infrared (FTIR) spectroscopy (Figure 2.8). All measured XPS and FTIR results and modeled values are detailed in Table 2.1 and Table 2.2 (Section 2.5), using the sulfur and similar B–H vibrational spectra under all conditions also measured with STM. Characteristic orbital energy peaks of each atomic species within the monolayer can be measured with XPS. Our results are consistent with prior XPS measurements in both monolayers deposited at neutral pH, where S 2p orbital peaks show shifts similar to previously reported values.[21] To test monolayer integrity, we also measured each monolayer after pH manipulation (Figures 2.12 and 2.13, Section 2.5). Values reported for XPS not only show the retention of S 2p shifts but also confirm the lack of any measured Cl^- or Na^+ within each monolayer after acid or base treatment. Using FTIR, we specifically tracked the B–H vibrational stretch, at ~2600 cm^{-1}, which is characteristic for carboranes.[19,64] Measured SAMs composed of 1O2 show similar vibrational features under all conditions; however, SAMs composed of 9O12 reveal significant intensity decreases of the peak centered at 2593 cm^{-1} and loss of the peak at 2559 cm^{-1} (Figures 2.14 and 2.15, Section 2.5), which are attributed to a change from majority monovalent to majority divalent binding in SAMs composed of 9O12 after deposition in base. Each experiment is repeated ($n > 3$) to track functional control at both the local and ensemble scales. Vibrational peaks were also modeled in the gas phase using DFT. We attribute measured peaks in SAMs composed of 1O2 to complicated collective modes of B–H stretching vibrations that involve significant contributions from all the boron vertices. In the observed doublet, the peak at higher frequency is composed of modes dominated by stretches of B–H vertices 3, 6, and 4, 5, 7, and 11, while the modes of the lower frequency peak include predominantly the stretches

of BH 8, 9, 10, and 12. In SAMs composed of 9O12, a triplet is measured with FTIR that is also modeled (Table 2.2, Section 2.5), with the calculated collective B–H stretching modes differentiated by much stronger dominance of individual vertices or their small groups. The peaks centered at ~2559 cm^{-1} belong to the stretching modes with major contribution from vertices 8 and 10, peaks at 2595 cm^{-1} are dominated by stretches at vertices 4, 5, 7, and 11, and peaks at 2633 cm^{-1} are formed by the modes involving predominantly vertices 3 and 6. Frequency calculations for the gold salts of both 1O2 and 9O12 show relative attenuation of the infrared absorption features connected with the B–H stretching modes with the major contribution from the vertices close to the S atoms upon binding the sulfur atom to gold. Especially in the 9O12 layer, the intensity decrease at ~2595 cm^{-1} and peak loss at 2595 cm^{-1} under basic conditions are consistent with our assignments and computational results. The loss of infrared absorption intensity of the stretching modes dominated by the groups of 4, 5, 7, 11 and 8, 10 B–H vertices is attributed to the effect of lateral intermolecular interactions.

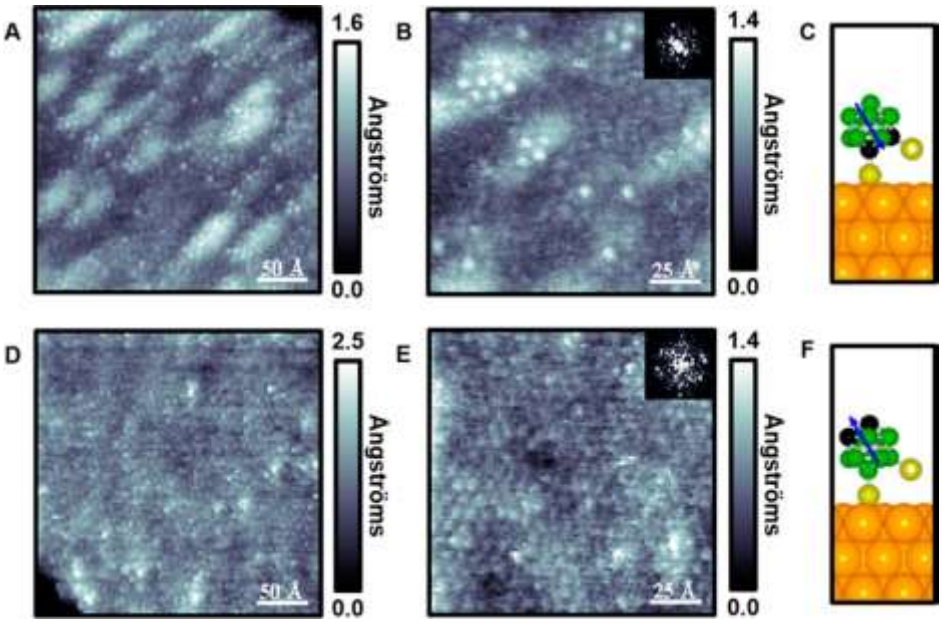

Figure 2.8 (A,B) Scanning tunneling microscope images (V_{sample} = −0.1 V, $I_{tunneling}$ = 100 pA, T = 298 K) of 1,2-$(HS)_2$-1,2-$C_2B_{10}H_{10}$ (1O2) on Au{111}/mica at two different resolutions under acidic deposition conditions (1:1, HCl:1O2). Inset depicts a fast Fourier transform (FFT) that shows a hexagonally close-packed arrangement with the same nearest-neighbor spacings measured in both basic and neutral conditions. (C) A minority push to the monovalent binding is achieved and depicted schematically. (D, E) Scanning tunneling topographs (V_{sample} = −0.1 V, $I_{tunneling}$ = 100 pA, T = 298 K) of 9,12-$(HS)_2$-1,2-$C_2B_{10}H_{10}$ (9O12) on Au{111}/mica at different resolutions after acidic deposition (1:1, HCl:9O12). Inset depicts a FFT showing the same arrangement and spacing as in neutral conditions. (F) As monolayers composed of 9O12 are already predominately monovalent, no change is measured, in comparison to neutral deposition conditions, for this system that is depicted schematically.

	1O2 n	9O12 n	1O2 b	9O12 b	1O2 a	9O12 a
Au 4f	84.0 eV	84.0 eV	84.0 eV	84.0 eV	84.0 eV	84.0 eV
B 1s	189.0 eV	189.0 eV	189.0 eV	189.0 eV	189.0 eV	189.0 eV
S 2p	162.2 eV	161.7 eV	162.2 eV	161.7 eV	162.2 eV	161.7 eV
C 1s	285.0 eV	285.0 eV	285.0 eV	285.0 eV	285.0 eV	285.0 eV
Na 1s	–	–	–	–	–	–
Cl 2p	–	–	–	–	–	–
B–H (FTIR)	2589 cm^{-1}	2559 cm^{-1}	2584 cm^{-1}	2593 cm^{-1}	2600 cm^{-1}	2564 cm^{-1}
	2598 cm^{-1}	2595 cm^{-1}	2596 cm^{-1}	2627 cm^{-1}	2591 cm^{-1}	2598 cm^{-1}
		2633 cm^{-1}				2630 cm^{-1}

Table 2.1 X-ray photoelectron spectroscopy energy shifts and Fourier transform spectroscopy frequency values in the B–H Region. Columns are titled with 1,2-$(HS)_2$-1,2-$C_2B_{10}H_{10}$ (1O2) or 9,12-$(HS)_2$-1,2-$C_2B_{10}H_{10}$ (9O12) and labeled with neutral (n), basic (b), or acidic (a) deposition conditions.

Binding configurations are further modeled on Au surfaces with all possible high-symmetry binding sites on the Au{111} surface: fcc three-fold hollow sites, hcp three-fold hollow sites, bridge sites, and atop sites. The most favorable binding modalities are presented in Tables 2.3 and 2.4 (Section 2.5), respectively, where the most stable 1O2 and 9O12 species are presented schematically in Figures 2.16 and 2.17, Section 2.5. Both monovalent and divalent binding modes, for 1O2 and 9O12, are energetically favorable.

We used both STM and STS to test the local valency within monolayers of carboranedithiols on Au{111} after control via pH. This control is monitored by apparent height in STM, dipole offsets in simultaneous STM topography and LBH measurements, infrared

spectroscopy, and XPS and is supported and understood with complementary density functional calculations.

2.3 Conclusions and Prospects

We have controlled the valency of binding within SAMs composed of different carboranedithiol isomers. These monolayers retain their two-dimensional lattice structures, independent of their binding configuration. With this level of control, we are able to dictate surface-atom-molecule stoichiometry with simple acid–base chemistry. We anticipate using these and related systems to explore the effects of valency on surface patterning[29-31,35,36,63] and dynamics.[65,66] A further step would be driving dynamics by chemistry, electric field, electrochemical potential, light, or other stimuli.[33,42-46,67-71] Systems such as these with significant chemical changes could play key roles in developing the ability to control motion at the nanoscale both for individual molecules and with coordination across assemblies.[33,44,68,70]

Creating monolayers with switchable substrate-molecule valency and bond strengths while preserving lattice constants enables exploration of this important interface and adds to the repertoire of controllable interactions at surface–molecule, molecule–molecule, and molecule–environment interfaces. By simply varying the headgroup, molecular backbone, and/or the tail group, extraordinary control is attainable.[1-3,6,8,13] Rigid cage molecules, especially carboranethiols, exhibit advantageous properties and provide test beds for independently exploring aspects of self-assembly, such as dipole interactions, molecular orientation, electron transfer, surface polarity, and now valency.[3,13,15-17,31,72] Here, bifunctional carboranedithiols assemble into well-ordered monolayers on Au surfaces with two distinct binding modes that are

confirmed by STM, STS, FTIR, XPS, and DFT. This opportunity to control is expected to be of specific use in chemical patterning, where the binding of molecules to substrates and stoichiometry of molecule-to-surface bonds are both critical.[31]

2.4 Materials and Methods

Monolayer Preparation: The chemicals 1O2 and 9O12 were synthesized and characterized in accordance with previously published methods.[21,24] Ethanol was used as received (Sigma-Aldrich, St. Louis, MO). The Au{111}/mica substrates (Agilent Technology, Tempe, AZ) were hydrogen-flame annealed prior to SAM formation with 10 passes at a rate of 0.4 Hz. Both unmodified SAMs were prepared by immersion into 1 mM ethanolic solutions and held at room temperature for approximately 24 h. Short deposition times (10 min), in acidic or basic solutions, were employed to decrease the possibility of molecular degradation. After deposition, each sample was rinsed thoroughly with neat ethanol and dried under a stream of ultrahigh-purity nitrogen for at least three cycles.

Since carboranes are known to degrade upon exposure to concentrated base,[73] we used dilute concentrations of acid and base to prevent side reactions. Hydochloric acid (12 M) and NaOH pellets were used as received (Sigma-Aldrich, St. Louis, MO). Acidic solutions were prepared by mixing 0.5 mL of 2 mM HCl in EtOH and 0.5 mL of 2 mM 1O2 or 9O12 in EtOH in a gasketed v-vial. Basic solutions were prepared by mixing 0.5 mL of 4 mM NaOH in EtOH and 0.5 mL of 2 mM 1O2 or 9O12 in EtOH. Monolayers were prepared by immersing flame-annealed Au{111}/mica substrates into modified solutions for 1 h. Larger ratios of both acid (2:1) and base (4:1) were tested, however, no differences were found.

Scanning Tunneling Microscopy: All STM measurements were performed with either a custom-built Besocke-style scanning tunneling microscope under ambient conditions or a custom-built Besocke-style scanning tunneling microscope held at cryogenic (4 K) and extreme high-vacuum ($<10^{-12}$ Torr) conditions.[74,75] Samples were held at a fixed bias ($V_{sample} = -0.5$ V), and both topographic and LBH modalities were measured in a constant current fashion (I_t = 15 pA). The tunneling gap distance was modulated above the microscope feedback loop (~3 kHz) with a sinusoidal amplitude (dz ~0.1 Å), and dI/dz was measured with a lock-in technique (Stanford Research Systems SR850 DSP, Sunnyvale, CA).[7,57] The well-known lattice of atomic Au{111}, held at 4 K, was measured and used to calibrate all low-temperature images, and the known lattice within SAMs of 1-dodecanethiolate were used to calibrate all images obtained at room temperature.

Image Analyses: All STM images were processed with automated routines developed in MATLAB (Mathworks, Natick, MA) to remove high-frequency noise and intensity spikes that may impair reliable interpretation.[7] Local maxima (minima) for both topography and LBH images were chosen as the highest (lowest) intensity pixel within a defined radial vector (the size of one molecule). Dipole offsets were computed using a block-matching approach,[16,61,62] where topographic image patches (size of one molecule) were correlated against larger LBH image patches (size of the nearest-neighbor spacing) to obtain a set of points (p and q) that were referenced and plotted. Correlated values (shown in Figure 2.5) were compared against connecting all points within a defined pixel radius, as a function of size, where correlation yielded the least artifacts (Figures 2.16 and 2.17). Gray scale threshold values were chosen based on apparent height differences to produce binary image highlights, which were further used to obtain percent coverages.

Infrared Spectroscopy: All infrared spectra were collected with a Nicolet 6700 FTIR spectrometer (Thermo Electron Corp., Waltam, MA) that was equipped with a mercury-cadmium-telluride detector, held at liquid nitrogen temperatures, and a Seagull variable-angle reflection accessory (Harrick Scientific, Inc., Ossining, NY). Water and carbon dioxide were removed from the spectrometer by an FTIR purge gas generator (Parker-Balston, Cleveland, OH). A grazing incidence reflection angle (82° with respect to the surface normal) with *p*-polarized light, a mirror speed of 1.27 cm/s, and a resolution of 2 cm^{-1} were used. Spectra were averaged over 5120 scans and normalized against spectra of perdeuterated *n*-dodecanethiolate monolayers on Au{111}.

X-ray Photoelectron Spectroscopy: All XPS spectra were collected with an AXIS Ultra DLD instrument (Kratos Analytical Inc., Chestnut Ridge, NY). A monochromatic Al K_α X-ray source (20 mA, 15 kV) with a 200 μm circular spot size that was held at ultrahigh vacuum (10^{-9} Torr) were used for all measurements. Spectra were acquired at a pass energy of 160 eV for survey spectra and 20 eV for high-resolution spectra of S 2p, C 1s, B 1s, and Au 4f regions that used a 200 ms dwell time. Different numbers of scans were carried out depending on the amount required for high-resolution spectra, which ranged from 20 scans for C 1s to 75 scans for S 2p. Binding energies were calibrated to the Au 4f peak at 83.98 eV.[76] Spectra were fit using CasaXPS software with Gaussian–Lorentzian lineshapes after Shirley background subtraction. Sulfur regions were fitted by a doublet structure with a 1.18 eV spin–orbit splitting and a defined intensity ratio ($2p_{3/2}$:$2p_{1/2}$, 2:1).

Computational Modeling: Density functional theory calculations were performed to understand the molecular chemisorption modes and their relation with the STM imaging. Geometry optimizations were performed with the plane-wave periodic DFT VASP program.[77-80]

Exchange and correlation effects were described within the generalized gradient approximation (GGA), using the Perdew–Burke–Ernzerhof (PBE) functional,[81] and electron–ion interactions are treated with the projector augmented wave approach.[82] In order to describe the dispersion interactions, the empirically constructed DFT-D3 method was used.[83] The calculations were performed in a spin-unrestricted fashion when applicable. The gold slab was modeled as a $(\sqrt{7} \times \sqrt{7})R19.12°$ supercell, with four layers along z. The bottom two layers were fixed during the optimization. The calculated lattice constant for Au was 2.95 Å, in good agreement with the experiment.

To avoid spurious interactions between images in the z-direction, a vacuum gap of 10 Å was inserted between the highest atom of the carboranedithiolate molecules and the repeated image of the slab's bottom layer. The cutoff energy for the plane-wave basis set was chosen to be 400 eV. A 5 × 5 × 1 Monkhorst–Pack *k*-point grid allowed for the numerical solution of Hamiltonian and overlap matrix elements. For the STM images and the charge density plots, a denser *k*-point grid (11 × 11 × 1) was used.

The STM images were simulated using the Tersoff-Hamann method[47] using VASP.

Natural bond orbital (NBO1.1)[84] analyses of the molecules on the support were performed. The periodic version of NBO also requires the wave function to be represented in an atom-centered basis, therefore we projected the plane-wave solution onto the Def2-TZVP[85,86] Gaussian-type orbital basis set.

2.5 Additional Figures and Tables

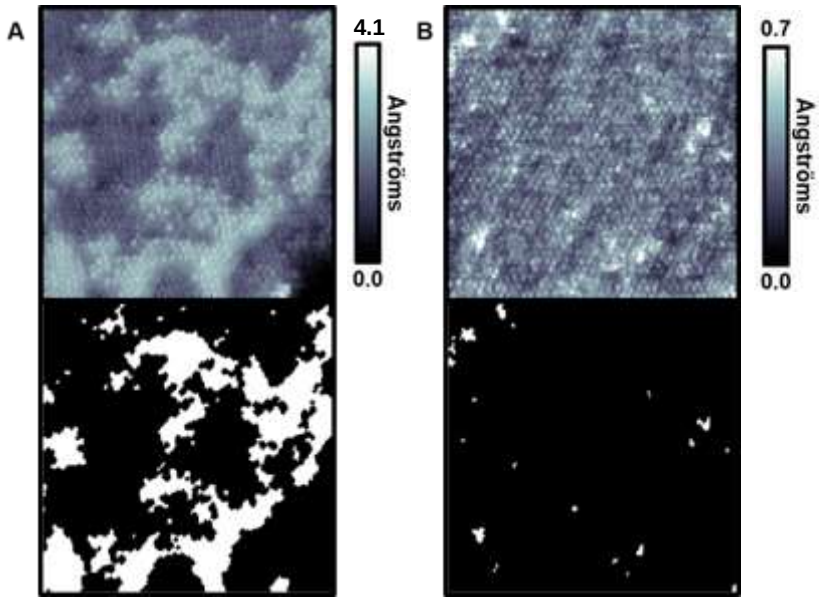

Figure 2.9 (A) Scanning tunneling microscope topographs (V_{sample} = -0.1 V, $I_{tunneling}$ = 100 pA) of 1,2-$(HS)_2$-1,2-$C_2B_{10}H_{10}$ (1O2) on Au{111}/mica, that was segmented by apparent height to highlight areas of different binding (GrayScaleThreshold = 0.75). (B) Scanning tunneling topograph (V_{sample} = -0.1 V, $I_{tunneling}$ = 100 pA) of 9,12-$(HS)_2$-1,2-$C_2B_{10}H_{10}$ (9O12) on Au{111}/mica that was segmented by apparent height to highlight binding mode concentrations (GrayScaleThreshold = 0.99).

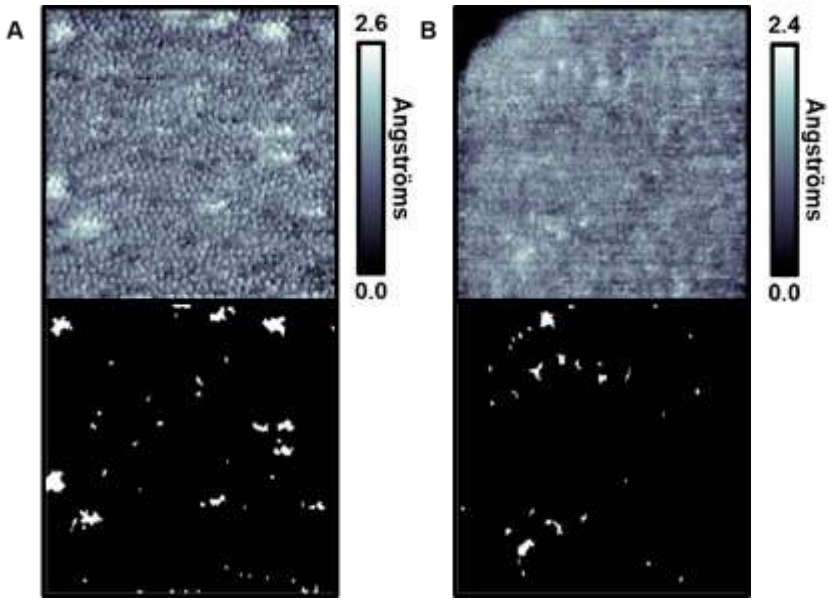

Figure 2.10 (A) Scanning tunneling microscope topograph (V_{sample} = -0.1 V, $I_{tunneling}$ = 100 pA) of 1,2-$(HS)_2$-1,2-$C_2B_{10}H_{10}$ (1O2) on Au{111}/mica after deposition in basic conditions that is segmented by apparent height to highlight binding mode density (GrayScaleThreshold = 0.975). (B) Scanning tunneling topograph (V_{sample} = -0.1 V, $I_{tunneling}$ = 100 pA) of 9,12-$(HS)_2$-1,2-$C_2B_{10}H_{10}$ (9O12) on Au{111}/mica deposited under basic conditions that is segmented by apparent height to highlight molecular binding mode concentrations (GrayScaleThreshold = 0.982).

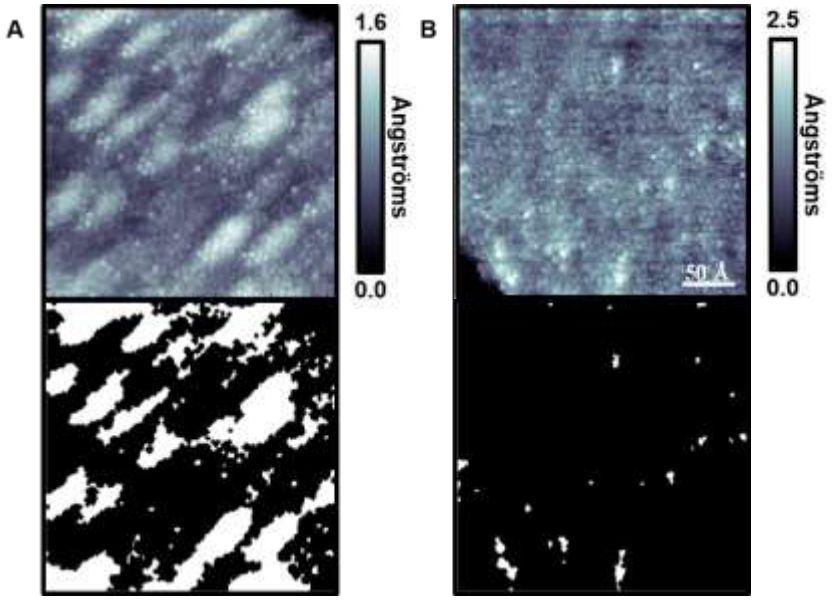

Figure 2.11 (A) Scanning tunneling microscope topograph (V_{sample} = -0.1 V, $I_{tunneling}$ = 100 pA) of 1,2-$(HS)_2$-1,2-$C_2B_{10}H_{10}$ (1O2) on Au{111}/mica after deposition under acidic conditions that is segmented by apparent height to highlight binding mode density (GrayScaleThreshold = 0.69). (B) Scanning tunneling topograph (V_{sample} = -0.1 V, $I_{tunneling}$ = 100 pA) of 9,12-$(HS)_2$-1,2-$C_2B_{10}H_{10}$ (9O12) on Au{111}/mica deposited under acidic conditions that is segmented by apparent height to highlight binding mode concentrations (GrayScaleThreshold = 0.985).

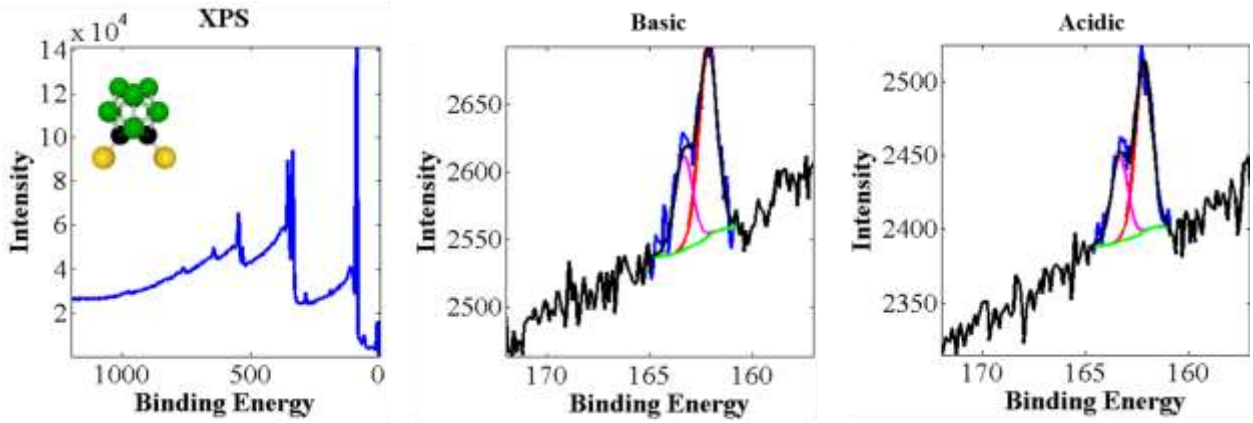

Figure 2.12 X-ray photoelectron spectra (XPS) of 1,2-$(HS)_2$-1,2-$C_2B_{10}H_{10}$ on Au on Si{100} that show the full sweep under neutral conditions, and high-resolution scans of the S 2p area. Binding energies are consistent and confirm monolayer integrity under all conditions reported.

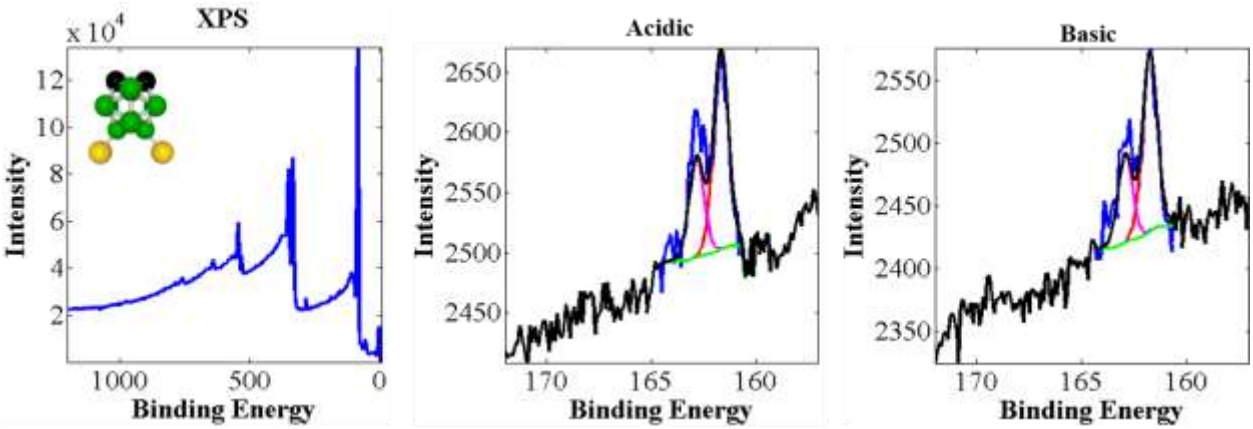

Figure 2.13 X-ray photoelectron spectra (XPS) of 9,12-$(HS)_2$-1,2-$C_2B_{10}H_{10}$ on Au on Si{100} that show the full sweep under neutral conditions and high-resolution scans of the S 2p area under both basic and acidic conditions. Binding energies under all conditions remain consistent and confirm monolayer integrity.

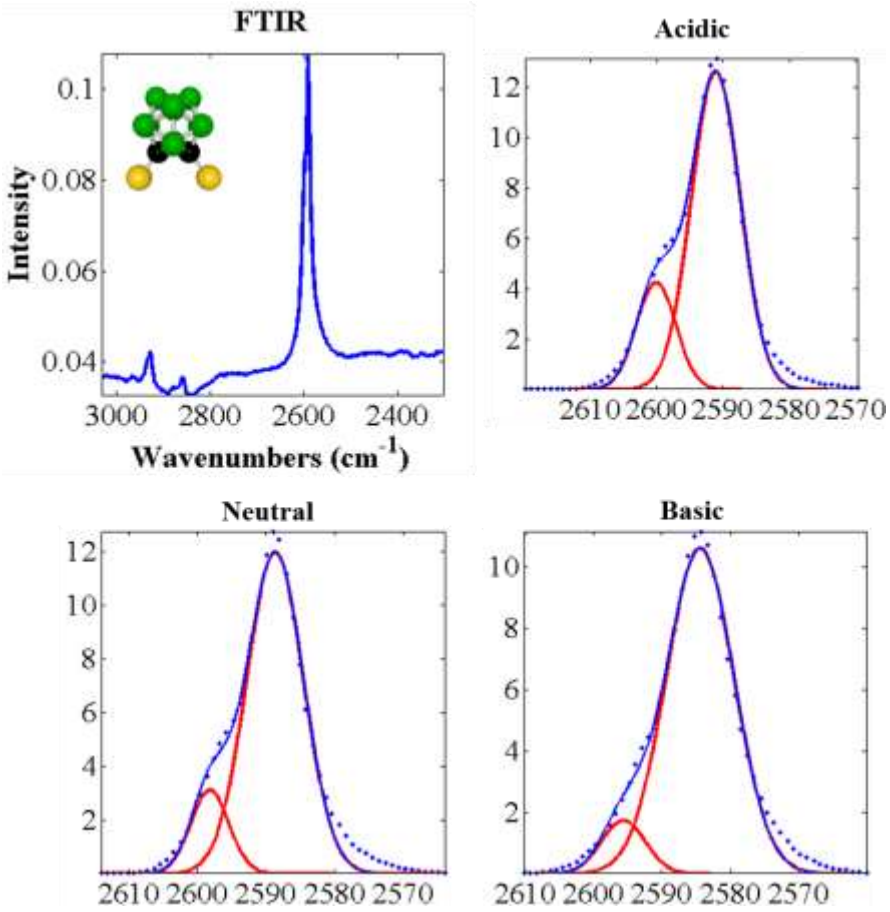

Figure 2.14 Fourier transform infrared spectroscopy (FTIR) that highlights the B-H region for 1,2-$(HS)_2$-1,2-$C_2B_{10}H_{10}$ on Au on Si{100} under all conditions reported. Here, B-H intensity remains nominally consistent throughout. Peaks and assignments are detailed in Table 2.2.

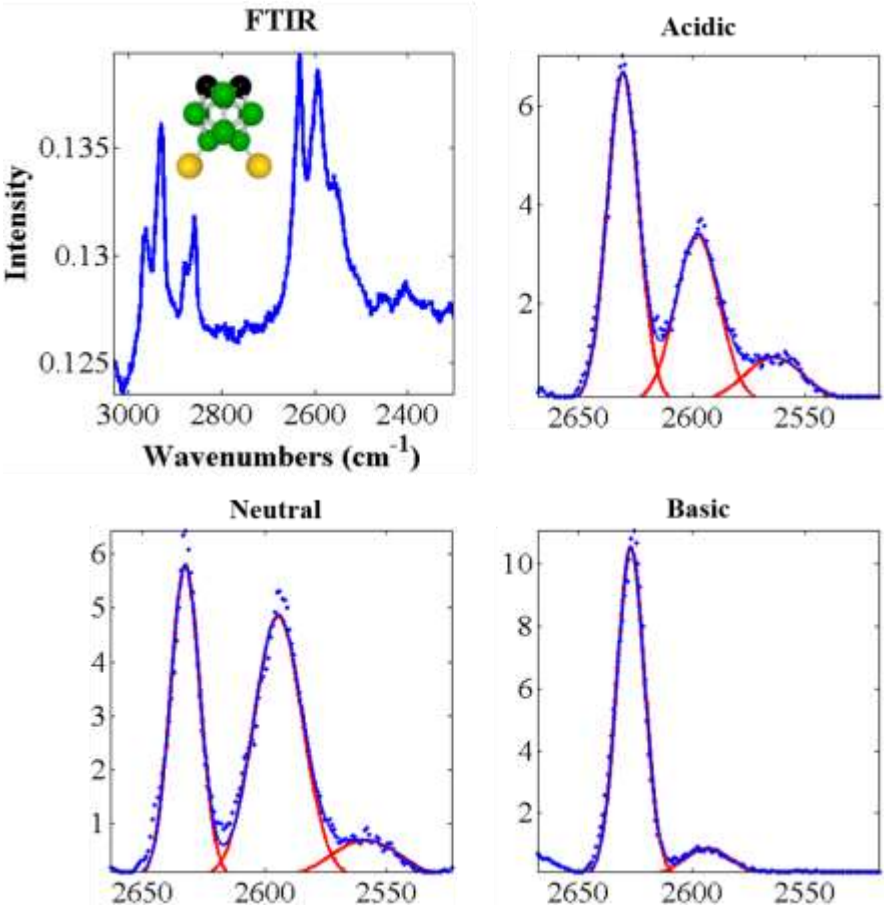

Figure 2.15 Fourier transform infrared spectra (FTIR) that highlight the B-H region for 9,12-$(HS)_2$-1,2-$C_2B_{10}H_{10}$ (9O12) on Au on Si{100} under the conditions reported. Peaks centered at 2600 cm^{-1} is reduced under acidic conditions, which is likely due to small-scale degradation. This peak, however, is significantly decreased under basic conditions, which we attribute to the bivalent nature of SAMs formed under Peaks centered at 2550 cm^{-1} show a slight increase under acidic conditions, and a complete disappearance under basic conditions. Peaks and assignments are further detailed in Table 2.2.

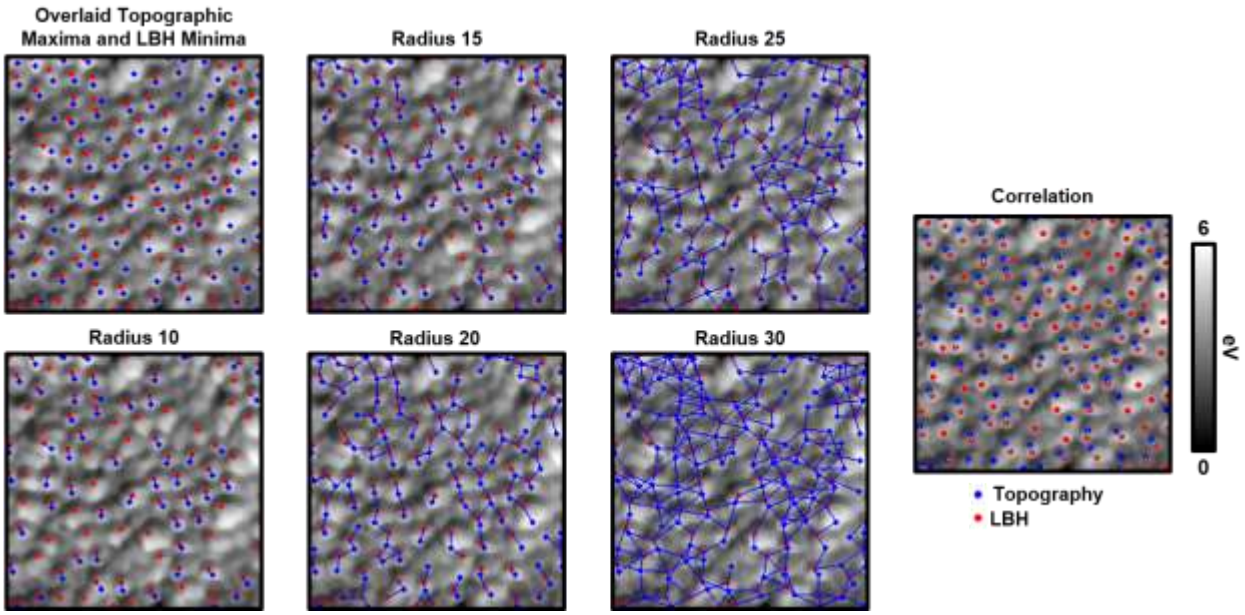

Figure 2.16 Scanning tunneling microscope local barrier images (V_{sample} = -0.5 V, $I_{tunneling}$ = 15 pA) of 1,2-$(HS)_2$-1,2-$C_2B_{10}H_{10}$ (1O2) on Au{111}/mica with overlaid topographic and local barrier height maxima. We connect all topographic maxima to all local barrier height maxima within a defined radial vector and compare with results obtained through block-matching.

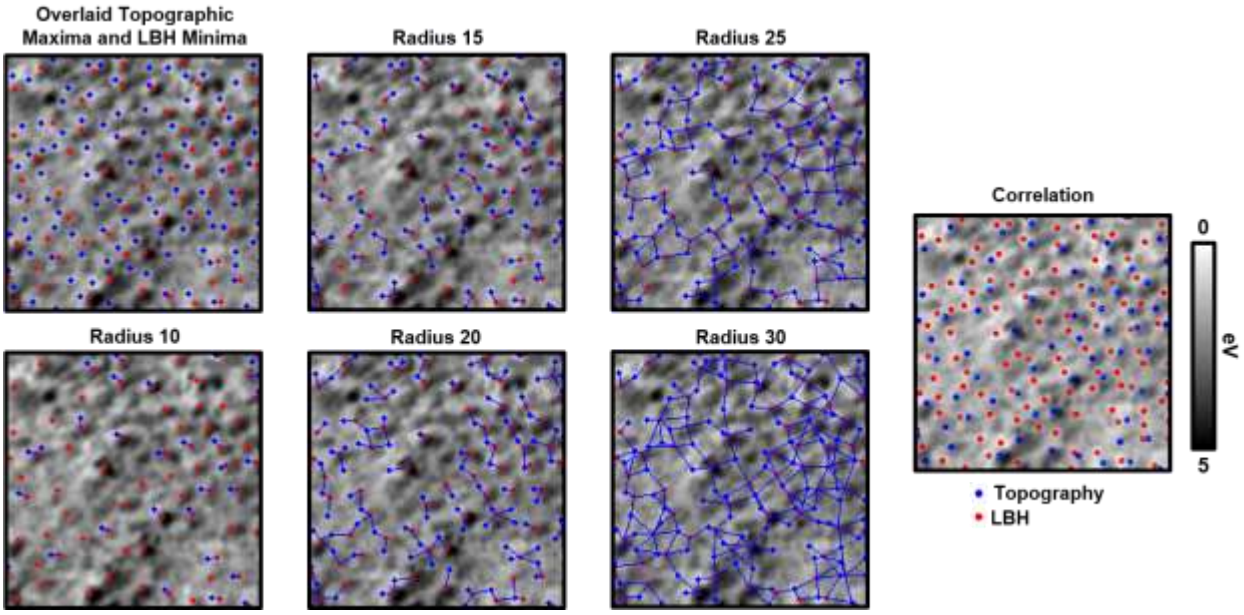

Figure 2.17 Scanning tunneling microscope local barrier images (V_{sample} = -0.5 V, $I_{tunneling}$ = 15 pA) of 9,12-$(HS)_2$-1,2-$C_2B_{10}H_{10}$ (9O12) on Au{111}/mica with overlaid topographic and local barrier height maxima (inverted to highlight dipole minima). We connect all topographic maxima to all local barrier height maxima within a defined radial vector and compare with correlated results.

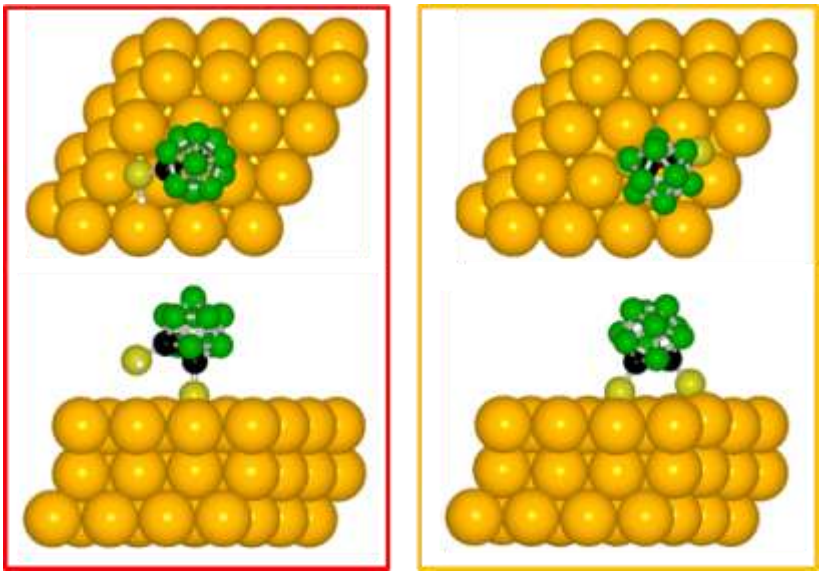

Figure 2.18 Optimized binding geometries for 1,2-carboranedithiolate on Au{111}. Binding energies were calculated ($E_{binding} = E_{system} - E_{molecule} - E_{substrate}$) for both the singly bound (red, -1.51 eV) and the divalent (yellow, -2.83 eV) molecules.

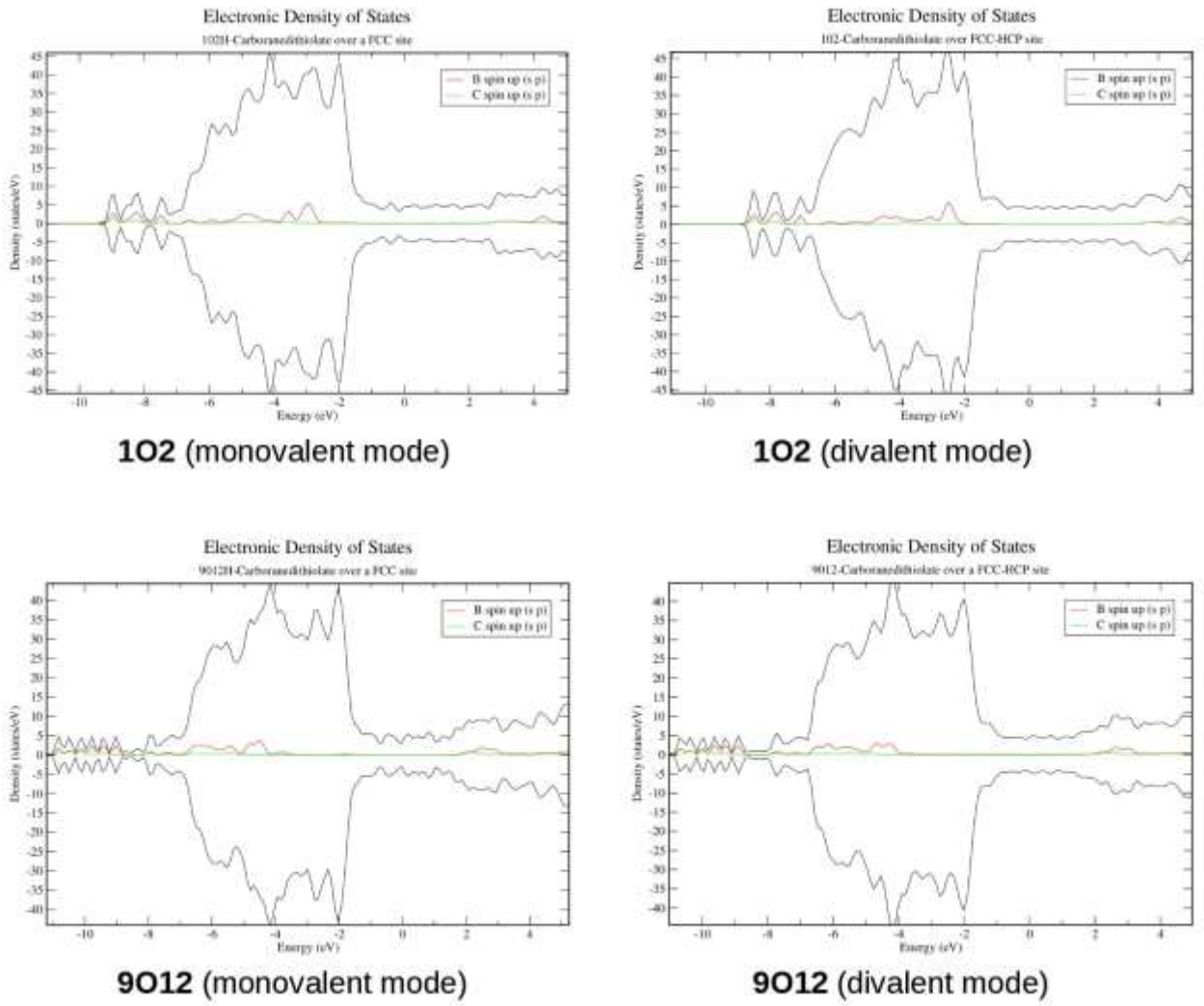

Figure 2.19 Projected density of states of 1,2-$(HS)_2$-1,2-$C_2B_{10}H_{10}$ (1O2) and 9,12-$(HS)_2$-1,2-$C_2B_{10}H_{10}$ (9O12) in their respective monovalent and divalent modes.

	1O2	9O12
B-H Measured by FTIR	2589 cm^{-1} 2598 cm^{-1}	2559 cm^{-1} 2595 cm^{-1} 2633 cm^{-1}
Modeled B-H Frequencies (Vertices)	2600 cm^{-1} (7,5) 2597 cm^{-1} (4,11) 2594 cm^{-1} (5,7) 2592 cm^{-1} and 2591 cm^{-1} (3,4,5,6,7,11) 2579 cm^{-1} (8,9,10,12) 2572 cm^{-1} (8,10) 2571 cm^{-1} (9,12)	2633 cm^{-1} and 2631 cm^{-1} (3,6) 2619 cm^{-1} (4,5,7,11) 2610 cm^{-1} (4) 2608 cm^{-1} (7) 2589 cm^{-1} (8) 2587 cm^{-1} (10)

Table 2.2 A compilation of all B-H stretches measured with infrared spectroscopy in neutral conditions along with their simulated values and cage vertex assignments (the latter shown in parentheses).

1O2 Binding site	Adsorption mode	BE (eV)	ΔE (eV)	α (º)	Min	Max
fcc-B	Divalent	-1.26	0.20	11.86	10.86	16.22
fcc-hpc	Divalent	-1.29	0.17	8.14	10.30	15.95
fcc-B	Divalent	-1.46	0.0	44.70	10.37	15.90
B-B	Divalent	-1.43	0.03	48.50	11.82	15.83
fcc	Monovalent	-1.27	0.02	28.02	10.88	16.47
hpc	Monovalent	-1.29	0.0	17.69	10.90	16.22
hpc-Top	Divalent*	-1.30	0.18	18.56	11.97	16.98
hpc-hpc	Divalent*	-1.47	0.02	73.74	14.90	17.91
hpc-B	Divalent*	-1.45	0.04	65.57	13.74	16.48
B-B	Divalent*	-1.48	0.01	66.92	11.70	16.66
Top-Top	Divalent*	-1.49	0.0	52.58	13.05	16.52
fcc-hpc	Divalent*	-1.41	0.08	52.26	12.78	16.62
fcc-B	Divalent*	-1.38	0.11	66.89	12.78	16.45

Table 2.3 Data corresponding to possible 1,2-$(HS)_2$-1,2-$C_2B_{10}H_{10}$ (1O2) carboranedithiol binding sites. The possible binding sites are face-centered cubic (fcc), hexagonally close-packed (hpc), bridge (B), and atop a single atom (Top); the possible binding modes are singly bound (Monovalent), doubly bound (Divalent), and doubly bound without being deprotonated (Divalent*). BE is the binding energy, ΔE the relative energy with respect to the global minimum, α is the tilt of the molecule with respect to the surface normal, and Min and Max stand for the minimum and maximum topographic ranges taken from the simulated scanning tunneling microscope images.

9O12 Binding site	Adsorption mode	BE (eV)	ΔE (eV)	α (º)	Min	Max
fcc-B	Divalent	-1.42	-0.18	11.27	11.16	16.55
fcc-hpc	Divalent	-1.41	-0.19	7.97	12.45	16.60
B-top	Divalent	-1.59	0.0	43.30	11.87	16.13
B-B	Divalent	-1.48	-0.12	36.44	10.73	16.41
fcc-B	Divalent	-1.40	-0.19	36.07	10.76	16.20
hpc-B	Divalent*	-1.73	0.0	78.03	11.11	16.01
B-Top	Divalent*	-1.72	-0.01	63.69	13.20	16.49
fcc-hpc	Divalent*	-1.67	-0.06	70.82	13.80	16.29
fcc-Top	Divalent*	-1.60	-0.13	47.66	14.13	17.21
hpc-Top	Divalent*	-1.61	-0.12	43.31	14.42	17.33
hpc-hpc	Divalent*	-1.60	-0.13	48.67	14.27	16.94
B-Top	Divalent*	-1.61	-0.11	69.12	14.08	16.49
hpc	Monovalent	-1.32	-0.14	25.19	11.75	16.54
fcc	Monovalent	-1.46	0.0	30.33	10.92	15.87

Table 2.4 Data corresponding to possible 9,12-$(HS)_2$-1,2-$C_2B_{10}H_{10}$ (9O12) carboranedithiol binding sites. The possible binding sites are face-centered-cubic (fcc), hexagonally close-packed (hpc), bridge (B), and atop a single atom (Top); the possible binding modes are singly bound (Monovalent), doubly bound (Divalent) and doubly bound without being deprotonated (Divalent*). BE is the binding energy, ΔE the relative energy with respect to the global minimum, α is the tilt of the molecule with respect to the surface normal, and Min and Max stand for the minimum and maximum topographic ranges taken from the simulated scanning tunneling microscope images.

2.6 References

(1) Love, J. C.; Estroff, L. A.; Kriebel, J. K.; Nuzzo, R. G.; Whitesides, G. M. Self-Assembled Monolayers of Thiolates on Metals as a Form of Nanotechnology. *Chem. Rev.* **2005**, *105*, 1103−1170.

(2) Weiss, P. S. Functional Molecules and Assemblies in Controlled Environments: Formation and Measurements. *Acc. Chem. Res.* **2008**, *41*, 1772−1781.

(3) Claridge, S. A.; Liao, W. S.; Thomas, J. C.; Zhao, Y.; Cao, H. H.; Cheunkar, S.; Serino, A. C.; Andrews, A. M.; Weiss, P. S. From the Bottom Up: Dimensional Control and Characterization in Molecular Monolayers. *Chem. Soc. Rev.* **2013**, *42*, 2725−2745.

(4) Ulman, A. Formation and Structure of Self-Assembled Monolayers. *Chem. Rev.* **1996**, *96*, 1533−1554.

(5) Poirier, G. E. Characterization of Organosulfur Molecular Monolayers on Au(111) using Scanning Tunneling Microscopy. *Chem. Rev.* **1997**, *97*, 1117−1128.

(6) Smith, R. K.; Lewis, P. A.; Weiss, P. S. Patterning Self-Assembled Monolayers. *Prog. Surf. Sci.* **2004**, *75*, 1−68.

(7) Han, P.; Kurland, A. R.; Giordano, A. N.; Nanayakkara, S. U.; Blake, M. M.; Pochas, C. M.; Weiss, P. S. Heads and Tails: Simultaneous Exposed and Buried Interface Imaging of Monolayers. *ACS Nano* **2009**, *3*, 3115−3121.

(8) Hohman, J. N.; Thomas, J. C.; Zhao, Y.; Auluck, H.; Kim, M.; Vijselaar, W.; Kommeren, S.; Terfort, A.; Weiss, P. S. Exchange Reactions between Alkanethiolates and Alkaneselenols on Au{111}. *J. Am. Chem. Soc.* **2014**, *136*, 8110−8121.

(9) Salmeron, M.; Neubauer, G.; Folch, A.; Tomitori, M.; Ogletree, D. F.; Sautet, P. Viscoelastic and Electrical Properties of Alkylthiol Monolayers on Gold(111) Films. *Langmuir* **1993**, *9*, 3600−3611.

(10) Nuzzo, R. G.; Allara, D. L. Adsorption of Bifunctional Organic Disulfides on Gold Surfaces. *J. Am. Chem. Soc.* **1983**, *105*, 4481−4483.

(11) Takami, T.; Delamarche, E.; Michel, B.; Gerber, Ch.; Wolf, H.; Ringsdorf, H. Recognition of Individual Tail Groups in Self-Assembled Monolayers. *Langmuir* **1995**, *11*, 3876−3881.

(12) Kim, M.; Hohman, J. N.; Cao, Y.; Houk, K. N.; Ma, H.; Jen, A. K.; Weiss, P. S. Creating Favorable Geometries for Directing Organic Photoreactions in Alkanethiolate Monolayers. *Science* **2011**, *331*, 1312−1315.

(13) Hohman, J. N.; Claridge, S. A.; Kim, M.; Weiss, P. S. Cage Molecules for Self-Assembly. *Mater. Sci. Eng., R* **2010**, *70*, 188−208.

(14) Spokoyny, A. M.; Machan, C. W.; Clingerman, D. J.; Rosen, M. S.; Wiester, M. J.; Kennedy, R. D.; Stern, C. L.; Sarjeant, A. A.; Mirkin, C. A. A Coordination Chemistry Dichotomy for Icosahedral Carborane-Based Ligands. *Nat. Chem.* **2011**, *3*, 590−596.

(15) Kim, J.; Rim, Y. S.; Liu, Y.; Serino, A. C.; Thomas, J. C.; Chen, H.; Yang, Y.; Weiss, P. S. Interface Control in Organic Electronics Using Mixed Monolayers of Carboranethiol Isomers. *Nano Lett.* **2014**, *14*, 2946−2951.

(16) Thomas, J. C.; Schwartz, J. J.; Hohman, J. N.; Claridge, S. A.; Auluck, H. S.; Serino, A. C.; Spokoyny, A. M.; Tran, G.; Kelly, K. F.; Mirkin, C. A.; Gilles, J.; Osher, S. J.; Weiss, P. S. Defect-Tolerant Aligned Dipoles within Two-Dimensional Plastic Lattices. *ACS Nano* **2015**, *9*, 4734−4742.

(17) Thomas, J. C.; Boldog, I.; Auluck, H. S.; Bereciartua, P.; Dušek, M.; Macháček, J.; Bastl, Z.; Weiss, P. S.; Baše, T. Self-Assembled *p*-Carborane Analog of *p*-Mercaptobenzoic Acid on Au{111}. *Chem. Mater.* **2015**, *27*, 5425−5435.

(18) Kristiansen, K.; Stock, P.; Baimpos, T.; Raman, S.; Harada, J. K.; Israelachvili, J. N.; Valtiner, M. Influence of Molecular Dipole Orientations on Long-Range Exponential Interaction Forces at Hydrophobic Contacts in Aqueous Solutions. *ACS Nano* **2014**, *8*, 10870−10877.

(19) Hohman, J. N.; Zhang, P.; Morin, E. I.; Han, P.; Kim, M.; Kurland, A. R.; McClanahan, P. D.; Balema, V. P.; Weiss, P. S. SelfAssembly of Carboranethiol Isomers on Au{111}: Intermolecular Interactions Determined by Molecular Dipole Orientations. *ACS Nano* **2009**, *3*, 527−536.

(20) Serino, A. C.; Anderson, M. E.; Saleh, L. M. A.; Dziedzic, R. M.; Mills, H.; Heidenreich, L. K.; Spokoyny, A. M.; Weiss, P. S. Work Function Control of Germanium through Carborane-Carboxylic Acid Surface Passivation. *ACS Appl. Mater. Interfaces* **2017**, *9*, 34592− 34596.

(21) Baše, T.; Bastl, Z.; Plzák, Z.; Grygar, T.; Plešek, J.; Carr, M.; Malina, V.; Šubrt, J.; Boháček, J.; Večerníková, E.; Kříž , O. Carboranethiol-Modified Gold Surfaces. A Study and Comparison of Modified Cluster and Flat Surfaces. *Langmuir* **2005**, *21*, 7776−7785.

(22) Baše, T.; Bastl, Z.; Šlouf, M.; Klementová, M.; Šubrt, J.; Vetushka, A.; Ledinský, M.; Fejfar, A.; Macháček, J.; Carr, M. J.; Londesborough, M. G. S. Gold Micrometer Crystals Modified with Carboranethiol Derivatives. *J. Phys. Chem. C* **2008**, *112*, 14446−14455.

(23) Baše, T.; Bastl, Z.; Havránek, V.; Lang, K.; Bould, J.;́ Londesborough, M. G. S.; Macháček, J.; Plešek, J. Carborane-Thiol-Silver Interactions. A Comparative Study of the Molecular Protection of Silver Surfaces. *Surf. Coat. Technol.* **2010**, *204*, 2639−2646.

(24) Lübben, J. F.; Baše, T.; Rupper, P.; Künniger, T.; Macháček, J.; Guimond, S. Tuning the Surface Potential of Ag Surfaces by Chemisorption of Oppositely-Oriented Thiolated Carborane Dipoles. J. *Colloid Interface Sci.* **2011**, *354*, 168−174.

(25) Langecker, J.; Fejfarová, K.; Dušek, M.; Rentsch, D.; Baše, T. Carbon-Substituted 9,12-Dimercapto-1,2-Dicarba-*closo*-Dodecaboranes *via* a 9,12-Bis(Methoxy-Methylthio)-1,2-Dicarba-*closo*-Dodecaborane Precursor. *Polyhedron* **2012**, *45*, 144−151.

(26) Baše, T.; Bastl, Z.; Havránek, V.; Macháček, J.; Langecker, J.; Malina, V. Carboranedithiols: Building Blocks for Self-Assembled Monolayers on Copper Surfaces. *Langmuir* **2012**, *28*, 12518−12526.

(27) Schwartz, J. J.; Mendoza, A. M.; Wattanatorn, N.; Zhao, Y.; Nguyen, V. T.; Spokoyny, A. M.; Mirkin, C. A.; Baše, T.; Weiss, P. S. Surface Dipole Control of Liquid Crystal Alignment. *J. Am. Chem. Soc.* **2016**, *138*, 5957−5967.

(28) Nuzzo, R. G.; Dubois, L. H.; Allara, D. L. Fundamental Studies of Microscopic Wetting on Organic-Surfaces. 1. Formation and Structural Characterization of a Self-Consistent Series of Polyfunctional Organic Monolayers. *J. Am. Chem. Soc.* **1990**, *112*, 558−569.

(29) Liao, W. S.; Cheunkar, S.; Cao, H. H.; Bednar, H. R.; Weiss, P. S.; Andrews, A. M. Subractive Patterning via Chemical Lift-Off Lithography. *Science* **2012**, *337*, 1517−1521.

(30) Kim, J.; Rim, Y. S.; Chen, H.; Cao, H. H.; Nakatsuka, N.; Hinton, H. L.; Zhao, C.; Andrews, A. M.; Yang, Y.; Weiss, P. S. Fabrication of High-Performance Ultrathin In2O3 Film Field-Effect Transistors and Biosensors Using Chemical Lift-Off Lithography. *ACS Nano* **2015**, *9*, 4572−4582.

(31) Andrews, A. M.; Liao, W.-S.; Weiss, P. S. Double-Sided Opportunities Using Chemical Lift-Off Lithography. *Acc. Chem. Res.* **2016**, *49*, 1449−1457.

(32) Monnell, J. D.; Stapleton, J. J.; Dirk, S. M.; Reinerth, W. A.; Tour, J. M.; Allara, D. L.; Weiss, P. S. Relative Conductances of Alkaneselenolate and Alkanethiolate Monolayers on Au{111}. *J. Phys. Chem. B* **2005**, *109*, 20343−20349.

(33) Zheng, Y. B.; Pathem, B. K.; Hohman, J. N.; Thomas, J. C.; Kim, M.; Weiss, P. S. Photoresponsive Molecules in Well-Defined Nanoscale Environments. *Adv. Mater.* **2013**, *25*, 302−312.

(34) He, H.-X.; Huang, W.; Zhang, H.; Li, Q. G.; Li, S. F. Y.; Liu, Z. F. Demonstration of High-Resolution Capability of Chemical Force Titration *via* Study of Acid/Base Properties of a Patterned Self-Assembled Monolayer. *Langmuir* **2000**, *16*, 517−521.

(35) Saavedra, H. M.; Thompson, C. M.; Hohman, J. N.; Crespi, V. H.; Weiss, P. S. Reversible Lability by *in Situ* Reaction of Self-Assembled Monolayers. *J. Am. Chem. Soc.* **2009**, *131*, 2252−2259.

(36) Saavedra, H. M.; Mullen, T. J.; Zhang, P.; Dewey, D. C.; Claridge, S. A.; Weiss, P. S. Hybrid Strategies in Nanolithography. *Rep. Prog. Phys.* **2010**, *73*, 036501−036600.

(37) Saadi, F. H.; Carim, A. I.; Verlage, E.; Hemminger, J. C.; Lewis, N. S.; Soriaga, M. P. CoP as an Acid-Stable Active Electrocatalyst for the Hydrogen-Evolution Reaction: Electrochemical Synthesis, Interfacial Characterization and Performance Evaluation. *J. Phys. Chem. C* **2014**, *118*, 29294−29300.

(38) Katano, S.; Kim, Y.; Matsubara, H.; Kitagawa, T.; Kawai, M. Hierarchical Chiral Framework Based on a Rigid Adamantane Tripod on Au(111). *J. Am. Chem. Soc.* **2007**, *129*, 2511−2515.

(39) Hatzor, A.; McCarty, G. S.; D'Onofrio, T. G.; Fuchs, D. J.; Allara, D. L.; Tour, J. M.; Weiss, P. S. Scanning Tunneling Microscopy and Spectroscopy of Caltrops on Au{111}; unpublished.

(40) Moore, A. M.; Dameron, A. A.; Mantooth, B. A.; Smith, R. K.; Fuchs, D. J.; Ciszek, J. W.; Maya, F.; Yao, Y.; Tour, J. M.; Weiss, P. S. Molecular Engineering and Measurements to Test Hypothesized Mechanisms in Single Molecule Conductance Switching. *J. Am. Chem. Soc.* **2006**, *128*, 1959−1967.

(41) Yao, Y.; Tour, J. M. Facile Convergent Route to Molecular Caltrops. *J. Org. Chem.* **1999**, *64*, 1968−1971.

(42) Jian, H.; Tour, J. M. En Route to Surface-Bound Electric Field-Driven Molecular Motors. *J. Org. Chem.* **2003**, *68*, 5091−5103.

(43) van Delden, R. A.; ter Wiel, M. K. J.; Pollard, M. M.; Vicario, J.; Koumura, N.; Feringa, B. L. Unidirectional Molecular Motor on a Gold Surface. *Nature* **2005**, *437*, 1337−1340.

(44) Ye, T.; Kumar, A. S.; Saha, S.; Takami, T.; Huang, T. J.; Stoddart, J. F.; Weiss, P. S. Changing Stations in Single Bistable Rotaxane Molecules under Electrochemical Control. *ACS Nano* **2010**, *4*, 3697−3701.

(45) Donhauser, Z. J.; Mantooth, B. A.; Kelly, K. F.; Bumm, L. A.; Monnell, J. D.; Stapleton, J. J.; Price, D. W., Jr.; Rawlett, A. M.; Allara, D. L.; Tour, J. M.; Weiss, P. S. Conductance Switching in Single Molecules through Conformational Changes. *Science* **2001**, *292*, 2303−2307.

(46) Lewis, P. A.; Inman, C. E.; Maya, F.; Tour, J. M.; Hutchison, J. E.; Weiss, P. S. Molecular Engineering of the Polarity and Interactions of Molecular Electronics Switches. *J. Am. Chem. Soc.* **2005**, *127*, 17421−17426.

(47) Tersoff, J.; Hamann, D. R. Theory and Application for the Scanning Tunneling Microscope. *Phys. Rev. Lett.* **1998**, *50*, 1998− 2001.

(48) McCarty, G. S.; Weiss, P. S. Scanning Probe Studies of Single Nanostructures. *Chem. Rev.* **1999**, *99*, 1983−1990.

(49) Claridge, S. A.; Schwartz, J. J.; Weiss, P. S. Electrons, Photons, and Force: Quantitative Single-Molecule Measurements from Physics to Biology. *ACS Nano* **2011**, *5*, 693−729.

(50) Bonnell, D. A.; Basov, D. N.; Bode, M.; Diebold, U.; Kalinin, S. V.; Madhavan, V.; Novotny, L.; Salmeron, M.; Schwarz, U. D.; Weiss, P. S. Imaging Physical Phenomena with Local Probes: From Electrons to Photons. *Rev. Mod. Phys.* **2012**, *84*, 1343−1381.

(51) Bumm, L. A.; Arnold, J. J.; Cygan, M. T.; Dunbar, T. D.; Burgin, T. P.; Jones, L., II; Allara, D. L.; Tour, J. M.; Weiss, P. S. Are Single Molecular Wires Conducting? *Science* **1996**, *271*, 1705−1707.

(52) Claridge, S. A.; Thomas, J. C.; Silverman, M. A.; Schwartz, J. J.; Yang, Y.; Wang, C.; Weiss, P. S. Differentiating Amino Acid Residues and Side Chain Orientations in Peptides Using Scanning Tunneling Microscopy. *J. Am. Chem. Soc.* **2013**, *135*, 18528−18535.

(53) Moore, A. M.; Yeganeh, S.; Yao, Y.; Claridge, S. A.; Tour, J. M.; Ratner, M. A.; Weiss, P. S. Polarizabilities of Adsorbed and Assembled Molecules: Measuring the Conductance through Buried Contacts. *ACS Nano* **2010**, *4*, 7630−7636.

(54) Thomas, J. C.; Goronzy, D. P.; Dragomeritskiy, K.; Zosso, D.; Gilles, J.; Osher, S. J.; Bertozzi, A.; Weiss, P. S. Mapping Buried Hydrogen-Bonding Networks. *ACS Nano* **2016**, *10*, 5446−5451.

(55) Yugay, D.; Goronzy, D. P.; Kawakami, L. M.; Claridge, S. A.; Song, T.-B.; Yan, Z.; Xie, Y.-H.; Gilles, J.; Yang, Y.; Weiss, P. S. Copper Ion Binding Site in β-Amyloid Peptide. *Nano Lett.* **2016**, *16*, 6282− 6289.

(56) Fujii, S.; Akiba, U.; Fujihira, M. Geometry for Self-Assembling of Spherical Hydrocarbon Cages with Methane Thiolates on Au(111). *J. Am. Chem. Soc.* **2002**, *124*, 13629−13635.

(57) Wade, K. The Structural Significance of the Number of Skeletal Bonding Electron-Pairs in Carboranes, the Higher Boranes and Borane Anions, and Various Transition-Metal Carbonyl Cluster Compounds. *J. Chem. Soc. D* **1971**, 792−793.

(58) Wiesendanger, R.; Eng, L.; Hidber, H. R.; Oelhafen, P.; Rosenthaler, L.; Staufer, U.; Güntherodt, H. J. Local Tunneling Barrier Height Images Obtained with the Scanning Tunneling Microscope. *Surf. Sci.* **1987**, *189−190*, 24−28.

(59) Olesen, L.; Brandbyge, M.; Sørensen, M. R.; Jacobsen, K. W.; Lægsgaard, E.; Stensgaard, I.; Besenbacher, F. Apparent Barrier Height in Scanning Tunneling Microscopy Revisited. *Phys. Rev. Lett.* **1996**, *76*, 1485−1488.

(60) Lang, N. D. Apparent Barrier Height in Scanning Tunneling Microscopy. *Phys. Rev. B: Condens. Matter Mater. Phys.* **1988**, *37*, 10395−10398.

(61) Jain, J.; Jain, A. Displacement Measurement and Its Application in Interframe Image Coding. *IRE Trans. Commun. Syst.* **1981**, *29*, 1799−1808.

(62) Love, N. S.; Kamath, C. An Empirical Study of Block Matching Techniques for the Detection of Moving Objects. *UCRL-TR-218038 Technical Report*; CASC, LLNL: Livermore, CA, **2006**; pp 1−36.

(63) Slaughter, L. S.; Cheung, K. M.; Kaappa, S.; Cao, H. H.; Yang, Q.; Young, T. D.; Serino, A. C.; Malola, S.; Olson, J. M.; Link, S.; Häkkinen, H.; Andrews, A. M.; Weiss, P. S. Patterning Supported Gold Monolayers *via* Chemical Lift-Off Lithography. *Beilstein J. Nanotechnol.* **2017**, *8*, 2648−2661.

(64) Leites, L. A. Vibrational Spectroscopy of Carboranes and Parent Boranes and its Capabilities in Carborane Chemistry. *Chem. Rev.* **1992**, *92*, 279−323.

(65) Stranick, S. J.; Parikh, A. N.; Allara, D. L.; Weiss, P. S. A New Mechanism for Surface Diffusion: Motion of a Substrate-Adsorbate Complex. *J. Phys. Chem.* **1994**, *98*, 11136−11142.

(66) Poirier, G. E.; Tarlov, M. J. Molecular Ordering and Gold Migration Observed in Butanethiol Self-Assembled Monolayers Using Scanning Tunneling Microscopy. *J. Phys. Chem.* **1995**, *99*, 10966− 10970.

(67) Kinbara, K.; Aida, T. Toward Intelligent Molecular Machines: Directed Motions of Biological and Artificial Molecules and Assemblies. *Chem. Rev.* **2005**, *105*, 1377−1400.

(68) Li, D.; Paxton, W. F.; Baughman, R. H.; Huang, T. J.; Stoddart, J. F.; Weiss, P. S. Molecular, Supramolecular, and Macromolecular Motors and Artificial Muscles. *MRS Bull.* **2009**, *34*, 671−681.

(69) Wang, J. Can Man-Made Nanomachines Compete with Nature Biomotors? *ACS Nano* **2009**, *3*, 4−9.

(70) Abendroth, J. M.; Bushuyev, O. S.; Weiss, P. S.; Barrett, C. J. Controlling Motion at the Nanoscale: Rise of the Molecular Machines. *ACS Nano* **2015**, *9*, 7746−7768.

(71) Cheng, C.; McGonigal, P. R.; Stoddart, J. F.; Astumian, R. D. Design and Synthesis of Nonequilibrium Systems. *ACS Nano* **2015**, *9*, 8672−8688.

(72) Shimizu, T. K.; Jung, J.; Otani, T.; Han, Y.-K.; Kawai, M.; Kim, Y. Two-Dimensional Superstructure Formation of Fluorinated Fullerene on Au(111): A Scanning Tunneling Microscopy Study. *ACS Nano* **2012**, *6*, 2679−2685.

(73) Wiesboeck, R. A.; Hawthorne, M. F. Dicarbaundecaborane(13) and Derivatives. *J. Am. Chem. Soc.* **1964**, *86*, 1642−1643.

(74) Bumm, L. A.; Arnold, J. J.; Charles, L. F.; Dunbar, T. D.; Allara, D. L.; Weiss, P. S. Directed Self-Assembly to Create Molecular Terraces with Molecularly Sharp Boundaries in Organic Monolayers. *J. Am. Chem. Soc.* **1999**, *121*, 8017−8021.

(75) Ferris, J. H.; Kushmerick, J. G.; Johnson, J. A.; Yoshikawa Youngquist, M. G.; Kessinger, R. B.; Kingsbury, H. F.; Weiss, P. S. Design, Operation, and Housing of an Ultrastable, Low Temperature, Ultrahigh Vacuum Scanning Tunneling Microscope. *Rev. Sci. Instrum.* **1998**, *69*, 2691−2695.

(76) Moulder, J. F. *Handbook of X-ray Photoelectron Spectroscopy: A Reference Book of Standard Spectra for Idenfication and Interpretation of XPS Data;* Perkin-Elmer Corporation, Physical Electronics Division: Eden Prairie, MN, 1992.

(77) Kresse, G.; Hafner, J. *Ab Initio* Molecular Dynamics for Liquid Metals. *Phys. Rev. B* **1993**, *47*, 558−561.

(78) Kresse, G.; Hafner, J. *Ab Initio* Molecular-Dynamics Simulation of the Liquid-Metal-Amorphous-Semiconductor Transition in Germanium. *Phys. Rev. B: Condens. Matter Mater. Phys.* **1994**, *49*, 14251− 14269.

(79) Kresse, G.; Furthmüller, J. Efficiency of *Ab-Initio* Total Energy Calculations for Metals and Semiconductors Using a Plane-Wave Basis Set. *Comput. Mater. Sci.* **1996**, *6*, 15−50.

(80) Kresse, G.; Furthmüller, J. Efficient Iterative Schemes for *Ab Initio* Total-Energy Calculations Using a Plane-Wave Basis Set. *Phys. Rev. B: Condens. Matter Mater. Phys.* **1996**, *54*, 11169−11186.

(81) Perdew, J. P.; Burke, K.; Ernzerhof, M. Generalized Gradient Approximation Made Simple. *Phys. Rev. Lett.* **1997**, *78*, 1396−3868.

(82) Kresse, G.; Joubert, D. From Ultrasoft Pseudopotentials to the Projector Augmented-Wave Method. *Phys. Rev. B: Condens. Matter Mater. Phys.* **1999**, *59*, 1758−1775.

(83) Grimme, S.; Antony, J.; Ehrlich, S.; Krieg, S. A Consistent and Accurate *Ab Initio* Parametrization of Density Functional Dispersion Correction (DFT-D) for the 94 Elements H-Pu. *J. Chem. Phys.* **2010**, *132*, 154104−154122.

(84) Dunnington, B. D.; Schmidt, J. R. Generalization of Natural Bond Orbital Analysis to Periodic Systems: Applications to Solids and Surfaces *via* Plane-Wave Density Functional Theory. *J. Chem. Theory Comput.* **2012**, *8*, 1902−1911.

(85) Weigend, F. Accurate Coulomb-Fitting Basis Sets for H to Rn. *Phys. Chem. Chem. Phys.* **2006**, *8*, 1057−1065.

(86) Weigend, F.; Ahlrichs, R. Balanced Basis Sets of Split Valence, Triple Zeta Valence and Quadruple Zeta Valence Quality for H to Rn: Design and Assessment of Accuracy. *Phys. Chem. Chem. Phys.* **2005**, *7*, 3297−3305.

Chapter 3: Dipole-Induced Stabilization in Carboraneselenolate Self-Assembled Monolayers

3.1 Introduction

Self-assembled monolayers (SAMs) are an advantageous platform to study the fundamental interactions that dictate structure and function of nanoscale constructs. Within these systems, characterizing the forces at the substrate monolayer interface, within the monolayer, and between the monolayer and the environment is critical to understanding how these supramolecular assemblies emerge and how they directly influence macroscale properties.[1-3] From early SAM research to today, the gold-thiol bond has been a staple of directing the assembly of these monolayers.[4,5] While well studied, the chemistry of metal-chalcogenide bonds continues to draw interest in materials research and fundamental surface research.[6-12] Analogous to the gold-thiol bond, selenols have also been used as a head group to produce ordered SAMs as they also bind strongly to the gold substrate.[13-18] Comparisons of the Au-S bond and the Au-Se bond are useful for understanding the electronic and structural interactions at the monolayer substrate interface and has been a point of study.[19-22] In prototypical well-ordered *n*-alkanethiolate SAMs, the monolayer morphology consists of large domains distinguished by prominent domain boundaries and significant defects;[23] however, in *n*-alkaneselenolate SAMs, the monolayer has a distinctive Moiré pattern that is continuous with limited domain boundaries and few substrate vacancy islands.[15] These monolayers have different assemblies and different distributions and densities of defects all due to the small alteration of having chalcogenide head groups of different size and electronic properties.

In order to probe the differences between thiol and selenol binding independently from interactions and structural defects within of the monolayer, Hohman *et al.* examined monolayers composed of 1-adamantaneselenol.[24] Adamantane is a cage molecule composed of 10 carbon atoms (and associated hydrogens); due to the rigid, symmetric structure of the backbone, the lattice

structure is primarily dominated by the size of the cage and has few defects. Self-assembled monolayers composed of the thiol analog, 1-adamantanethiol, have been well characterized and while the cage is sterically bulky, the intermolecular interactions within these monolayers are relatively weak.[25-28]

In the case of 1-adamantaneselenolate SAMs, it was observed that the molecules on the surface have two binding configurations, a high-conductance state and a low-conductance state. Low-conductance state molecules are in ordered monolayers with a minority of high-conductance state randomly arranged on the surface. These molecules are dynamic on the timescale of several minutes, with switching occurring between the two binding states. This behavior is consistent with what has been previous described of the Au-Se bond as being more mobile and promiscuous than the Au-S bond. Furthermore, upon dry-annealing of the post deposition monolayer at 70 °C, reorganization occurs, resulting in long-range ordered dimers of the high-conductance molecules. This rearrangement is not observed at lower annealing temperatures; higher annealing temperature results in molecular desorption and a disordered surface. Since the intermolecular interactions between the adamantane backbones are relatively weak, the emergence of this ordered state is attributed to substrate-mediated interactions of the Au-Se bond, with the annealing process providing favorable kinetics to the already dynamic monolayer enabling this surface rearrangement.

Another class of cage molecule for self-assembly that has received significant interest is the carboranethiol. Carboranes have an icosahedral cage with the central structure composed of two carbon atoms and 10 boron atoms. Self-assembled monolayers composed of carboranethiol molecules are relatively pristine and defect-free, as is the case with other cage molecules assemblies, but these monolayers can also have significant dipole-dipole interactions.[26,29] These

dipole-dipole networks are long range and can influence material properties at the surface.[30-32] The orientation and magnitude of the molecular dipole varies between different carborane isomers and as such, the dipole-dipole interactions can be tuned.[33] The carborane cage is also amenable to functionalization, a feature that has been used previously to modulate the substrate-monolayer interface.[32,34] Herein, we describe the characterization of carboraneselenolate monolayers, which exhibit the same type of dynamic switching between high- and low-conductance binding states as 1-adamantaneselenolate SAMs, but are stable against rearrangement and desorption upon thermal annealing. This stability is attributed to the strong dipole-dipole interactions within the monolayers.

3.2 Results and Discussion

In this study, we examined two carboraneselenol isomers, 1-HSe-1,7-$C_2B_{10}H_{11}$ and 9-HSe-1,7-$C_2B_{10}H_{11}$, henceforth referred to as *m*-1-carboraneselenol (M1Sel) and *m*-9-carboraneselenol (M9Sel), respectively. Monolayers of these molecules were assembled on Au{111} substrates. The structures of these isomers are shown in Figure 3.1 and are analogous to their carboranethiol counterparts; these two isomers primarily distinguish themselves with their different dipole moments. In the case of the thiol analogs, *m*-1-carboranethiol has a calculated dipole moment that is tilted 105° with respect to the surface normal, whereas *m*-9-carboranethiol has a calculated dipole moment tilted 20° with respect to the surface normal.[33]

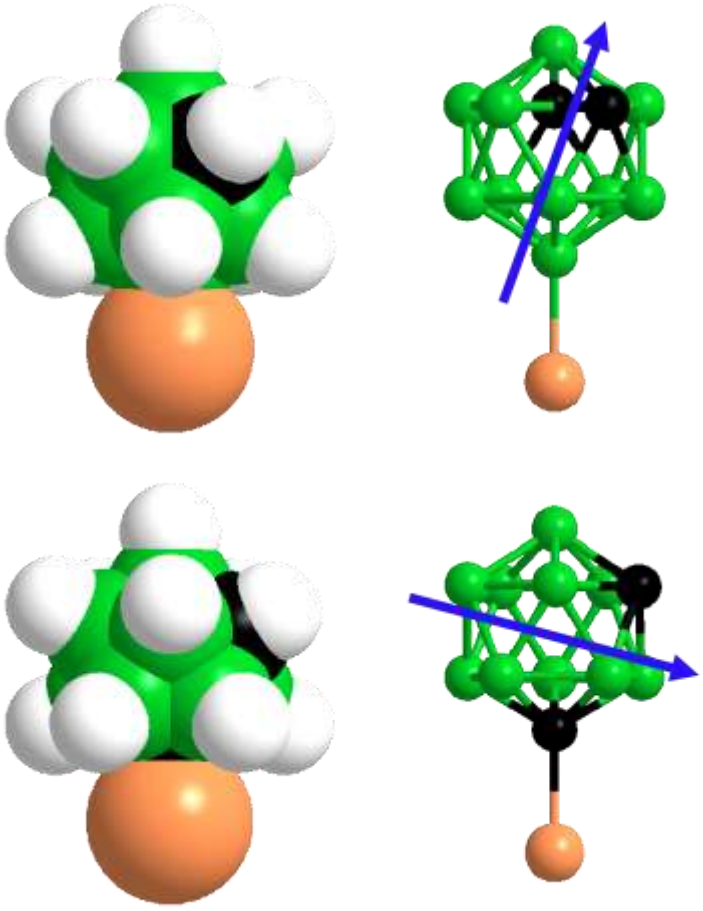

Figure 3.1 (Left) Space filling models and (Right) ball and stick models with hydrogens not displayed of (Top) *m*-9-carboraneselenolate (M9Sel) and (Bottom) *m*-1-carboraneselenolate (M1Sel). The central cage is composed of 10 boron atoms (green) and two carbon atoms (black) with hydrogen atoms at the vertices (white) and a selenium atom (orange) for surface attachment. The dipole moment (blue) of the molecules is largely determined by the position of the carbon atoms is the cage. As such, in the case of M9Sel the dipole moment is primarily normal to the surface whereas the dipole moment of M1Sel is almost parallel to the substrate.

Despite the increased size of the selenium atom, in comparison to sulfur, the size of the carborane cage backbone is the primary contributor to the steric requirements of the molecule on the surface, as is the case for all such symmetric, otherwise unfunctionalized cage molecules self-assembled on surface. The nearest neighbor distance, as measured by scanning tunneling microscopy (STM) images, in these carboraneselenol systems is 7.4 ± 0.7 Å, which is consistent with the 7.2 Å that has been previous reported for carboranethiol systems.[29,35] However, these

carboraneselenolate SAMs differ from their thiolate counterparts in that these monolayers show the presence of two binding modes, as seen in Figure 3.2, reminiscent of the previously studied 1-adamtaneselenolate SAM.[24] These carboraneselenolate monolayers are composed largely of molecules in a low-conductance binding mode, with a minority of molecules in a high-conductance binding mode, which is approximately 1 Å greater in apparent height (1.1 ± 0.1 Å) in STM images. The monolayers, as deposited, are in a random mixture with isolated molecules in the high-conductance binding state to several molecules in a cluster all in that configuration. We do, however, see differences in the degree of surface coverage of the two modes between the M9Sel SAMs and the M1Sel SAMs. In the case of the M9Sel isomer, the surface coverage of the high-conductance binding state is 13 ± 4%, whereas with the M1Sel isomer the surface coverage is higher and also more variable at 32 ± 11%. This difference could be a result of the different electronic properties of the molecule-substrate bonds. In the M9Sel isomer, the selenol head group is attached to an electron-rich boron vertex as opposed to the M1Sel isomer, where the selenol head group is on an electron-poor carbon vertex.[36]

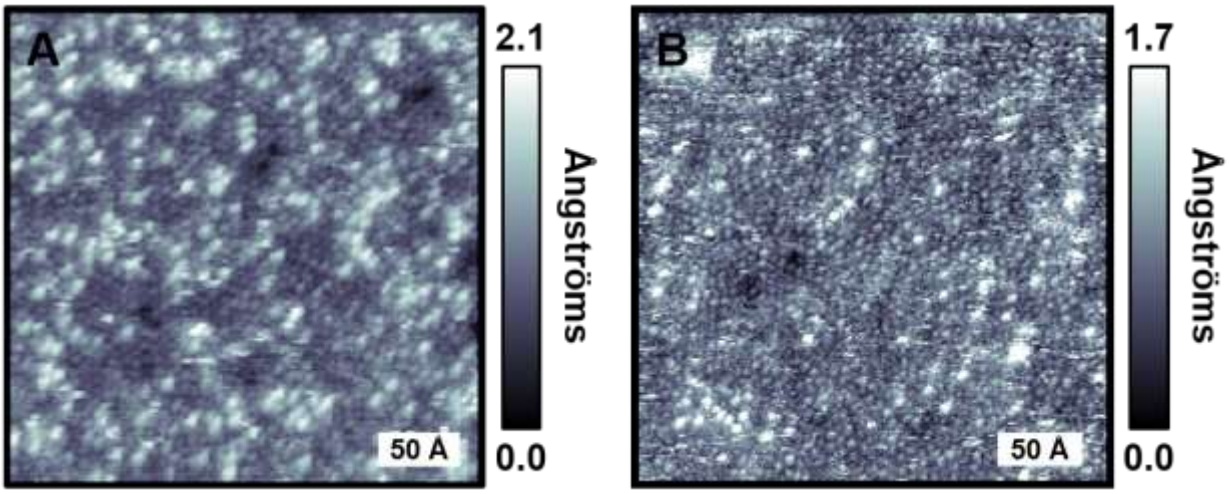

Figure 3.2 Scanning tunneling microscopy images of (A) *m*-1-carboraneselenol and (B) *m*-9-carboraneselenol showing self-assembled monolayers composed of a mixture of molecules in a minority high-conductance binding mode and a majority low-conductance binding mode. (V_{sample} = 0.1 V, I_t = 100 pA)

Additionally, these carboraneselenolate SAMs are dynamic with molecules switching between the high- and low-conductance binding states at room temperature. In sequential STM images taken over the course of several minutes, we observe individual molecules changing their conductance state, as seen in Figure 3.3. Typically, stochastic conductance switching is observed upon a chemical or isomerization reaction of a surface molecule.[37-42] However, since the chemical structure of the carborane cage is stable under these experimental conditions, we attribute the switching in this case to a change in attachment chemistry, consistent with the interpretation of switching between the two binding modes.[43-45] Approximately, 2% of molecules within an STM image exhibit conductance switching within the timescale of acquiring sequential images. This timescale can only provide us limited information about the switching rate as an individual molecule is only observed for a few seconds over the course of compiling the image (scan rate is 0.6 sec/nm for a 15 nm × 15 nm image). Furthermore, it appears that the rate of high to low conductance switching is equivalent to the rate of low to high. These features of the kinetics are

akin to those seen in the 1-adamataneselenolate SAMs, further highlighting the similarities of the Au-Se bond in these two systems.

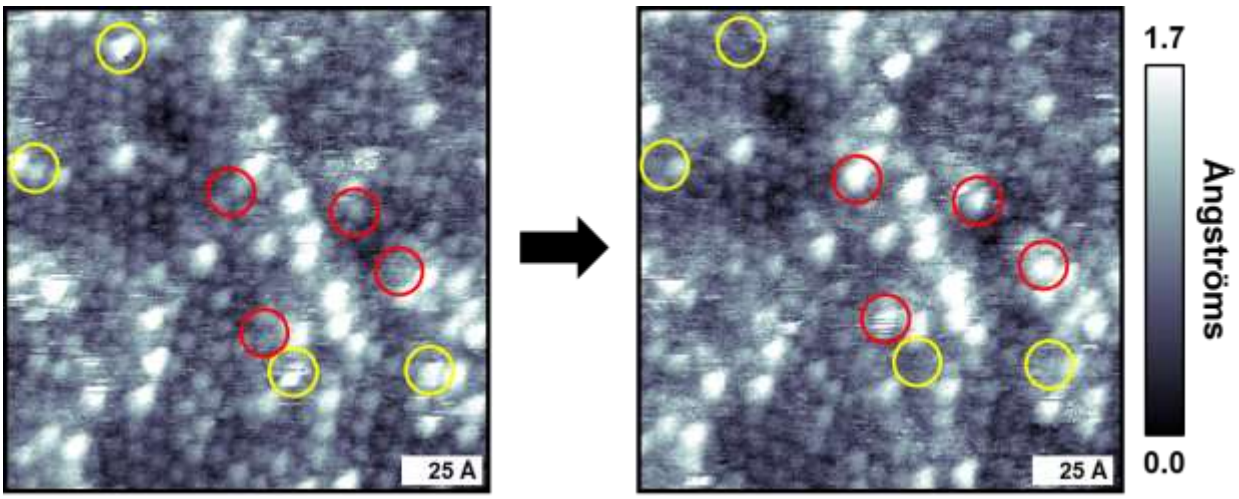

Figure 3.3 Sequential scanning tunneling microscopy images of a *m*-1-carboraneselenolate self-assembled monolayer showing stochastic conductance switching of molecules on the surface. Yellow circles highlight molecules switching from a high to low-conductance binding state and red circles highlight molecules switching from a low to high-conductance binding state. (V_{sample} = 0.1 V, I_t = 80 pA)

The initial deposition of these types of SAMs results in a kinetically favored adlayer driven by the strong interaction of the Au and the chalcogen head group; in some cases monolayers can be processed into more thermodynamically favorable states.[1,46] The 1-adamanetaneselenolate SAM is one such system, where thermal annealing can induce a long-range ordered dimer state driven by substrate-mediated interactions. Given that we already see how similar the interactions between the selenolates and the Au are in these various cage molecule systems, are these monolayer characteristics indicative of similar substrate-mediated forces being present in M1Sel and M9Sel SAMs? Furthermore, do the dynamics of the molecules on the surface mean there is potential for rearrangement into a long-range ordered state? The temperature window required to induce this rearrangement in the adamantaneselenolate system is quite narrow; annealing at 60°C has no effect, but above 70°C the monolayer begins to desorb and to become disordered. This

behavior could not be reproduced in M1Sel and M9Sel, however, where annealing up to temperatures of 78°C showed no change in the morphology of the monolayers, as shown in Figure 3.4.

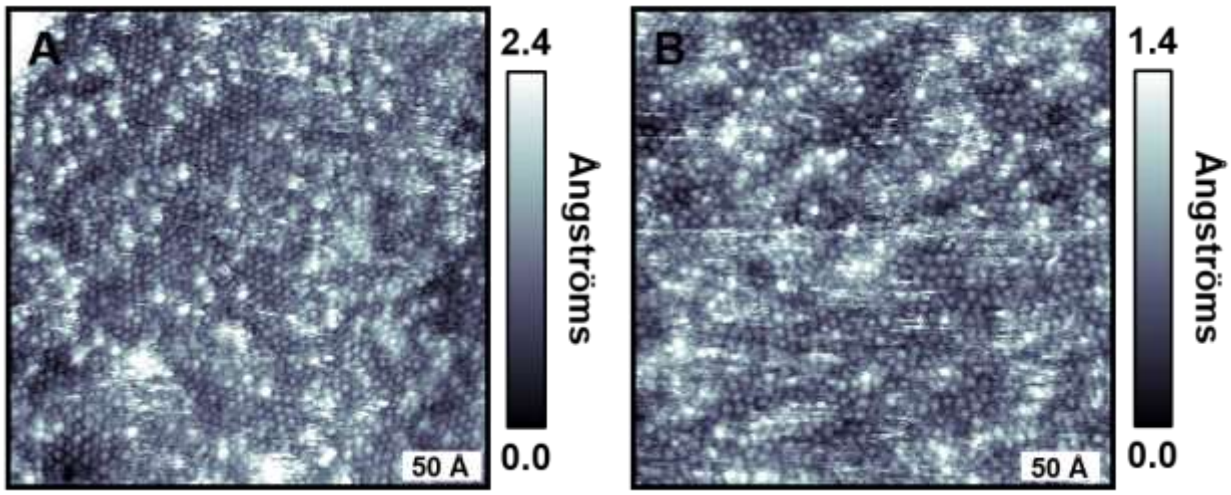

Figure 3.4 (A) Scanning tunneling microscopy image of a *m*-1-carboranselenolate self-assembled monolayer (SAM) after dry-annealing at 70°C for 24 h (V_{sample} = 0.1 V, I_t = 70 pA). (B) Scanning tunneling microscopy image of a *m*-9-carboranselenolate SAM after dry annealing at 78°C for 120 h (V_{sample} = 0.1 V, I_t = 110 pA). Both monolayers show no changes in surface organization due to the annealing.

Thus, it appears that these carboraneselenolate monolayers are stabilized against rearrangement as well as against desorption. One possible explanation is that the electronic structure of the carborane cage makes it more difficult for the selenolate to be reduced and to form a stable diselenide upon desorption. However, based on the majority peak shown in cyclic voltammograms (Figure 3.5), the M1Sel monolayer desorbs at 0.93 ± 0.04 V and M9Sel at 0.88 ± 0.03 V, which similar to the desorption voltages of prototypical *n*-alkanethiolate monolayers, which are typically ca. 1 V.[1] As such, a more probable explanation for the stabilization of these monolayers is the dipole-dipole networks present in them. It has been shown that the dipole-dipole interactions within carboranethiolate monolayers can be long range and that greater in-plane dipole-dipole interactions can resist displacement of the monolayers.[29,30] The results in this study suggest that these dipole-

dipole interactions are strong enough to outweigh other driving forces within the monolayer, such as substrate-mediated interactions.

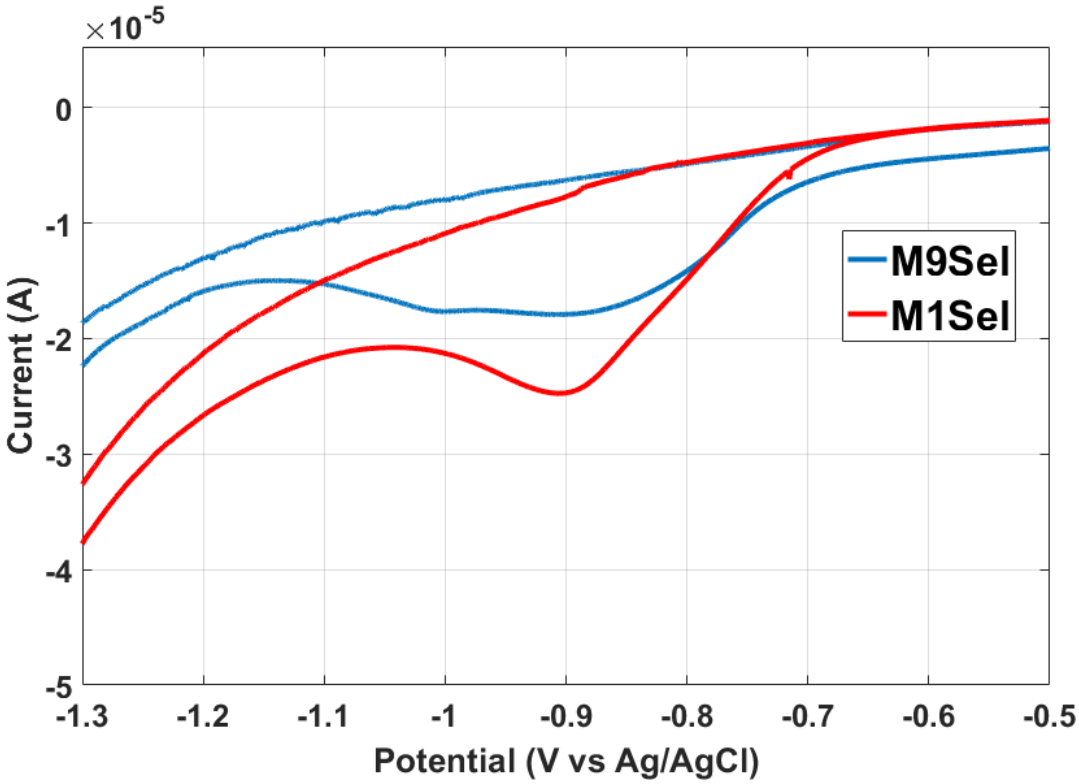

Figure 3.5 Cyclic voltammograms peaks corresponding to the reductive desorption of (blue) *m*-9-carboraneselenolate (M9Sel) and (red) *m*-1-carboraneselenolate (M1Sel). The M1Sel monolayer desorbs at 0.93 ± 0.04 V and M9Sel at 0.88 ± 0.03 V.

3.3 Conclusions and Prospects

The two carboraneselenol isomers, *m*-1-carboraneselenol and *m*-9-carboraneselenol, form pristine monolayers with packing densities determined by the bulky cage backbone, analogous to their carboranethiol counterparts. Scanning tunneling microscopy images reveal however that these selenolate monolayers exhibit a dynamic double lattice, like those of with 1-adamtaneselenolate SAMs, another cage molecule on Au{111} selenolate. In

carboraneselenolate SAMs there exist two binding modes, a high-conductance state and a low-conductance state, and surface molecules stochastically switch between the two states. We observe this switching through sequential STM images and find that the dynamics are similar to those of 1-adamtaneselenolate. In the case of both carboraneselenolate isomers, the high-conductance state is the minority mode, however, the only observable difference between the isomeric monolayers is that the surface coverage of the high-conductance state is higher in M1Sel than in M9Sel. Critically, we see that these monolayers are stable under thermal annealing up to 78°C against desorption and against rearrangement to a surface configuration driven by substrate-mediated interactions. This stability is likely a result of the strong dipole-dipole interactions within the monolayers.

These carboraneselenolate systems are a useful platform for probing the balance between forces at the substrate-monolayer interface and forces within the monolayer. As such, it is necessary to characterize further the stability of these monolayers and to determine at which temperature they begin to desorb and whether a temperature window exists that favors the thermodynamic balance between interactions of the selenium atom and the gold substrate. This further understanding of monolayer stability can also provide insight into the difference between the two isomers and their respective dipole-dipole networks. The comparison of these isomeric systems can help elucidate the differences in properties of the Au-Se-B bond *versus* the Au-Se-C bond. Thus, this study highlights the variability in chalcogenide-gold chemistry and the forces within self-assembled monolayers; carboraneselenol molecules remain an avenue for exploring these properties further.

3.4 Materials and Methods

Scanning tunneling microscopy sample preparation and image analysis: *m*-1-carboraneselenol and *m*-9-carboraneselenol were synthesized as previously described in the literature and stored in a glovebox environment with solutions prepared immediately before use.[47] Samples for imaging were prepared on Au{111}/mica substrates (Agilent Technology, Tempe, AZ), which were hydrogen-flame annealed with 10 passes at a rate of 0.4 Hz prior to SAM formation. Substrates were placed in 1 mM ethanolic solutions for 24 h at room temperature. Ethanol was used as received (Sigma-Aldrich, St. Louis, MO). After deposition, samples where rinsed with neat ethanol and dried under a stream of ultra high-purity nitrogen for at least three cycles. Samples were then imaged or sealed in an empty glass vial and dry-annealed at the prescribed temperature and time duration. All STM measurements were performed with a custom-built Besocke-style STM with a platinum/iridium tip (80:20).[48,49] The known lattice of the 1-dodecanethiolate SAMs on Au{111} was used for calibration. The STM image analyses was done using MATLAB (Mathworks, Natick, MA) and Gwyddion (http://gwyddion.net/).

Reductive desorption: Cyclic voltammograms were recorded with a Reference 600 Potentiostat/Galvanostat/ZRA (Gamry Instruments, Warminster, PA, USA). A three-electrode setup was used with the sample as the working electrode, a Ag/AgCl reference electrode, and a platinum wire counter electrode. The working electrode area was 0.08 cm^2. Samples were mounted to a custom Teflon cell, and electrical contact was established through a gold ring on top of the surface. A rubber O-ring was inserted into the interior of the gold ring to prevent leakage. The electrolyte solution used was 1x phosphate-buffered saline. The scan rate was 50 mV/s.

3.5 References

(1) Love, J. C.; Estroff, L. A.; Kriebel, J. K.; Nuzzo, R. G.; Whitesides, G. M. Self-Assembled Monolayers of Thiolates on Metals as a Form of Nanotechnology. *Chem. Rev.* **2005,** *105*, 1103-1170.

(2) Smith, R. K.; Lewis, P. A.; Weiss, P. S. Patterning Self-Assembled Monolayers. *Prog. Surf. Sci.* **2004,** *75*, 1-68.

(3) Claridge, S. A.; Liao, W.-S.; Thomas, J. C.; Zhao, Y.; Cao, H. H.; Cheunkar, S.; Serino, A. C.; Andrews, A. M.; Weiss, P. S. From the Bottom Up: Dimensional Control and Characterization in Molecular Monolayers. *Chem. Soc. Rev.* **2013,** *42*, 2725-2745.

(4) Vericat, C.; Vela, M. E.; Benitez, G.; Carro, P.; Salvarezza, R. C. Self-Assembled Monolayers of Thiols and Dithiols on Gold: New Challenges for a Well-Known System. *Chem. Soc. Rev.* **2010,** *39*, 1805-1834.

(5) Nuzzo, R. G.; Allara, D. L. Adsorption of Bifunctional Organic Disulfides on Gold Surfaces. *J. Am. Chem. Soc.* **1983,** *105*, 4481-4483.

(6) Woodruff, D. P. The Interface Structure of *n*-Alkylthiolate Self-Assembled Monolayers on Coinage Metal Surfaces. *Phys. Chem. Chem. Phys.* **2008,** *10*, 7211-7221.

(7) Lopez-Acevedo, O.; Akola, J.; Whetten, R. L.; Grönbeck, H.; Häkkinen, H. Structure and Bonding in the Ubiquitous Icosahedral Metallic Gold Cluster $Au_{144}(Sr)_{60}$. *J. Phys. Chem. C* **2009,** *113*, 5035-5038.

(8) Maksymovych, P.; Voznyy, O.; Dougherty, D. B.; Sorescu, D. C.; Yates, J. T. Gold Adatom as a Key Structural Component in Self-Assembled Monolayers of Organosulfur Molecules on Au(111). *Prog. Surf. Sci.* **2010,** *85*, 206-240.

(9) Tsuji, Y.; Staykov, A.; Yoshizawa, K. Orbital Views of Molecular Conductance Perturbed by Anchor Units. *J. Am. Chem. Soc.* **2011,** *133*, 5955-5965.

(10) Xue, Y.; Li, X.; Li, H.; Zhang, W. Quantifying Thiol–Gold Interactions Towards the Efficient Strength Control. *Nat. Commun.* **2014,** *5*, 4348.

(11) Bürgi, T. Properties of the Gold–Sulphur Interface: From Self-Assembled Monolayers to Clusters. *Nanoscale* **2015,** *7*, 15553-15567.

(12) Trang, B.; Yeung, M.; Popple, D. C.; Schriber, E. A.; Brady, M. A.; Kuykendall, T. R.; Hohman, J. N. Tarnishing Silver Metal into Mithrene. *J. Am. Chem. Soc.* **2018,** *140*, 13892-13903.

(13) Shaporenko, A.; Ulman, A.; Terfort, A.; Zharnikov, M. Self-Assembled Monolayers of Alkaneselenolates on (111) Gold and Silver. *J. Phys. Chem. B* **2005,** *109*, 3898-3906.

(14) Monnell, J. D.; Stapleton, J. J.; Dirk, S. M.; Reinerth, W. A.; Tour, J. M.; Allara, D. L.; Weiss, P. S. Relative Conductances of Alkaneselenolate and Alkanethiolate Monolayers on Au{111}. *J. Phys. Chem. B* **2005,** *109*, 20343.

(15) Monnell, J. D.; Stapleton, J. J.; Jackiw, J. J.; Dunbar, T.; Reinerth, W. A.; Dirk, S. M.; Tour, J. M.; Allara, D. L.; Weiss, P. S. Ordered Local Domain Structures of Decaneselenolate and Dodecaneselenolate Monolayers on Au{111}. *J. Phys. Chem. B* **2004,** *108*, 9834-9841.

(16) Huang, F. K.; Horton, R. C.; Myles, D. C.; Garrell, R. L. Selenolates as Alternatives to Thiolates for Self-Assembled Monolayers: A Sers Study. *Langmuir* **1998,** *14*, 4802-4808.

(17) Bashir, A.; Käfer, D.; Müller, J.; Wöll, C.; Terfort, A.; Witte, G. Selenium as a Key Element for Highly Ordered Aromatic Self-Assembled Monolayers. *Angew. Chem. Int. Ed.* **2008,** *47*, 5250-5252.

(18) Szelągowska-Kunstman, K.; Cyganik, P.; Schüpbach, B.; Terfort, A. Relative Stability of Thiol and Selenol Based Sams on Au(111)-Exchange Experiments. *Phys. Chem. Chem. Phys.* **2010,** *12*, 4400-4406.

(19) Yaliraki, S. N.; Kemp, M.; Ratner, M. A. Conductance of Molecular Wires: Influence of Molecule−Electrode Binding. *J. Am. Chem. Soc.* **1999,** *121*, 3428-3434.

(20) Protsailo, L. V.; Fawcett, W. R.; Russell, D.; Meyer, R. L. Electrochemical Characterization of the Alkaneselenol-Based Sams on Au(111) Single Crystal Electrode. *Langmuir* **2002,** *18*, 9342-9349.

(21) Patrone, L.; Palacin, S.; Bourgoin, J. P. Direct Comparison of the Electronic Coupling Efficiency of Sulfur and Selenium Alligator Clips for Molecules Adsorbed onto Gold Electrodes. *Appl. Surf. Sci.* **2003,** *212-213*, 446-451.

(22) Yokota, K.; Taniguchi, M.; Kawai, T. Control of the Electrode-Molecule Interface for Molecular Devices. *J. Am. Chem. Soc.* **2007,** *129*, 5818-5819.

(23) Poirier, G. E. Characterization of Organosulfur Molecular Monolayers on Au(111) Using Scanning Tunneling Microscopy. *Chem. Rev.* **1997,** *97*, 1117-1128.

(24) Hohman, J. N.; Kim, M.; Schüpbach, B.; Kind, M.; Thomas, J. C.; Terfort, A.; Weiss, P. S. Dynamic Double Lattice of 1-Adamantaneselenolate Self-Assembled Monolayers on Au{111}. *J. Am. Chem. Soc.* **2011,** *133*, 19422-19431.

(25) Kim, M.; Hohman, J. N.; Morin, E. I.; Daniel, T. A.; Weiss, P. S. Self-Assembled Monolayers of 2-Adamantanethiol on Au{111}: Control of Structure and Displacement. *The Journal of Physical Chemistry A* **2009,** *113*, 3895-3903.

(26) Hohman, J. N.; Claridge, S. A.; Kim, M.; Weiss, P. S. Cage Molecules for Self-Assembly. *Materials Science and Engineering: R: Reports* **2010,** *70*, 188-208.

(27) Dameron, A. A.; Charles, L. F.; Weiss, P. S. Structures and Displacement of 1-Adamantanethiol Self-Assembled Monolayers on Au{111}. *J. Am. Chem. Soc.* **2005,** *127*, 8697-8704.

(28) Saavedra, H. M.; Barbu, C. M.; Dameron, A. A.; Mullen, T. J.; Crespi, V. H.; Weiss, P. S. 1-Adamantanethiolate Monolayer Displacement Kinetics Follow a Universal Form. *J. Am. Chem. Soc.* **2007,** *129*, 10741-10746.

(29) Hohman, J. N.; Zhang, P.; Morin, E. I.; Han, P.; Kim, M.; Kurland, A. R.; McClanahan, P. D.; Balema, V. P.; Weiss, P. S. Self-Assembly of Carboranethiol Isomers on Au{111}: Intermolecular Interactions Determined by Molecular Dipole Orientations. *ACS Nano* **2009,** *3*, 527-536.

(30) Thomas, J. C.; Schwartz, J. J.; Hohman, J. N.; Claridge, S. A.; Auluck, H. S.; Serino, A. C.; Spokoyny, A. M.; Tran, G.; Kelly, K. F.; Mirkin, C. A.; Gilles, J.; Osher, S. J.; Weiss, P. S. Defect-Tolerant Aligned Dipoles within Two-Dimensional Plastic Lattices. *ACS Nano* **2015,** *9*, 4734-4742.

(31) Kim, J.; Rim, Y. S.; Liu, Y.; Serino, A. C.; Thomas, J. C.; Chen, H.; Yang, Y.; Weiss, P. S. Interface Control in Organic Electronics Using Mixed Monolayers of Carboranethiol Isomers. *Nano Lett.* **2014,** *14*, 2946-2951.

(32) Serino, A. C.; Anderson, M. E.; Saleh, L. M. A.; Dziedzic, R. M.; Mills, H.; Heidenreich, L. K.; Spokoyny, A. M.; Weiss, P. S. Work Function Control of Germanium through Carborane-Carboxylic Acid Surface Passivation. *ACS Applied Materials & Interfaces* **2017,** *9*, 34592-34596.

(33) Schwartz, J. J.; Mendoza, A. M.; Wattanatorn, N.; Zhao, Y.; Nguyen, V. T.; Spokoyny, A. M.; Mirkin, C. A.; Baše, T.; Weiss, P. S. Surface Dipole Control of Liquid Crystal Alignment. *J. Am. Chem. Soc.* **2016,** *138*, 5957-5967.

(34) Thomas, J. C.; Goronzy, D. P.; Serino, A. C.; Auluck, H. S.; Irving, O. R.; Jimenez-Izal, E.; Deirmenjian, J. M.; Macháček, J.; Sautet, P.; Alexandrova, A. N.; Baše, T.; Weiss, P. S. Acid–Base Control of Valency within Carboranedithiol Self-Assembled Monolayers: Molecules Do the Can-Can. *ACS Nano* **2018,** *12*, 2211-2221.

(35) Thomas, J. C.; Boldog, I.; Auluck, H. S.; Bereciartua, P. J.; Dušek, M.; Macháček, J.; Bastl, Z.; Weiss, P. S.; Baše, T. Self-Assembled *p*-Carborane Analogue of *p*-Mercaptobenzoic Acid on Au{111}. *Chem. Mater.* **2015,** *27*, 5425-5435.

(36) Grimes, R. N. *Carboranes*. Academic Press: New York, 1970.

(37) Lewis, P. A.; Inman, C. E.; Yao, Y.; Tour, J. M.; Hutchison, J. E.; Weiss, P. S. Mediating Stochastic Switching of Single Molecules Using Chemical Functionality. *J. Am. Chem. Soc.* **2004,** *126*, 12214-12215.

(38) Donhauser, Z. J.; Mantooth, B. A.; Kelly, K. F.; Bumm, L. A.; Monnell, J. D.; Stapleton, J. J.; Price, D. W.; Rawlett, A. M.; Allara, D. L.; Tour, J. M.; Weiss, P. S. Conductance Switching in Single Molecules through Conformational Changes. *Science* **2001,** *292*, 2303.

(39) Iancu, V.; Hla, S.-W. Realization of a Four-Step Molecular Switch in Scanning Tunneling Microscope Manipulation of Single Chlorophyll-a Molecules. *Proc. Natl. Acad. Sci. U. S. A.* **2006,** *103*, 13718.

(40) Kim, M.; Hohman, J. N.; Cao, Y.; Houk, K. N.; Ma, H.; Jen, A. K. Y.; Weiss, P. S. Creating Favorable Geometries for Directing Organic Photoreactions in Alkanethiolate Monolayers. *Science* **2011,** *331*, 1312.

(41) Cho, J.; Berbil-Bautista, L.; Levy, N.; Poulsen, D.; Fréchet, J. M. J.; Crommie, M. F. Functionalization, Self-Assembly, and Photoswitching Quenching for Azobenzene Derivatives Adsorbed on Au(111). *J. Chem. Phys.* **2010,** *133*, 234707.

(42) Kumar, A. S.; Ye, T.; Takami, T.; Yu, B.-C.; Flatt, A. K.; Tour, J. M.; Weiss, P. S. Reversible Photo-Switching of Single Azobenzene Molecules in Controlled Nanoscale Environments. *Nano Lett.* **2008,** *8*, 1644-1648.

(43) Wang, K.; Zhang, C.; Loy, M. M. T.; Xiao, X. Time-Dependent Tunneling Spectroscopy for Studying Surface Diffusion Confined in Nanostructures. *Phys. Rev. Lett.* **2005,** *94*, 036103.

(44) Moore, A. M.; Dameron, A. A.; Mantooth, B. A.; Smith, R. K.; Fuchs, D. J.; Ciszek, J. W.; Maya, F.; Yao, Y.; Tour, J. M.; Weiss, P. S. Molecular Engineering and Measurements to Test Hypothesized Mechanisms in Single Molecule Conductance Switching. *J. Am. Chem. Soc.* **2006,** *128*, 1959-1967.

(45) Moore, A. M.; Mantooth, B. A.; Donhauser, Z. J.; Maya, F.; Price, D. W.; Yao, Y.; Tour, J. M.; Weiss, P. S. Cross-Step Place-Exchange of Oligo(Phenylene−Ethynylene) Molecules. *Nano Lett.* **2005,** *5*, 2292-2297.

(46) Kim, M.; Hohman, J. N.; Serino, A. C.; Weiss, P. S. Structural Manipulation of Hydrogen-Bonding Networks in Amide-Containing Alkanethiolate Monolayers Via Electrochemical Processing. *J. Phys. Chem. C* **2010,** *114*, 19744-19751.

(47) Spokoyny, A. M.; Machan, C. W.; Clingerman, D. J.; Rosen, M. S.; Wiester, M. J.; Kennedy, R. D.; Stern, C. L.; Sarjeant, A. A.; Mirkin, C. A. A Coordination Chemistry Dichotomy for Icosahedral Carborane-Based Ligands. *Nat. Chem.* **2011,** *3*, 590.

(48) Frohn, J.; Wolf, J. F.; Besocke, K.; Teske, M. Coarse Tip Distance Adjustment and Positioner for a Scanning Tunneling Microscope. *Rev. Sci. Instrum.* **1989,** *60*, 1200-1201.

(49) Ferris, J. H.; Kushmerick, J. G.; Johnson, J. A.; Yoshikawa Youngquist, M. G.; Kessinger, R. B.; Kingsbury, H. F.; Weiss, P. S. Design, Operation, and Housing of an Ultrastable, Low Temperature, Ultrahigh Vacuum Scanning Tunneling Microscope. *Rev. Sci. Instrum.* **1998,** *69*, 2691.

Chapter 4: Influence of Terminal Carboxyl Group on Structure and Reactivity of Functionalized *m*-Carboranethiolate Self-Assembled Monolayers

4.1 Introduction

Two-dimensional self-assembled materials, in addition to their utility for numerous applications, are important tools in advancing our understanding of the principles of self-assembly.[1-4] As such, developing building blocks is of fundamental importance in enabling the investigation of specific steric and electronic effects or intermolecular interactions within self-assembled monolayers (SAMs).[5] Organic molecules have been extensively explored in this field, offering possible analogies to naturally occurring biological systems and allowing studies of the impact of defined chemical modifications.[2] Introduction of additional ω-functionality such as carboxyl groups resulted in different properties of the surfaces, determined by the hydrogen-bonding intermolecular interactions and hydrophilic character.[6-8] Several systems, including carboxyl-terminated alkanethiols and mercapto-benzoic acids, have been investigated as convenient building blocks on both flat and colloidal surfaces.[9-11] In these particular systems, the anchoring thiol and the exposed carboxyl groups are separated by either conformationally flexible aliphatic -$(CH_2)_x$- alkyl chains or sheet-like aromatic -(C_6H_4)- benzene rings with different steric requirements and mutual interactions.

In our laboratories, we have introduced carborane building blocks that due to symmetry have lower total numbers and fewer defects within their molecular monolayers compared to organic systems.[12-14] These differences are at least partly due to their rigid molecular architectures with lower conformational freedom. Carborane–based systems enable us to obtain surface assemblies of different isomers in identical or highly similar surface patterns. The *para*-carboranethiol cage analogue of *para*-mercaptobenzoic acid has been shown to assemble into a hexagonal pattern identical to that of its non-carboxylated parent analogue, with no influence of the carboxyl group on the nearest neighbor spacing.[11] The closest hexagonal packing of carboranethiol molecules on flat surfaces simply compares to the tightest filling of the surface by solid spheres, *i.e.*, the projection of the cage onto the surface, similar to previously observed

behaviors of other architecturally rigid bulk molecules such as adamantane derivatives.[15-17] The structurally rigid bodies of carboranes enable unprecedented variability of isomeric structures whilst the surface lattice remains either the same or is only gently modified.[5,18-21] In this regard, special attention has been paid to the dipole moment orientation, which is mainly given by the positioning of the (electron-deficient) carbon atoms in the cage, and to its effect on work function changes.[22-25]

Building on these advances, we prepared two isomeric bifunctional cage molecules based on the *meta*-carborane skeleton, juxtaposing them to their organic analogue, *meta*-mercaptobenzoic acid, as well as the previously studied *para*-isomer as building blocks for SAMs. Both new isomers show practically identical orientations of functional groups with respect to the centroid of the *meta*-carborane cage but differ in chemical and physical properties as determined by the electron-donating and -withdrawing properties of the molecular cage scaffold. In addition, they differ in their symmetry; one of them belonging to a rather rarely investigated group of chiral cage borane derivatives.[26] Assemblies of chiral molecules on surfaces are currently of interest due to their spin-filtering effects in electron transport.[27-29]

The interactions of both functional groups, interspaced by the *meta*-carborane skeleton, were analyzed in SAMs *vis-à-vis* the differences of the two isomers. Furthermore, the effect of increased lateral interactions on the assembly of these monolayers was experimentally examined and the results were compared to computational models. Lastly, the change in behavior of the carboxyl functional group was probed, as it moves from a three-dimensional environment to the exposed interface of a two-dimensional array.

4.2 Results and Discussion

4.2.1 Intrinsic Properties and Characteristics of Carboxylated *meta*-Carboranes

Isomeric bifunctional carborane species were synthesized from the respective thiol derivatives of *meta*-carborane by their lithiation and subsequent reaction with CO_2 followed by acidic hydrolytic quenching: 1-SH-1,7-$C_2B_{10}H_{11}$ (**M1**) produced 1-COOH-7-SH-1,7-$C_2B_{10}H_{10}$ (**M1-COOH**) and 9-SH-1,7-$C_2B_{10}H_{11}$ (**M9**) was transformed into *racem*-1-COOH-9-SH-1,7-$C_2B_{10}H_{10}$ (**M9-COOH**). A schematic representation is shown in the additional figures (Scheme 4.1). X-ray diffraction studies confirmed that both isomers have almost identical geometries with the angle α[C_{COOH}, centroid, S_{SH}] of 114.54° in **M1-COOH** and 115.31° in **M9-COOH**. Figure 4.1 shows the crystallographically determined structures of both isomers. Computationally optimized geometries, also shown in Figure 4.1, were consistent with experimental data and include the projections of the orientations and the relative strengths of the dipole moments. Both isomeric molecules exhibit different molecular symmetries due to the specific positioning of functional groups on the *meta*-carborane cluster core, which are reflected in their ^{11}B NMR spectra (Figures 4.8-4.10, Tables 4.6 and 4.7). For both of these isomers the carboxyl group is attached to an electron-accepting carbon vertex; the thiol functional group in **M1-COOH** is also attached to an electron-accepting carbon vertex, in contrast to an electron-donating boron vertex in **M9-COOH**. The **M9-COOH** isomer is chiral with both enantiomers resolved in racemic single-crystal structure analysed by X-ray diffraction (Figure 4.11, Tables 4.8 and 4.9). Molecules of both isomers exhibit similar intermolecular hydrogen interactions in their supramolecular crystal structure; dominated by the carboxyl and thiol functional groups. Additionally both molecules showed similar isotopic distributions in their ESI mass spectra and were further characterized by infrared spectroscopy (Figures 4.12-4.19 and 4.20 and 4.21)

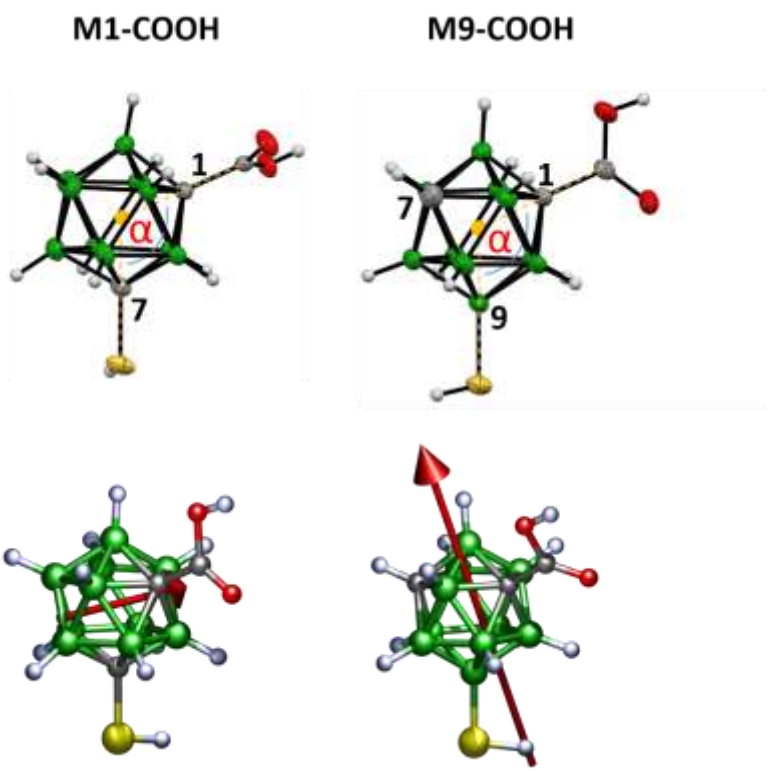

Figure 4.1 Structure of carboxylated *meta*-carborane isomers. Crystallographically determined molecular structures of **M1-COOH** and **M9-COOH** with 50% probability ellipsoids for the non-hydrogen atoms (upper panel). The lower schematics of both isomers show computationally optimized structures with arrows indicating the orientations and the relative magnitudes of the dipole moments. The yellow dots in the crystallographically determined structures represent the centroids of the C_2B_{10} cage parts of the molecules.

The difference between the effects of the electron-accepting carbon and the electron-donating boron vertices on the thiol group is consistent with previous studies, which relate the thiol group character to the type of the carborane skeleton (*ortho*-, *meta*-, or *para*-) and to the thiol group's position on the cage.[30-33] The new bifunctional molecular system with one carboxyl group and one thiol group enabled us to investigate their mutual influence dependence on their positions on the *meta*-carborane cage. In the case of **M1-COOH**, both functional groups are attached to the carbon atoms, the electron-withdrawing vertices of the *meta*-carborane scaffold. In the isomer **M9-COOH**, the thiol group is attached to a boron atom, through which *meta*-carborane manifests a relatively strong electron-donating effect. Table 4.1 provides a summary of selected characteristic parameters related to the chemical natures of

both functional groups; these properties are important for their mutual intramolecular communication, as well as for their behavior as building blocks of self-assembled monolayers, as discussed below. The ^{1}H NMR shifts of the respective thiol groups and the carboxyl pK_a values of both isomers are displayed in Table 4.1 (See also Tables 4.6 and 4.7 and Figure 4.22). For comparison, the pK_a value of the *meta*-carborane-1-carboxylic acid (**M-COOH**) is also reported. Both **M1** and **M1-COOH** show practically the same values of ^{1}H NMR shift of their thiol groups at about 3.4 - 3.5 ppm. In comparison, the ^{1}H NMR shifts of the thiol groups in both **M9** and **M9-COOH** is lower, at about 0.5 ppm, which is in accord with the electron-donating character of the boron vertex of *meta*-carborane. Note that the thiol chemical shifts in the ^{1}H NMR spectrum not only manifest the electron-accepting (as in **M1** or **M1-COOH**) and electron-donating (as in **M9** and **M9-COOH**) effects of the *m*-carboranyl cage moiety but also show, consistent with our previous findings, that the carboxyl group does not significantly influence the thiol group in this regard. By contrast, the thiol group interacts significantly with the molecular skeleton and thus increases the carboxyl group acidity as evident from the lower pK_a values in both isomers compared to **M-COOH** (1-COOH-*m*-$C_2B_{10}H_{11}$).

Derivative	^{1}H NMR (SH)	pK_a (COOH)
M1	3.39	−
M1-COOH	3.46	3.01
M9	0.47	−
M9−COOH	0.52	3.23
M−COOH	−	3.76

Table 4.1 Experimental ^{1}H NMR chemical shifts of the thiol (SH) groups and the carboxyl (COOH) pK_a values of the new isomeric derivatives and their parent compounds.

4.2.2 Characterization of Self-Assembled Monolayers *via* Scanning Tunneling Microscopy

Scanning tunneling microscopy (STM) was used to image homogeneous SAMs of both **M1-COOH** and **M9-COOH** on Au{111}/mica with molecular resolution under ambient conditions. Both isomers form into hexagonal close-packed structures with a nearest-neighbor distance of 8.4 ± 0.4 Å (Figures 4.2 and 4.23). These results are remarkable given that in the previous study of the *para*-isomer, molecularly resolved images of the homogeneous carboxylic-acid terminated monolayer were unattainable.[11] Furthermore, the attachment of a carboxyl group to the parent molecules **M1** and **M9** increases the steric demands of both isomeric molecules as compared with the lateral steric requirements of the parent non-carboxylated derivatives, which both have a nearest-neighbor distance of 7.2 ± 0.4 Å.[13] The molecular symmetry differences between the isomers have no direct influence on the geometry of the surface lattice, as evidenced by isostructural monolayers with experimentally indistinguishable nearest neighbor spacing. Two phases were observed in the monolayers,

which differed in apparent height by 1.0 ± 0.3 Å in both **M1-COOH** and **M9-COOH** SAMs. The higher apparent protrusion is the minority phase with coverage of 3 ± 1% in SAMs of both isomers (Figure 4.24). This feature has been observed previously and attributed to a mixture of thiolate- and thiol-bound moieties, with the latter being the more protruding apparent height feature.[11] Alternatively, the carboxylic acid may have converted to an ester in the molecules in the minority phase, as the relative population size of the phase is consistent with spontaneous esterification. We also observed rotational domains in the monolayers; and, as has been reported previously for other carboranethiol SAMs, these domains did not have prominent domain boundaries in STM images.[13]

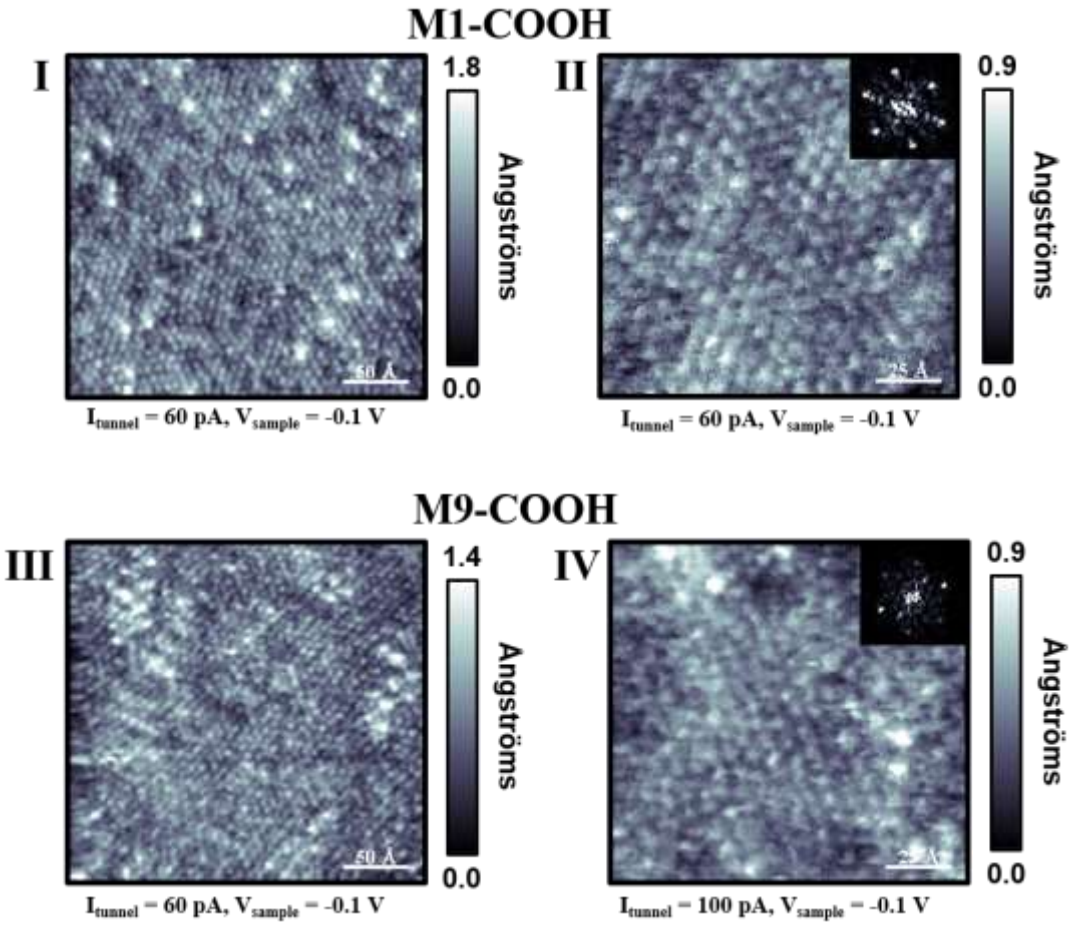

Figure 4.2 Scanning tunneling microscopy images of (I, II) **M1-COOH** and (III, IV) **M9-COOH** self-assembled on Au{111}. All images were taken at ambient conditions. Insets depicting Fourier transforms of (II) and (IV) show hexagonal close-packed arrays with an identical nearest-neighbor distance of 8.4 ± 0.4 Å for both isomers.

Possible unit cells, which are commensurate with the gold registries, are (5 × 5) and (3 × 3); they have nearest–neighbor distances of 8.3 Å and 8.64 Å, respectively, with reference to the 2.88 Å lattice constant of the Au{111} surface, both therefore close to the experimentally determined value. The (3 × 3) unit cell consists of one SAM molecule binding with its sulfur atom to a two-fold bridge site, while the (5 × 5) unit cell consists of three SAM molecules binding atop and three-fold hollow sites in a 1:2 ratio.

4.2.3 Computational Analysis of the Self-Assembled Monolayer Structure

As determined by the STM analysis, the presence of a carboxyl functional group increases the steric demands of the molecules within the SAM. To explore these lateral interactions further we performed several computational analyses. In examining the space-filling model from projection onto the surface, we find that a molecular tilt of 13-16° minimizes the projection and therefore maximizes packing density. This minimum corresponds to a nearest-neighbor distance of 8.6 Å, which is in close agreement with what we observed experimentally with STM (Figure 4.3).

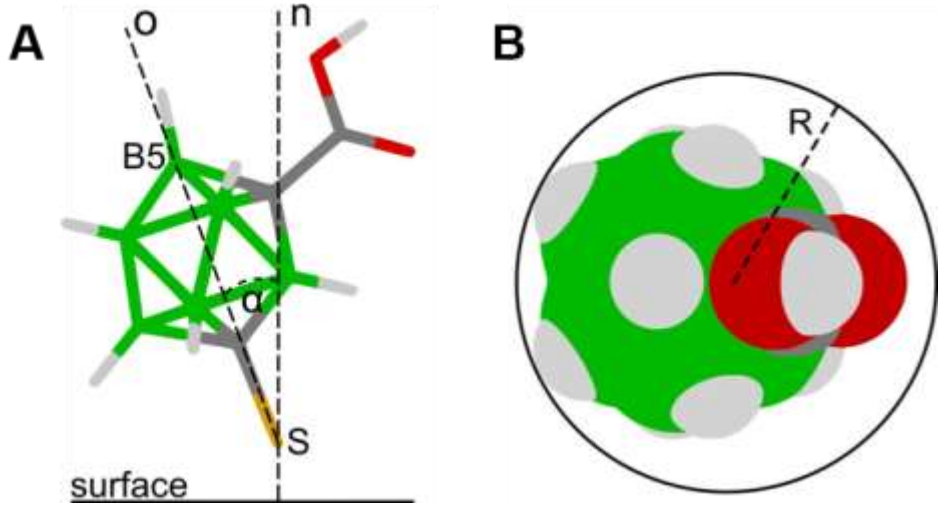

Figure 4.3 (A) Schematic representation of the isomeric molecule **M1-COOH** tilted 13-16° (α) from the surface normal and (B) the respective space-filling model projection onto the surface (R=8.6 Å).

Although this geometric, space-filling model is highly intuitive and the nearest-neighbor distance derived from it corresponds well to the experimental data, it also requires assumptions about the rigidity of the molecule, such as the static axis intersecting the sulfur atom and the antipodal boron vertex. As such, we performed density functional theory (DFT) calculations using the SCAN-rVV10 functional for both isomeric species to provide rigorous details about the molecular tilt on the surface. Both the (3 × 3) and (5 × 5) unit cells were examined, but only the (3 × 3) unit cell corresponds to a densely packed monolayer and thus provides a comparison to the acquired experimental data. The results are summarized in Table 4.2 and depicted in Figure 4.4. Optimized geometries revealed two different conformations (A and B), one of which shows the molecule tilted backwards to expose the carboxyl group to the monolayer-environment interface (A); the other conformation shows the molecule leaning with the carboxyl group towards the neighboring molecule and exhibiting a hydrogen-bonding interaction in the lateral direction (B). While the first conformation can be understood as a result of favorable steric preferences, the second conformation could result from favorable lateral interactions between the positively charged carboxyl proton and negatively charged cluster vertices of an adjacent molecule. Similar interactions between acidic hydrogen atoms and BH cluster vertices of the appropriate charge have been previously reported to occur in 3D single-crystals.[34] The energy difference between geometries A and B is relatively small, ~1 $kJ \cdot mol^{-1}$, (Figure 4.4) and as a result we cannot distinguish which configuration is more energetically favorable.

Computationally, **M1-COOH** is found to be stable in both conformations while **M9-COOH** is only stable in configuration B. However, we do *not* see evidence for the existence of two conformations in the STM data; we see neither a mixture of configurations A and B in SAMs of **M1-COOH** nor structural differences between the SAMs of the two isomers.

It is possible that ambient STM cannot differentiate between the two configurations. Calculations show that the charge density that the STM probes is located mostly in the central cage of the molecule and as such the two configurations would look similar; this observation is further supported with simulated STM images. (Figures 4.25 and 4.26) Thus, it is inconclusive whether both configurations occur in the SAMs simultaneously or only one configuration is present.

Moreover, as with many other cage-molecule SAMs, we do not observe the typical defects that accompany molecular tilt, which the computational analysis predicts is required in order to achieve the packing density that was observed experimentally. One possible explanation for absence of tilt defects is that long-range intermolecular interactions, which in the case of these molecules could be a combination of hydrogen-bonding and dipole-dipole interactions, have azimuthally locked the molecules into one orientation. Note that only in configuration B, in which molecules lean on its neighbors and form rows, are hydrogen-bonding interactions possible and computationally predicted. Both hydrogen-bonding networks and dipole-dipole interactions have previously been shown to overcome traditional domain boundaries in SAMs.[23,35] Additionally, given the propensity of carboxylic acids to form dimers we wanted to model this interaction. The model predicted that this interaction is only stable with a significantly larger nearest neighbor spacing in a (6 × 3) unit cell (Figure 4.27). Given this model and the fact that we do not see any evidence of dimers in the STM data, it is unlikely that they are present in the SAMs. Lastly, we should note that the computational model does not incorporate adatoms in the computation; adatoms have previously been shown to significantly contribute to the structural characteristics of molecules on a gold surface.[36-38]

Configuration		E_C (eV)	$\Theta_{S\text{-}Cage}$ (°)	Θ_{Cage} (°)
M1-COOH	(3 × 3) A	-1.56	36.2	28.7
M1-COOH	(3 × 3) B	-1.57	21.6	16.7
M9-COOH	(3 × 3) B	-1.60	15.5	10.5

Table 4.2 Dissociative chemisorption energies, E_C (eV), and molecular tilt angles $\Theta_{S\text{-}Cage}$ (°) and Θ_{Cage} (°) schematically shown in Figure 4.28.

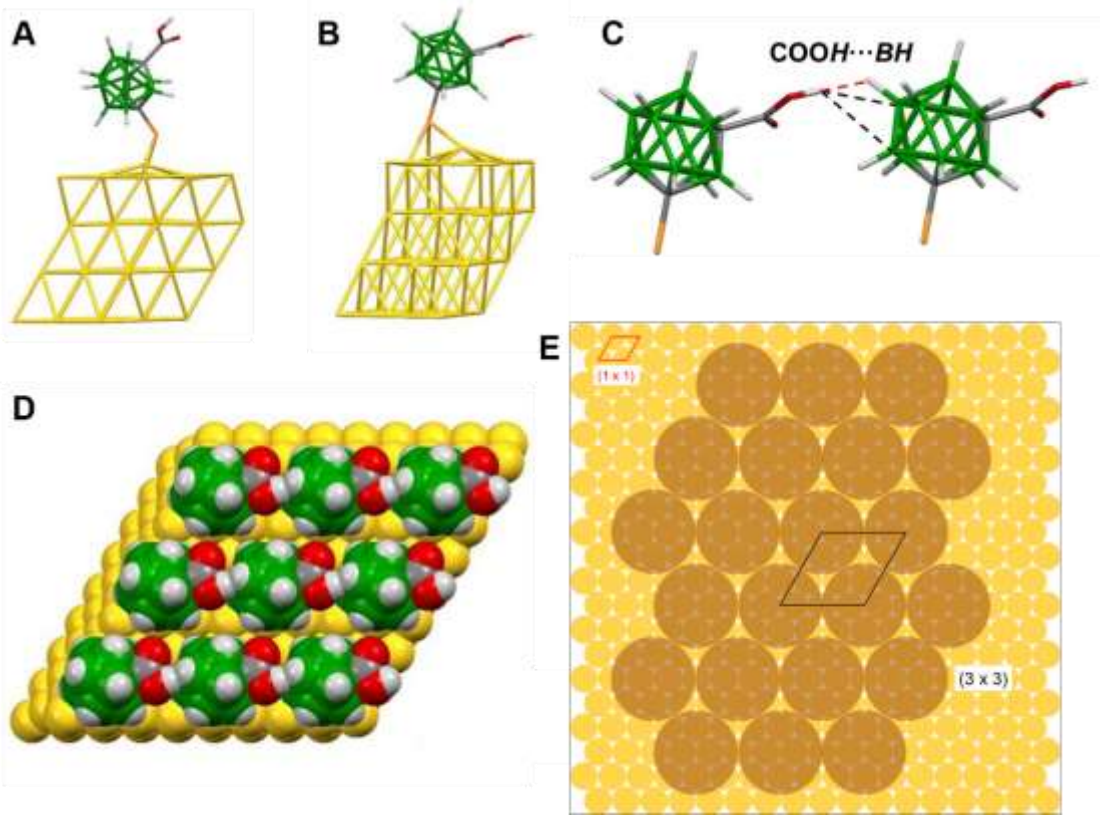

Figure 4.4 Two stable conformations (A and B) of **M1-COOH**. (C) Schematic of the lateral hydrogen bonding of COOH—HB (red) and COOH—BH black, with bond lengths of 1.826 Å and 2.833 Å, respectively. (D) Space-filling model and (E) schematic of a densely packed monolayer with a (3 × 3) unit cell with respect to the underlying gold.

4.2.4 Interaction with the Au{111} Substrate

The bonding of both isomeric molecules to gold surfaces was investigated by X-ray photoelectron spectroscopy (Table 4.3), which showed the molecules adsorb as thiolates. The measured atomic concentrations of boron and sulfur fitted the nominal stoichiometry of the molecules, $B_{10}S_1$. The measured binding energy values of S $2P_{3/2}$ electrons at 162.3 eV for **M1-COOH** and at 161.7 eV for **M9-COOH** indicated typical thiolate bonds. The difference of ~0.6 eV between both isomers is evidence of the previously discussed electron-accepting and -donating properties of the particular *meta*-carborane vertices in the SAM molecules. In **M9-COOH**, the *meta*-carboranyl moiety increases the electron density on the thiolate sulfur atoms, which leads to the lower binding energy value of the S $2P_{3/2}$ electrons compared to **M1-COOH**.

Sample	S $2P_{3/2}$
M1	162.2 (0.8)
M1-COOH	162.3 (0.8)
M9	161.7 (0.8)
M9-COOH	161.7 (0.8)

Table 4.3 Measured Core-Level Binding Energies and FWHM (in parentheses) for Au films modified with **M1**, **M9**, **M1-COOH**, **M9-COOH**.

4.2.5 Carboxylic Acid at the Exposed Interface

Anchoring of both isomeric molecules to gold surfaces gives us the opportunity to probe the chemical character of the exposed carboxyl groups, which enables the SAM to engage in further interactions and reactions. We have examined the carboxyl functional group's nature by measuring dynamic contact angles (Table 4.4) and probed the accessibility for further chemical bonding with several ions. In both cases, the constituent makes the surface more hydrophilic compared to the SAMs of their parent non-carboxylated derivatives **M1** and **M9**.

Sample	Θ_a	Θ_r
M1[13]	82 ± 2	71 ± 1
M9[13]	72 ± 4	52 ± 1
M1-COOH	60.5 ± 0.6	41.6 ± 0.5
M9-COOH	65.8 ± 0.5	54.5 ± 0.7

Table 4.4 Dynamic contact angles for parent **M1** and **M9** isomeric species, as reported in Ref. 13, and the respective carboxylated analogues **M1-COOH** and **M9-COOH** assembled on a gold surface. (N = 8) Θ_a: advancing contact angle, Θ_r: receding contact angle.

To study the sensitivity of the carboxyl group to the attachment of a thiol group at either the second carbon or the boron atom of the *meta*-carborane skeleton, we analyzed the carboxyl group acidity of both isomers assembled on gold surfaces, *i.e.*, after the thiol group scission and thiolate-gold bond formation. We probed the acidity on the surface *via* contact angle titration.[39] In this titration, the advancing contact angle is measured at a range of pH points. A decrease in the contact angle signifies a deprotonation event as the newly formed ion increases the surface hydrophilicity. As such, the midpoint between the protonated and deprotonated states can be defined as an apparent surface pK_a. To control for confounding factors of acidic pH on surface assemblies, we used starting pH between 2 and 4 in the titration experiments, with similar results. The results of the contact angle titration provided an apparent surface pK_a of 5.1 ± 0.6 and 4.8 ± 0.7 for **M1-COOH** and **M9-COOH**, respectively (Figure 4.5). By comparison, the control experiment **M9** SAM shows no change in contact angle as a function of pH (Figure 4.29). Thus, the pK_a shifts from solution to surface by approximately two pH units for both isomers, consistent with previous observations with carboxylic acid-terminated monolayers.[39,40] The two isomers did not significantly differ in apparent surface pK_a although we may have missed smaller differences due to variability of measurements; controlling for

several technical variables, including ambient humidity, batch-to-batch variation, and substrate fabrication did not reduce the measurement variability.

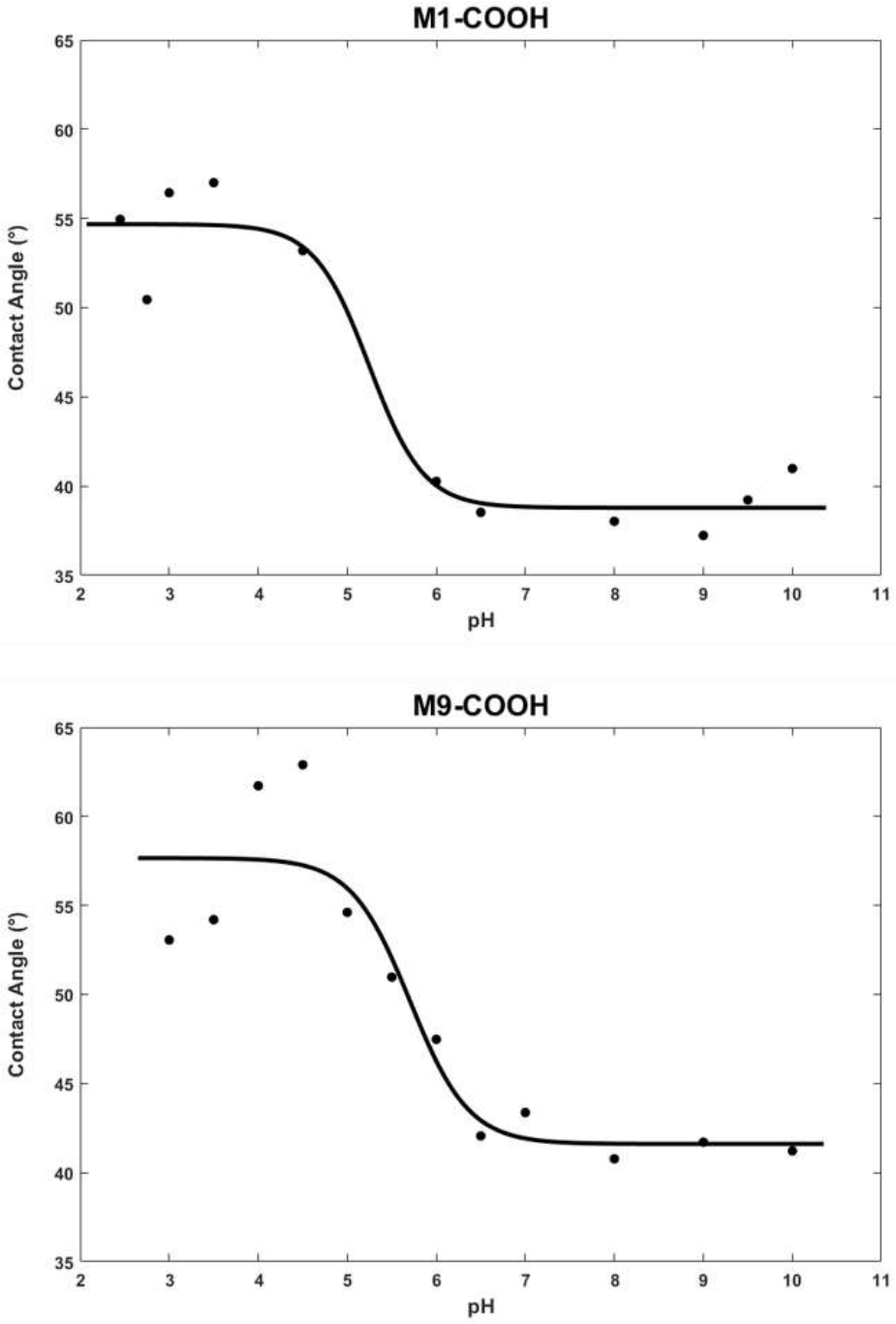

Figure 4.5 Representative contact angle titration curves for (top) **M1-COOH** and (bottom) **M9-COOH**. The surface pK_a for the two isomers are 5.1 ± 0.6 and 4.8 ± 0.7, respectively (N=5).

To understand the altered state of the carboxylic acid on the surface, we performed computational modeling and explored possible mechanisms that could drive the shift in pK_a from solution to surface. Previous studies have suggested that the decreased dielectric on the surface could be a driving force.[40,41] Alternatively or in addition, the thiol deprotonation upon surface binding may have a similar effect on the carboxylic acid. However, our computational analysis showed that the charge density of the adsorbate molecule when bound to the surface as a thiolate is similar to the molecule with a protonated thiol for both models with and without solvent (Figures 4.30-4.33 and Tables 4.10 and 4.11). Given these results, it appears unlikely that the shift in pK_a is a result of the thiol deprotonation upon surface binding and additionally that the thiol form might represent a reasonably simplified model for further computational analysis. We proceeded to calculate the predicted pK_a of a single molecule in water for both isomers. In both cases, the predicted pK_a was lower than what we observed experimentally in solution titration with the difference of 1.9 and 2.2 for **M1-COOH** and **M9-COOH**, respectively (Table 4.12).

To assess the effect of the dielectric on the surface, we first looked at the pK_a shift due to interactions between neighboring molecules, in the form of a dimer model (Figure 4.34). These calculations predicted an increase in pK_a for both isomers with pK_a shifts from single molecule to dimer configuration of 1.9 and 1.1 respectively for **M1-COOH** and **M9-COOH (**Table 4.13**).** These shifts are comparable but slightly smaller than the ones we see experimentally between solution and surface pK_a, suggesting that molecular interactions within the monolayers play a major role in the differences between the three-dimensional and two-dimensional environments but there may be other influencing factors. Additionally, for the shifts given above, the molecular dimers were in configuration B as shown in Figure 4.4, with the carboxyl group positioned more laterally. We also modeled a dimer in configuration A for

M1-COOH, which had a pK_a shift of 0.1 from the free molecule. This model suggests that the characteristics of configuration A are similar to a free molecule in solution, further provides evidence that it is configuration B that is present on the surface for both isomers. We further calculated a range of pK_a *vs.* dielectric by modeling the molecule in different solvation fields for both **M1-COOH** and **M9-COOH** (Figure 4.6)**.** For both isomers, the modeling shows an exponential trend that as dielectric decreases, pK_a increases. The corresponding dielectric based on the pK_a in the dimer configuration is 17 for **M1-COOH** and 25 for **M9-COOH**. Overall, our computational analysis suggests that the shift in pK_a is driven by the dielectric of the environment that the carboxyl group experiences on the surface. A factor of this dielectric is the interaction with neighboring molecules, but proximity to the Au surface and partial desolvation likely also make contributions. The computational model does take into account the effect of desolvation, but does not take into account the presence of the surface. However, given that the Au surface is relatively far from the carboxyl group and is shielded by the molecular backbone, we believe that this model reasonable simulates the surface environment.

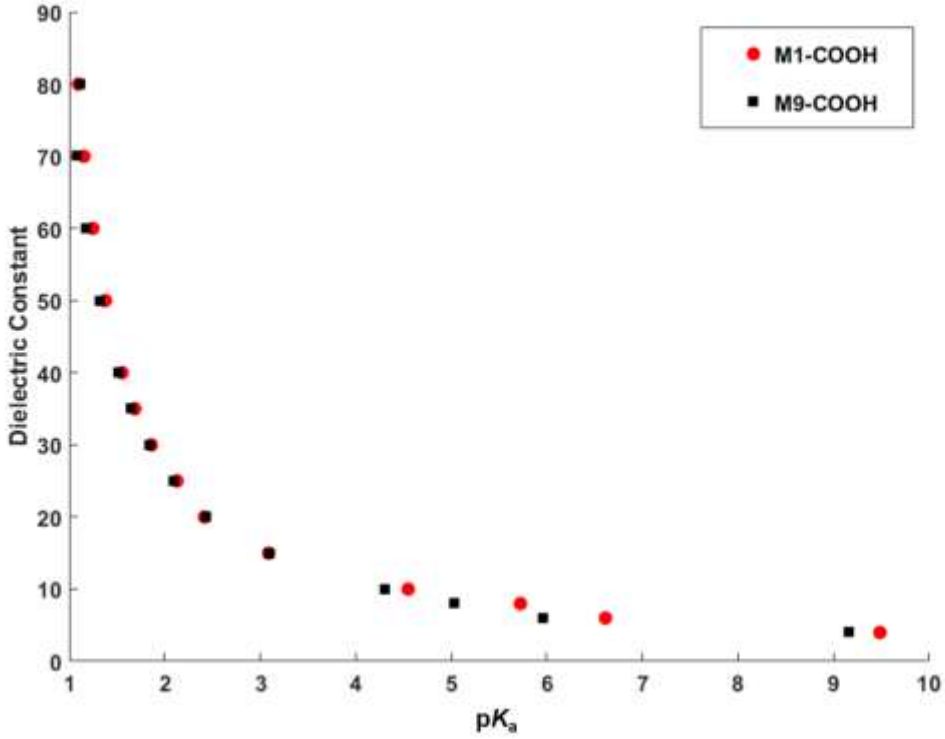

Figure 4.6 Computational results of the pK_a shift in solvents with a range of dielectric constants for both isomers. The results show an exponential relationship between the pK_a and the dielectric. Based on the pK_a calculated for the dimer configurations, the associated dielectrics are 17 and 25 for **M1-COOH** and **M9-COOH**, respectively.

Accessibility of carboxyl groups for surface-supported coordination chemistry was probed by examining the interaction between carboxyl-terminated SAMs and various ions. The SAMs of the carboxylated isomers were exposed to dilute solutions of metal cations and the formation of metal coordination complexes was analyzed *via* XPS (Tables 3.14-4.16 and Figures 4.35 – 4.45). A total of 16 representative ions from across the periodic table were used, Na(I), Mg(II),Ca(II), Sr(II), Ba(II), Fe(II), Fe(III), Co(II), Ni(II), Cu(II), Zn(II), La(III), Sm(III), Tb(III), Tl(I), and Pb(II). All of the ions interacted with the carboxyl-terminated SAMs and successfully replaced the intrinsically present Na(I) ions, which might originate from the ambient atmosphere or solvents used for the preparation of the samples. Both starting SAMs of **M1-COOH** and **M9-COOH** were examined broadly; since the SAMs were found to have indistinguishable surface patterns and practically identical chemical behaviors, SAMs of **M9-**

COOH were examined in greater detail. As well, SAMs of the **M9** isomer were used as control samples to test if the ions bind exclusively to the carboxylic moiety. The SAMs of **M9** were analyzed both before and after exposure to solutions of Na(I) and Mg(II) ions with no metal ions detected in those samples with XPS.

In addition, quantitative XPS analyses determining the metal ion/**M9-COOH** surface ratios for the pristine **M9-COOH** SAM and for the **M9-COOH** SAM modified with Mg(II) and Ba(II) ions, summarized in Table 4.5, indicate possible formation of bridging intermolecular surface complexes within the adsorbed monolayers, which is of interest due to its additional stabilizing effect.

SAM	Metal ion	Metal ion/**M9-COOH** ratio
M9-COOH	Na	0.8 (415 eV)
M9-COOH + Mg(II)	Mg	0.3 (1180 eV), 0.5 (183 eV)
M9-COOH + Ba(II)	Ba	0.5 (706 eV)

Table 4.5 Measured ratios of the number of deposited metal ions to the number of **M9-COOH** molecules within the adsorbed monolayers, together with the nominal kinetic energies of the photoelectrons used for the quantification of the metal ion (in parentheses).

Our previous investigations of *para*-carboranethiol, 1-SH-1,12-$C_2B_{10}H_{11}$ (**P1**) and of its carboxylated derivative, 1-COOH-12-SH-1,12-$C_2B_{10}H_{10}$ (**P1-COOH**) showed a fraction of molecules physisorbed as thiols and thus more prone to desorption.[11] Fitting with these previous reports, the self-assembled monolayers in this study proved labile when exposed to an excess of H_3O^+ ions, *i.e.* to acidic conditions. The anchoring thiolate groups are protonated into a weakly bound thiol species, which have a binding energy of 163.5 eV (Figure 4.7), and may be subsequently washed away by rinsing with an excess of pure solvent. The loss of surface coverage has been observed in XPS for all the samples subjected to acidic environment, *i.e.* SAMs of **M9** and **M9-COOH**, and **P1-COOH** for comparison and also as a reference to our previous study. The stoichiometries of the acidified monolayers exhibited higher content

of the substrate gold when compared to the pristine SAMs due to the removal of carboranethiol molecules (Table 4.15).

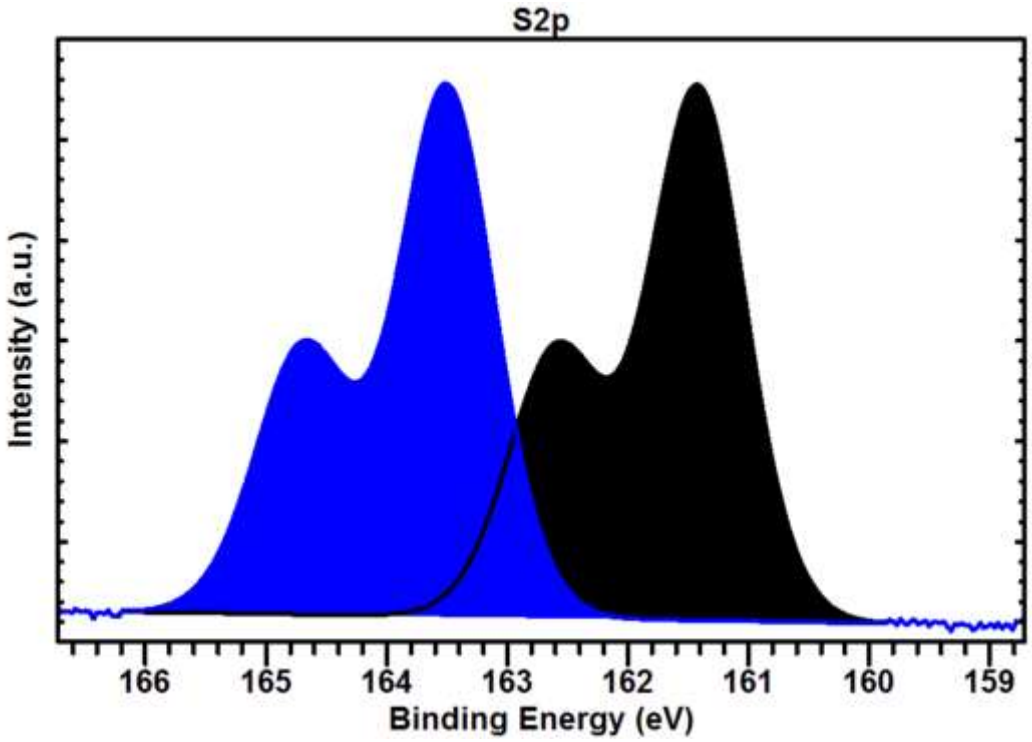

Figure 4.7 X-ray photoelectron spectrum of S 2P photoelectrons with the contributions of both the thiolate (black) and the thiol (blue) -bound molecules of M**9-COOH** on Au{111}. The two doublets are separated by approximately 2 eV and are thus easily distinguishable.

4.3 Conclusions and Prospects

Two new isomeric bifunctional cage molecules, derived from twelve-vertex *m*-carborane, were synthesized and characterized using structural and spectroscopic methods. Both new building blocks for self-assembled monolayers on Au surfaces have greater steric demands compared to their parent non-carboxylated derivatives. The impact of the structural and chemical properties of these building blocks on the properties of their respective SAMs was investigated. These molecules represent a system that enables analyses of intramolecular communication between functional groups interspaced by *meta*-carborane skeletons. The

effects of the carboxyl group are neither detected on the free thiol group in the ^{1}H NMR spectrum nor on the BE value of S $2P_{3/2}$ electrons upon surface adsorption. Both isomers show greater carboxyl group acidities compared to 1-COOH-*meta*-carborane reference, which are attributed to the effect of the thiol groups. This result is of general interest due to the *pseudo*-aromatic character of carboranes and their skeletal interactions with various functional groups. Although the molecules of both isomers exhibit different symmetries with one isomer being chiral, they arrange into identical hexagonal close-packed arrays on Au{111}. The greater steric demands of both isomers compared to their parent non-carboxylated molecules lead only to an increase of the nearest neighbor spacing from 7.2 ± 0.4 Å to 8.4 ± 0.4 Å, which is in good agreement with tilting the molecules 13-16º to minimize their lateral steric requirements and maximize packing density. The addition of a lateral carboxyl group thus exerts a significant influence on the nearest neighbor spacing in the SAM. The analysis of the surface structure also suggests the presence of long-range interactions, which could be due to a combination of hydrogen-bonding and dipole-dipole interactions within the monolayer. The interactions of both isomeric molecules with gold surfaces were investigated by XPS, which shows that the molecules adsorb as thiolates. More detailed measurements show that the binding energies of S $2P_{3/2}$ electrons are influenced by electron-accepting and electron-donating properties of the carboranyl moiety. The assemblies also showed a change in behavior of the carboxyl terminus at the environmental interface of the monolayer, resulting in a pK_a shift of ~2 pH units. Based on computational modeling, this shift appears to be a result of the dielectric of the environment that the carboxyl group experiences; this dielectric is determined by the interactions between neighboring molecules, proximity to the Au surface, and partial desolvation. The exposed surface of the SAMs is also accessible for several different types of ions to interact with the carboxylic group. These results show that the carboxyl-terminated *meta*-carborane building blocks open the monolayers to further interactions with different types of ions or molecules.

Understanding the influence on assembly and the reactivity of the carboxylic group in these carboranethiolate monolayers lays the groundwork for performing additional chemistry and developing further applications using the reactive interface. The tunable characteristics of carboranethiolate SAMs makes them advantageous for use in nanoscale devices and organic electronics. These terminal carboxylic acids provide an avenue for fabricating three-dimensional heterostructures by facilitating such techniques as atomic layer deposition. Furthermore, given the acid-base reactivity of these SAMs there is also opportunity for their use in pH sensors.

Beyond interest in these materials for devices, the functionalized carboranethiolate SAMs also serve as a model system for questions in biochemistry and biology. The reactivity of ionizable amino acids located internally in proteins are critical for function and catalysis.[42] These amino acids experience multiple microenvironments and their pK_a values along with the structure of the protein adjust accordingly.[43,44] Shifts in pK_a have been observed in protein systems similar to the behavior we report in this study and are linked to the dielectric of the microenvironment.[42,45,46] These functionalized carboranethiolate monolayers can thus serve as a model platform to study the driving forces relevant to pK_a shifts in more complicated biological and chemical systems.[44,47] Additionally, given the two-dimensional nature of these monolayers they may be particular relevant for comparison to membrane-bound biological structures.

4.4 Materials and Methods

Chemicals: The starting *meta*-carborane, 1-SH-*m*-carborane (**M1**) and 9-SH-*m*-carborane (**M9**) were purchased from Katchem s.r.o. and used as received in further synthesis. *n*-Butyllithium (2.5 M in hexanes) was purchased from Sigma-Aldrich. Diethylether (p.a. grade, Penta s.r.o., Czech Republic) was additionally dried with sodium in the presence of

benzophenon (99.8%, purchased from Sigma-Aldrich). Aqueous solution of hydrochloric acid (33%, p.a. grade) and magnesium sulphate anhydrous (p.a. grade) were both used as received from Penta s.r.o. NMR spectra were measured in $CDCl_3$ (99.8% D) as received from Eurisotop.

Synthesis: 1-mercapto-1,7-dicarba-*closo*-dodecaborane-7-carboxylic acid (**M1-COOH**) and 9-mercapto-1,7-dicarba-*closo*-dodecaborane-1-carboxylic acid (**M9-COOH**) were synthesized by lithiations their parental thiol derivatives with two equivalents of *n*-BuLi and subsequent reaction with carbon dioxide followed by quenching with an aqueous solution of hydrochloric acid (Scheme 4.1).

1-COOH-1,7-$C_2B_{10}H_{11}$:*meta*–Carborane (4 g, 27.7 mmol) was dissolved in ~80 ml of dry and freshly distilled diethyl ether under argon atmosphere and cooled to ~-78°C (dry ice/acetone). *n*–Butyllithium (10.2 ml, 25.5 mmol) was added dropwise over 5 min and the mixture was further stirred for 1 h. Excess dry ice was added and the mixture was then left at room temperature to warm up slowly, within approximately 1 h, under argon atmosphere. A white precipitate was observed in the mixture. Distilled water (50 ml) was added, the mixture was well shaken, and the ether fraction was separated. The aqueous solution was acidified with 30 ml of aqueous solution of hydrochloric acid (~15%) and white solid immediately precipitated. The mixture was extracted 3× with 30 ml of Et_2O and the collected ether fractions were dried over anhydrous $MgSO_4$ overnight. The mixture was filtered, solvent evaporated under reduced pressure on a rotary evaporator and the crude product was crystallized from a saturated pentane/chloroform (1/1) solution in a freezer (-20 °C) as a white crystalline product. Yield: 1.7 g (33%).

1-COOH-9-SH-1,7-$C_2B_{10}H_{10}$ (**M9-COOH**): 9-Mercapto-*meta*-carborane (3.0 g, 17.0 mmol) was dissolved in ~200 ml of dry and freshly distilled diethyl ether under argon atmosphere and cooled to ~-78 °C (dry ice/acetone). *n*-Butyllithium (15.0 ml, 37.5 mmol) was added dropwise over ~10 min. White solid precipitated shortly after the addition of

n-butyllithium and the mixture was further stirred for 1 h. Excess dry ice was added and the mixture was then left at room temperature to warm up slowly (~1 h) under argon atmosphere. White precipitate was observed in the mixture. Distilled water (300 ml) was added, the mixture was well shaken and the ether fraction was separated. The aqueous solution was acidified with 30 ml of aqueous solution of hydrochloric acid (~15%) and white solid immediately precipitated. The mixture was extracted 3 × 30 ml of Et_2O and the collected ether fractions were dried over anhydrous $MgSO_4$ overnight. The mixture was filtered, solvent evaporated under reduced pressure on a rotary evaporator and the crude product was purified by sublimation (80 °C, 6.0×10^{-2} mbar) to yield 1.3 g (35%) of white crystalline product.

1-COOH-7-SH-1,7-$C_2B_{10}H_{10}$ (**M1-COOH**): 1-Mercapto-*meta*-carborane (1.0 g, 5.7 mmol) was dissolved in ~80 ml of dry and freshly distilled diethyl ether under argon atmosphere and cooled to ~-78 °C (dry ice/acetone). *n*–Butyllithium (5.0 ml, 12.5 mmol) was added dropwise over ~10 min. White solid precipitated within 30 min after the addition of *n*-butyllithium and the mixture was further stirred for 1 h. Excess dry ice was added and the mixture was then left at room temperature to warm up slowly (~1 h) under argon atmosphere. A white precipitate was observed in the mixture. Distilled water (50 ml) was added, the mixture was well shaken, and the ether fraction was separated. The aqueous solution was acidified with 30 ml of aqueous solution of hydrochloric acid (~15%) and a white solid immediately precipitated. The mixture was extracted 3 × 30 ml of Et_2O and the collected ether fractions were dried over anhydrous $MgSO_4$ overnight. The mixture was filtered, the solvent was evaporated on a rotary evaporator under reduced pressure, and the crude product was purified by sublimation (80 °C, 1.0×10^{-1} mbar) to yield 0.83 g (66%) of white crystalline product.

NMR spectroscopic characterization: ^{11}B, ^{1}H, and ^{13}C NMR spectra of both new compounds were measured using a Varian Mercury Plus NMR spectrometer under standard conditions. ^{11}B chemical shifts are given relative to $[BF_3(OEt)_2]$, and ^{1}H and ^{13}C chemical shifts

relative to TMS. The reference frequencies were estimated based on the frequency of the lock signal as a secondary standard. All resonances were assigned to the respective atoms (Tables 4.6 and 4.7) (Figures 4.8-4.10).

X-ray structural analysis: The molecular structures of both **M1-COOH** and **M9-COOH** isomeric species were obtained by single-crystal X-ray diffraction analysis (Tables 4.8 and 4.9 and Figure 4.11). Crystals suitable for single-crystal X-ray crystallography were obtained by slow sublimation in a sealed ampoule over a few weeks. The data were measured at 120 K with up to 0.87 Å resolution on an Agilent diffractometer Xcalibur using mirror-collimated Cu K_α radiation (Gemini ultra Cu) from a sealed X-ray tube, and CCD detector Atlas. Data were processed using program CrysAlis PRO, with empirical absorption correction. Structures were solved by charge flipping with Superflip[48] and refined with Jana2006, http://jana.fzu.cz (Structure Determination Software Programs, Institute of Physics, Prague, Czech Republic).[49] The sample was a twin rotated by 180° around the reciprocal axis c*. This twinning operation generated overlaps of some diffraction spots; the overlaps were detected by the data processing program CrysAlis PRO and encoded to the reflection file in a form of so-called hklf5 format. Using this format, the partial overlaps due to twinning could be taken into the account by the refinement program Jana2006. This procedure considerably improved the sensitivity of refinement to hydrogen atoms.

All hydrogen atoms appeared in difference Fourier maps. Hydrogen atoms attached to boron were restrained to have the same B-H distance while hydrogen atoms attached to oxygen of carboxyl were refined with the O-H distance ~0.8Å. All crystallographic figures were made in Mercury (https://www.ccdc.cam.ac.uk/solutions/csd-system/components/mercury/). Selected collection and refinement data are listed in Tables 4.8 and 4.9 together with the CCDC number. Supplementary crystallographic data can be obtained free of charge via http://www.ccdc.cam.ac.uk/conts/retrieving.html, or from the Cambridge Crystallographic

Data Centre, 12 Union Road, Cambridge CB2 1EZ, UK; fax: (+44) 1223-336-033; or e-mail: deposit@ccdc.cam.ac.uk.

Acid-base titration: All derivatives were titrated with an aqueous solution of sodium hydroxide, and the titration curves are displayed in Figure 4.22. The results show that both isomers are diprotic acids. Dissociation of the COOH group prior to the SH group is in accord with the acidity constant order, and corresponds to our computational results at the CC2/def2-TZVP level of theory. A comparison of both isomers **M1-COOH** and **M9-COOH** with 1,7-carborane-1-carboxylic acid, 1-COOH-1,7-$C_2B_{10}H_{11}$, enables the analysis of the effect of SH attachment to both carbon and boron atom of the skeleton.

Mass spectrometry analysis: Both isomeric species (**M1-COOH** and **M9-COOH**) show similar patterns in their ESI Mass spectra (Figures 4.12-4.19). Mass spectrometry measurements were performed on a Thermo Scientific LCQ Fleet Ion Trap instrument using electrospray (ESI) ionization with helium (5.0 Messer) as a collision gas in the ion trap. The sample was dissolved in acetonitrile (concentration ~100 ng/ml) and introduced through a fused-silica sample tube of 0.100 mm (inner diameter) × 0.19 mm (outer diameter) to the ion source from a Hamilton syringe using infusion at 15 μL/min, source voltage 5.47 kV, tube lens voltage -44.71 V, capillary voltage -23.06 V, capillary temperature 165.01 °C, and N_2 (isolated from air in NitroGen N1118LA, Peak Scientific) as a nebulizing sheath gas (flow rate 14.97 p.d.u.). Only negative ions of the respective molecular peaks were detected.

Infrared Spectroscopy: Infrared spectra (Figs. 4.20 and 4.21) of both isomeric compounds (~1-1.5 mg) were measured in KBr pellets using a Nicolet Nexus 670 FTIR spectrometer.

Geometric Structural Analysis: The computed structure of M1-COOH as a set of atomic coordinates was imported to EXCEL software. Translation and rotation transformation matrices were then used to move the molecule such that the S atom is in the beginning of the

coordination system, the molecular axis intersecting the S atom and the antipodal B atom is in the z coordinate axis and the plane intersecting the S atom, the antipodal B atom, and the C atom, to which the −COOH group is bonded, are in the yz plane.

Rotation transformation matrix together with van der Waals atomic radii were used to find the densest packing of molecules on the surface. For isotropic packing the molecule was rotated around the x axis to scan for the tilt in which the distance of the most distant component (atom coordinates + VdW atomic radii) from the z axis acquires the smallest value, this distance is the nearest neighbor distance. The method was easily reversed to find the tilt for isotropic packing with the nearest neighbor distance of 8.6 Å.

Conformational analysis: Molecular conformational analysis was done by quantum chemistry calculations, which were performed by the NWChem package.[50] The geometries were optimised[51] by the means of the density functional theory with the hybrid exchange–correlation functional PBE0[52] using Jensen's triple-zeta basis pc-2.[53] A series of optimizations were performed on internal coordinates with the torsion angles defining the orientation of the carboxyl and thiol groups with respect to the carborane cages kept fixed. Subsequently, the NMR shielding parameters were calculated by DFT method with the same XC functional using Jensen's triple–zeta basis pcS-2 optimised[54] for this type of calculations. Individual conformations were sorted according to their calculated energies, and their relative Boltzmann factors at the laboratory temperature 300 K used as the weights for the mean values of their chemical shifts.

Scanning tunneling microscopy analysis: Samples for imaging where prepared on Au{111}/mica substrates (Agilent Technologies, Santa Clara, CA), which were hydrogen-flame annealed with 10 passes at a rate of 0.4 Hz prior to monolayer deposition. Substrates were placed into a capped vial with 1 mL of a 1 mM solution of the respective isomer in ethanol. Ethanol was used as received (Sigma-Aldrich, St. Louis, MO). The samples were left at room

temperature (*ca.* 25 °C) or heated at 78 °C in a Barnstead Thermolyne 1400 furnace (ThermoFisher Scientific, Waltham, MA) for 24 h; no difference was observed between these conditions. Subsequently, samples were cleaned with neat ethanol and dried with a stream of nitrogen gas before loading into the custom-built Besocke-style scanning tunneling microscope with a platinum/iridium tip (80:20) under ambient conditions.[55] Samples were held within a −1 to −0.1 V bias range, and 256 × 256 pixel images were collected in constant-current mode. The known lattice of the 1-dodecanethiolate SAMs on Au{111} was used for calibration. Image analyses was done using MATLAB (Mathworks, Natick, MA) and Gwyddion (http://gwyddion.net/).

Simulated scanning tunneling microscopy analysis: The constant-current STM images are simulated using the Tersoff-Hamann method[56] using VASP. The two optimized **M1-COOH** SAMs on the 3 × 3 four-layer Au(111) slab with periodic boundary conditions are used as the input structures. The isovalue for the charge density is 10^{-4}, and the images are generated for energy from the Fermi energy (E_F) to E_F – 0.1 eV, to simulate the experimental condition V_{sample} = -0.1 V. (Figures 4.25 and 4.26)

Contact angle measurements: Samples were prepared by the same procedures as for STM sample preparation, except substrates were silicon wafers coated in a 5 nm chromium adhesion layer and 100 nm of gold. Contact angle measurements were preformed using an FTA1000 drop shape instrument contact angle goniometer (First Ten Angstroms, Inc., Portsmouth, VA) under ambient conditions (21-23 °C, 50-60% relative humidity). A drop of DI water, with a volume of 4 μL was applied to the surface. The drop was then allowed to settle on the substrate for 4 s; thereafter a cycle of pumping in and out by the syringe was started with 1.25 s pumping and 8.75 s of rest on the surface, to assess the advancing and receding contact angle. For each drop, 800 images were recorded and analysed using FTA32 software based on the Young-Laplace equation. Each data point represents three drops taken at different locations

on the substrate. For contact angle titrations, a range of buffers from pH 2 to 12 at 50 mM were used. For each pH point the substrate was immersed in the buffer for ~1 h, dried with nitrogen, and then measured with a droplet of the buffer solution.

Computational modeling of pK_a: To study the local dielectric effects, we performed *Ab initio* calculations to compute the pK_a values for **M1-COOH** and **M9-COOH** SAMs. To reduce the computational cost, the monolayer is represented by a two-molecule model, in which the Au(111) surface is replaced by a H atom. To validate our model, we performed Bader charge analysis[57] on the molecular model and the **M1-COOH** SAMs, optimized on a 3×3 four-layer Au(111) surface, both with periodic boundary conditions using VASP.[58-61] In the molecular model, the substitute H position is relaxed while the positions of other atoms are fixed at their SAM positions. The implicit solvation model implemented in VASPsol[62,63] is used for molecules in water. The results show that the charges on the carboxyl group are similar between the molecular model and the SAM on surface. The charge difference is less than 0.001 per atom in gas phase and less than 0.01 in water for the carboxyl group, which indicates that the molecular model is reasonable for pK_a calculations.

To maintain the local environment of the carboxyl group in SAMs, the SAM is represented by two molecules with the same distance as they are on surface, and only the carboxyl group between the two molecules is allowed to deprotonate in our calculations. The pK_a values can be calculated from free energies of protonated and deprotonated structures by

$$\mathrm{pKa} = \left[G_{aq}(\mathrm{AH}) - G_{aq}(A^-) - G_{aq}(H^+)\right]/(2.303RT)$$

and the experimental value for free energy of H^+, $G_{aq}(H^+) = 269.0$ kcal/mol is used in the calculations.[64] We use GAUSSIAN 09 package[65] to perform electronic structure and frequency calculations at B3LYP/6-31+G(d) level.[66-69] The CPCM model is used to model the solvation effects.[70,71] We also plot the dielectric curve for free molecules in solvent. In these calculations, both protonated and deprotonated structures are fully relaxed.

X-ray photoelectron spectroscopy (XPS): Platypus Temple-Stripped Gold Chips were used as the substrate for all of the experiments. The Platypus chips were cleaved short before use to minimize their exposure to air. For the deposition of **M9**, **M9-COOH** and 1-COOH-12-SH-1,12-$C_2B_{10}H_{10}$ (**P1-COOH**), the substrate was immersed in to a 96% ethanol solution of the corresponding compound (concentration ranging from 1 to 4 mmol · dm^{-3}) for 50 to 70 min. Ethanoic solutions of the carboxylated species were prone to turn opaque several hours after their preparation; thus, fresh solutions were prepared every time. The chips were then rinsed with 96% ethanol, dried in a stream of argon or nitrogen, and stored under inert atmosphere, and subsequently used for further modification or measurements within the next 30 min.

For the subsequent modification of SAMs of **M9** and **M9-COOH** with metal ions, the freshly prepared samples were immersed in to an aqueous solution of the corresponding salt (concentration of 7 ± 3 mmol · dm^{-3}), *i.e.*, NaCl, $MgSO_4$, $CaCl_2$, $SrCl_2$, $BaCl_2$, $Pb(NO_3)_2$, $Fe_2(SO_4)_3$, $Ni(NO_3)_2$, $Co(NO_3)_2$, $CuSO_4$, $ZnSO_4$, $La_2(SO_4)_3$, $Sm_2(SO_4)_3$ and $Tb_2(SO_4)_3$. The Fe(II) ions were deposited from aqueous solutions with 7 mmol · dm^{-3} concentration of $FeSO_4$ acidified with HCl to give 2.8 μmol · dm^{-3} H_3O^+ ion concentration. All the solutions, but that of Na_2SO_4, $FeSO_4$, $Fe_2(SO_4)_3$ and $MgSO_4$, which were prepared fresh, were prepared two days in advance. Each sample was treated separately to avoid cross-contamination. The immersion time was 50 to 70 min, the samples were then briefly rinsed with 96% ethanol, dried under an argon or nitrogen stream, and stored under inert atmosphere until analysed, that is, for 30 min at most.

For exposure of the SAMs of **M9**, **M9-COOH** and **P1-COOH** to acidic conditions, the freshly prepared samples were immersed in a 1.15 mM aqueous solution of HCl for 1 hour,

then briefly rinsed with 96% ethanol, dried under an argon or nitrogen stream, and stored under inert atmosphere until analysed, that is for 30 min at most.

Sulfate compounds used for determination of relative sensitivity factors (RSFs), as discussed below, were crushed under ambient conditions into a fine powder, which was then pressed onto double-sided scotch tape and immediately mounted into the XPS instrument for analysis.

XPS analysis was performed on a XPS Kratos Axis Supra instrument, using ESCApe software. Aluminum anode with 15 mA emission current was used, charge compensation electron gun was used with filament current of 0.43 A, filament bias of 1.05 V and charge balance of 4.6 V for all the samples but bare gold, for which the electron gun was turned off. The charge compensation was, however, not necessary for the SAM samples, as they behaved as conductors. The hybrid lenses and a slot or 110 μm apertures were used in the electron optics setup. The analysis was done under vacuum of 10^{-8} to 10^{-9} torr for the SAM samples, the analyses of the powdered sulfates were done under less favorable vacuum, but not rising above 10^{-7} torr.

The obtained data were processed in CasaXPS software. Transmission function was used as obtained from the Kratos Axis Supra instrument technician. The Shirley-type background was used for all the photoelectron (PE) lines of the reference sulfate samples, and for the Au 4f PE lines of all the SAM samples. The linear-type background was used for all the PE lines, but the Au 4f PE lines, in all of the SAM samples. The RSFs given in Kratos Axis library were used for Au 4f, B 1s, O 1s, C 1s and S 2p PE lines. The RSFs for Na 1s, Mg 1s, Mg KLL and Ba 3d PE and Auger lines were obtained from XPS analysis of sulfates with known stoichiometries.

To acquire the empirical RSFs, the spectra obtained for powdered Na_2SO_4, $MgSO_4$, and $BaSO_4$, were analyzed in accordance to the approach of Marel *et al.* for multilayer systems,[72] the samples were assumed to consist of a homogeneous, infinitely thick substrate sulfate, contaminated with a thin film of hydrocarbons containing both carbon and oxygen. The intensities for oxygen 1s PE line were split to match the sulphate stoichiometry, and the excess intensity was assigned to the adventitious overlayer. The intensity of the PE line corresponding to the acquired RSF, was determined artificially based on the known stoichiometry of the sulfate and the experimentally acquired intensity of the sulfur 2p PE line. The elastic attenuation length used in the Marel's model was substituted with the inelastic mean free path which was obtained from the NIST Electron Inelastic-Mean-Free-Path Database software[73] using a TPP-2M equation for a $C_{26}H_{54}$ molecules with a band gap of 5 eV and density of $0.9\ g \cdot cm^{-3}$. The RSF value was obtained by division of the measured intensity with the computed one, after the determination of the correct thickness of the adventitious overlayer. The intensities obtained for the SAM samples were divided by the corresponding RSFs and normalized to yield a stoichiometry with 10 boron atoms, no correction for the multilayer attenuation was used for the SAM samples.

4.5 Additional Figures and Tables

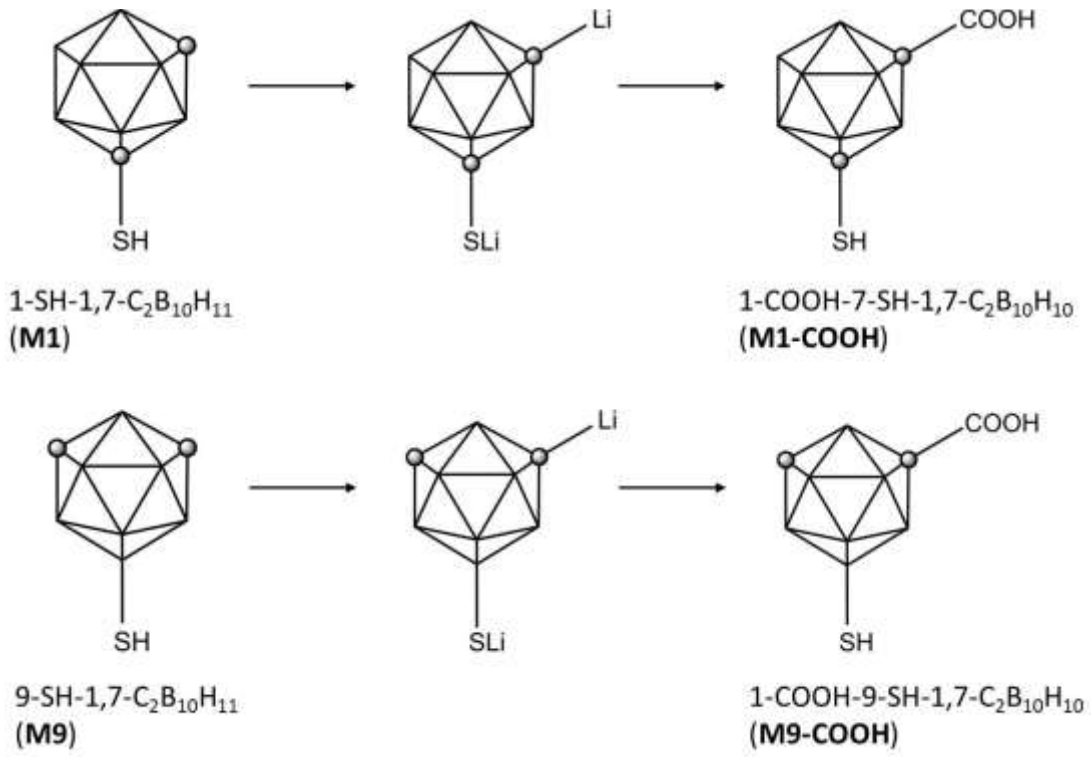

Scheme 4.1 Synthesis of carboxylic acids of 1-SH-1,7-$C_2B_{10}H_{11}$ (**M1**) and 9-SH-1,7-$C_2B_{10}H_{11}$ (**M9**).

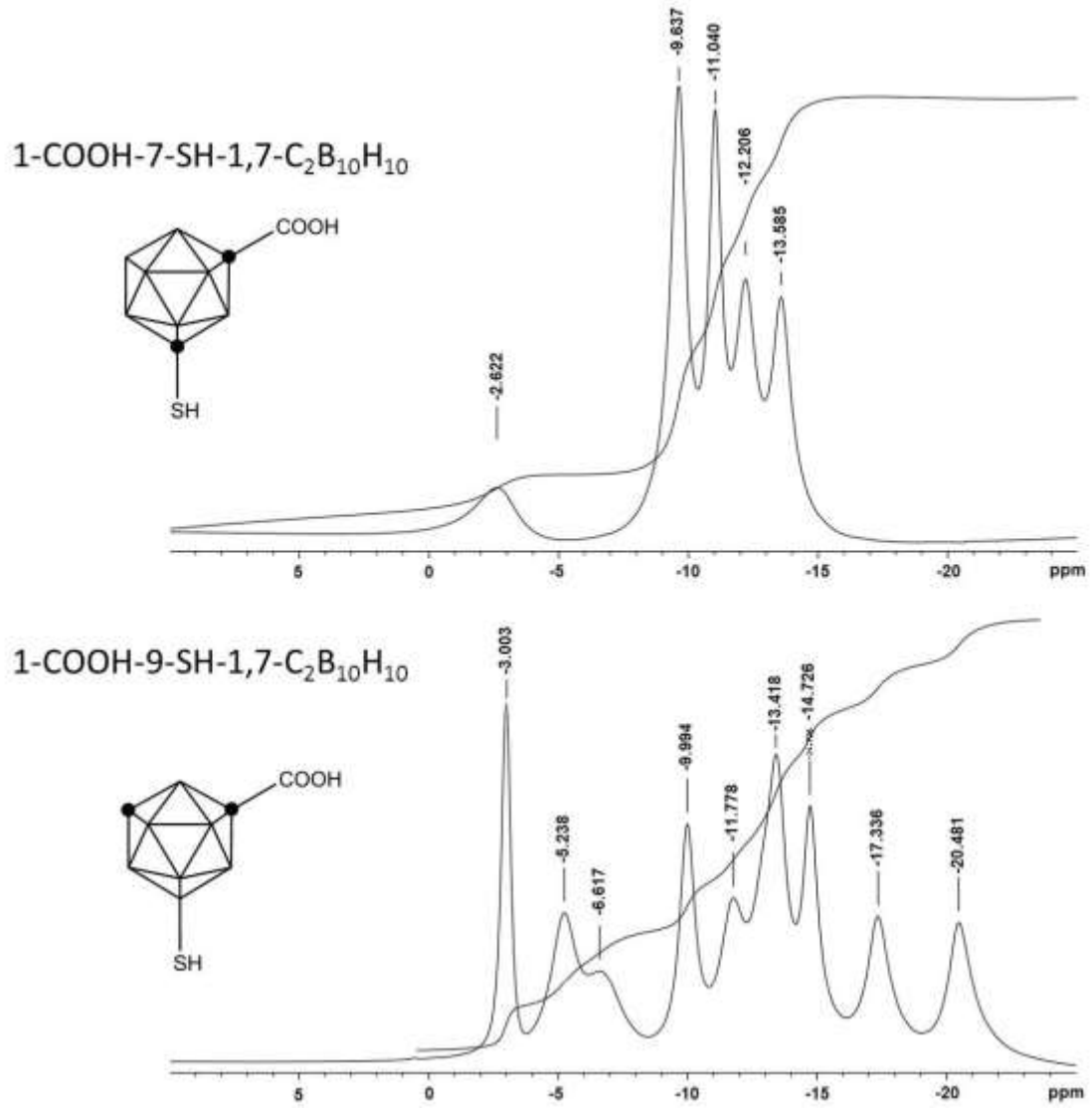

Figure 4.8 Experimental ^{11}B NMR spectra of 1-COOH-7-SH-1,7-$C_2B_{10}H_{10}$ (**M1-COOH**) (top) and 1-COOH-9-SH-1,7-$C_2B_{10}H_{10}$ (**M9-COOH**) (bottom).

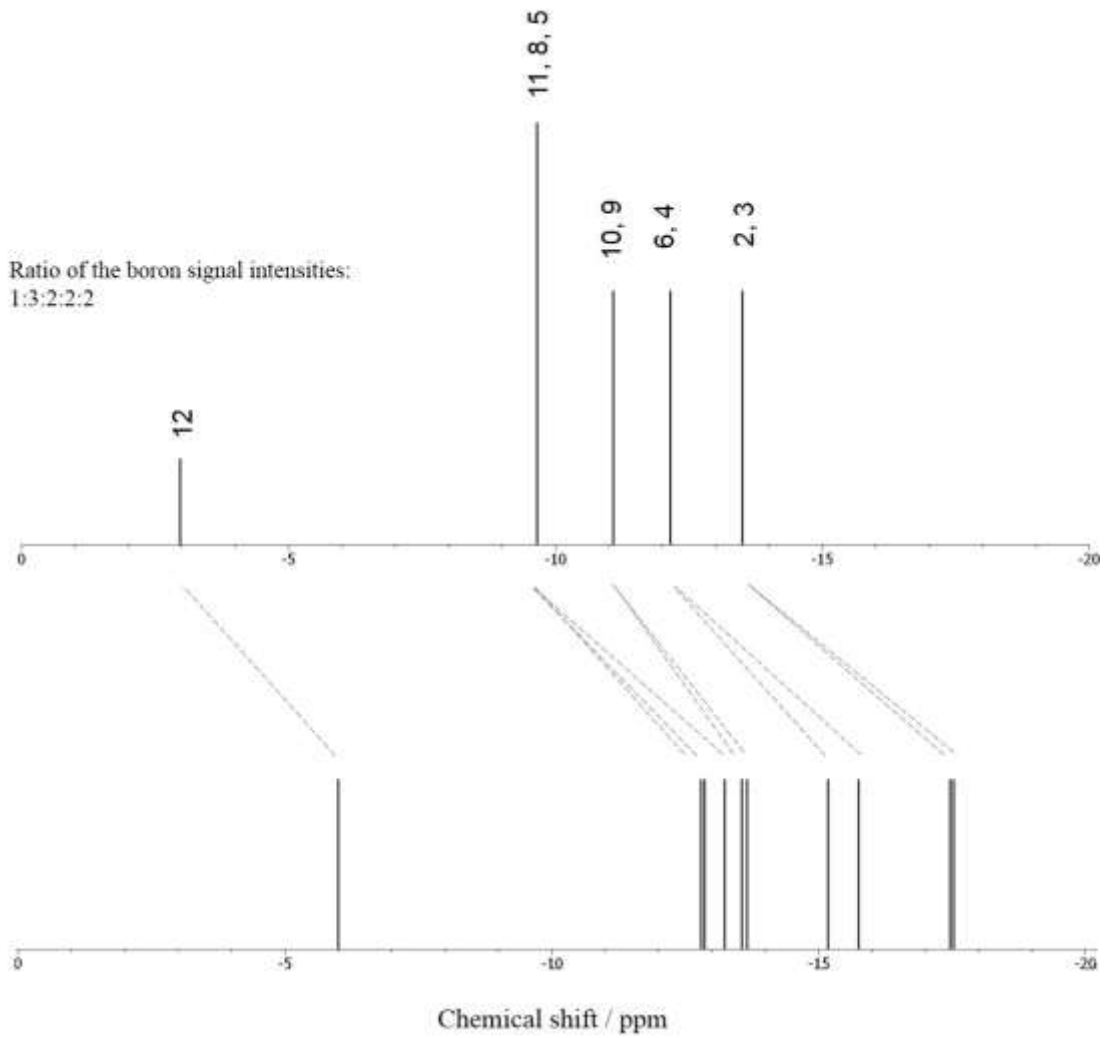

Figure 4.9. Correlation between the experimental (top) and computational (bottom) ^{11}B NMR spectra of 1-COOH-7-SH-1,7-$C_2B_{10}H_{10}$ (**M1-COOH**).

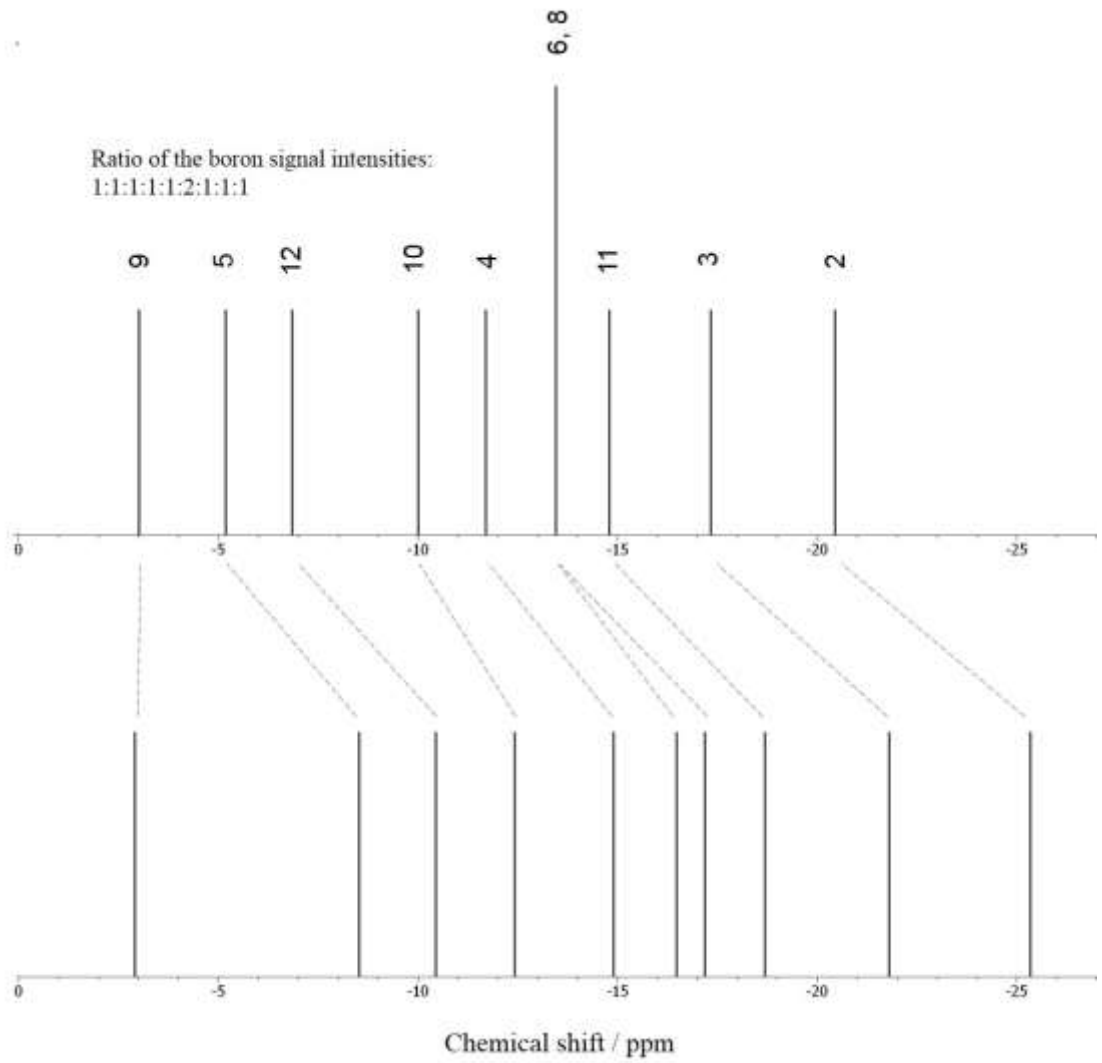

Figure 4.10 Correlation between the experimental (top) and computational (bottom) ^{11}B NMR spectra of 1-COOH-9-SH-1,7-$C_2B_{10}H_{10}$ (**M9-COOH**).

	1-COOH-7-SH-1,7-$C_2B_{10}H_{10}$			
	(M1-COOH)			
Assign.	$\delta(^{11}B)^{exp}$	$\delta(^{11}B)^{calc}$	$\delta(^{1}H)^{exp}$	$\delta(^{13}C)^{calc}$
1	-	-	10.41^{COOH}	81.73^{CH}, 174.59^{COOH}
2	-13.51	-17.47		-
3	-13.51	-17.54		-
4	-12.16	-15.76		-
5	-9.66	-13.25		-
6	-12.16	-15.18		-
7	-	-	3.46^{SH}	77.78^{CH}
8	-9.66	-12.87		-
9	-11.09	-13.66		-
10	-11.09	-13.56		-
11	-9.66	-12.81		-
12	-2.98	-6.01		-

Table 4.6 Measured ^{11}B, ^{13}C, and ^{1}H NMR chemical shift data for 1-COOH-7-SH-1,7-$C_2B_{10}H_{10}$ (**M1-COOH**) in $CDCl_3$ solution at 300 K.

	1-COOH-9-SH-1,7-$C_2B_{10}H_{10}$			
	(M9-COOH)			
Assign.	$\delta(^{11}B)^{exp}$	$\delta(^{11}B)^{calc}$	$\delta(^{1}H)^{exp}$	$\delta(^{13}C)^{calc}$
1	-	-	9.84^{COOH}	79.57^{CH}, 174.56^{COOH}
2	-20.46	-25.35	-	-
3	-17.34	-21.81		-
4	-11.71	-14.90		-
5	-5.19	-8.54		-
6	-13.47	-16.48		-
7	-	-	3.09^{CH}	62.38
8	-13.47	-17.19		-
9	-3.03	-2.92	0.47^{SH}	-
10	-10.02	-12.43		-
11	-14.80	-18.70		-
12	-6.86	-10.45		-

Table 4.7 Measured ^{11}B, ^{13}C, and ^{1}H NMR chemical shift data for 1-COOH-9-SH-1,7-$C_2B_{10}H_{10}$ (**M9-COOH**) in $CDCl_3$ solution at 300 K.

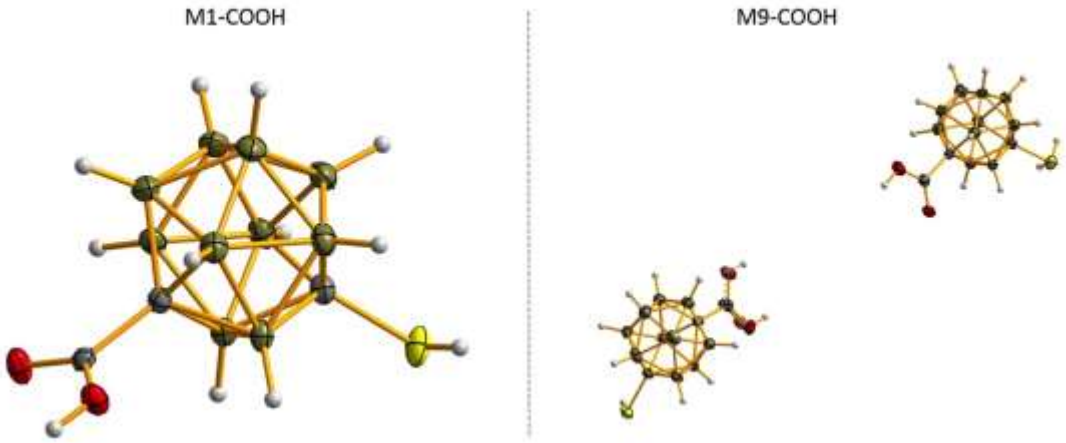

Figure 4.11 Crystallographically determined molecular structures of 1-COOH-9-SH-1,7-$C_2B_{10}H_{10}$ (**M9-COOH**) and 1-COOH-7-SH-1,7-$C_2B_{10}H_{10}$ (**M1-COOH**).

	M1-COOH
CCDC	
Empirical formula	$C_3 H_{12} B_{10} O_2 S_1$
Diffractometer	four-cycle diffractometer Xcalibur, AtlasS2, Gemini ultra
M_r /g mol^{-1}	220.30
T/K	120
Wavelength / Å	1.54184
Crystal system	Monoclinic
Space group	P21/n
a/Å	7.8784(5)
b/Å	13.2904(10)
c/Å	11.1831(9)

	M1-COOH
α/deg	90
β/deg	93.449(6)
γ/deg	90
V/Å^3	1168.83(15)
Z	4
Calc. density/g cm^{-3}	1.2518
μ mm^{-1}	2.146
F(000)	448
Crystal size /mm3	0.18 x 0.13 x 0.05
θ range /°	5.2 - 66.7
Index ranges /*hkl*	[-9,5]; [-13,15]; [-13,12]
Reflections collected (R_{int})	3661 (0.031)
Independent reflections	2009
Completeness /% to θ /°	98% to 65.59
Absorption correction	multi-scan
Max. and min. transmission	0.76 and 1
Data / restraints / parameters	2009/9/181
Goodness-of-fit on F2	1.22
*R*1, *wR*2 [I>3σ(I)]	0.0362, 0.0895
*R*1, *wR*2 (all data)	0.0473, 0.0966

	M1-COOH
Largest diff. peak and hole, eÅ^{-3}	0.21 and -0.22

Table 4.8 Crystallographic collection and refinement data for 1-COOH-7-SH-1,7-$C_2B_{10}H_{10}$ (**M1-COOH**).

	M9-COOH
CCDC	
Empirical formula	C_6 H_{24} B_{20} O_4 S_2
Diffractometer	four-cycle diffractometer Xcalibur, AtlasS2, Gemini ultra
M_r /g mol^{-1}	440.6
T/K	120
Wavelength / Å	1.54184
Crystal system	Monoclinic
Space group	C2/c
a/Å	32.2102 (4)
b/Å	6.9016 (1)
c/Å	23.2398 (5)
α/deg	90
β/deg	119.7080 (16)
γ/deg	90
V/Å^3	4487.21 (15)

	M9-COOH
Z	8
Calc. density/g cm^{-3}	1.304
μ mm^{-1}	2.24
F(000)	1792
Crystal size /mm^3	0.83 x 0.10 x 0.07
θ range /°	4.4 - 66.9
Index ranges /*hkl*	[-38,38]; [-7,8]; [-27,27]
Reflections collected (R_{int})	35917 (0.031)
Independent reflections	3932
Completeness /% to θ /°	0.99 to 66.9
Absorption correction	multi-scan
Max. and min. transmission	0.496 and 1
Data / restraints / parameters	3932/24/348
Goodness-of-fit on F^2	2.29
*R*1, *wR*2 [I>2σ(I)]	0.0376, 0.1149
*R*1, *wR*2 (all data)	0.0404, 0.1173
Largest diff. peak and hole, $eÅ^{-3}$	0.58 and -0.32

Table 4.9 Crystallographic collection and refinement data for 1-COOH-9-SH-1,7-$C_2B_{10}H_{10}$ (**M9-COOH**).

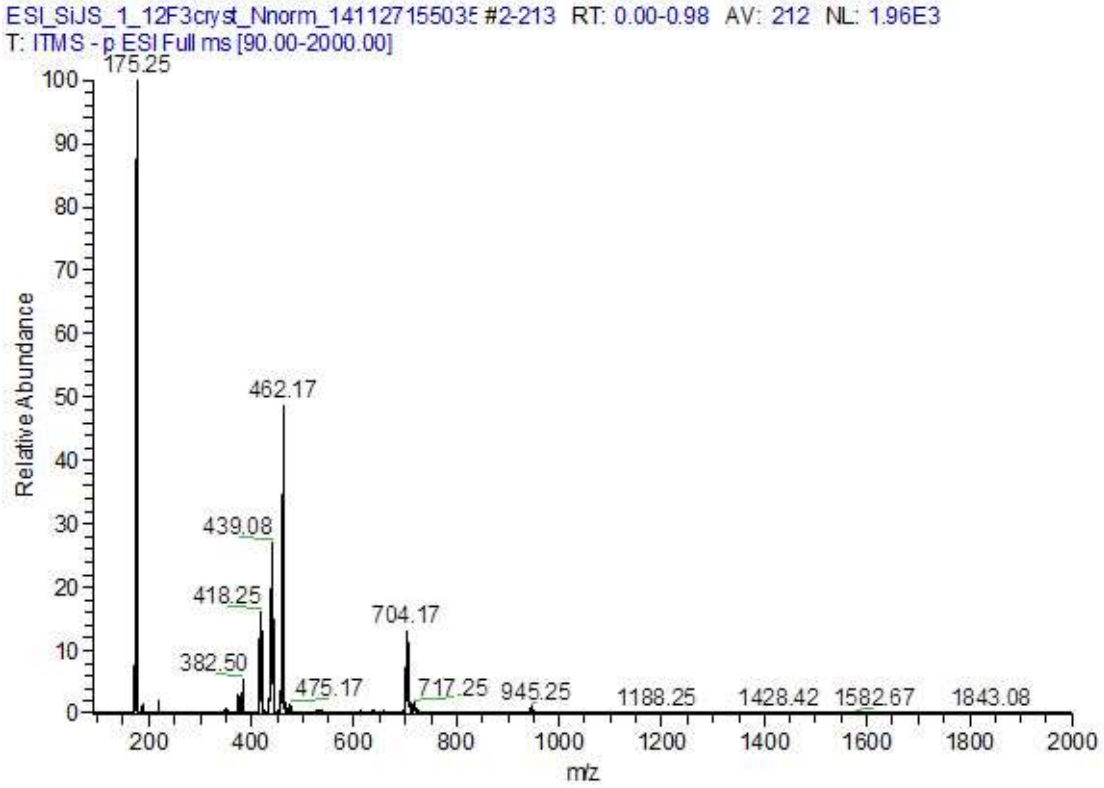

Figure 4.12 ESI Mass spectrum of 1-COOH-9-SH-1,7-$C_2B_{10}H_{10}$ (**M9-COOH**).

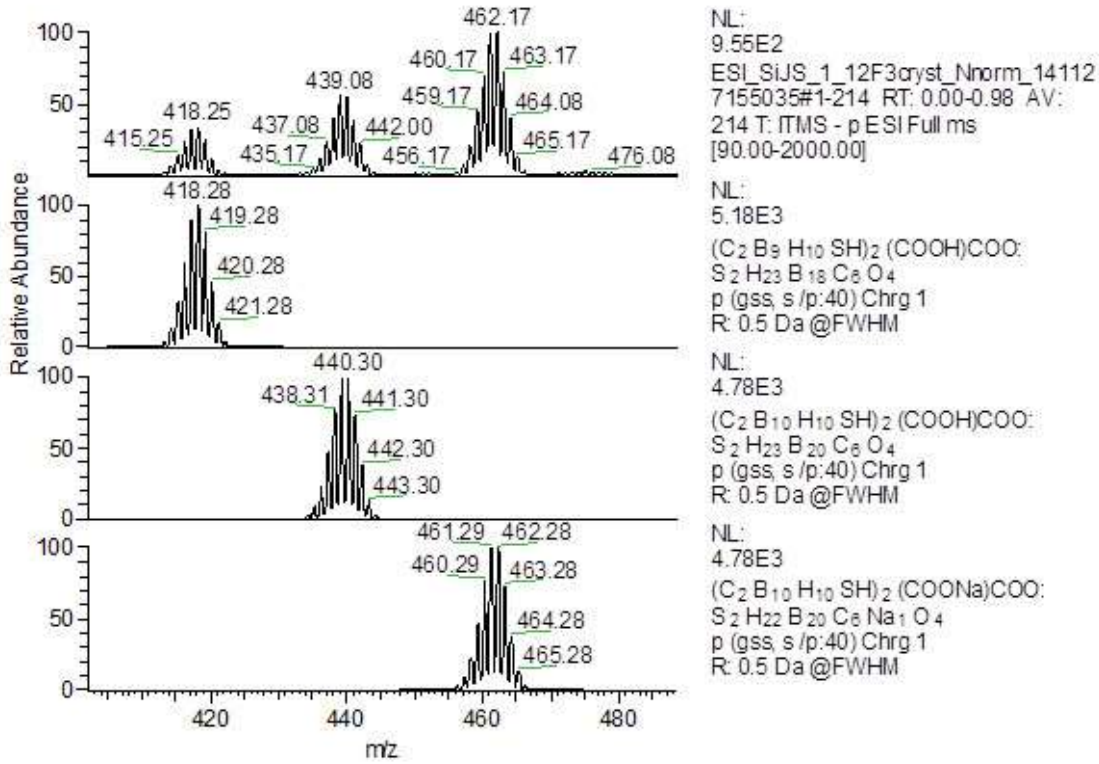

Figure 4.13 Measured (top) and calculated (bottom) isotopic distribution envelopes for the molecular masses corresponding to 2M-2H+1Na, 2M-H and for 2M-H-2B.

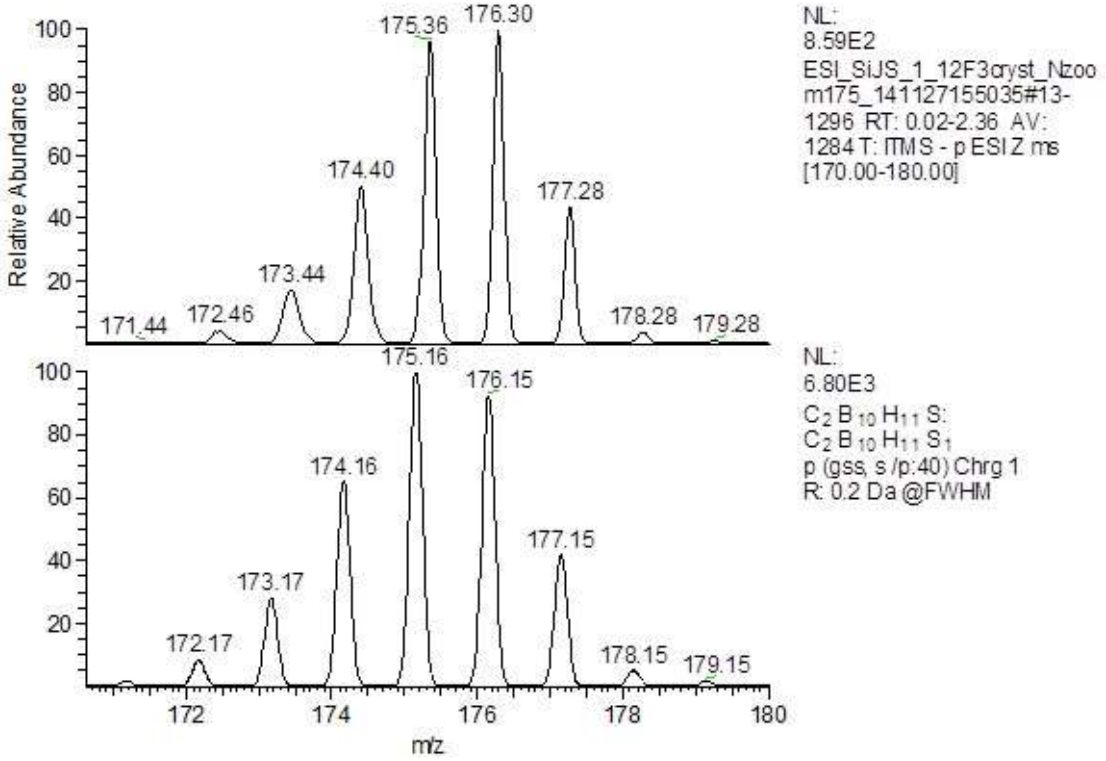

Figure 4.14 Measured (top) and calculated (bottom) isotopic distribution envelopes for the molecular mass corresponding to M-COOH.

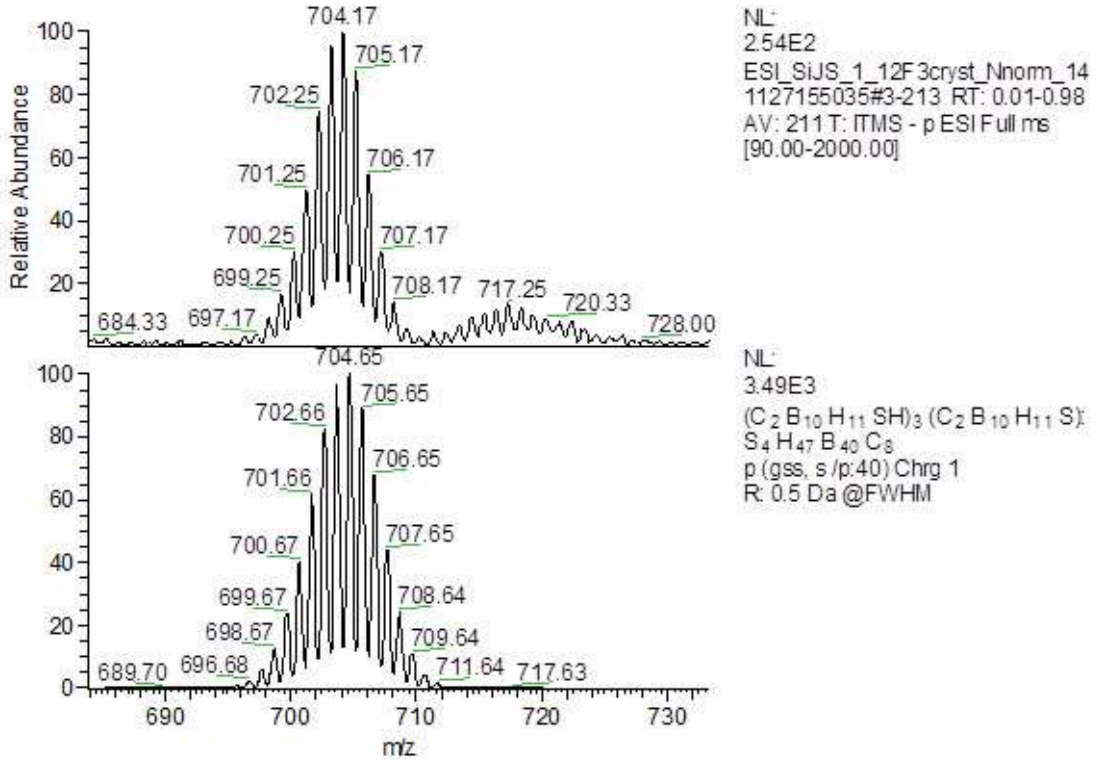

Figure 4.15 Measured (top) and calculated (bottom) isotopic distribution envelopes for the molecular mass corresponding to 4×(M-COOH).

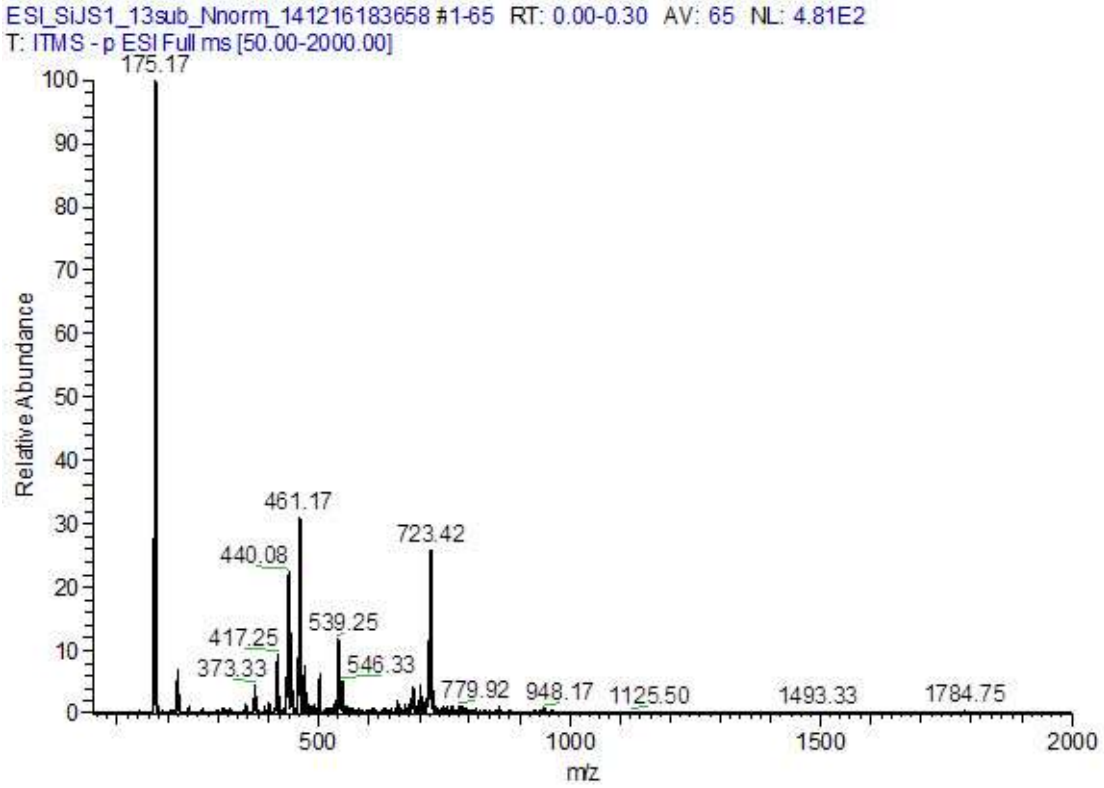

Figure 4.16 ESI Mass spectrum of 1-COOH-7-SH-1,7-$C_2B_{10}H_{10}$ (**M1-COOH**).

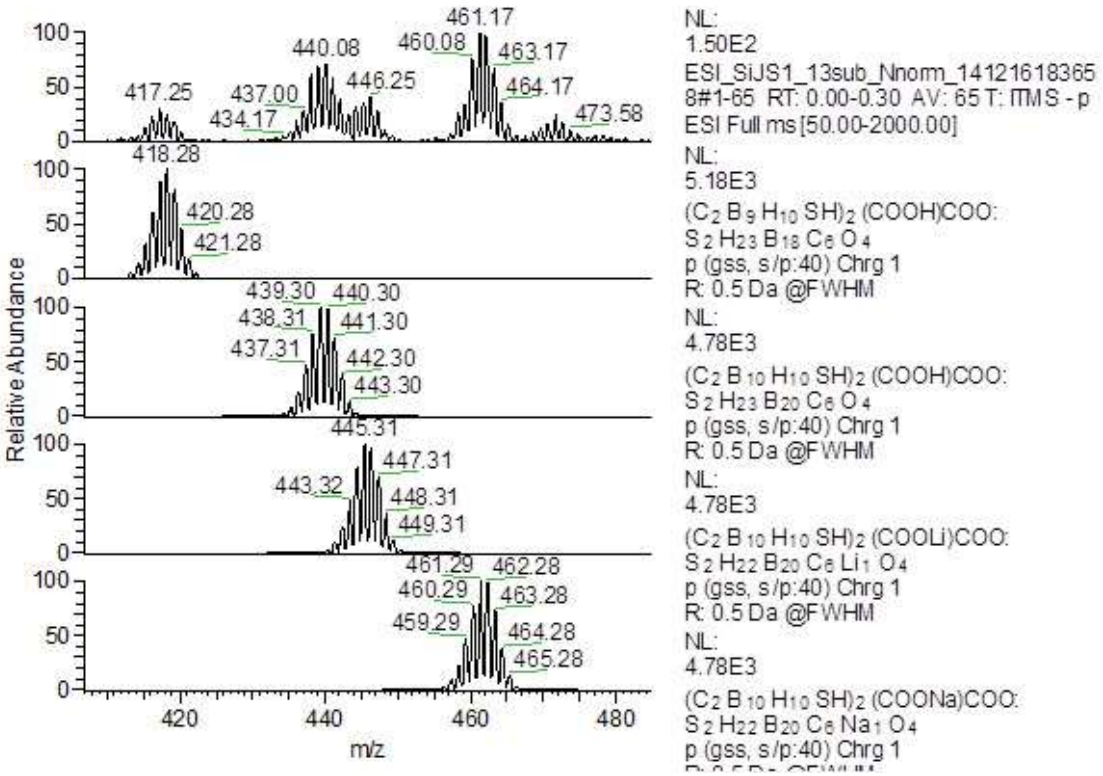

Figure 4.17 Measured (top) and calculated (bottom) isotopic distribution envelopes for the molecular masses corresponding to 2M-2H+1Na, 2M-H+1Li, 2M-H and to 2M-H-2B.

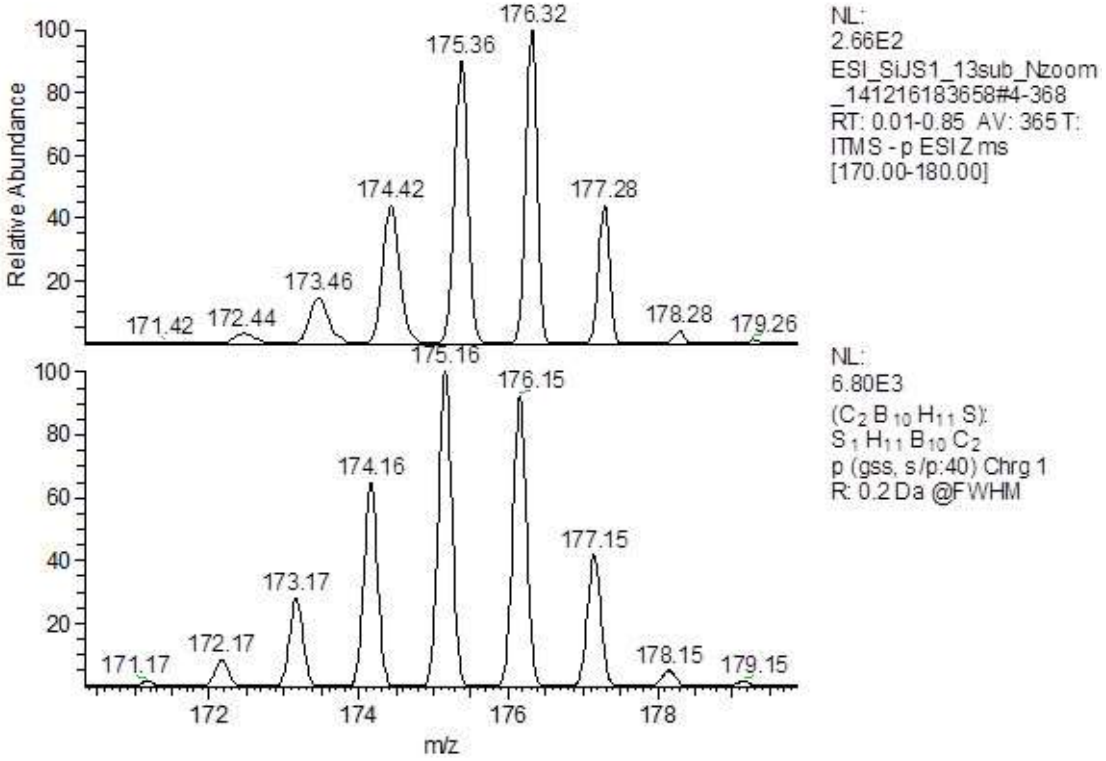

Figure 4.18 Measured (top) and calculated (bottom) isotopic distribution envelopes for the molecular mass corresponding to M-COOH.

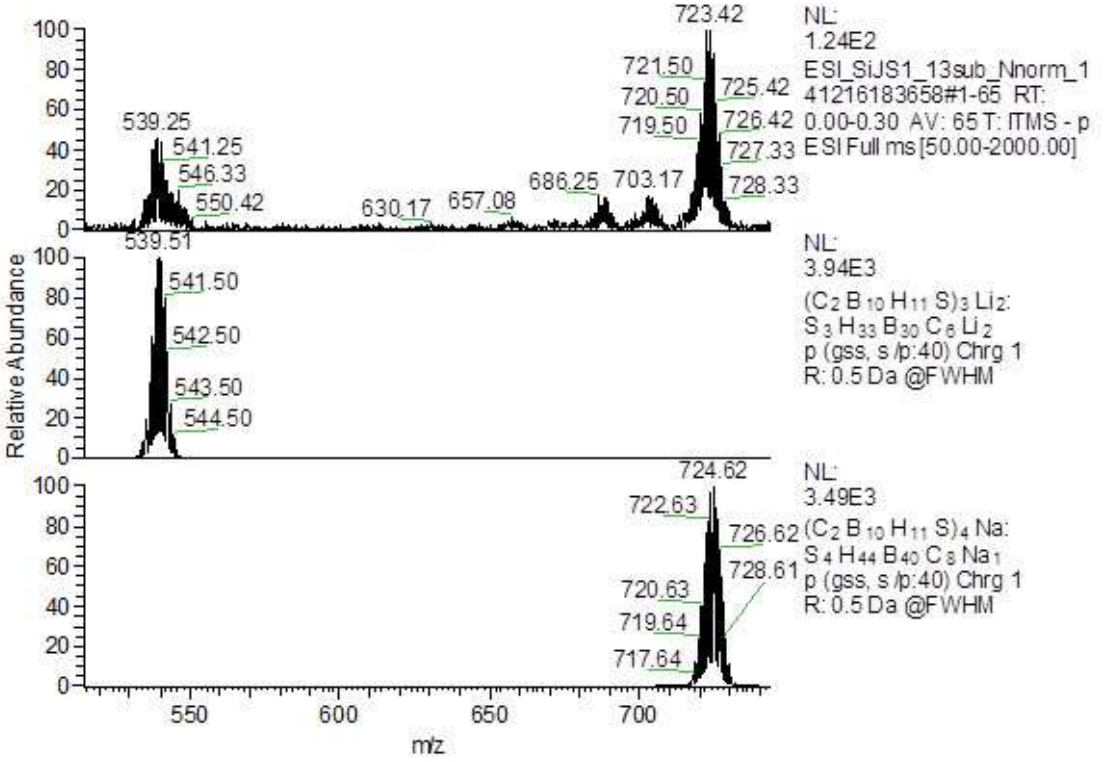

Figure 4.19 Measured (top) and calculated (bottom) isotopic distribution envelopes for the molecular mass corresponding to 3×(M-COOH)+2Li and 4×(M-COOH)+1Na.

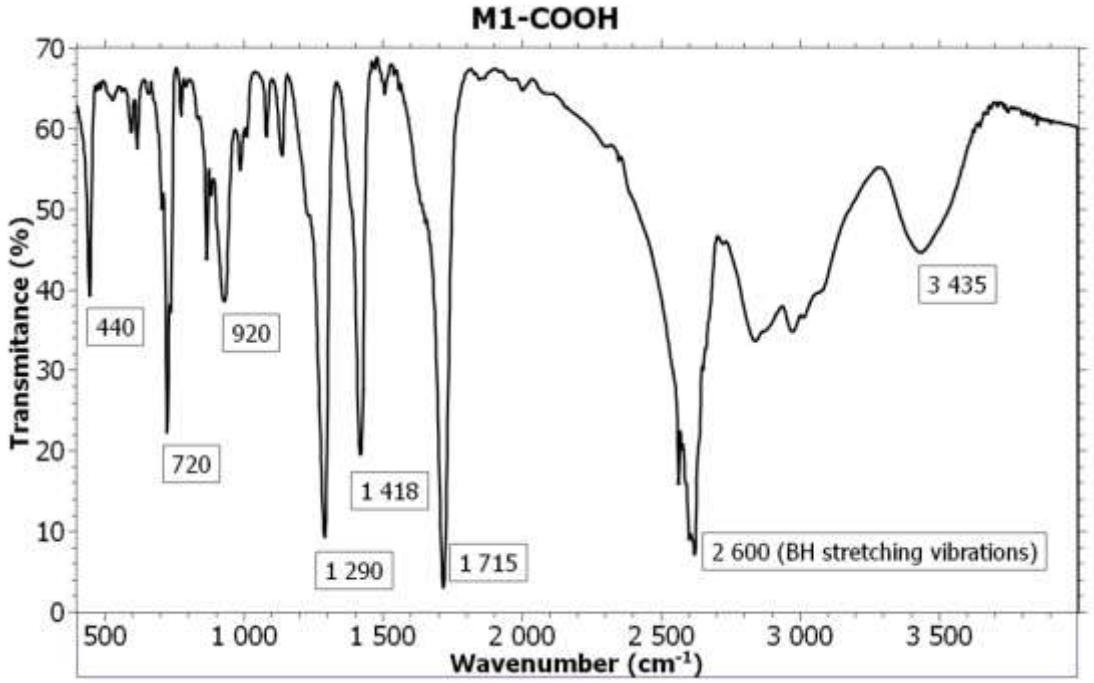

Figure 4.20 Infrared spectrum of 1-COOH-7-SH-1,7-$C_2B_{10}H_{10}$ (**M1-COOH**).

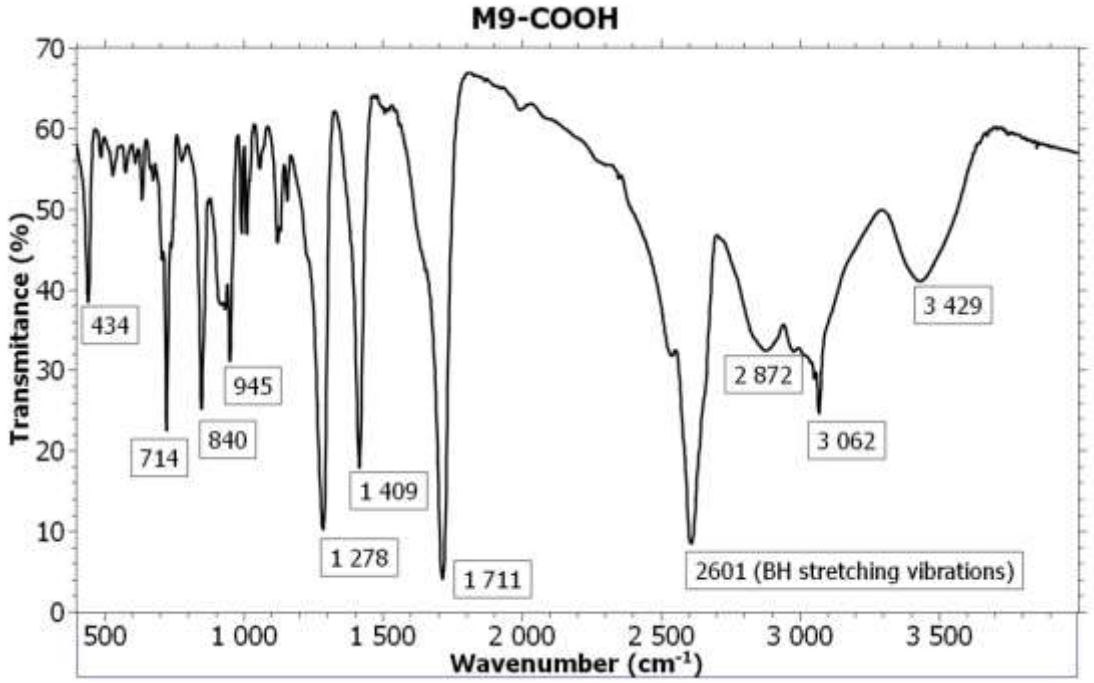

Figure 4.21. Infrared spectrum of *racem*-1-COOH-9-SH-1,7-$C_2B_{10}H_{10}$ (**M9-COOH**).

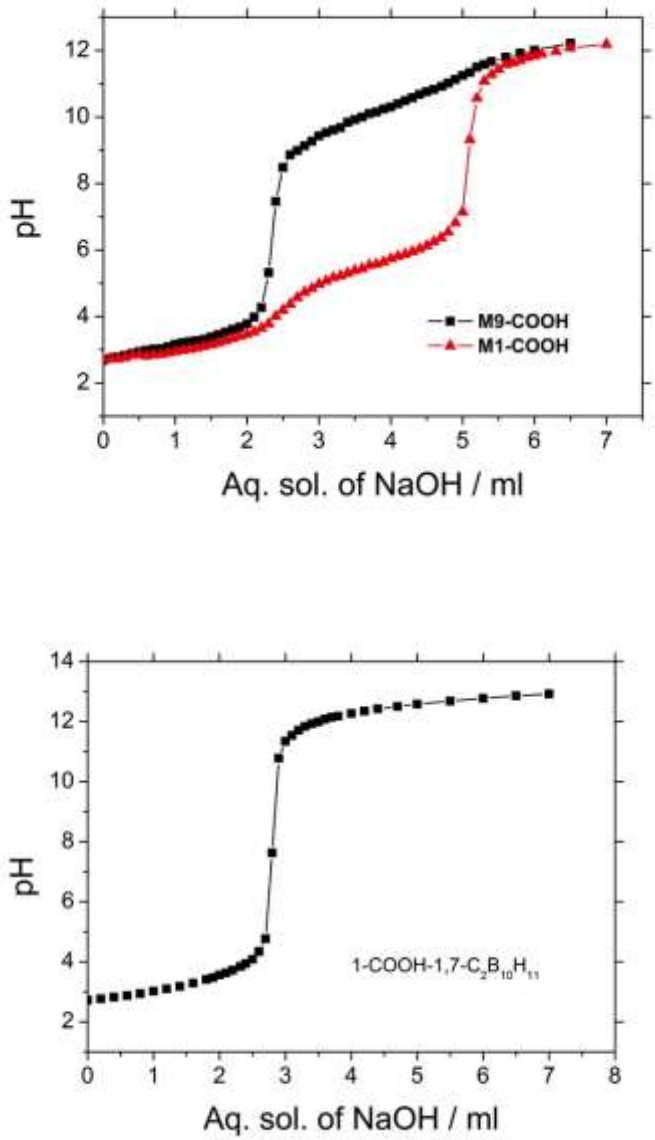

Figure 4.22 Acid-base titration curves of 1-COOH-7-SH-1,7-$C_2B_{10}H_{10}$ (**M1-COOH**), 1-COOH-9-SH-1,7-$C_2B_{10}H_{10}$ (**M9-COOH**) and 1-COOH-1,7-$C_2B_{10}H_{11}$.

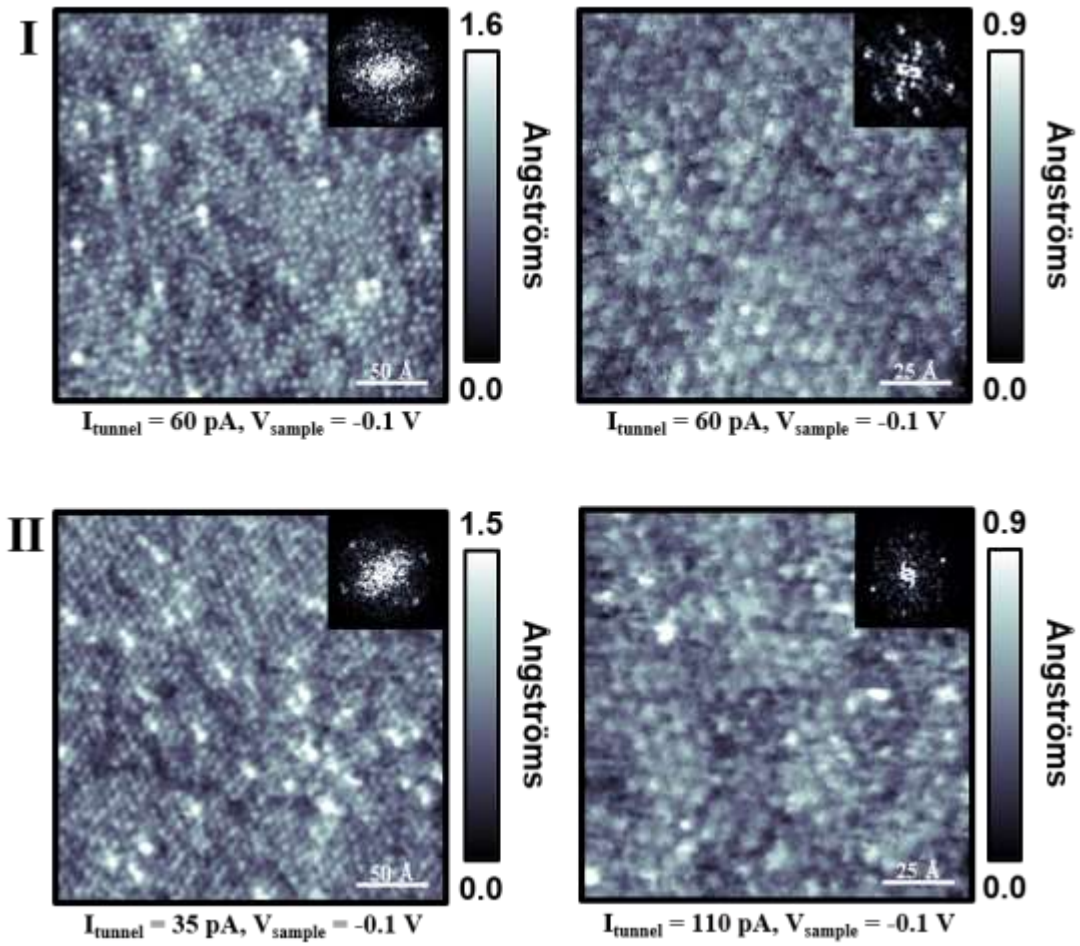

Figure 4.23 Compilation of scanning tunneling microscopy images, with hexagonally close-packed arrays of (I) 1-COOH-7-SH-1,7-$C_2B_{10}H_{10}$ (**M1-COOH**) and (II) 1-COOH-9-SH-1,7-$C_2B_{10}H_{10}$ (**M9-COOH**) on Au{111}/mica. Both isomers show a two phase monolayer with a nearest neighbour distance of 8.4 ± 0.4 Å. Each image inset depicts a Fourier transform used to measure the lattice spacings.

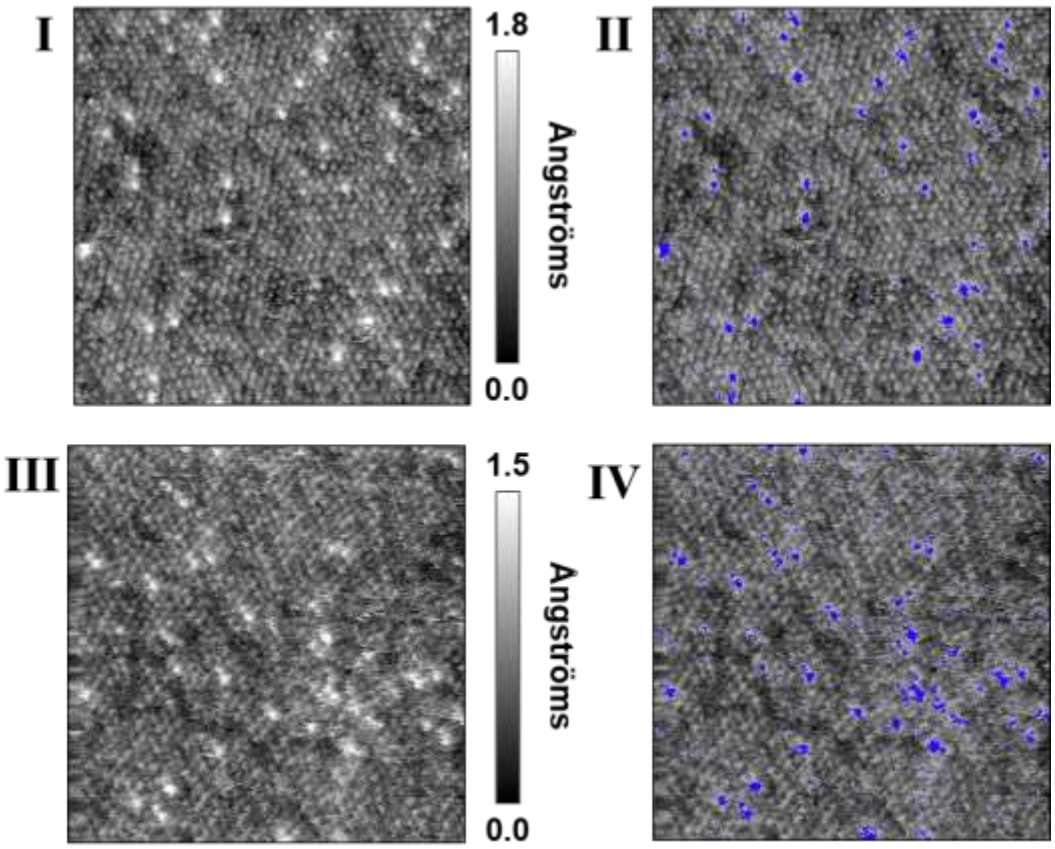

Figure 4.24 (I) Scanning tunneling microscopy image of 1-COOH-7-SH-1,7-$C_2B_{10}H_{10}$ (**M1-COOH**) and (II) thresholded by apparent height. By using this masking technique we can analyse the two phases of the self-assembled monolayer, showing that the higher intensity protrusion composes 3±1%. The same analysis was done for 1-COOH-9-SH-1,7-$C_2B_{10}H_{10}$ (**M9-COOH**) (III and IV), showing identical characteristics.

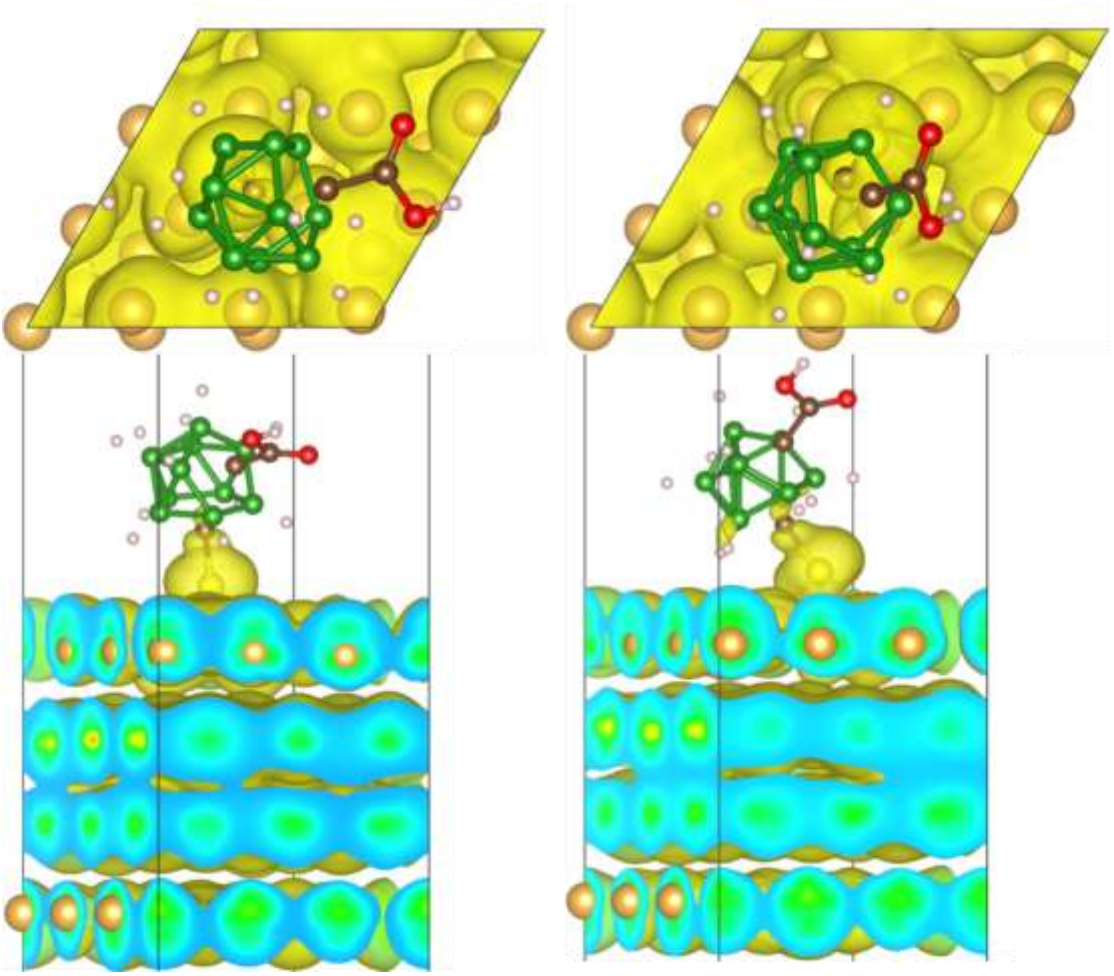

Figure 4.25 Partial charge density plots from EF – 0.1 to EF of 1-COOH-7-SH-1,7-$C_2B_{10}H_{10}$ (**M1-COOH**) in (Left) configuration B and (Right) configuration A. The images are plotted with an isodensity value of 10-4.

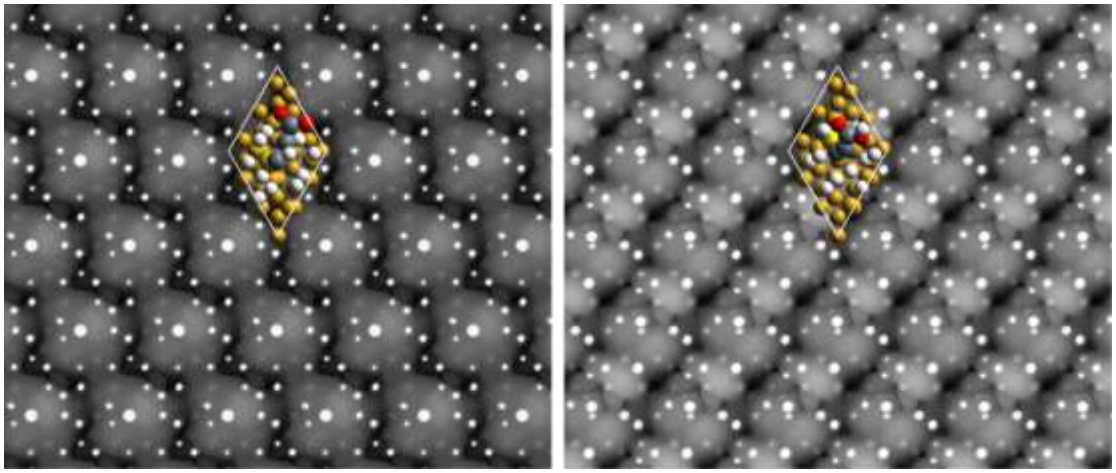

Figure 4.26 Simulated constant current scanning tunneling microscopy images of 1-COOH-7-SH-1,7-$C_2B_{10}H_{10}$ (**M1-COOH**) in (Left) configuration B and (Right) configuration A. The isovalue for the charge density is 10-4, and the range of band is from EF – 0.1 to EF, to simulate the experimental condition Vsample = -0.1 V.

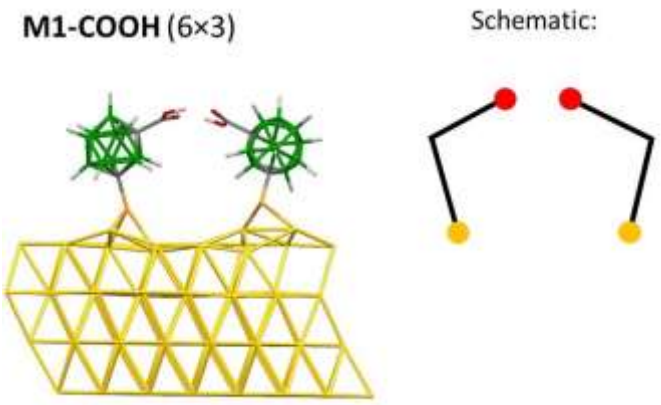

Figure 4.27 Two molecules of 1-COOH-7-SH-1,7-$C_2B_{10}H_{10}$ (**M1-COOH**) interacting *via* their carboxylic functional groups.

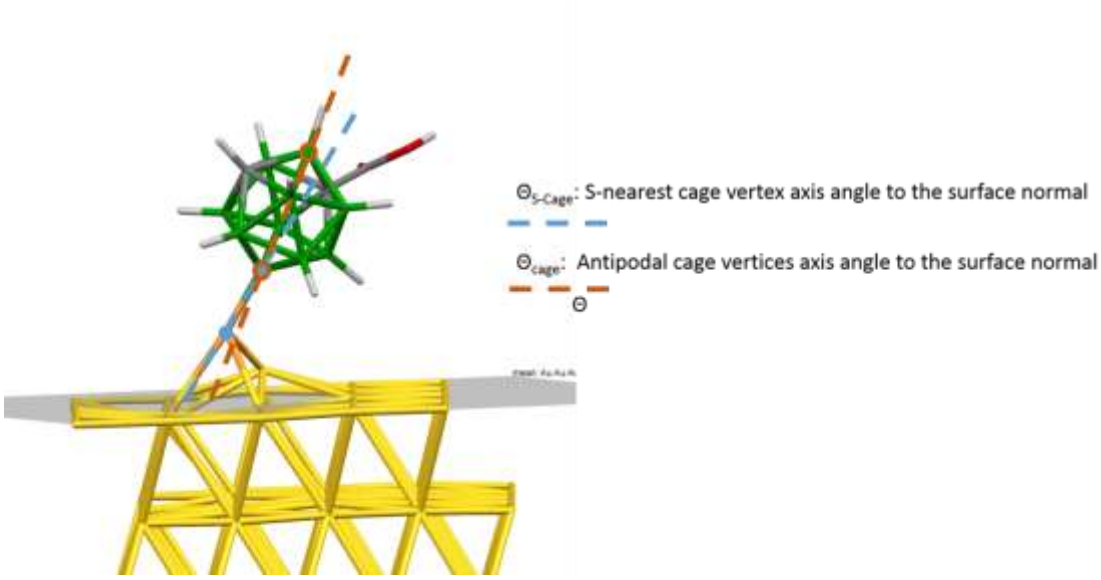

Figure 4.28 Schematic representation of two axes: *S atom - nearest Cage vertex* ($\Theta_{S\text{-}Cage}$) axis (blue dashed line) and *antipodal Cage vertices* (Θ_{Cage}) axis (orange dashed line). The values of $\Theta_{S\text{-}Cage}$ and Θ_{Cage} are the respective angles of these axes to the surface normal.

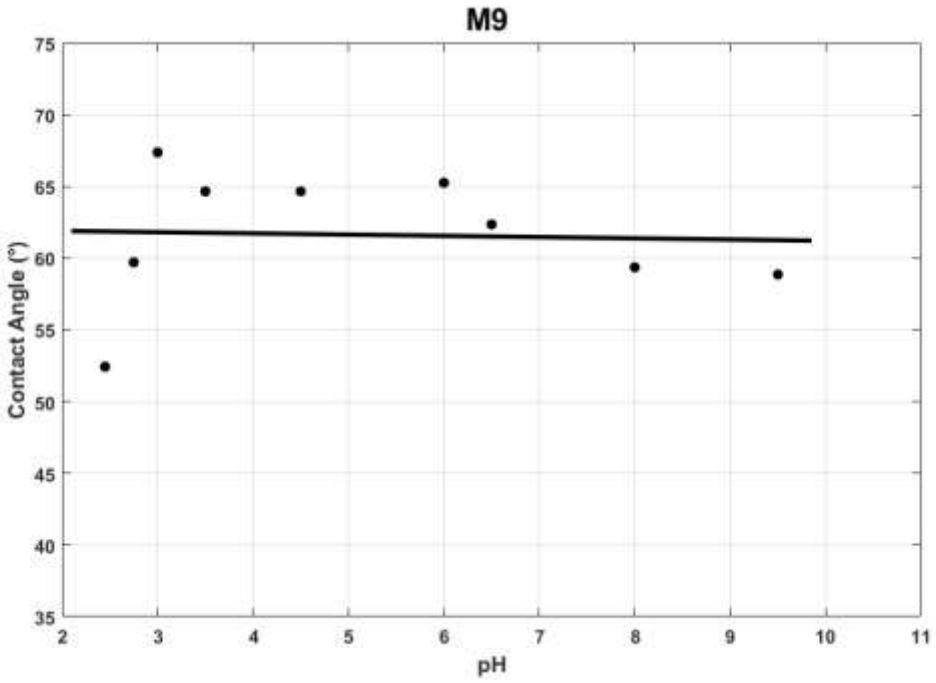

Figure 4.29 Contact angle titration control performed on a 9-SH-1,7-$C_2B_{10}H_{11}$ (**M9**) self-assembled monolayer, which does not have a terminal acid group and therefore the contact angle is not a function of pH.

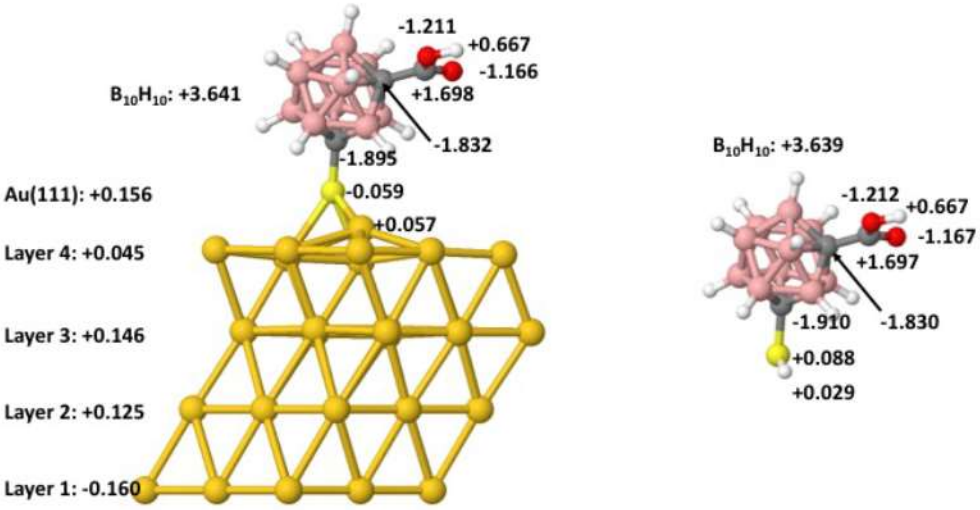

Figure 4.30 Bader charge for 1-COOH-7-SH-1,7-$C_2B_{10}H_{10}$ (**M1-COOH**) oriented in configuration B (Left) on a surface and (Right) as a molecule in vacuum.

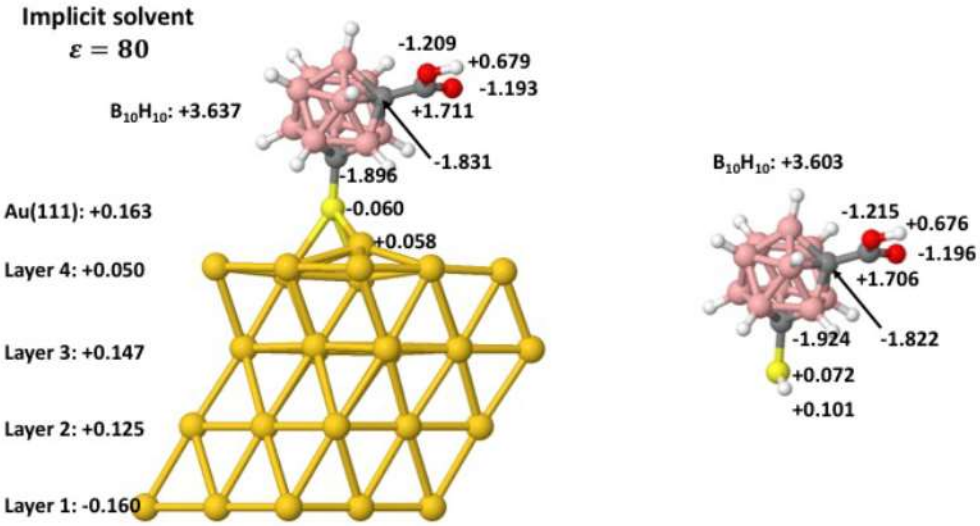

Figure 4.31 Bader charge for 1-COOH-7-SH-1,7-$C_2B_{10}H_{10}$ (**M1-COOH**) oriented in configuration B (Left) on a surface and (Right) as a molecule in water.

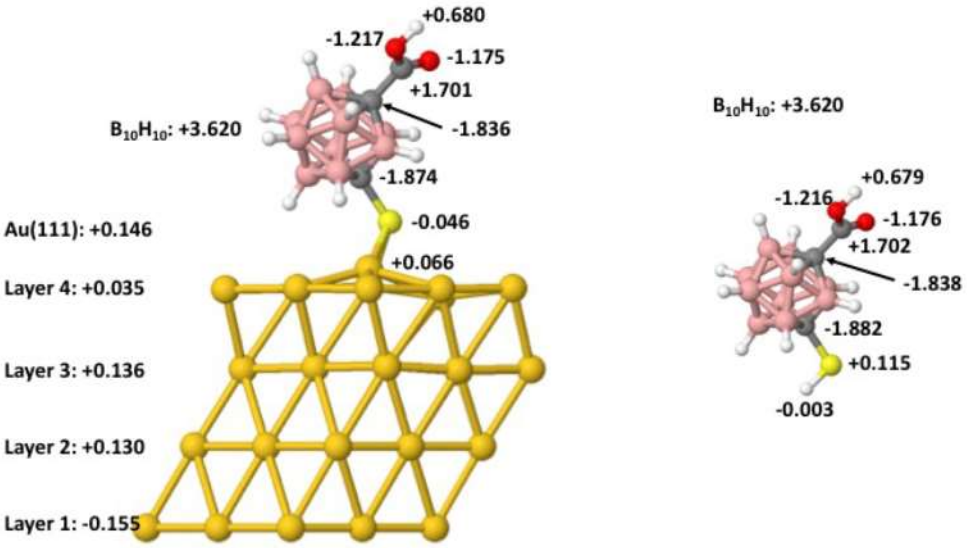

Figure 4.32 Bader charge for 1-COOH-7-SH-1,7-$C_2B_{10}H_{10}$ (**M1-COOH**) oriented in configuration A (Left) on a surface and (Right) as a molecule in vacuum.

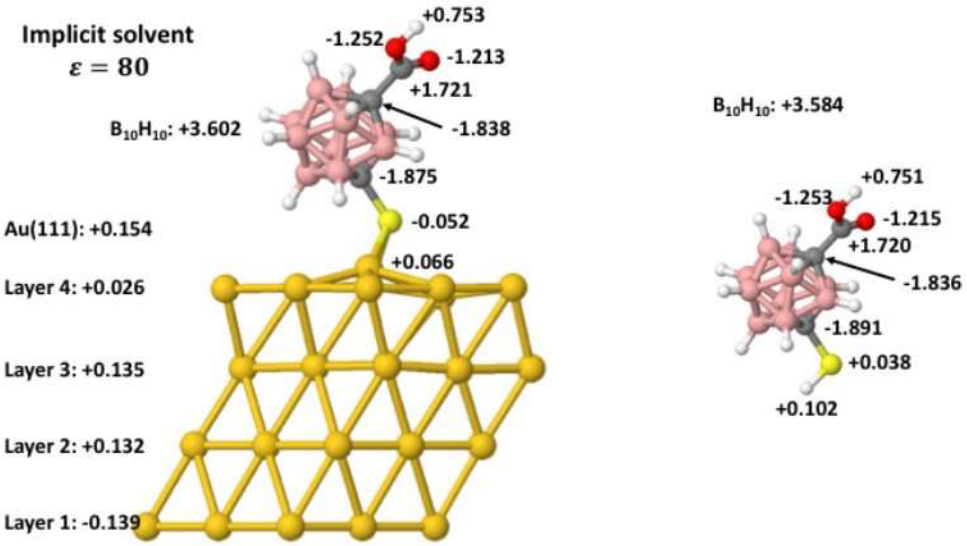

Figure 4.33 Bader charge for 1-COOH-7-SH-1,7-$C_2B_{10}H_{10}$ (**M1-COOH**) oriented in configuration A (Left) on a surface and (Right) as a molecule in water.

	M1-COOH Configuration A		M1-COOH Configuration B	
	On Au{111}	Free Molecule	On Au{111}	Free Molecule
H1	0.680	0.679	0.667	0.667
O2	-1.217	-1.216	-1.211	-1.212
O3	-1.175	-1.176	-1.166	-1.167
C4	1.701	1.702	1.698	1.697
-COOH	-0.01	-0.012	-0.012	-0.015
C5	-1.836	-1.838	-1.832	-1.83
C6	-1.874	-1.882	-1.895	-1.91
$B_{10}H_{10}$	3.62	3.62	3.641	3.639
$B_{10}H_{10}C_2$	-0.09	-0.1	-0.086	-0.101
S	-0.046	0.115	-0.059	0.088
Au{111}/H	0.146	-0.003	0.156	0.029

Table 4.10 Bader charge of 1-COOH-7-SH-1,7-$C_2B_{10}H_{10}$ (**M1-COOH**) in vacuum.

	M1-COOH Configuration A		M1-COOH Configuration B	
	On Au{111}	Free Molecule	On Au{111}	Free Molecule
H1	0.753	0.751	0.679	0.676
O2	-1.252	-1.253	-1.209	-1.215
O3	-1.213	-1.215	-1.193	-1.196
C4	1.721	1.72	1.711	1.706
-COOH	0.009	0.003	-0.013	-0.029
C5	-1.838	-1.836	-1.831	-1.822
C6	-1.875	-1.891	-1.896	-1.924
$B_{10}H_{10}$	3.602	3.584	3.637	3.603
$B_{10}H_{10}C_2$	-0.111	-0.143	-0.09	-0.144
S	-0.052	0.038	-0.06	0.072
Au{111}/H	0.154	0.102	0.163	0.101

Table 4.11 Bader charge of 1-COOH-7-SH-1,7-$C_2B_{10}H_{10}$ (**M1-COOH**) in water.

Isomer		E_{ele} (a.u.)	Correction (a.u.)	G(a.u.)	pK_a	Expt. pK_a
M1-COOH	A-	-918.441	0.13859	-918.303	1.11	3.01
	AH	-918.884	0.15045	-918.734		
	Diff	0.44294	-0.01186	0.43109		
M9-COOH	A-	-918.48	0.13996	-918.34	1.02	3.23
	AH	-918.923	0.15209	-918.77		
	Diff	0.44303	-0.01213	0.4309		

Table 2.12 Energies of neutral (AH) and deprotonated (A-) single molecules and the difference (Diff) between the two states for 1-COOH-7-SH-1,7-$C_2B_{10}H_{10}$ (**M1-COOH**) and 1-COOH-9-SH-1,7-$C_2B_{10}H_{10}$ (**M9-COOH**) in water. $E_s(H^+)$ = -269 kcal/mol (-0.42869 a.u.) is from experiments.

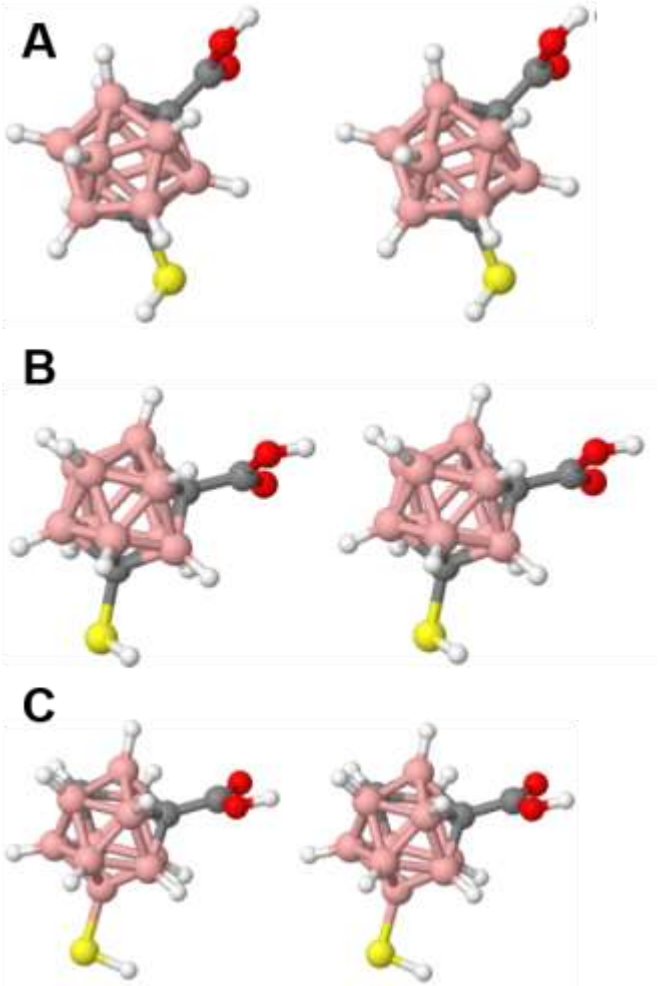

Figure 4.34 Dimer geometries of (A) 1-COOH-7-SH-1,7-$C_2B_{10}H_{10}$ (**M1-COOH**) in configuration A, (B) **M1-COOH** in configuration B, and (C) 1-COOH-9-SH-1,7-$C_2B_{10}H_{10}$ (**M9-COOH**).

Isomer		E_{ele} (a.u.)	Correction (a.u.)	G(a.u.)	pK_a	Expt. pK_a
M1-COOH Config. A	A-	-1837.32	-0.02642	-1837.35	1.21	5.10
	AH	-1837.76	-0.01423	-1837.78		
	Diff	0.44352	-0.0122	0.43133		
M1-COOH Config. B	A-	-1837.32	-0.02558	-1837.34	2.99	
	AH	-1837.76	-0.0137	-1837.78		
	Diff	0.44706	-0.01189	0.43518		
M9-COOH	A-	-1837.39	-0.02566	-1837.42	2.14	4.80
	AH	-1837.84	-0.01319	-1837.85		
	Diff	0.44581	-0.01246	0.43334		

Table 4.13 Energies of neutral (AH) and deprotonated (A-) and the difference (Diff) between the two states for dimer molecules of 1-COOH-7-SH-1,7-$C_2B_{10}H_{10}$ (**M1-COOH**) in configuration A, **M1-COOH** in configuration B, and 1-COOH-9-SH-1,7-$C_2B_{10}H_{10}$ (**M9-COOH**), all in water. $E_s(H^+)$ = -269 kcal/mol (-0.42869 a.u.) is from experiments.

SAM	PE line	BE (eV)	FWHM (eV)
M9-COOH + Sr(II)	Au $4f_{7/2}$	84.0	0.67
	Sr 3d	134.0	1.34
	S $2p_{3/2}$	161.7	0.84
	B 1s	189.3	1.20
	C 1s	285.3	1.69
M9-COOH + Fe(II)	S $2p_{3/2}$	162,.2	1.93
	B 1s	189.7	1.88
	C 1s	285.0	2.53
	Fe 2p	711.4	7.4
M9-COOH + Co(II)	Au $4f_{7/2}$	84.0	0.71
	S $2p_{3/2}$	161.8	0.83
	B 1s	284.9	1.93
	C 1s	532.0	1.89
	O 1s	189.2	1.22
	Co 2p	781.4	1.76
M9-COOH + Ni(II)	Au $4f_{7/2}$	84.1	0.66
	S $2p_{3/2}$	162.0	0.87

	B 1s	**189.4**	**1.40**
	C 1s	**285.0**	**1.91**
	O 1s	**532.0**	**2.56**
	Ni 2p	**856.1**	**1.59**
M9-COOH + Cu(II)	**S $2p_{3/2}$**	**162.5**	**2.32**
	B 1s	**189.8**	**2.07**
	C 1s	**285.0**	**2.53**
	Cu 2p	**932.6**	**3.11**
M9-COOH + Zn(II)	**S $2p_{3/2}$**	**162.0**	**1.98**
	B 1s	**189.6**	**2.15**
	C 1s	**285.0**	**2.74**
	O 1s	**532.3**	**2.72**
	Zn 2p	**1022.7**	**2.58**
M9-COOH + La(III)	**S $2p_{3/2}$**	**163.1**	**2.15**
	B 1s	**189.6**	**1.53**
	C 1s	**285.0**	**2.45**
	O 1s	**532.5**	**2.55**
	La $3d_{5/2}$	**839.2**	**65.70**

	La $3d_{3/2}$	**855.9**	**5.42**
M9-COOH + Sm(III)	**S $2p_{3/2}$**	**162.0**	**1.88**
	B 1s	**189.7**	**1.62**
	C 1s	**285.0**	**2.33**
	O 1s	**532.8**	**2.64**
	Sm 3d	**10.85.5**	**4.67**
M9-COOH + Tb(III)	**Tb $4d_{3/2}$**	**152.6**	**6.71**
	S $2p_{3/2}$ (thiolate)	**162.0**	**1.87**
	S $2p_{3/2}$ (sulfate)	**169.8**	**0.40**
	B 1s	**189.3**	**2.31**
	C 1s	**285.0**	**2.86**
	O 1s	**532.2**	**2.62**
	Tb $3d_{5/2}$	**1243.6**	**9.79**
	Tb $3d_{3/2}$	**1277.0**	**4.15**
M9-COOH + Tl(I)	**Tl 4f**	**117.9**	**1.01**
	S $2p_{3/2}$	**161.8**	**1.33**
	B 1s	**189.3**	**1.38**
	C 1s	**284.6**	**1.68**

	O 1s	**531.0**	**2.37**
M9-COOH + Pb(II)	**Pb 4f**	**139.6**	**1.36**
	S $2p_{3/2}$	**162.2**	**1.07**
	B 1s	**189.8**	**1.27**
	C 1s	**285.0**	**2.01**
	Pb $4d_{5/2}$	**414.6**	**3.28**
	Pb $4d_{3/2}$	**436.5**	**2.52**
	O 1s	**531.9**	**2.33**

Table 4.14 Photoelectron (PE) lines used for qualitative XPS analysis of carborane-carboxylated SAMs exposed to solutions of the denoted ions, together with the corresponding bonding energies (BE) and observed full-width-half-maximum (FWHM). SAMs of 1-COOH-9-SH-1,7-$C_2B_{10}H_{10}$ (**M9-COOH**) were examined.

SAM	PE line	Stoichiometry	BE (eV)	KE (eV)	FWHM (eV)
M9-COOH + Mg(II)	Au $4f_{7/2}$	40.4	84.0	1401.7	0.80
	S $2p_{3/2}$	0.8	161.7	1324.0	0.86
	B 1s	10.0	189.3	1296.4	1.38
	C 1s	10.5	284.9	1200.8	1.93
	Mg KLL	0.3	306.3	1179.4	1.84
	O 1s	3.7	531.9	953.8	2.25
	Mg 1s	0.5	1304.6	181.1	1.52
M9-COOH + Ba(II)	Au $4f_{7/2}$	41.9	84.0	1401.7	0.84
	S $2p_{3/2}$	0.9	161.6	1324.0	2.17
	B 1s	10.0	189.4	1296.4	1.54
	C 1s	26.3	2.85	1200.8	1.75
	O 1s	3.1	531.6	953.8	2.23
	Ba $3d_{5/2}$	0.5	780.6	705.1	1.65
M9-COOH	Au $4f_{7/2}$	50.7	84.0	1401.7	0.81
	S $2p_{3/2}$	0.7	161.7	1324.0	0.85
	B 1s	10.0	189.4	1296.4	1.39

	C 1s	**21.9**	**285.1**	**1200.8**	**2.00**
	O 1s	**4.0**	**531.5**	**953.8**	**2.87**
	Na 1s	**0.8**	**1071.9**	**413.8**	**1.51**
M9-COOH + H_3O^+	**Au $4f_{7/2}$**	**74.4**	**84.0**	**1401.7**	**0.80**
	S $2p_{3/2}$	**0.8**	**161.7**	**1324.0**	**0.68**
	B 1s	**10.0**	**189.4**	**1296.4**	**1.29**
	C 1s	**38.3**	**285.1**	**1200.8**	**1.57**
	O 1s	**6.1**	**531.5**	**953.8**	**3.21**
	Na1s	**0.9**	**1071.9**	**413.8**	**1.53**
M9	**Au $4f_{7/2}$**	**55.5**	**84.0**	**1401.7**	**0.80**
	S $2p_{3/2}$	**0.9**	**161.7**	**1324.0**	**1.07**
	B 1s	**10.0**	**189.4**	**1296.4**	**1.45**
	C 1s	**32.5**	**285.1**	**1200.8**	**1.35**
	O 1s	**6.3**	**531.5**	**953.8**	**1.36**
	Na 1s	**0.0**	**~1071.9**	**~413.8**	**-**
M9 + H_3O^+	**Au $4f_{7/2}$**	**64.0**	**84.0**	**1401.7**	**0.80**
	S $2p_{3/2}$	**0.9**	**161.7**	**1324.0**	**0.94**
	B 1s	**10.0**	**189.4**	**1296.4**	**1.44**

	C 1s	**24.4**	**285.1**	**1200.8**	**1.51**
	O 1s	**6.1**	**531.5**	**953.8**	**1.50**
	Na 1s	**0.1**	**1071.9**	**413.8**	**0.69**
P1-COOH	**Au $4f_{7/2}$**	**42.7**	**84.0**	**1401.7**	**0.80**
	S $2p_{3/2}$	**0.8**	**161.7**	**1324.0**	**0.89**
	B 1s	**10.0**	**189.4**	**1296.4**	**1.00**
	C 1s	**11.1**	**285.1**	**1200.8**	**2.33**
	O 1s	**2.9**	**531.5**	**953.8**	**2.28**
	Na 1s	**0.3**	**1071.9**	**413.8**	**1.53**
P1-COOH + H_3O^+	**Au $4f_{7/2}$**	**86.6**	**84.0**	**1401.7**	**0.79**
	S $2p_{3/2}$	**1.0**	**161.7**	**1324.0**	**0.65**
	B 1s	**10.0**	**189.4**	**1296.4**	**1.20**
	C 1s	**31.8**	**285.1**	**1200.8**	**1.42**
	O 1s	**3.5**	**531.5**	**953.8**	**2.45**
	Na 1s	**0.4**	**1071.9**	**413.8**	**1.47**

Table 4.15 Stoichiometries obtained by quantitative XPS analysis of pristine, as well as ion-modified SAMs, together with the bonding energies (BE), kinetic energies (KE) and full-width-half-maxima (FWHM) of the corresponding photoelectron lines (PE). No additional elements were detected. SAMs of 1-COOH-9-SH-1,7-$C_2B_{10}H_{10}$ (**M9-COOH**), 9-SH-1,7-$C_2B_{10}H_{11}$ (**M9**), and 1-COOH-12-SH-1,12-$C_2B_{10}H_{10}$ (**P1-COOH**) were examined.

Sample	PE line	BE (eV)	FWHM (eV)
Na_2SO_4	C 1s	285.0	1.38
	S $2p_{3/2}$	168.9	1.92
	Na KLL	497.3	1.98
	O 1s	531.9	1.46
	Na 1s	1071.6	1.51
$MgSO_4$	S $2p_{3/2}$	169.6	2.16
	C 1s	285.0	1.69
	Mg KLL	307.7	2.46
	O 1s	532.6	1.87
	Mg 1s	1305.3	1.88
$BaSO_4$	S $2p_{3/2}$	168.9	2.10
	C 1s	285.0	1.69
	O 1s	532.0	1.76
	Ba $3d_{5/2}$	780.4	1.89
	Ba $3d_{3/2}$	795.7	1.92

Table 4.16 Photoelectron (PE) lines used for quantitative XPS analysis of sulfates used as reference samples for determination of relative sensitivity factors. No additional elements were detected on the sample surfaces.

Figure 4.35 The survey and detail XPS spectra together with the subtracted background, as measured for SAM of 1-COOH-9-SH-1,7-$C_2B_{10}H_{10}$ (**M9-COOH**) modified with Mg(II).

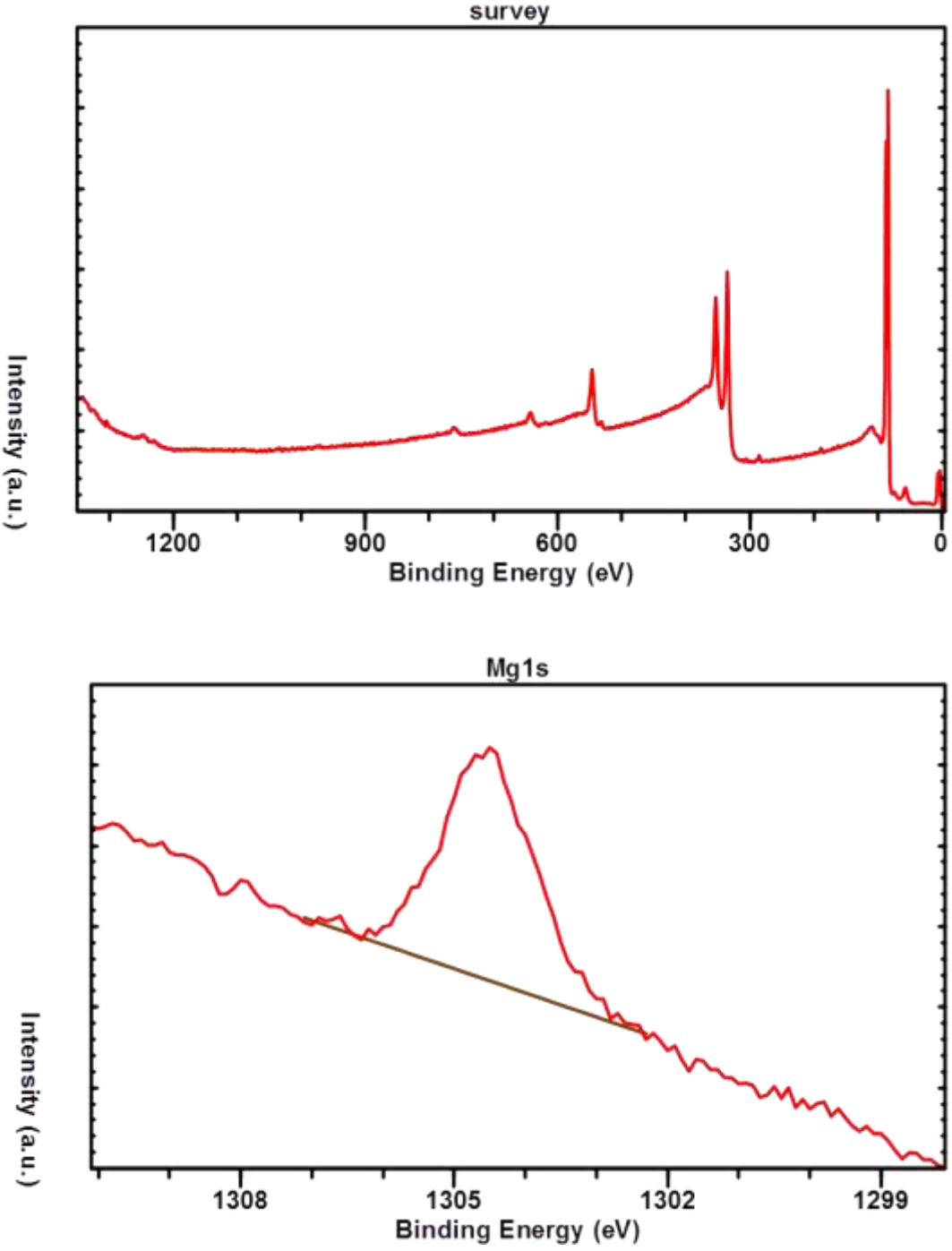

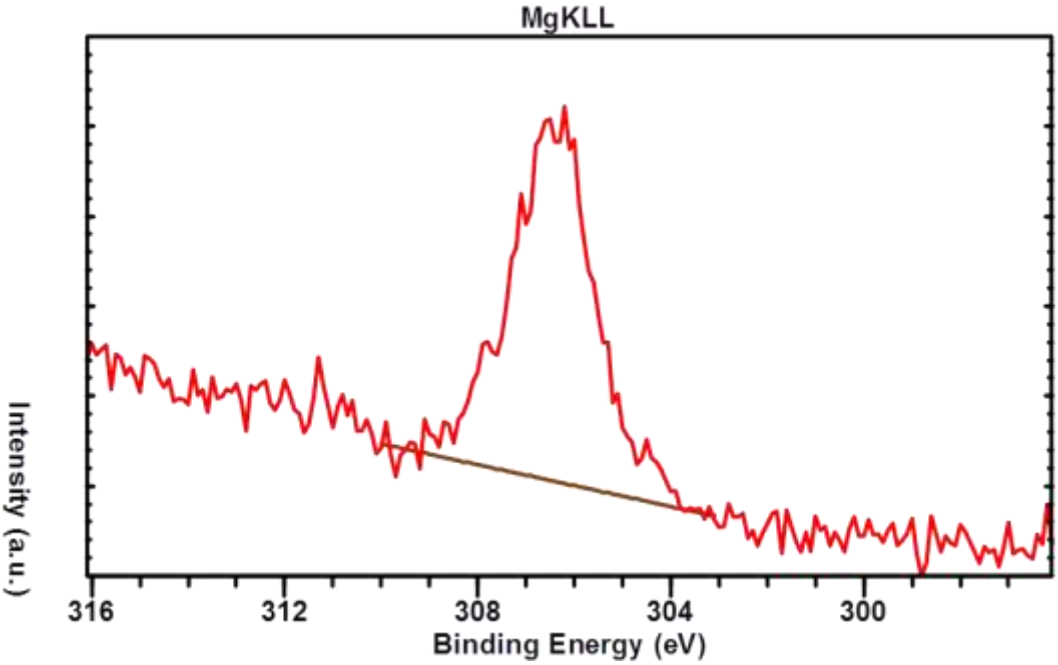
MgKLL
Intensity (a.u.)
316
312
308
304
300
Binding Energy (eV)

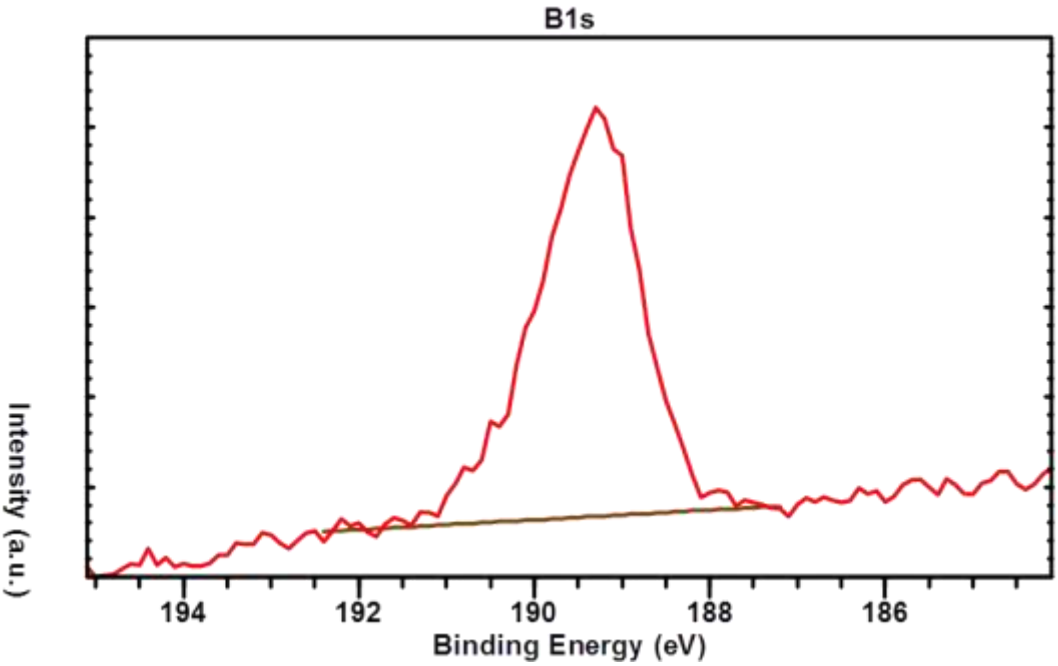
B1s
Intensity (a.u.)
194
192
190
188
186
Binding Energy (eV)

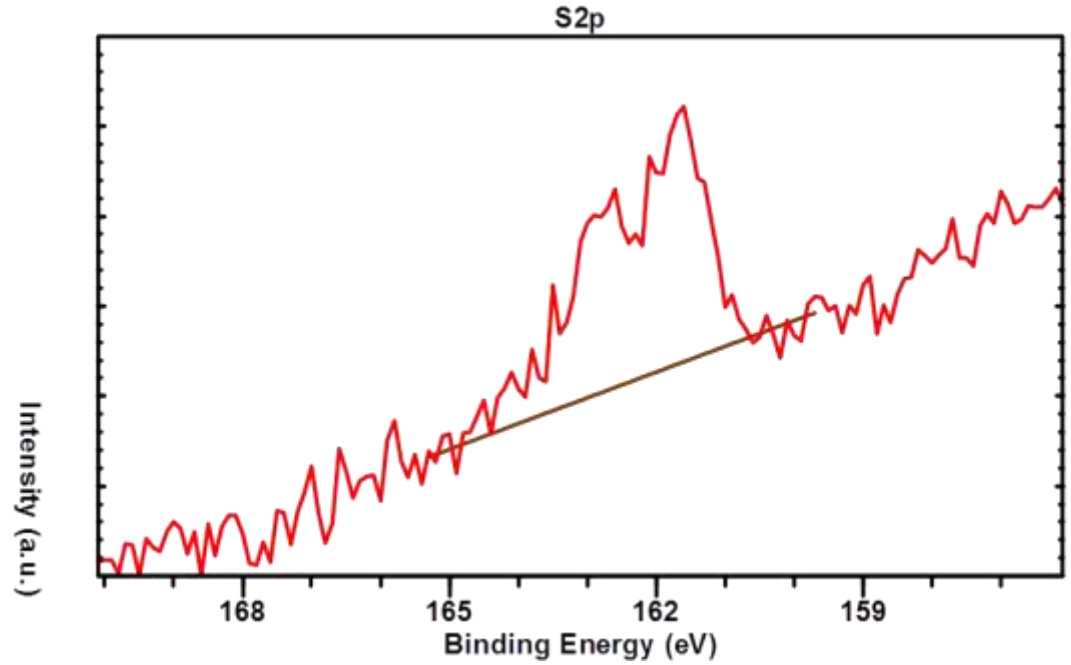
S2p
Intensity (a.u.)
168
165
162
159
Binding Energy (eV)

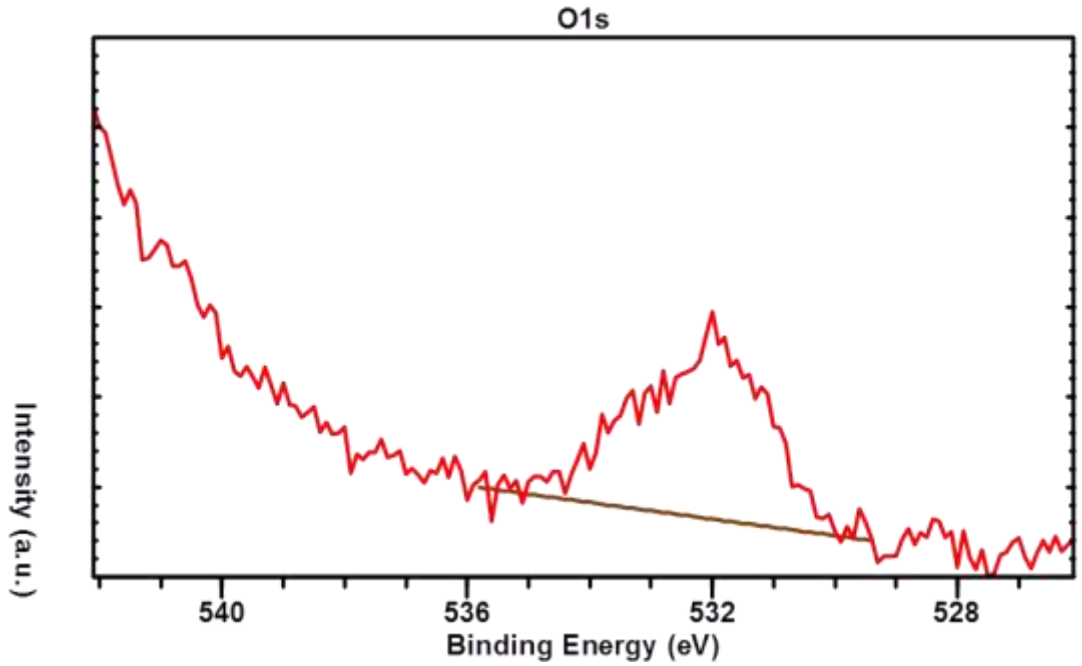
O1s
Intensity (a.u.)
540
536
532
528
Binding Energy (eV)

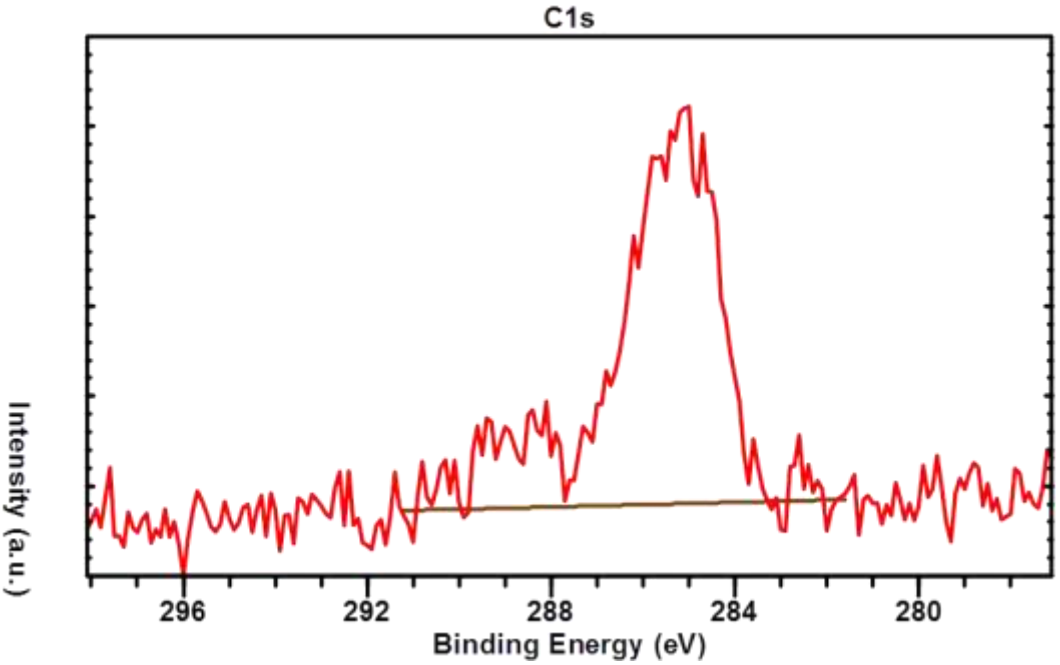
C1s
Intensity (a.u.)
296
292
288
284
280
Binding Energy (eV)

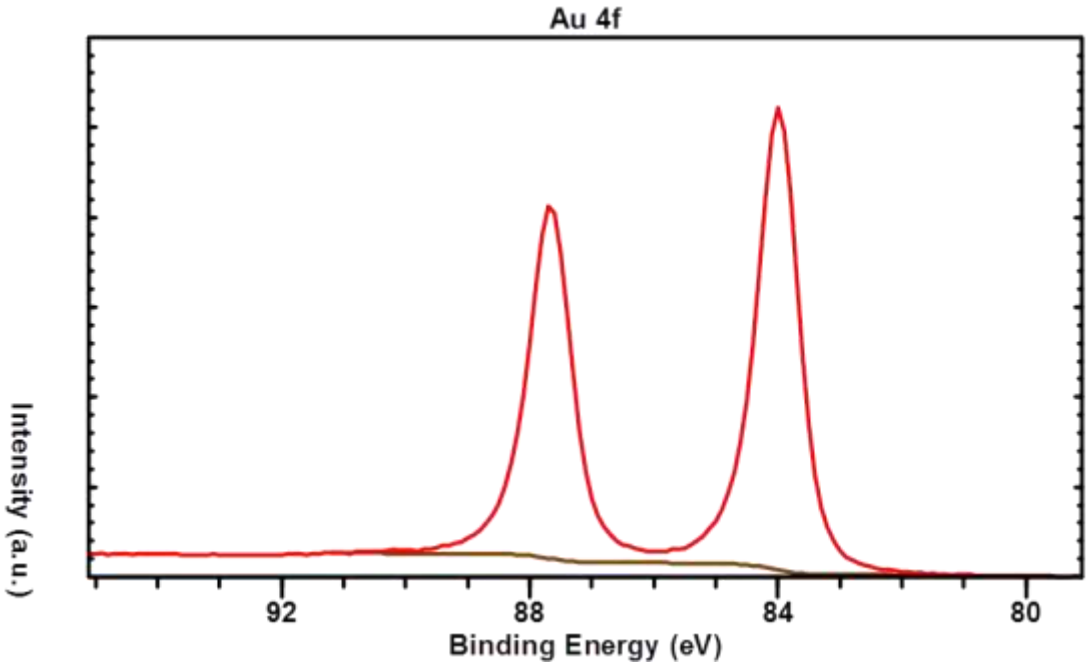
Au 4f
Intensity (a.u.)
92
88
84
80
Binding Energy (eV)

Figure 4.36 The survey and detail XPS spectra together with the subtracted background, as measured for SAM of 1-COOH-9-SH-1,7-$C_2B_{10}H_{10}$ (**M9-COOH**) modified with Ba(II).

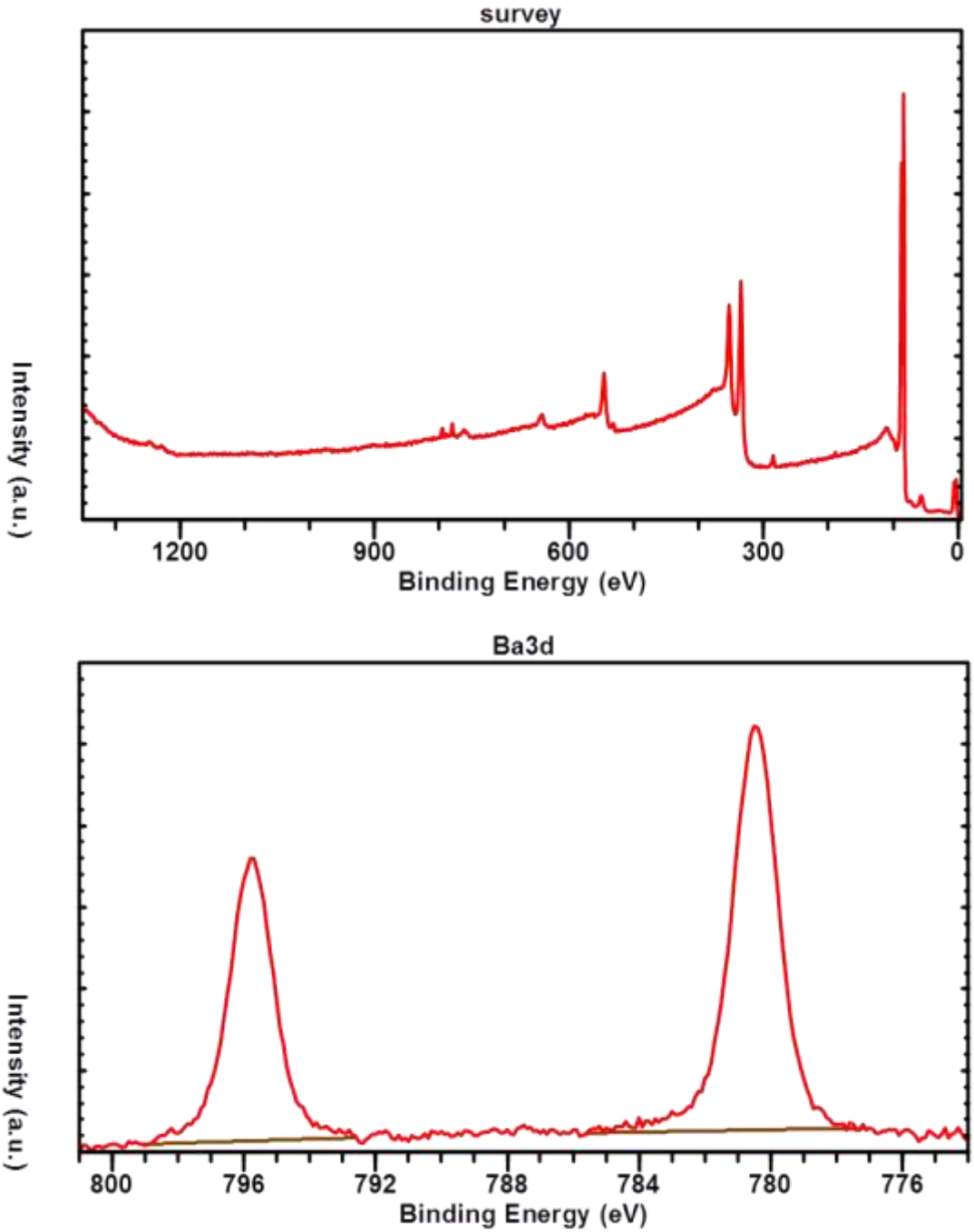

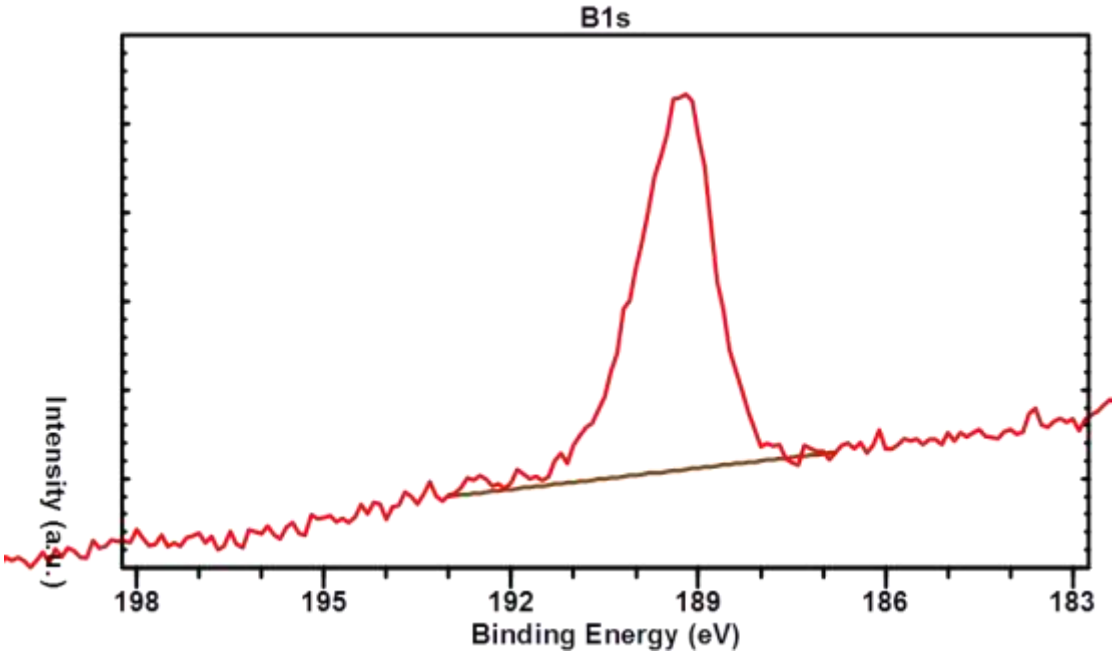
B1s
Intensity (a.u.)
198
195
192
189
186
183
Binding Energy (eV)

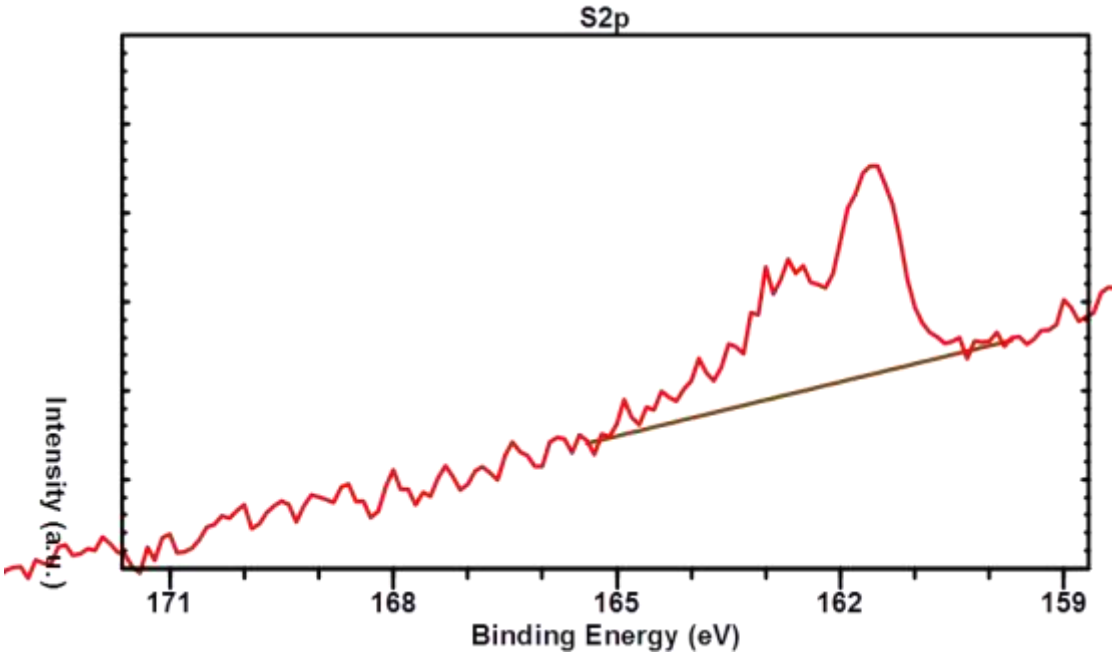
S2p
Intensity (a.u.)
171
168
165
162
159
Binding Energy (eV)

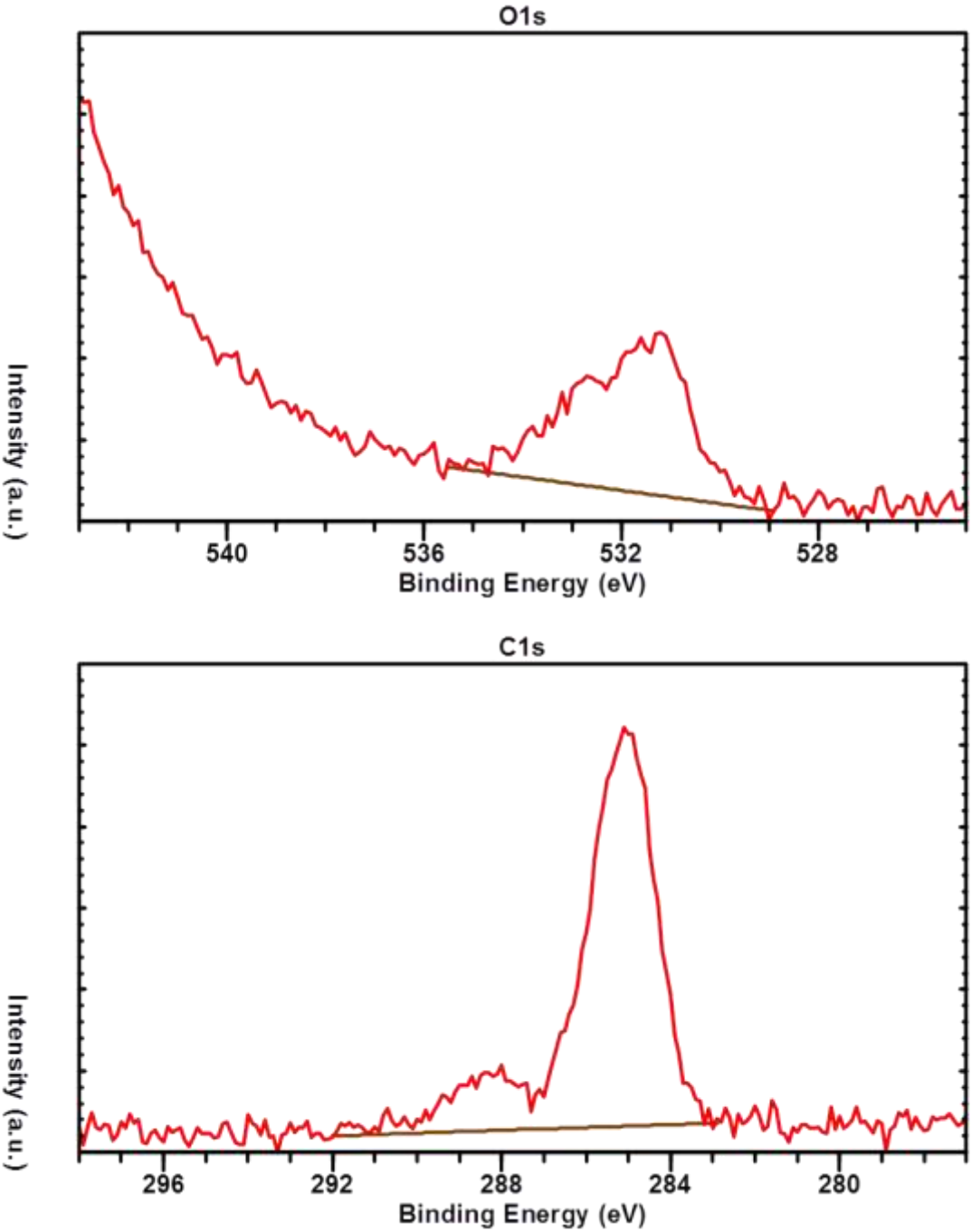
O1s
Intensity (a.u.)
540
536
532
528
Binding Energy (eV)
C1s
Intensity (a.u.)
296
292
288
284
280
Binding Energy (eV)

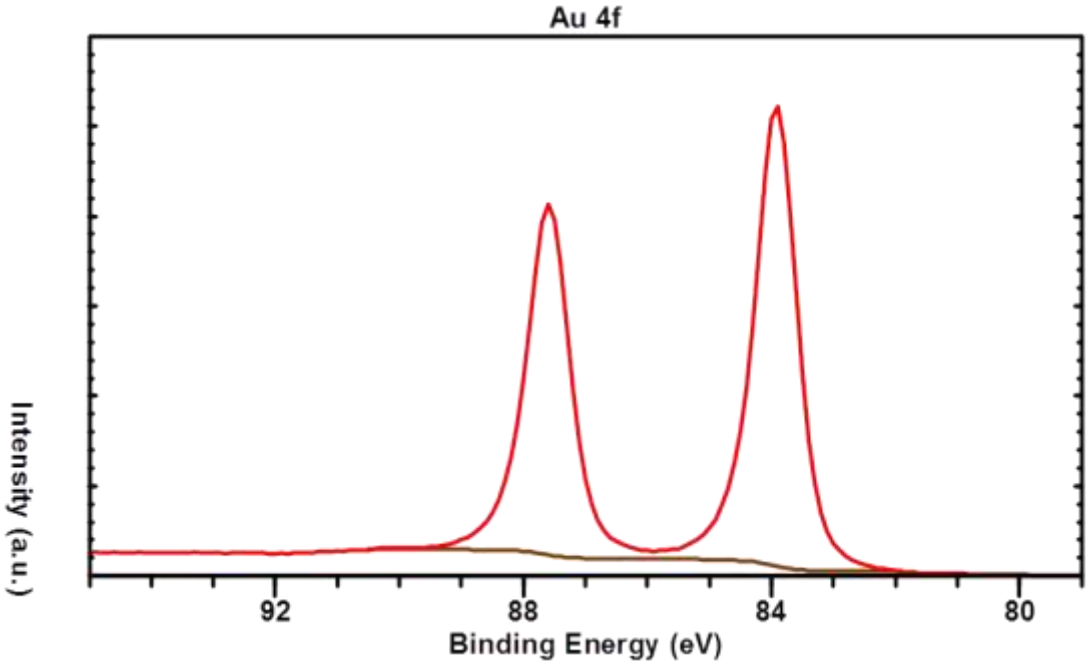
Au 4f
Intensity (a.u.)
92
88
84
80
Binding Energy (eV)

Figure 4.37 The survey and detail XPS spectra together with the subtracted background, as measured for a pristine SAM of 1-COOH-9-SH-1,7-$C_2B_{10}H_{10}$ (**M9-COOH**)

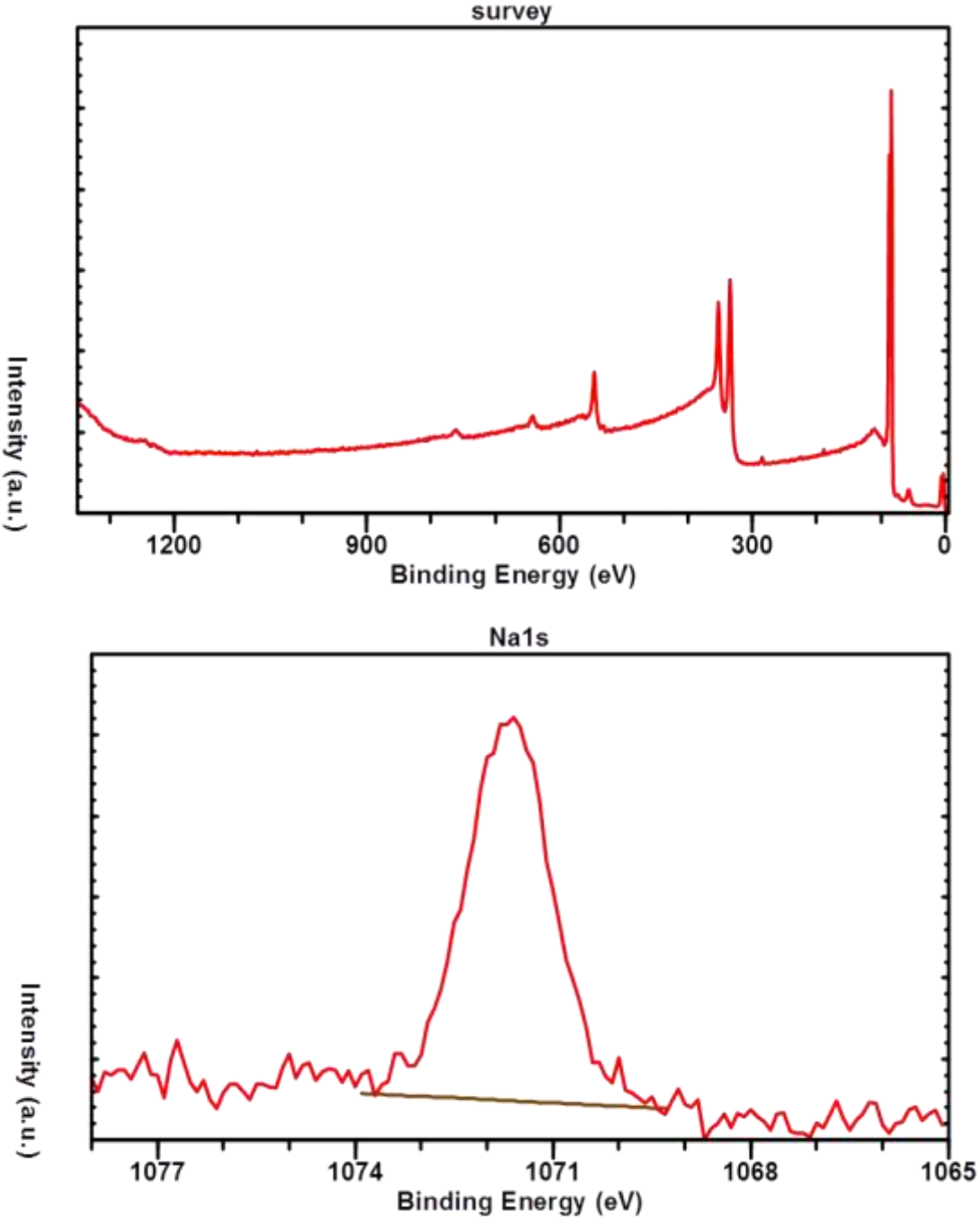

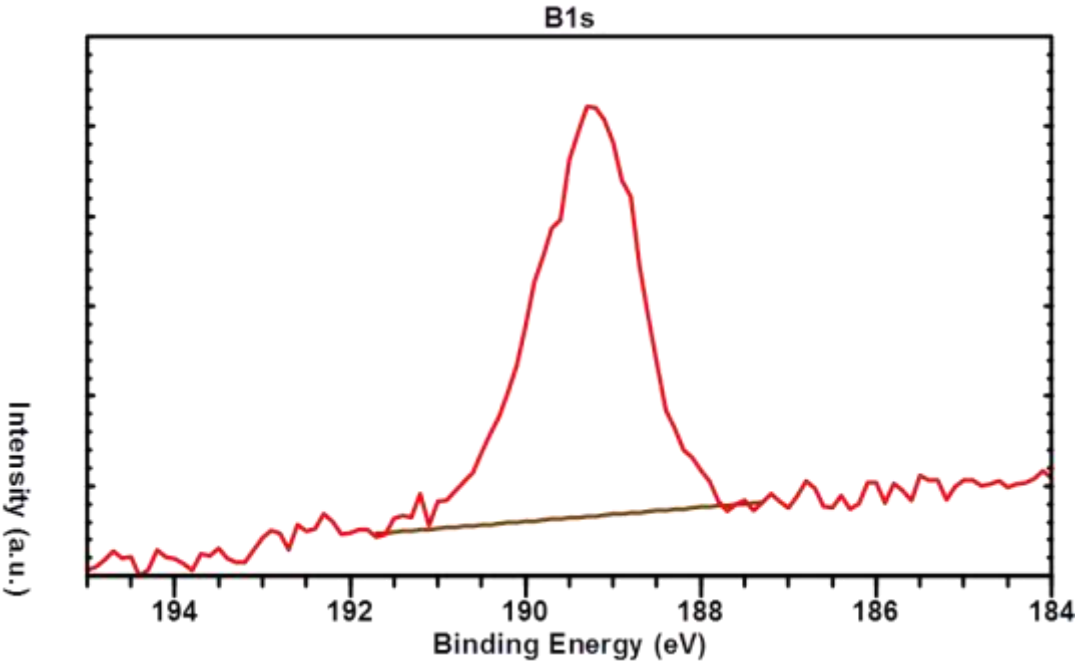
B1s
Intensity (a.u.)
194
192
190
188
186
184
Binding Energy (eV)

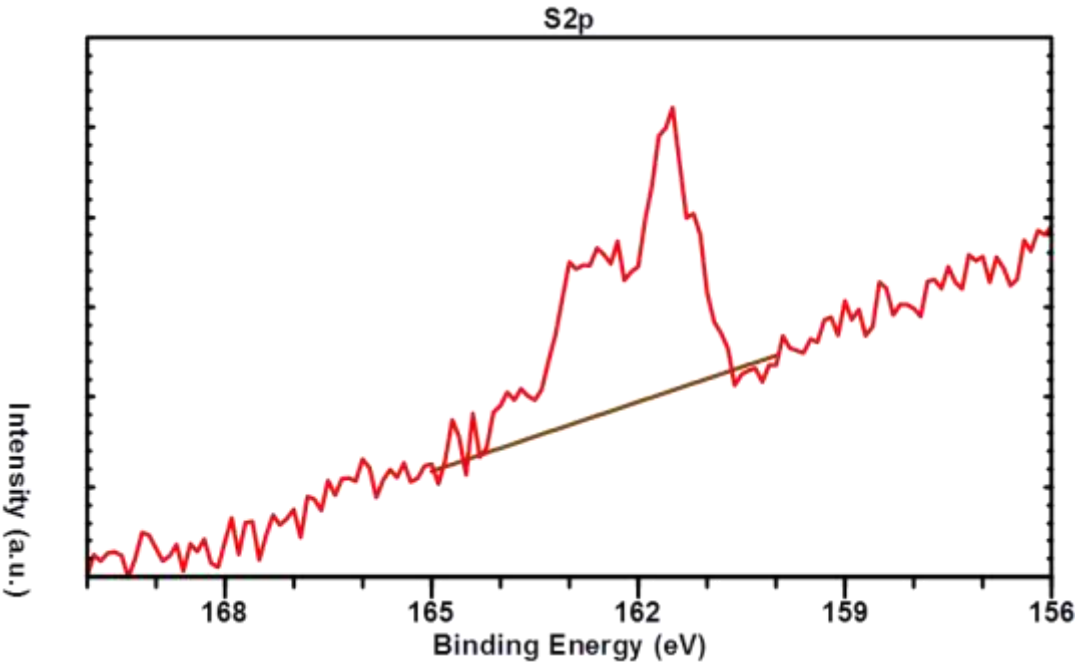
S2p
Intensity (a.u.)
168
165
162
159
156
Binding Energy (eV)

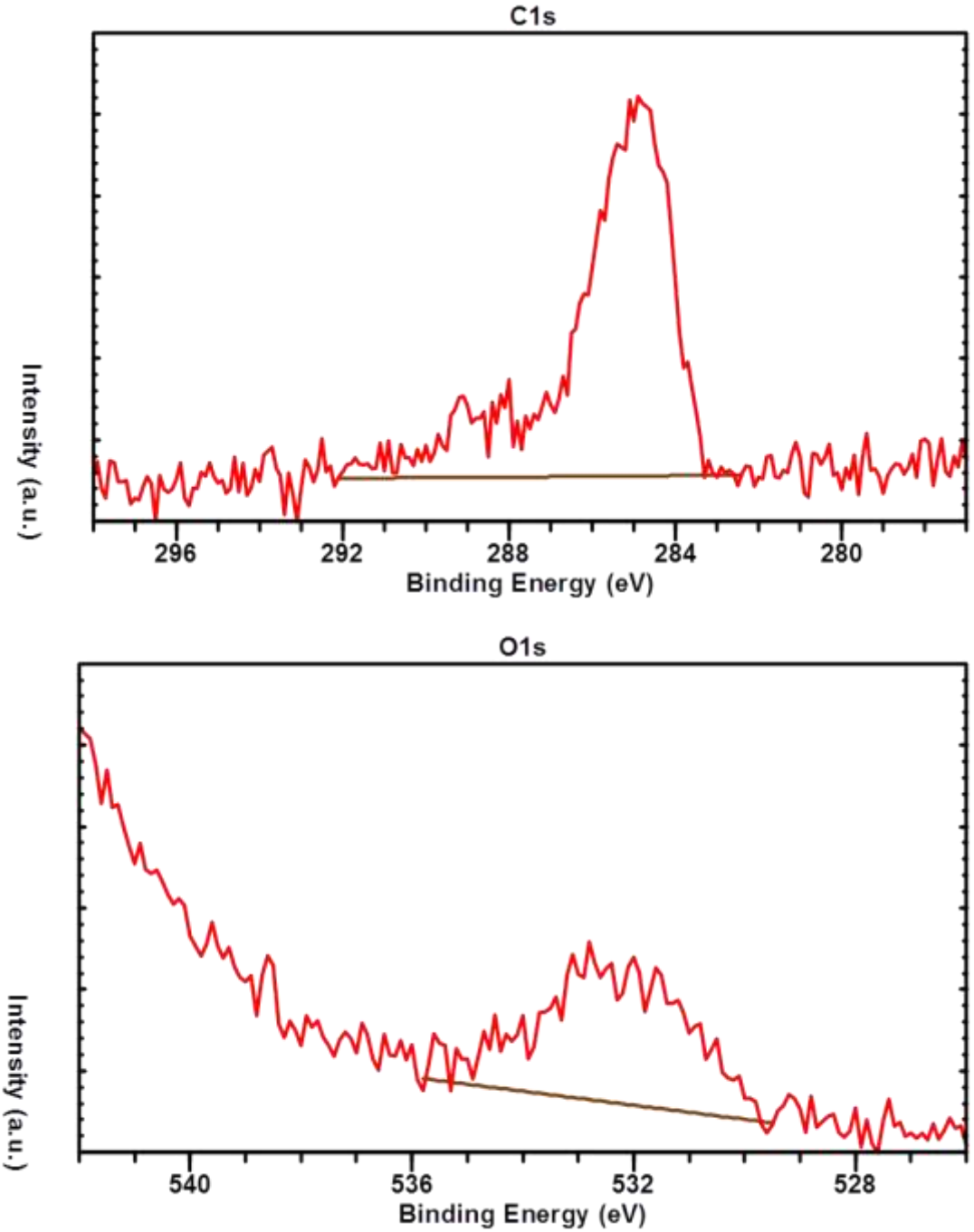
C1s
Intensity (a.u.)
296
292
288
284
280
Binding Energy (eV)
O1s
Intensity (a.u.)
540
536
532
528
Binding Energy (eV)

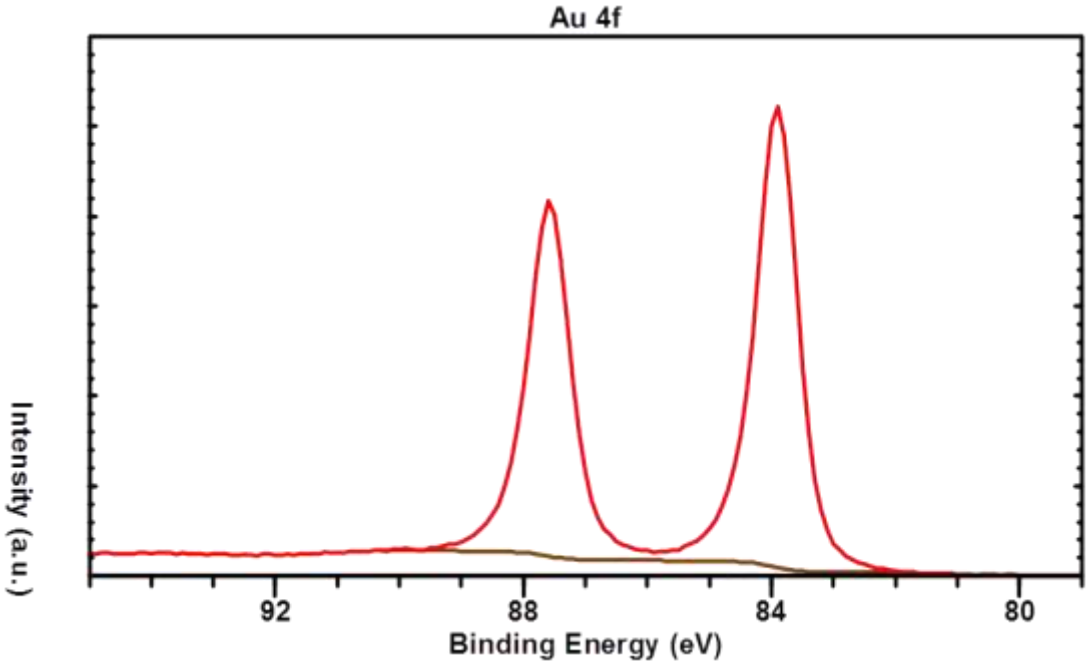

Figure 4.38 The survey and detail XPS spectra together with the subtracted background, as measured for SAMs of 1-COOH-9-SH-1,7-$C_2B_{10}H_{10}$ (**M9-COOH**) modified with H_3O^+.

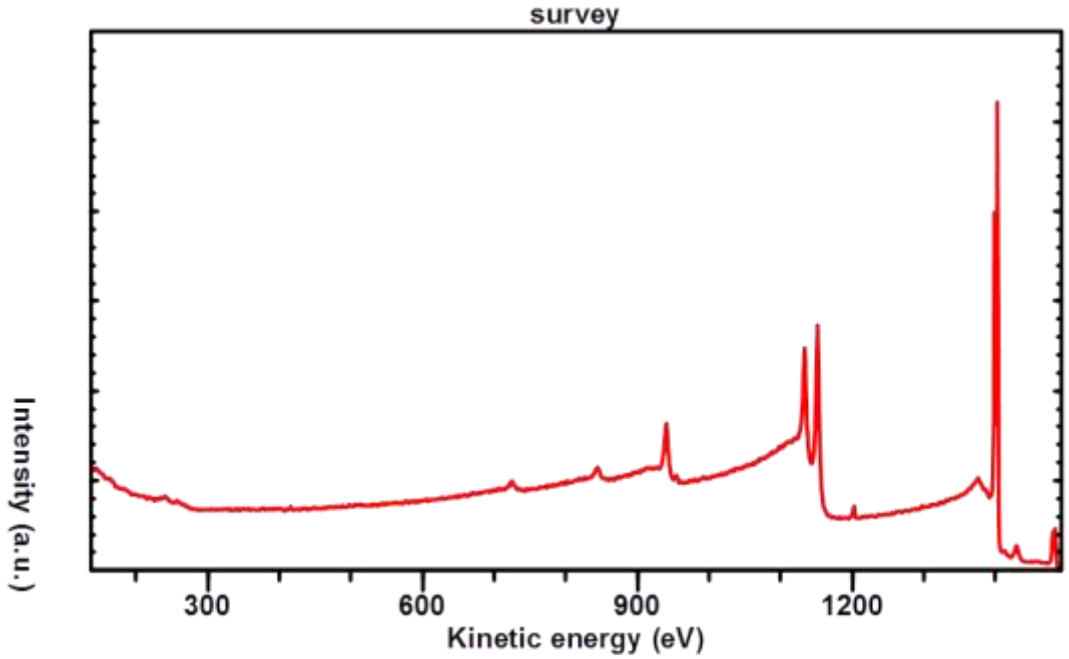

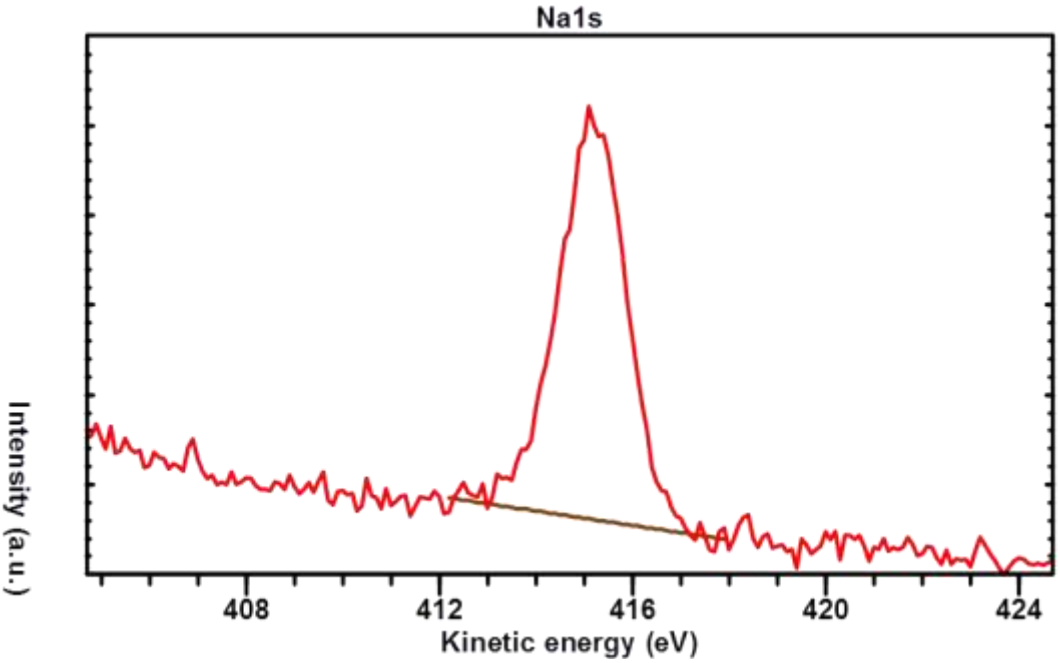
Na1s
Intensity (a.u.)
408
412
416
420
424
Kinetic energy (eV)

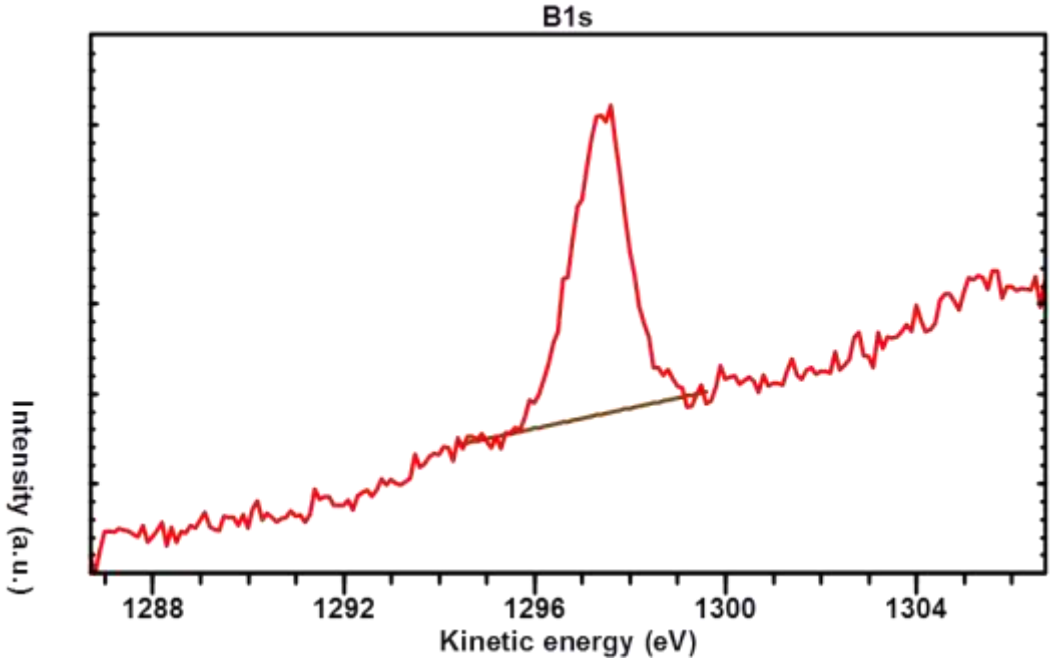
B1s
Intensity (a.u.)
1288
1292
1296
1300
1304
Kinetic energy (eV)

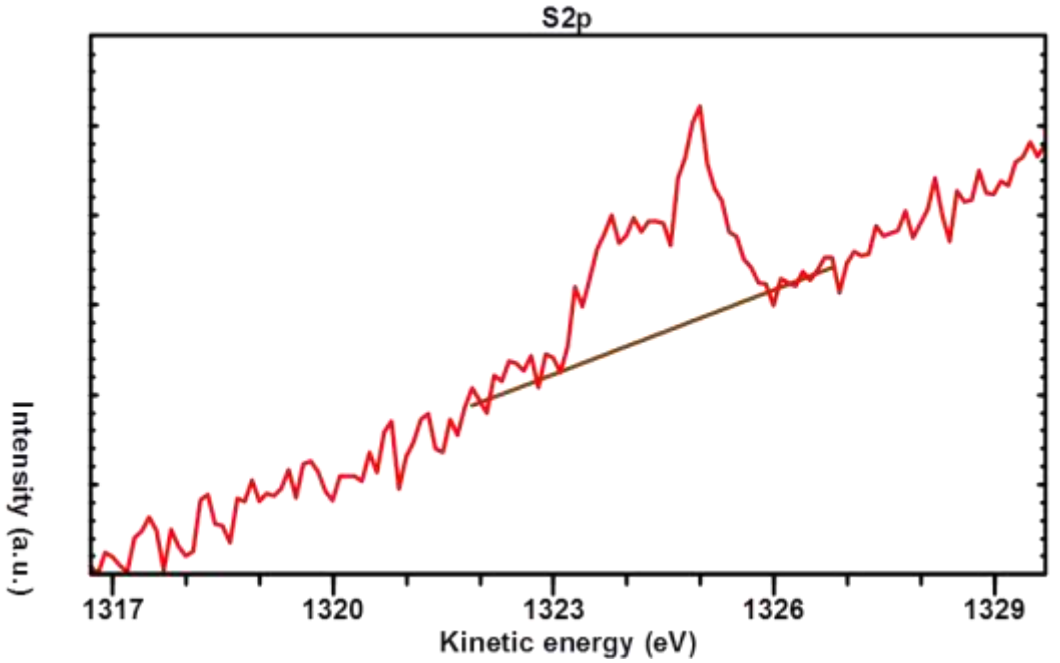
S2p
Intensity (a.u.)
1317
1320
1323
1326
1329
Kinetic energy (eV)

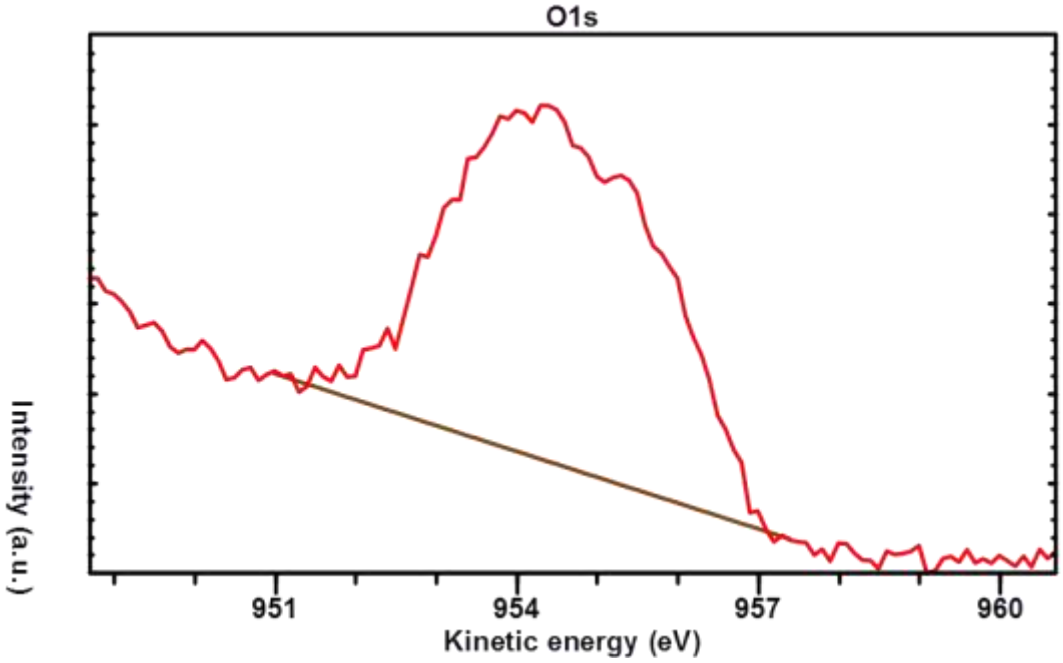
O1s
Intensity (a.u.)
951
954
957
960
Kinetic energy (eV)

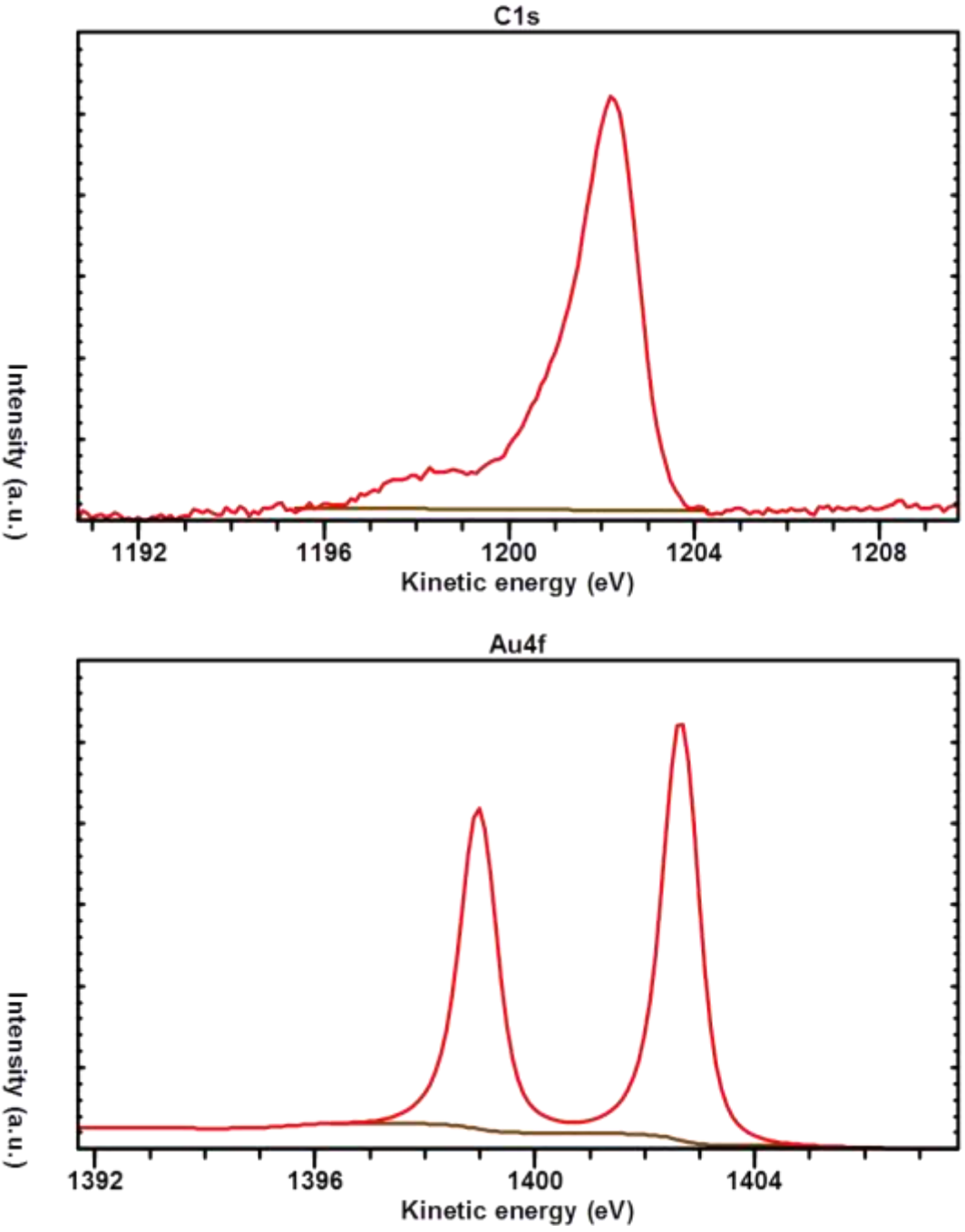
C1s
Intensity (a.u.)
1192
1196
1200
1204
1208
Kinetic energy (eV)
Au4f
Intensity (a.u.)
1392
1396
1400
1404
Kinetic energy (eV)

Figure 4.39 The survey and detail XPS spectra together with the subtracted background, as measured for a pristine SAM of 9-SH-1,7-$C_2B_{10}H_{11}$ (**M9**).

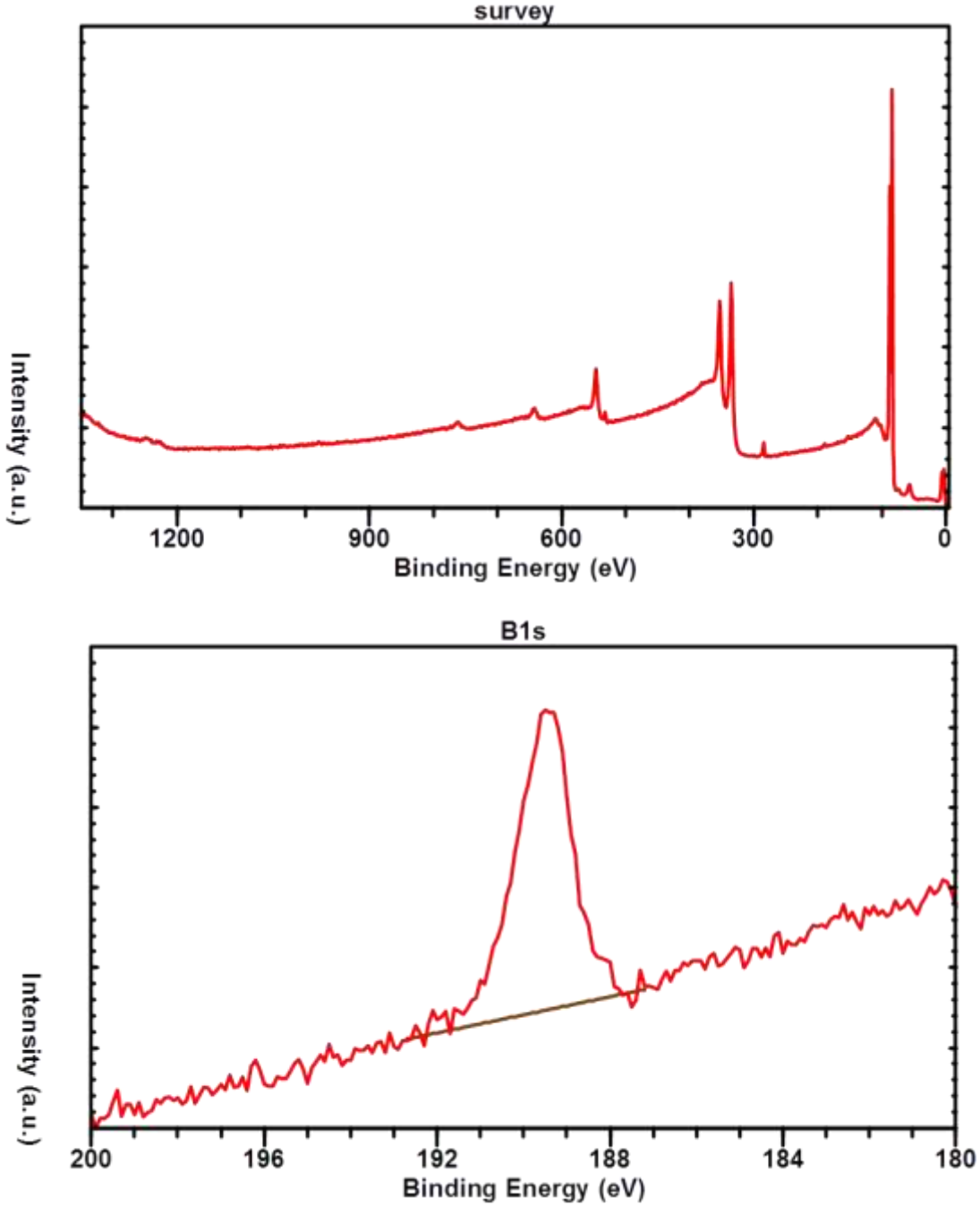

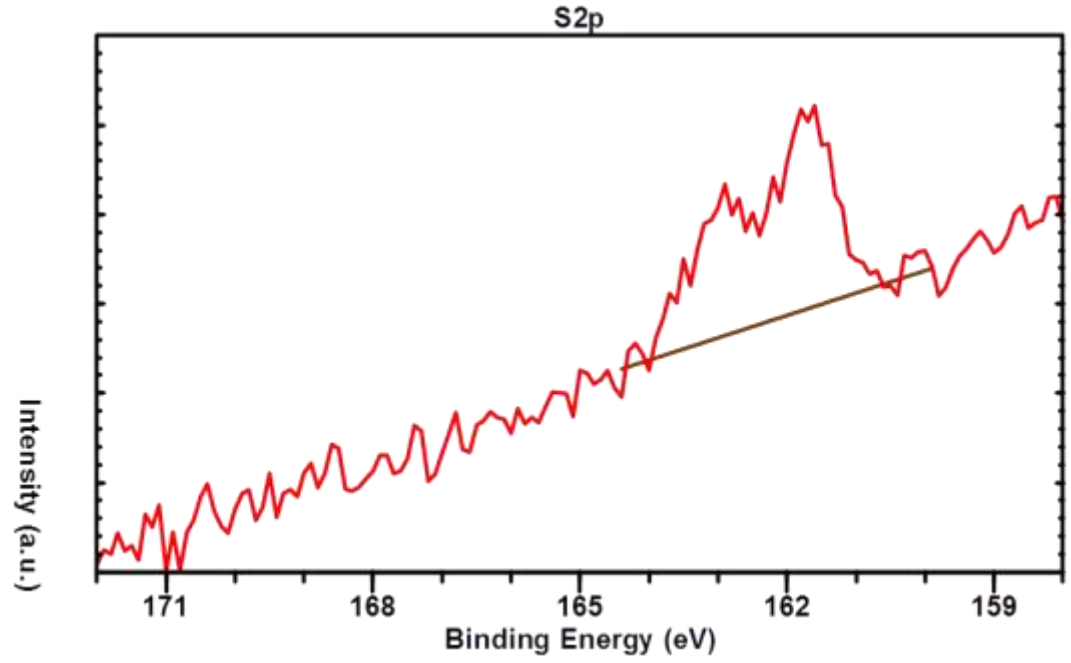
S2p
Intensity (a.u.)
171
168
165
162
159
Binding Energy (eV)

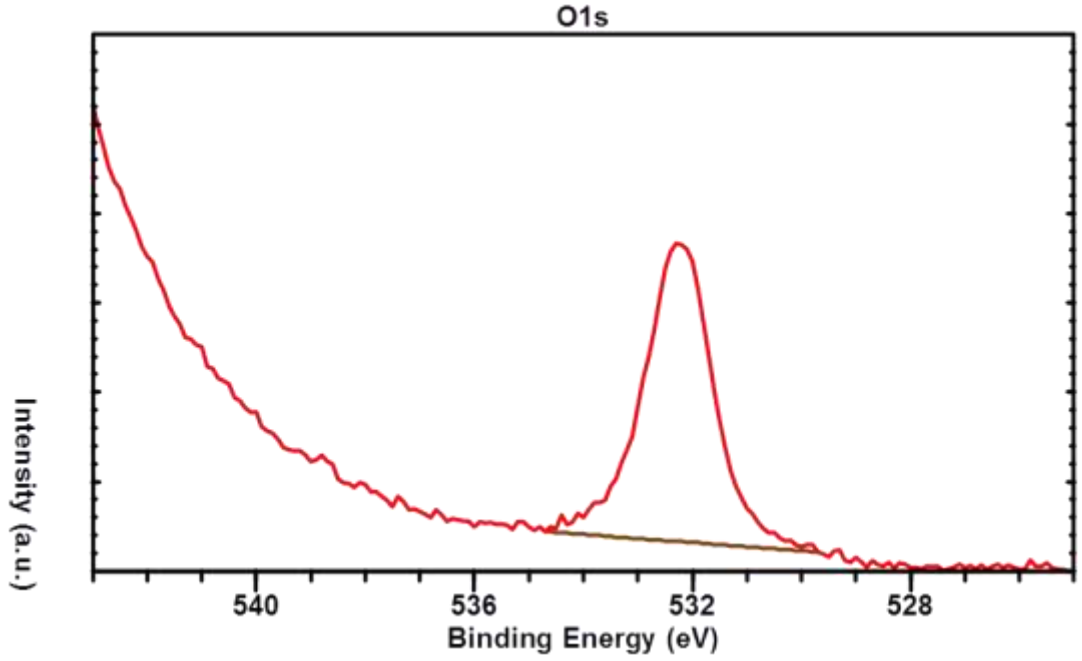
O1s
Intensity (a.u.)
540
536
532
528
Binding Energy (eV)

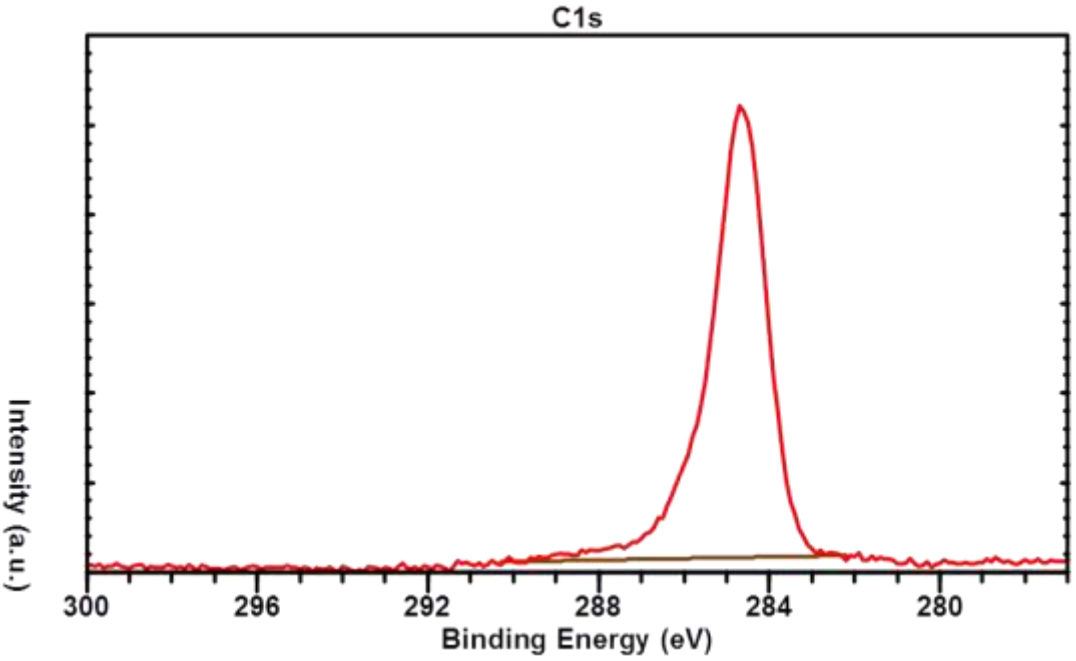
C1s
Intensity (a.u.)
300
296
292
288
284
280
Binding Energy (eV)

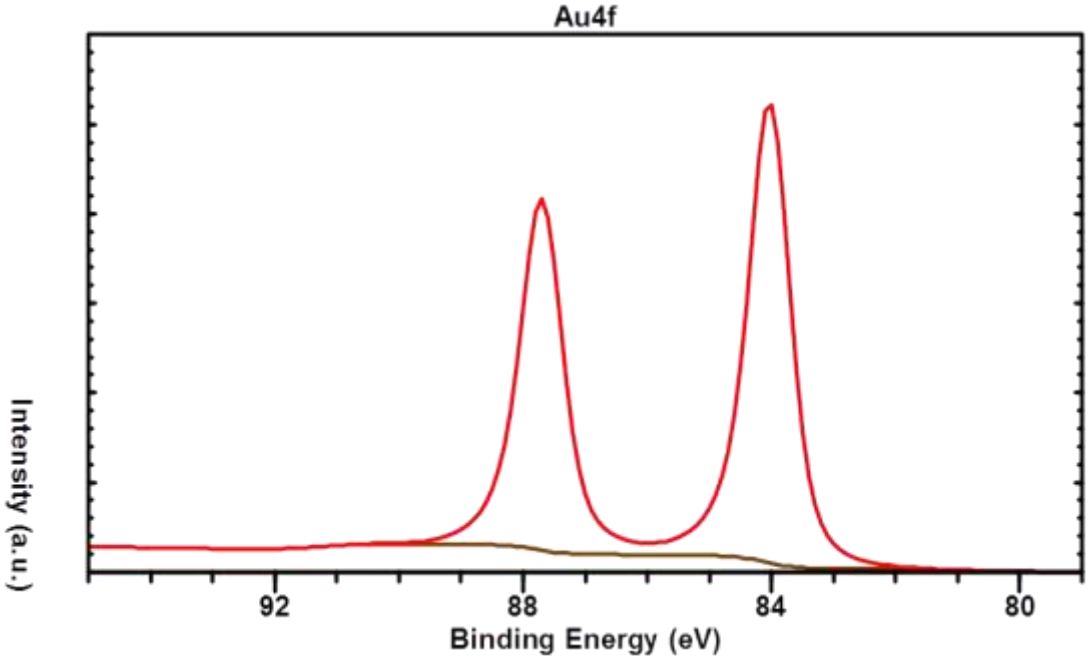
Au4f
Intensity (a.u.)
92
88
84
80
Binding Energy (eV)

Figure 4.40 The survey and detail XPS spectra together with the subtracted background, as measured for SAM of 9-SH-1,7-$C_2B_{10}H_{11}$ (**M9**) modified with H_3O^+.

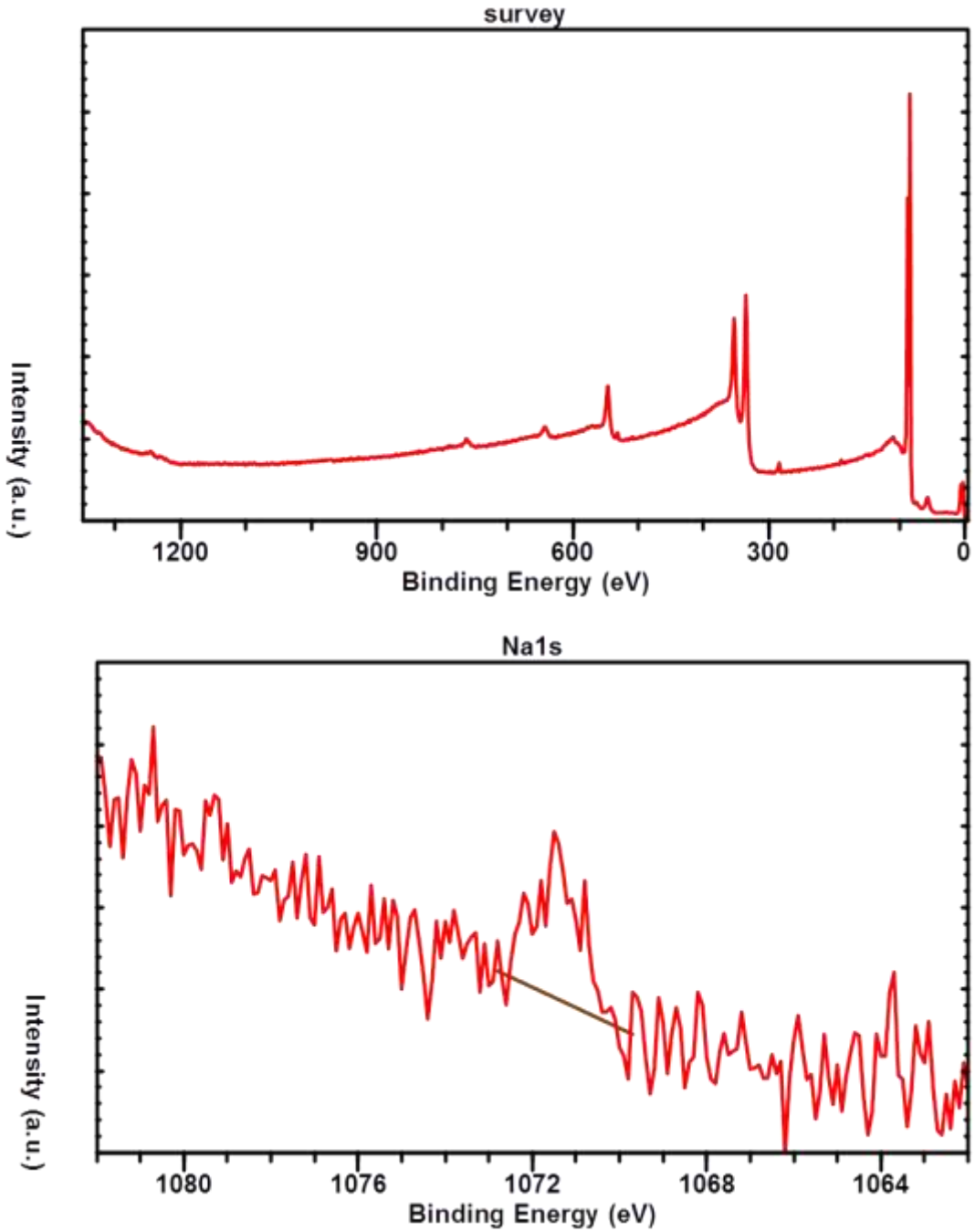

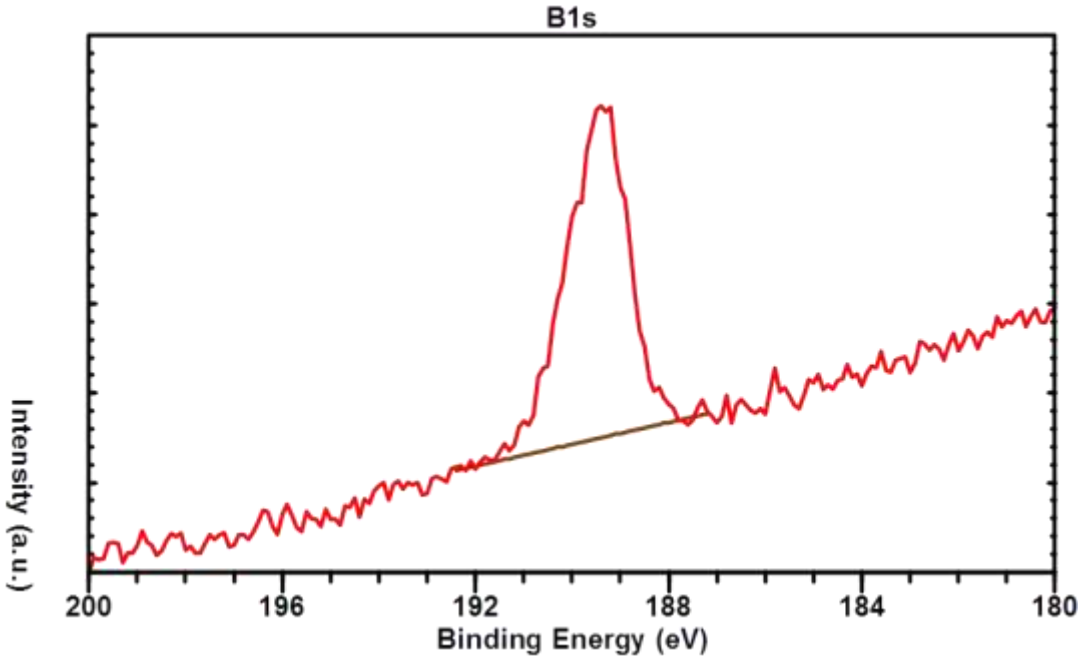
B1s
Intensity (a.u.)
200
196
192
188
184
180
Binding Energy (eV)

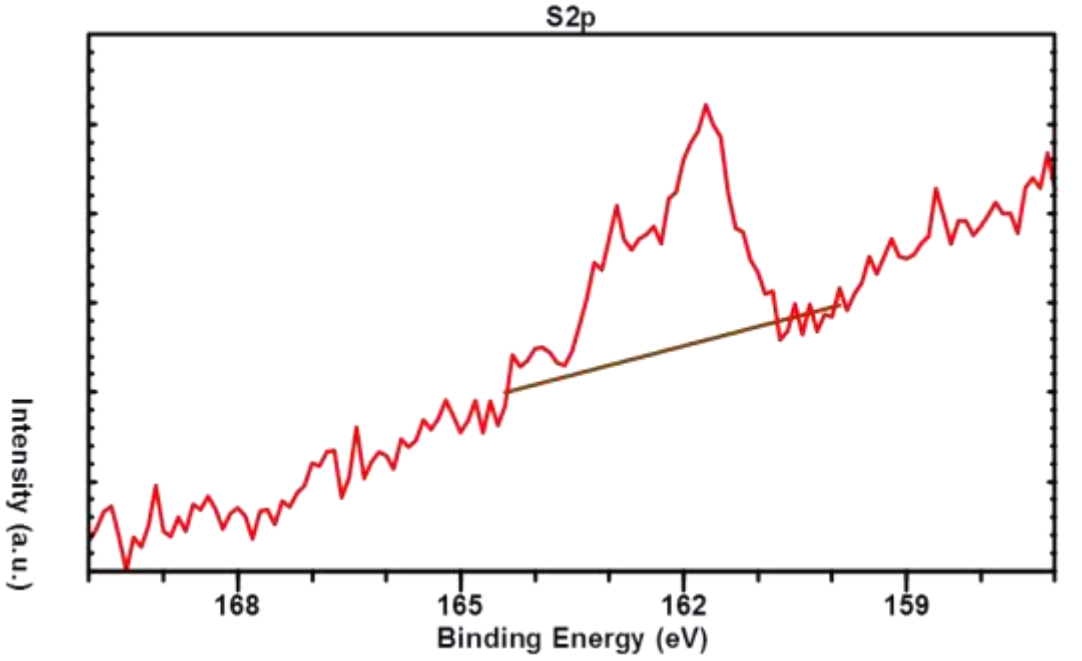
S2p
Intensity (a.u.)
168
165
162
159
Binding Energy (eV)

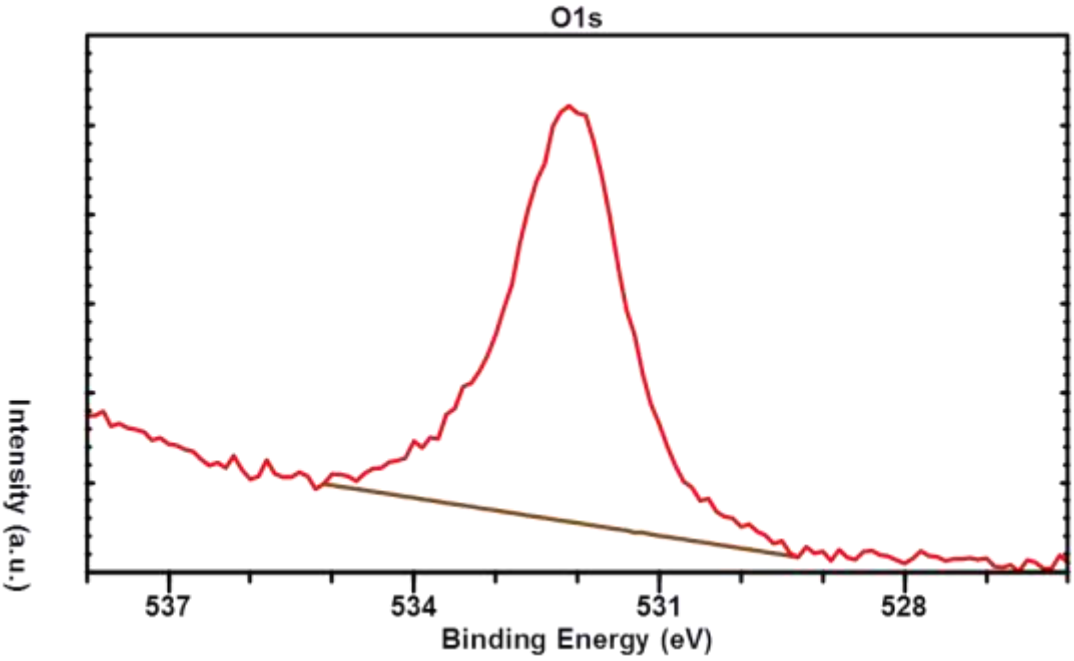
O1s
Intensity (a.u.)
537
534
531
528
Binding Energy (eV)

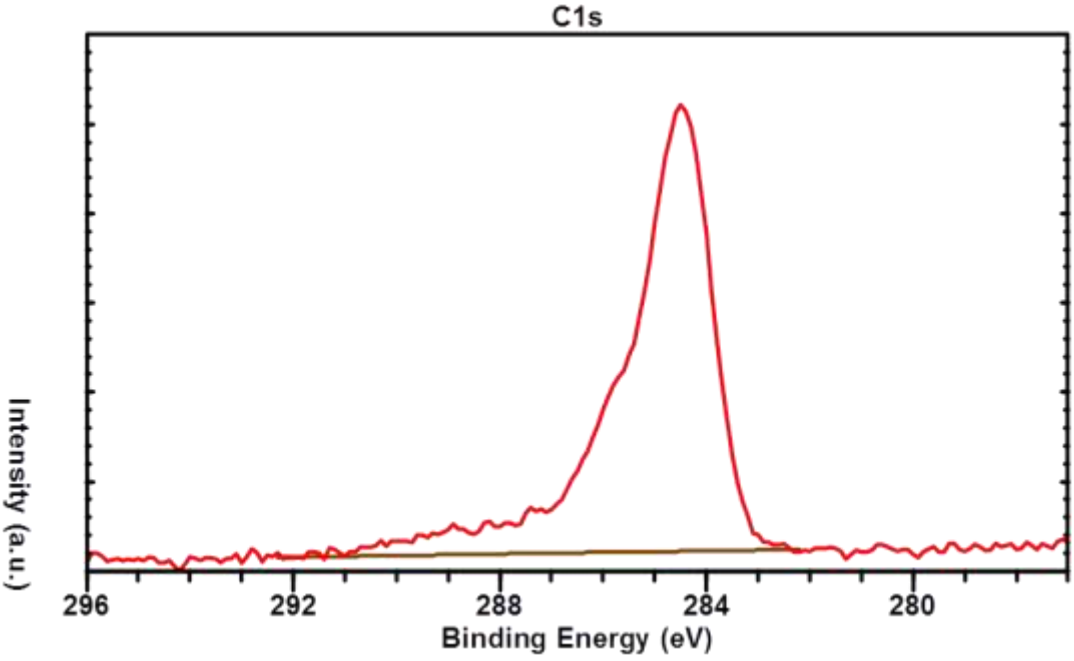
C1s
Intensity (a.u.)
296
292
288
284
280
Binding Energy (eV)

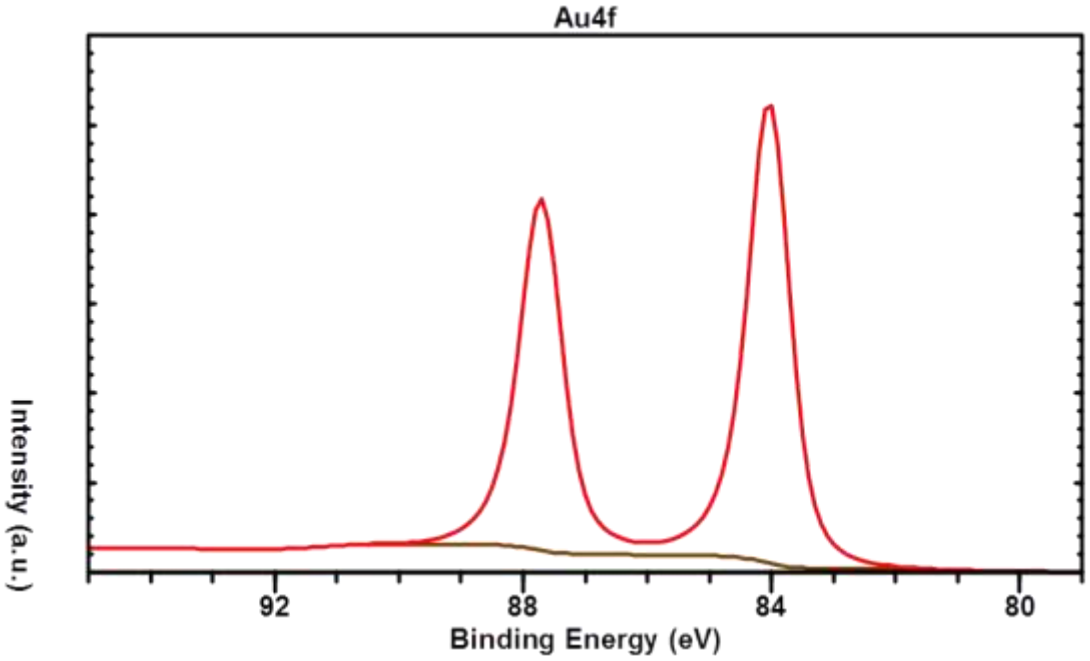
Au4f
Intensity (a.u.)
92
88
84
80
Binding Energy (eV)

Figure 4.41 The survey and detail XPS spectra together with the subtracted background, as measured for SAM of 1-COOH-12-SH-1,12-$C_2B_{10}H_{10}$ (**P1-COOH**) modified with H_3O^+.

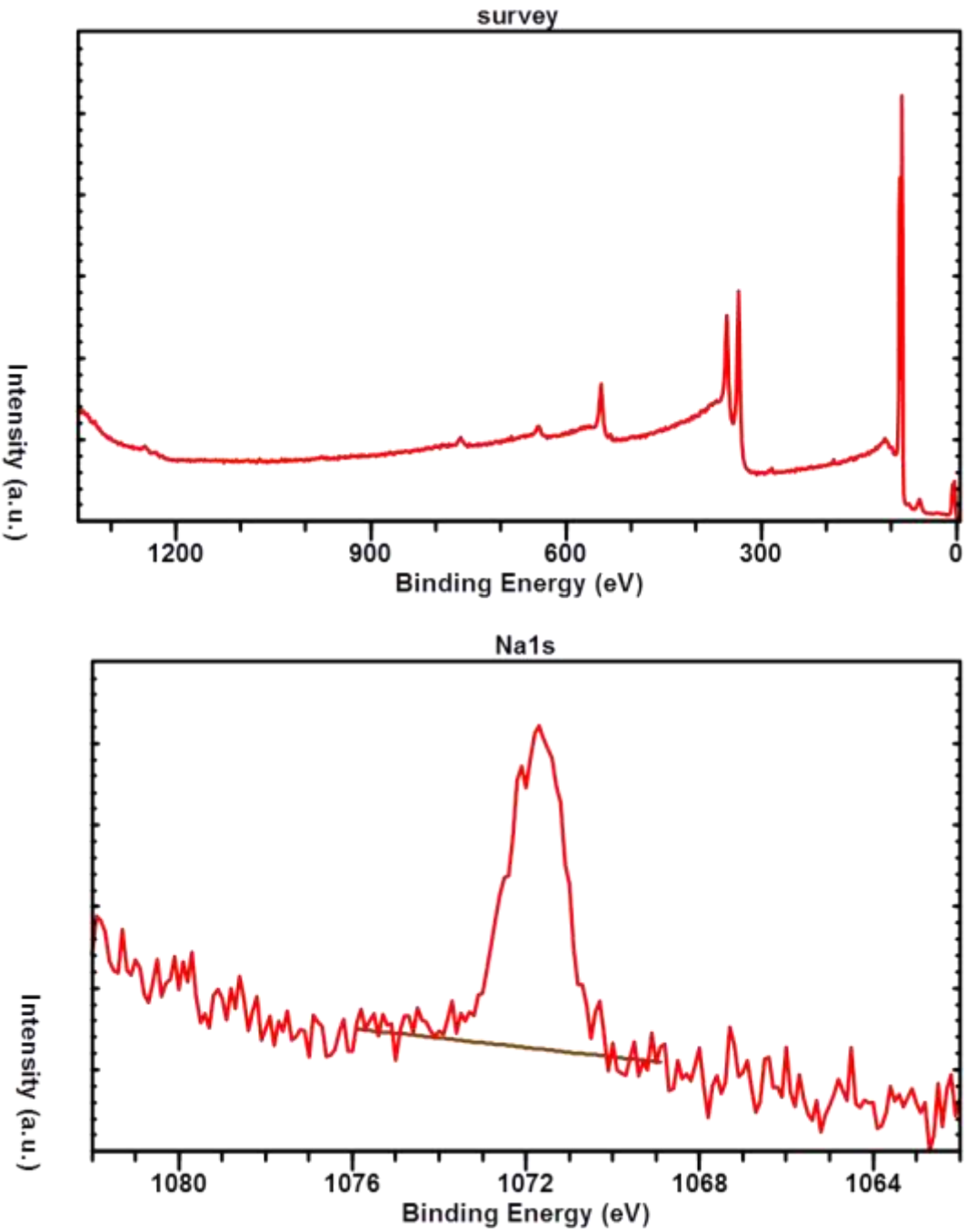

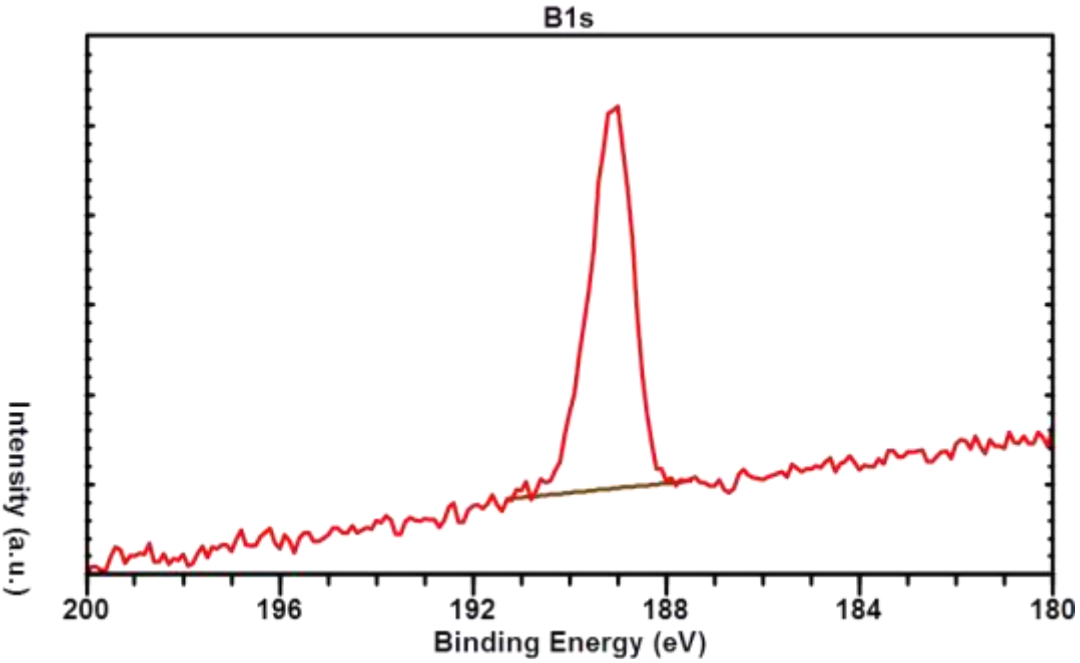
B1s
Intensity (a.u.)
200
196
192
188
184
180
Binding Energy (eV)

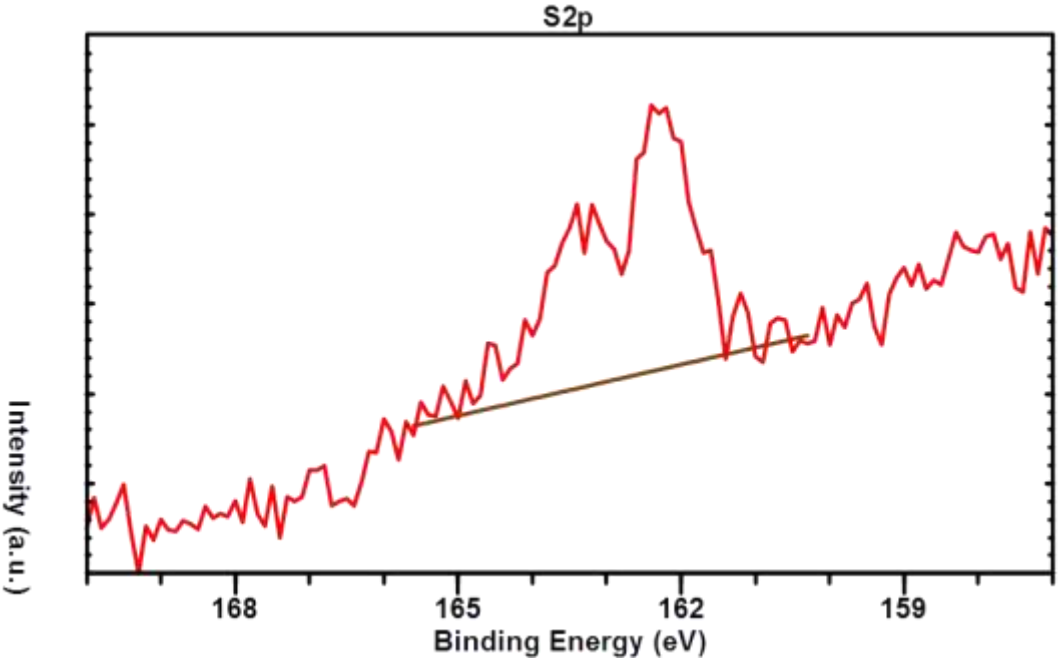
S2p
Intensity (a.u.)
168
165
162
159
Binding Energy (eV)

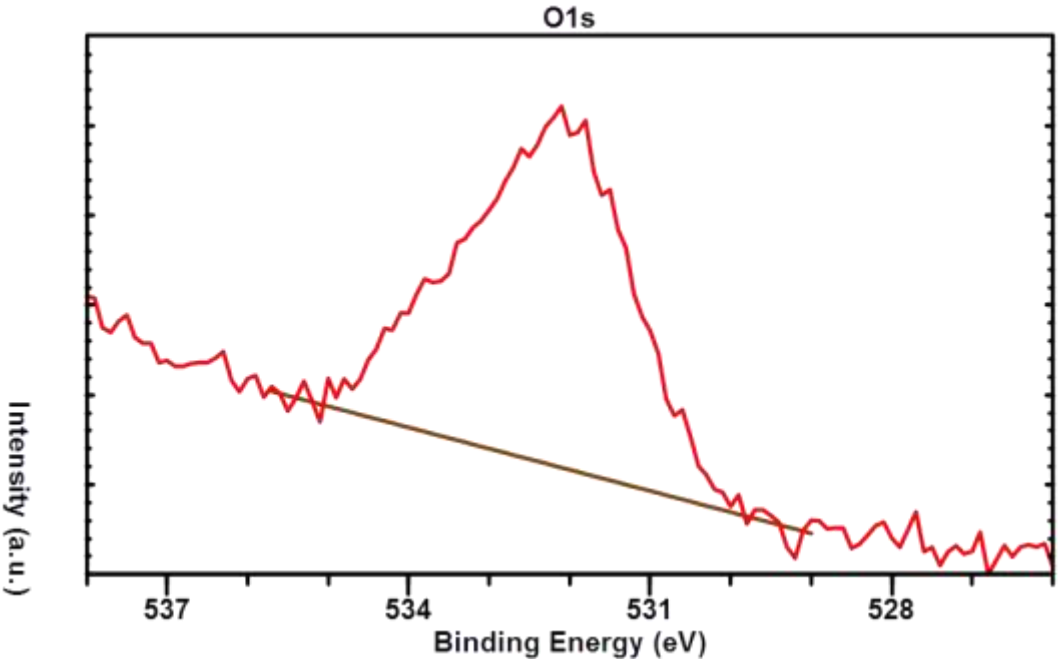
O1s
Intensity (a.u.)
537
534
531
528
Binding Energy (eV)

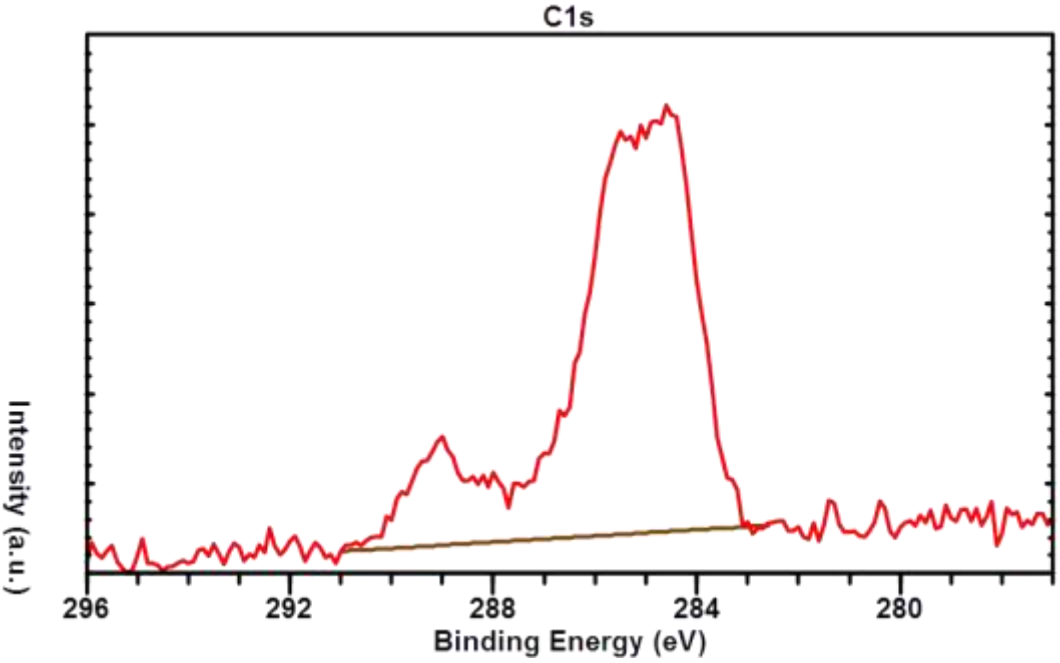
C1s
Intensity (a.u.)
296
292
288
284
280
Binding Energy (eV)

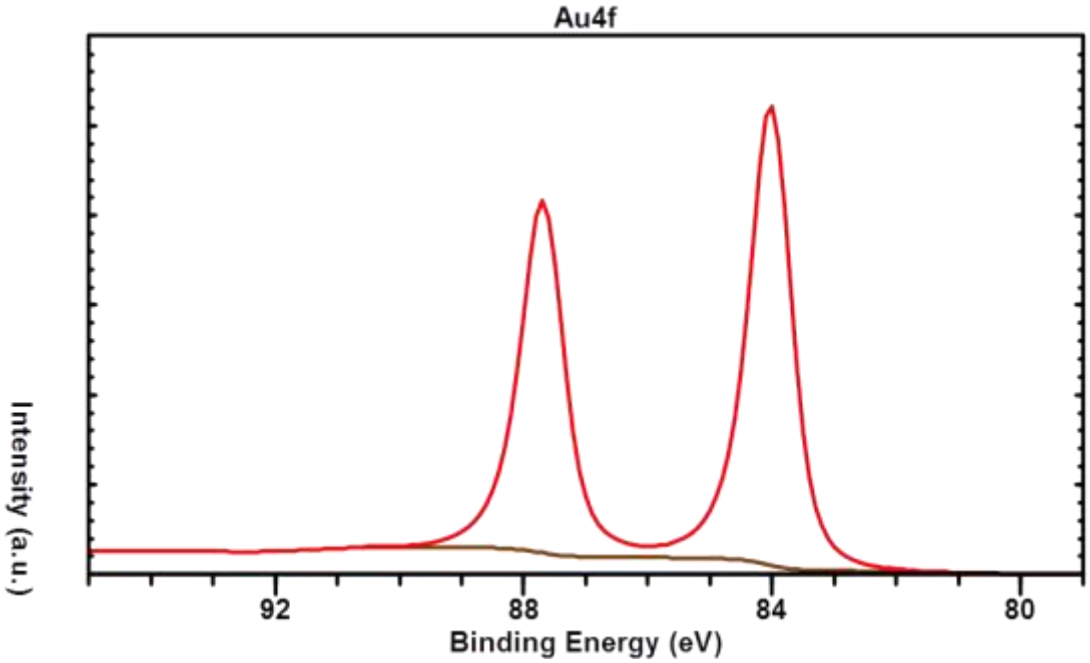
Au4f
Intensity (a.u.)
92
88
84
80
Binding Energy (eV)

Figure 4.42 The survey and detail XPS spectra together with the subtracted background, as measured for SAM of 1-COOH-12-SH-1,12-$C_2B_{10}H_{10}$ (**P1-COOH**) modified with H_3O^+.

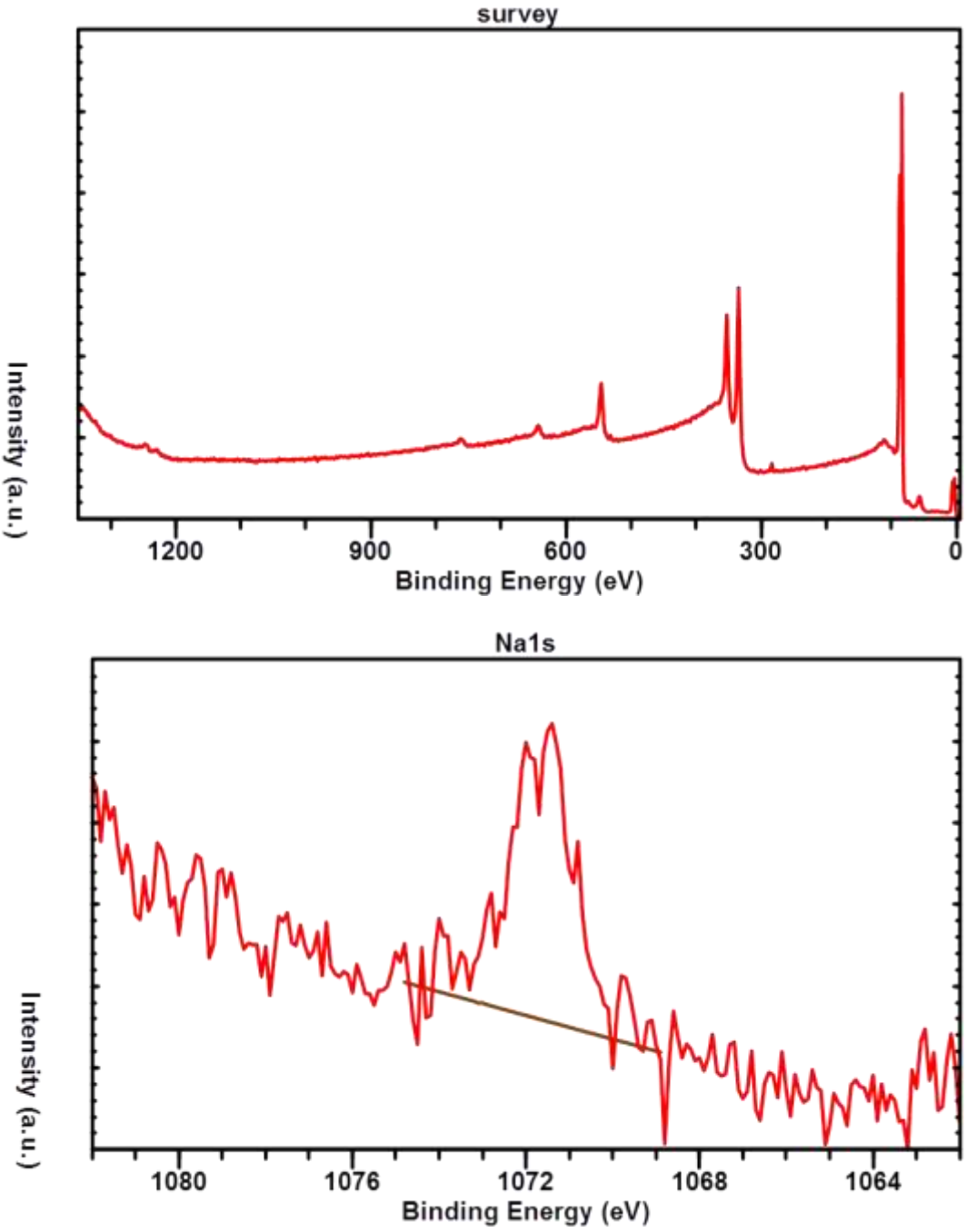

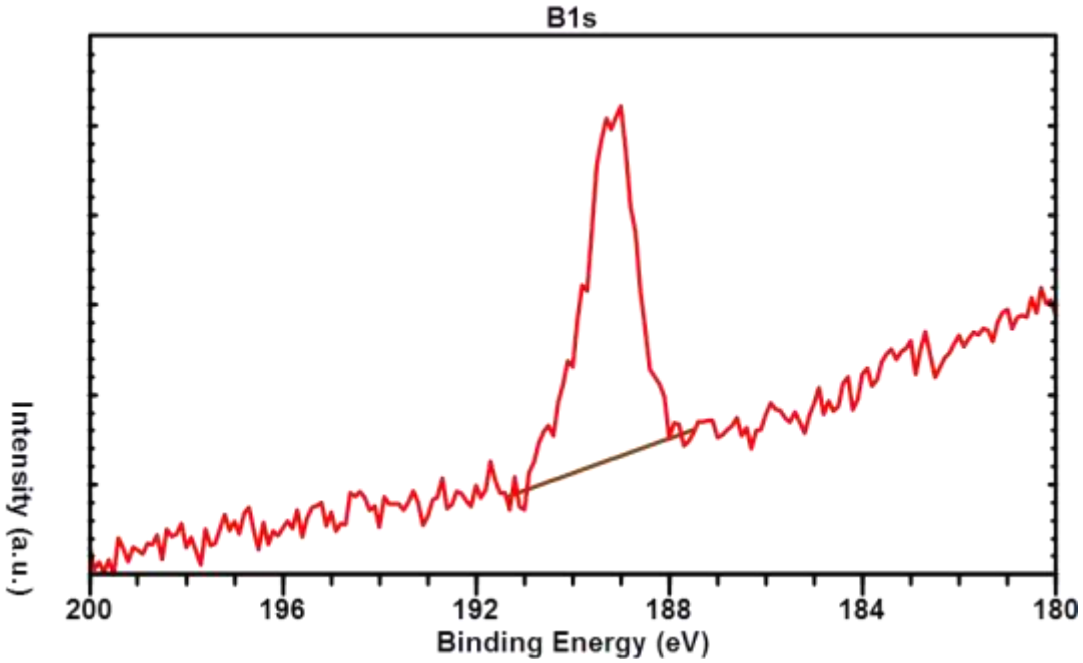
B1s
Intensity (a.u.)
200
196
192
188
184
180
Binding Energy (eV)

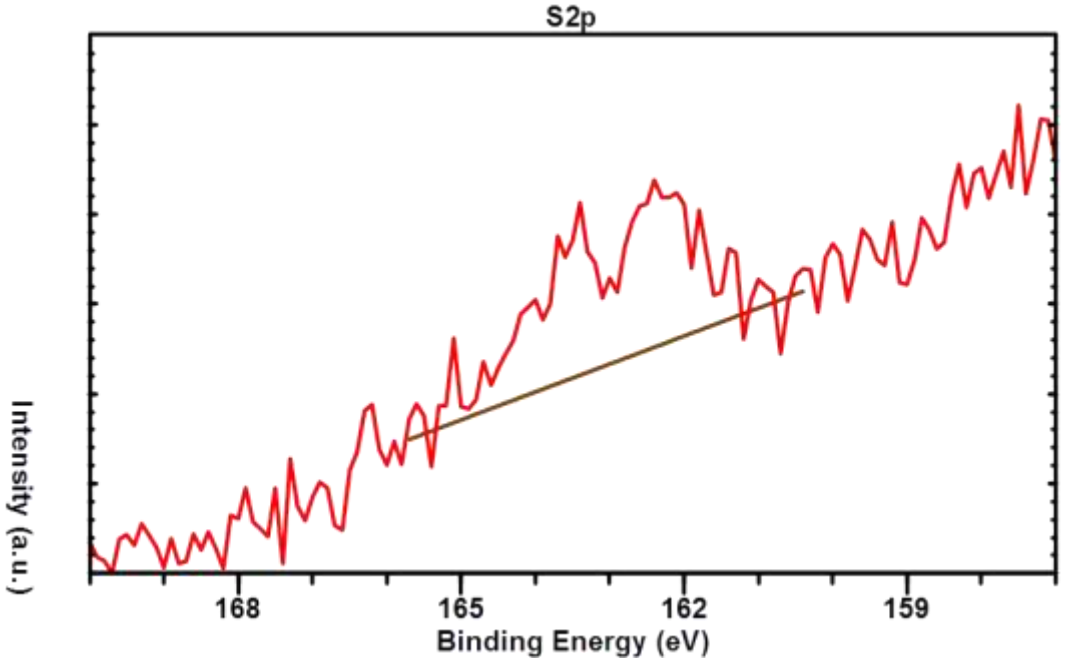
S2p
Intensity (a.u.)
168
165
162
159
Binding Energy (eV)

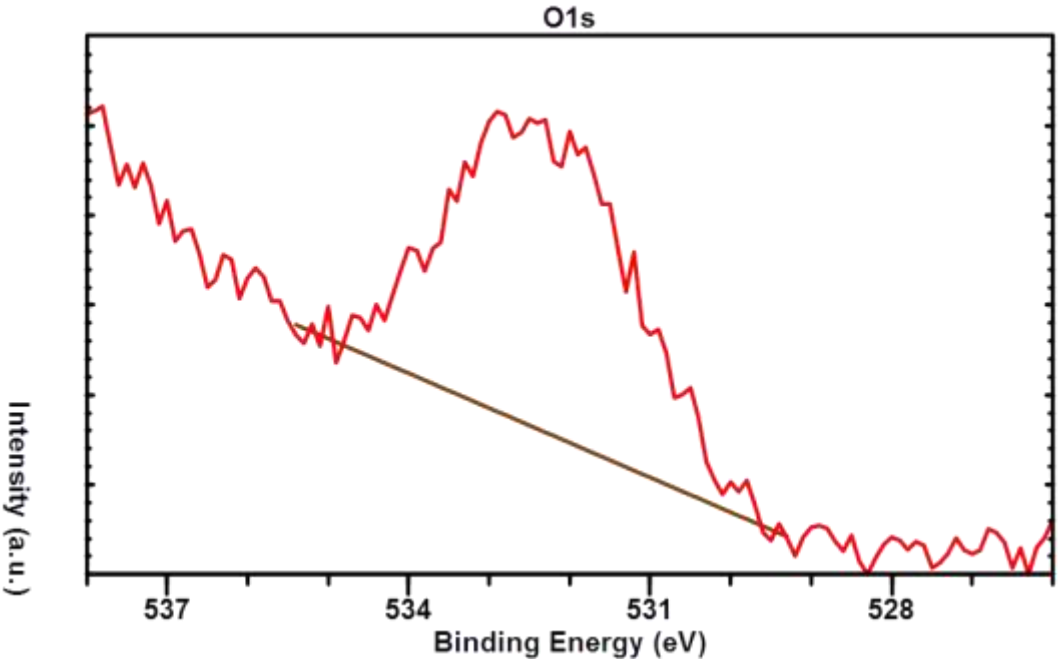
O1s
Intensity (a.u.)
537
534
531
528
Binding Energy (eV)

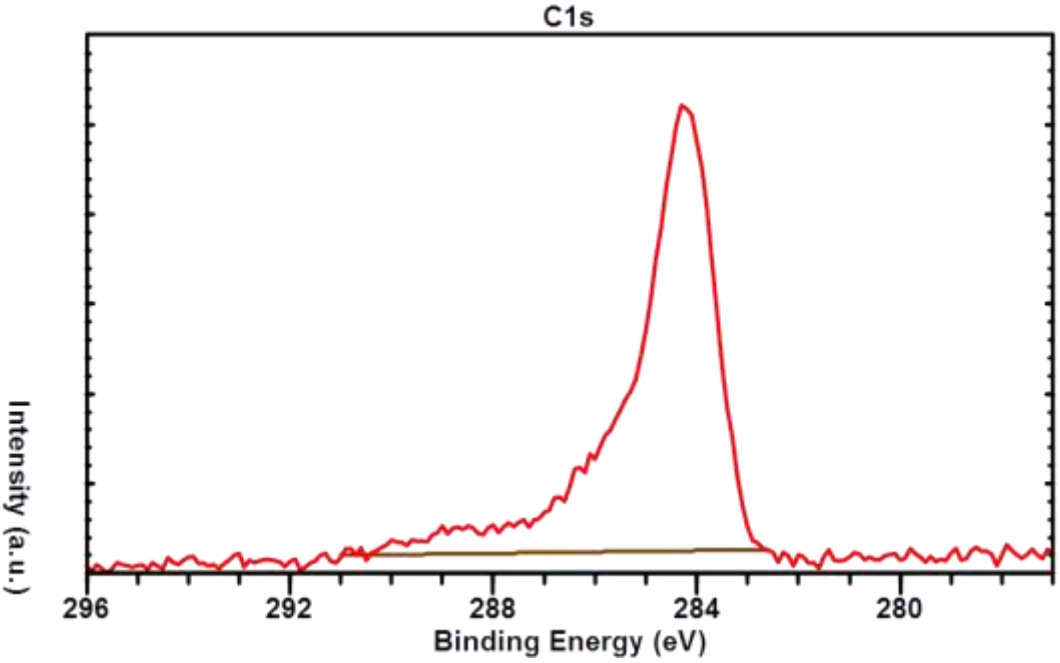
C1s
Intensity (a.u.)
296
292
288
284
280
Binding Energy (eV)

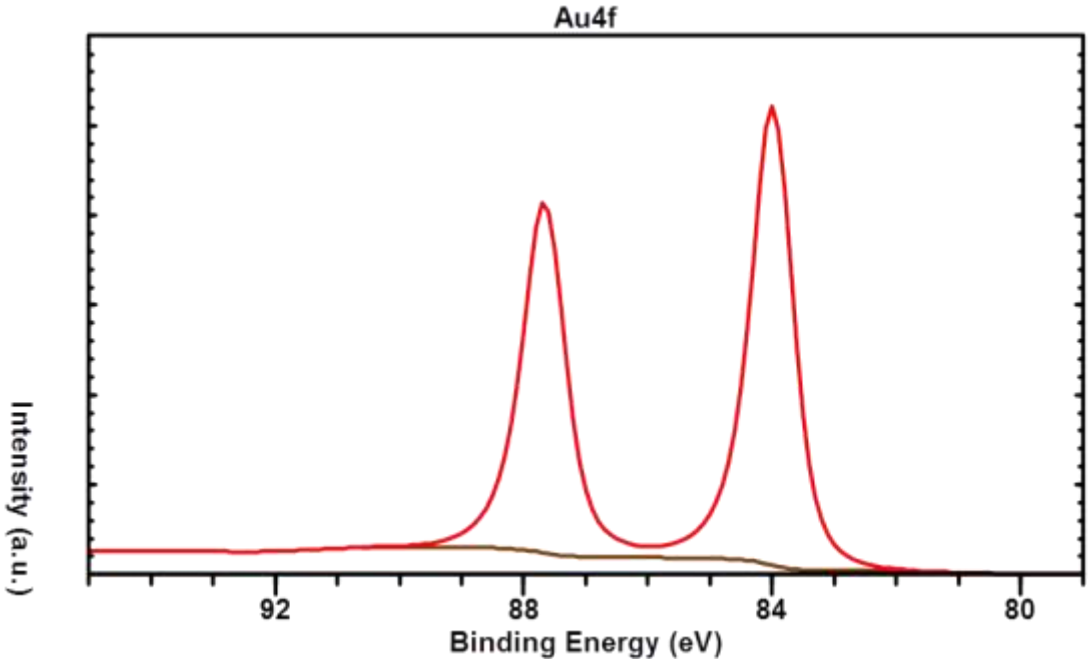
Au4f
Intensity (a.u.)
92
88
84
80
Binding Energy (eV)

Figure 4.43 The survey and detail XPS spectra together with the subtracted background, as measured for Na_2SO_4.

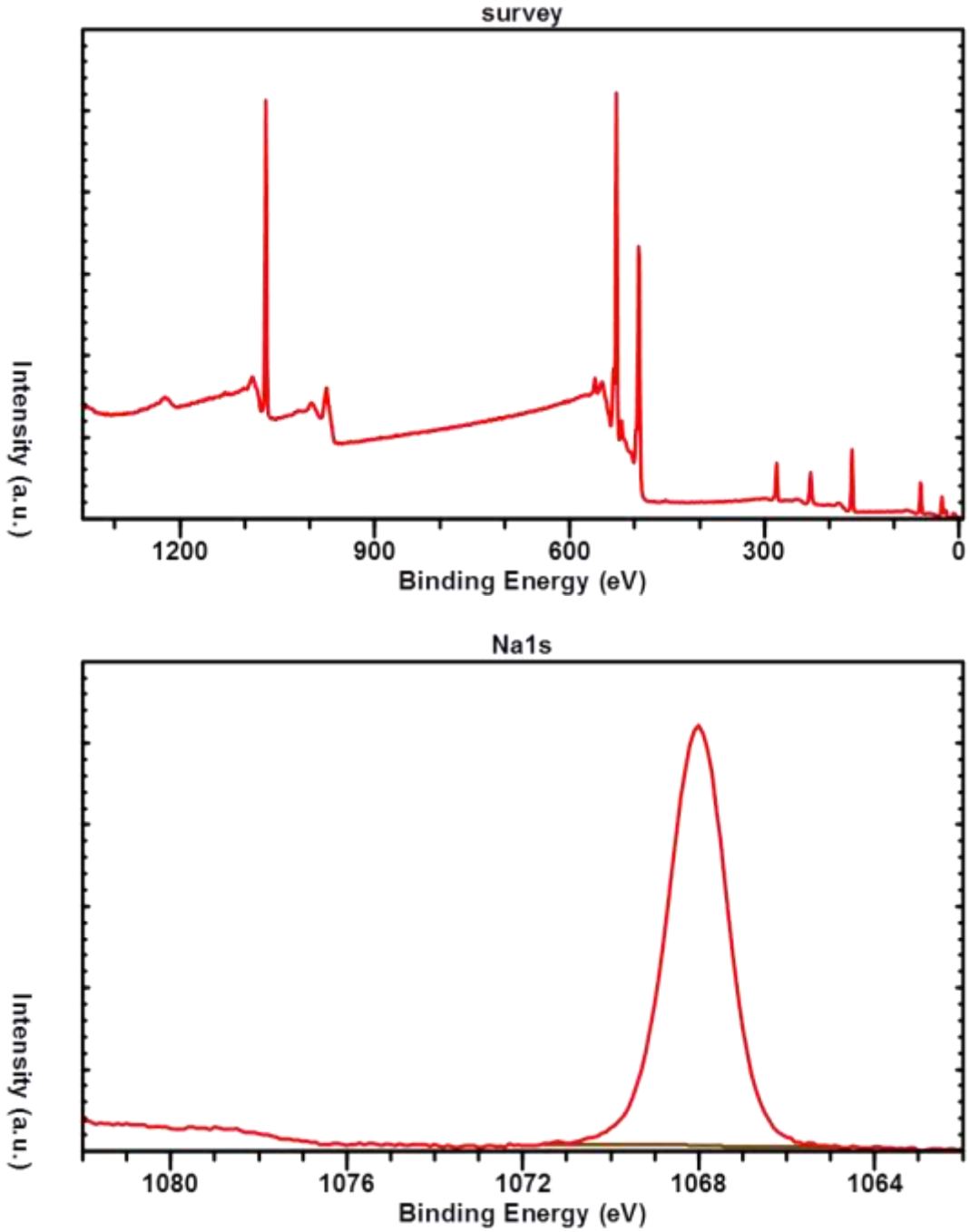

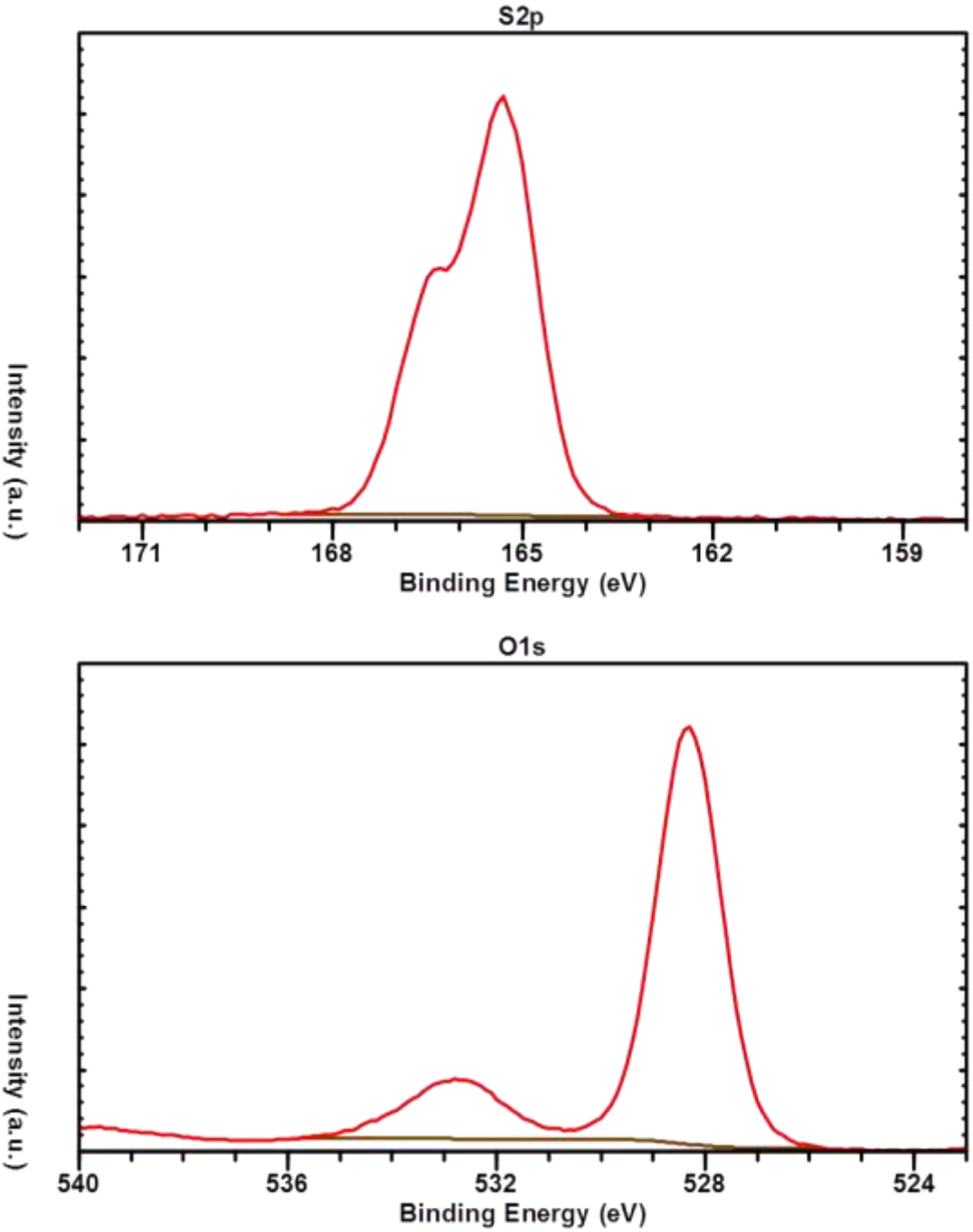
S2p
Intensity (a.u.)
171
168
165
162
159
Binding Energy (eV)
O1s
Intensity (a.u.)
540
536
532
528
524
Binding Energy (eV)

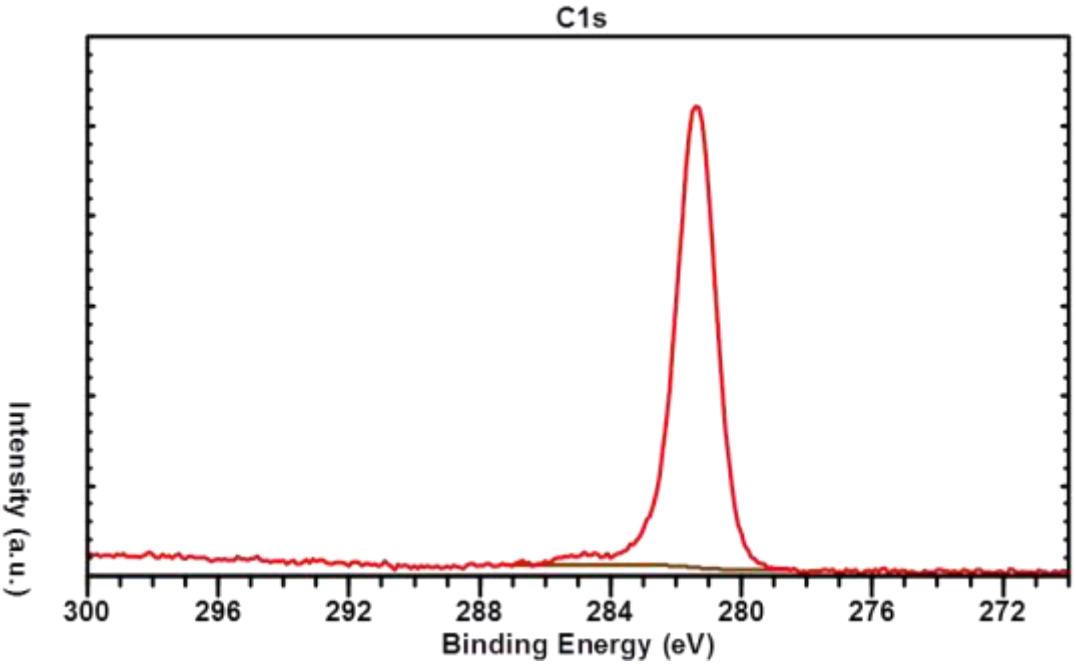
C1s
Intensity (a.u.)
300
296
292
288
284
280
276
272
Binding Energy (eV)

Figure 4.44 The survey and detail XPS spectra together with the subtracted background, as measured for $MgSO_4$.

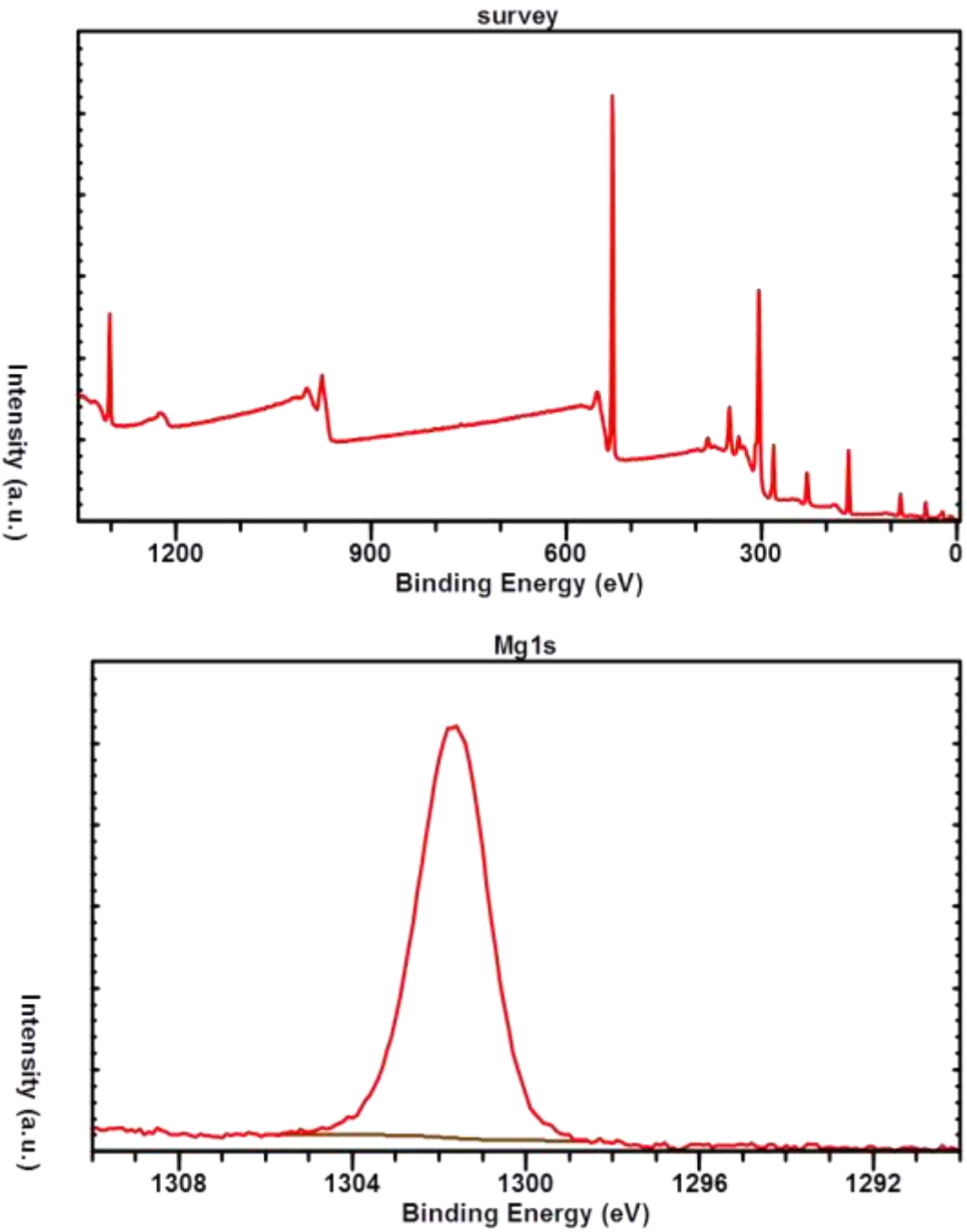

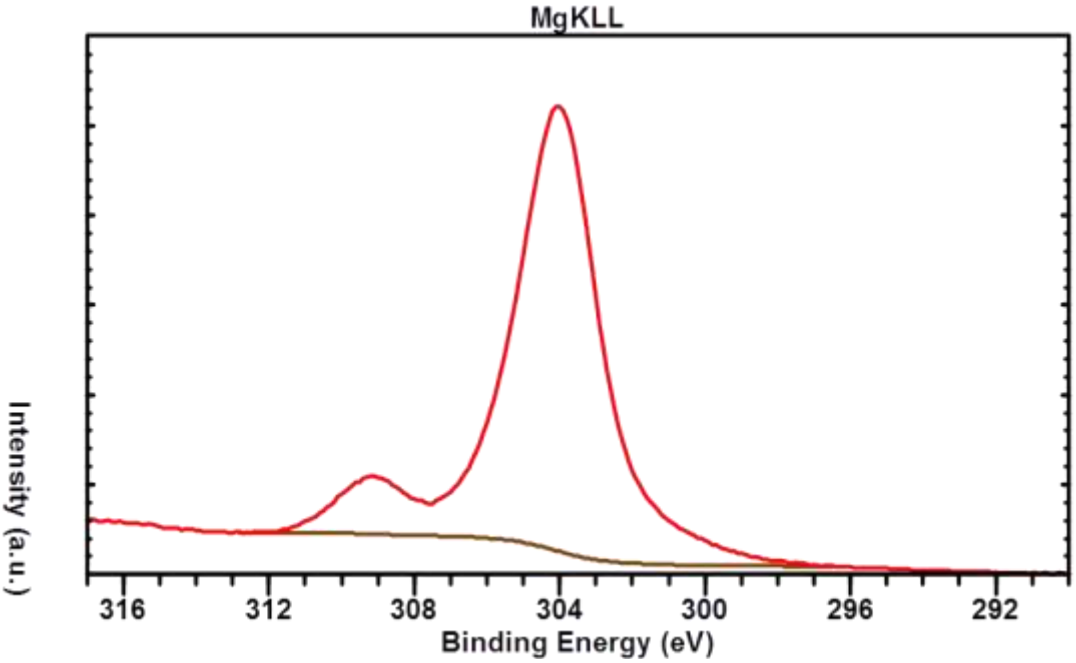
MgKLL
Intensity (a.u.)
316
312
308
304
300
296
292
Binding Energy (eV)

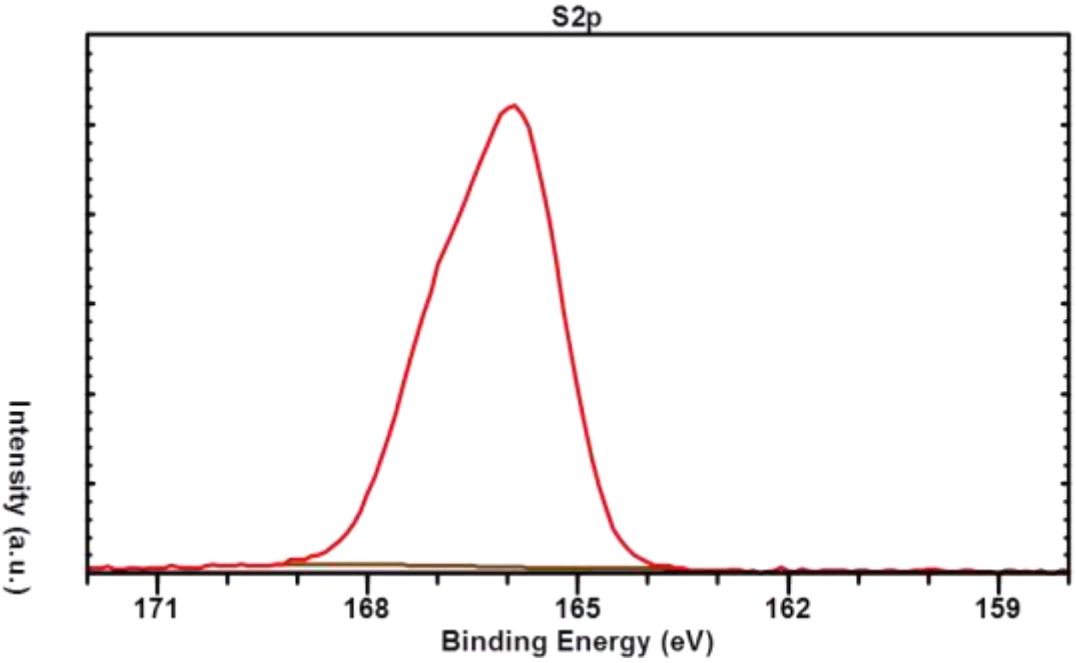
S2p
Intensity (a.u.)
171
168
165
162
159
Binding Energy (eV)

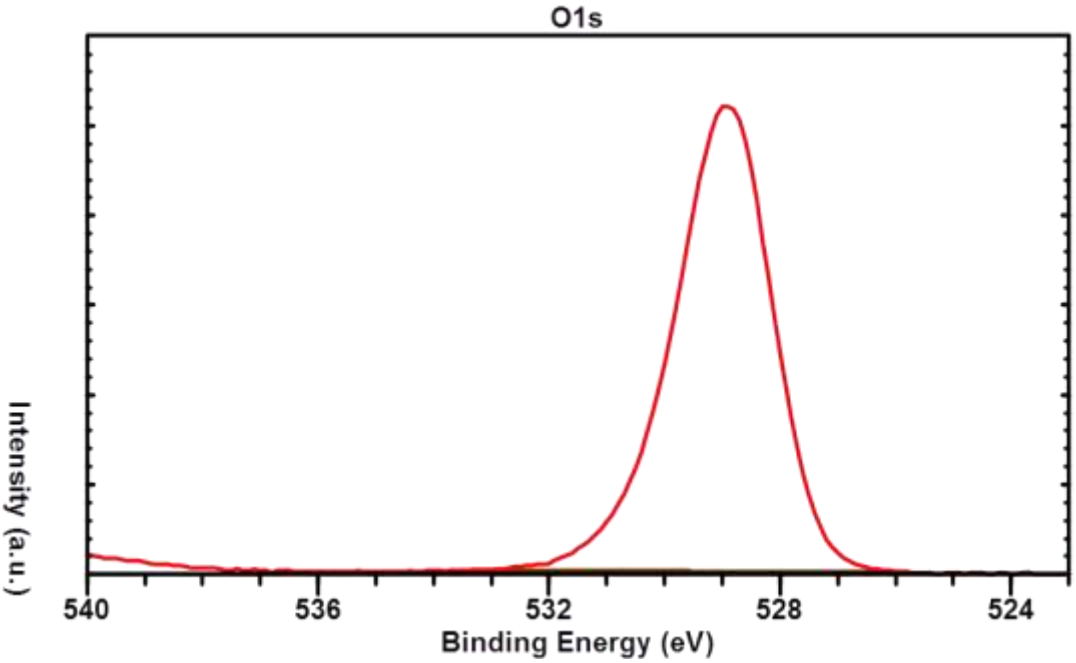
O1s
Intensity (a.u.)
540
536
532
528
524
Binding Energy (eV)

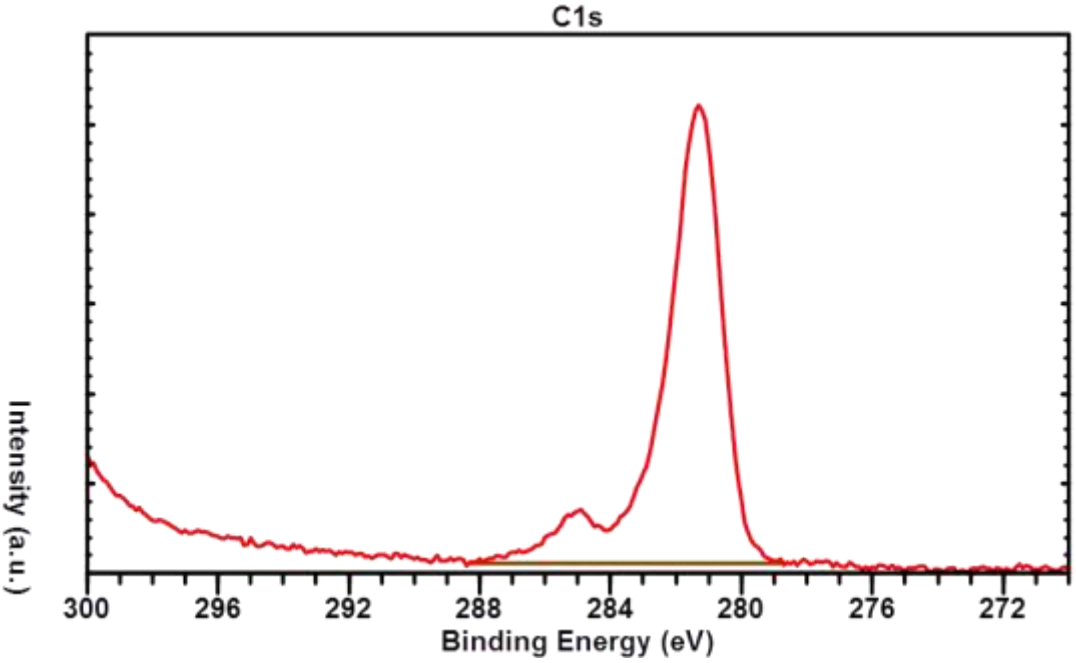
C1s
Intensity (a.u.)
300
296
292
288
284
280
276
272
Binding Energy (eV)

Figure 4.45 The survey and detail XPS spectra together with the subtracted background, as measured for $BaSO_4$.

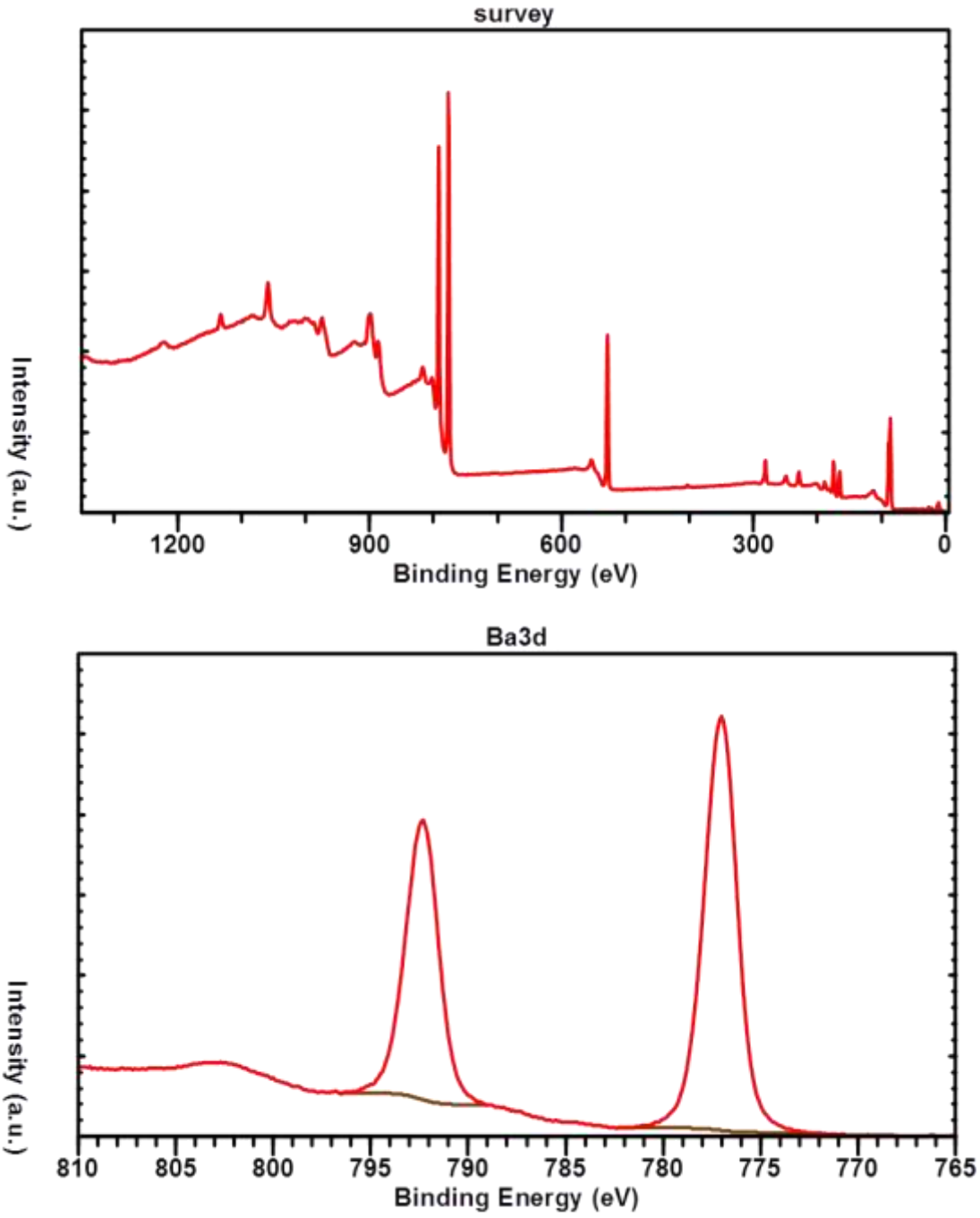

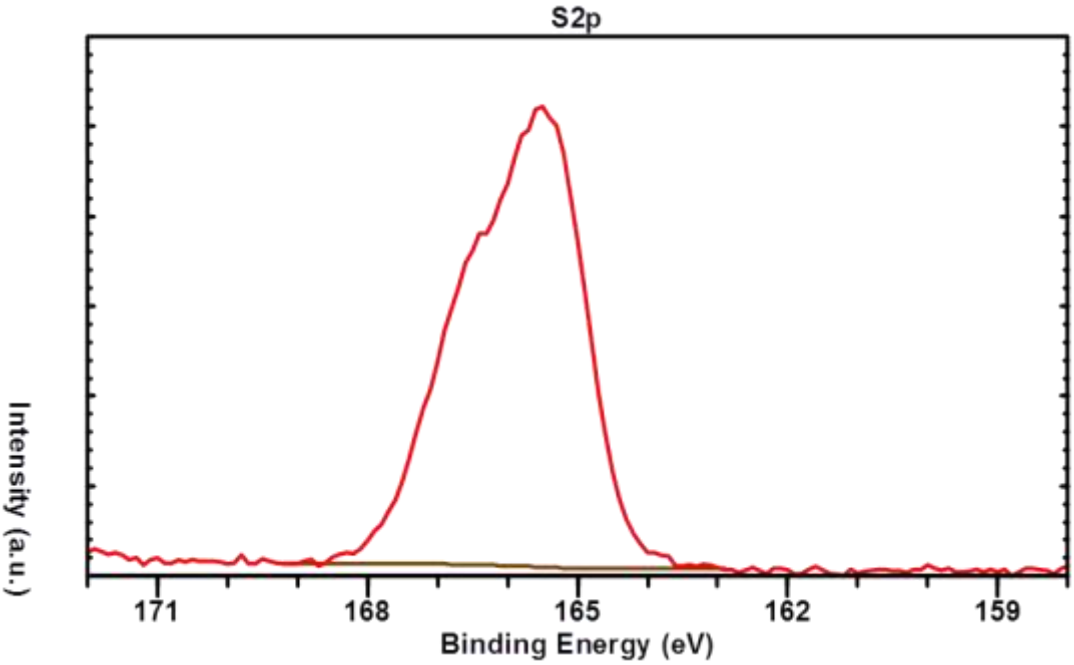
S2p
Intensity (a.u.)
171
168
165
162
159
Binding Energy (eV)

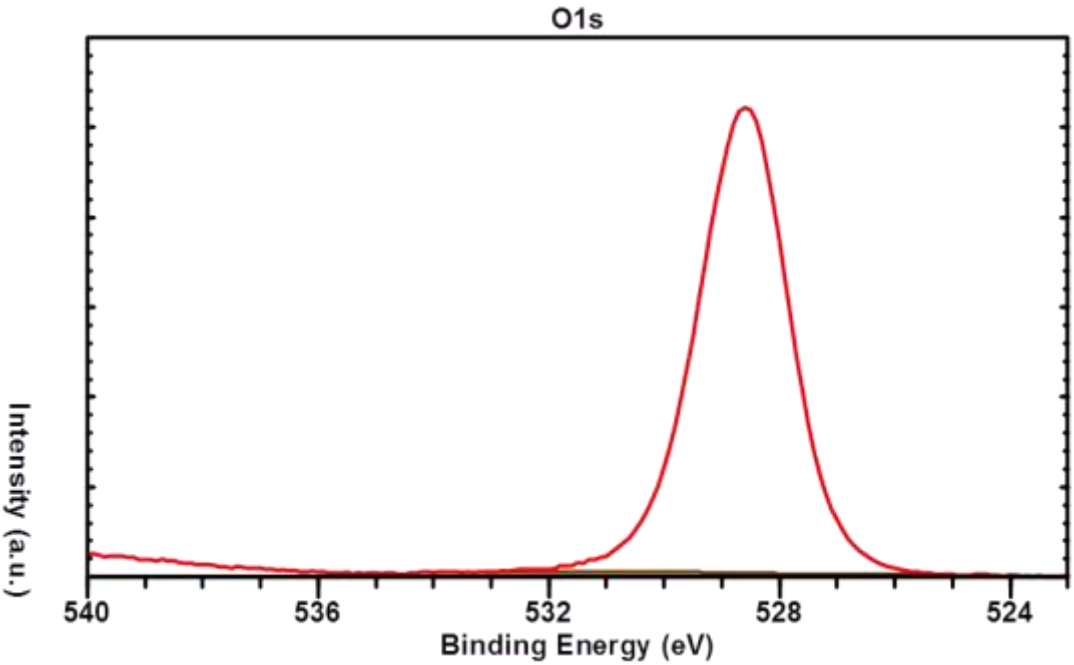
O1s
Intensity (a.u.)
540
536
532
528
524
Binding Energy (eV)

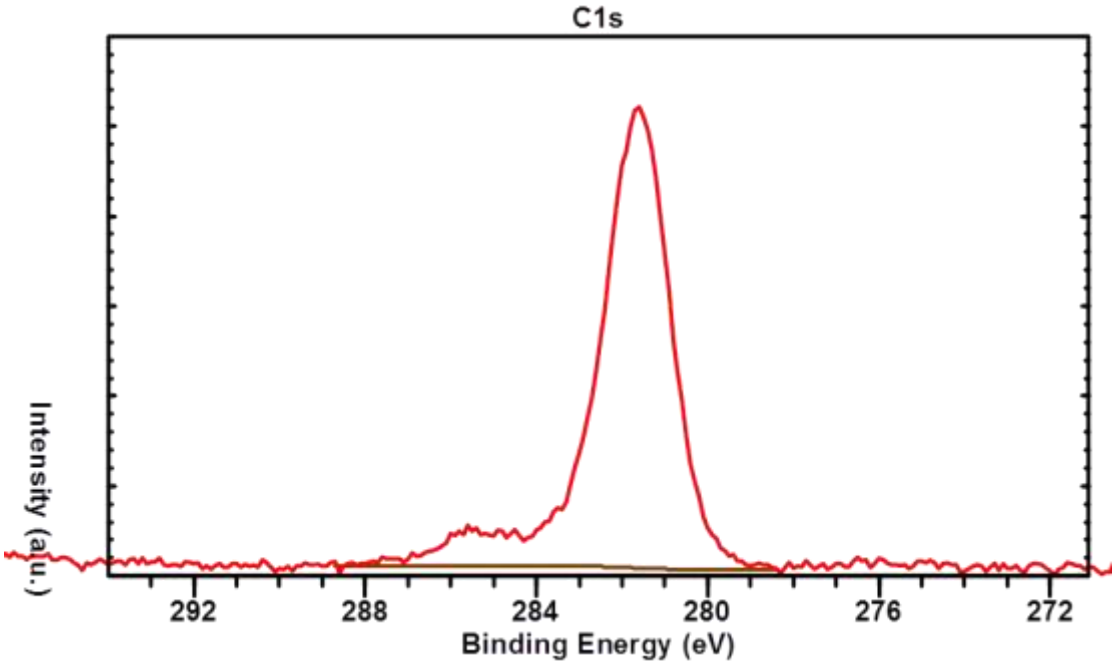
C1s
Intensity (a.u.)
292
288
284
280
276
272
Binding Energy (eV)

4.6 References

(1) Love, J. C.; Estroff, L. A.; Kriebel, J. K.; Nuzzo, R. G.; Whitesides, G. M. Self-Assembled Monolayers of Thiolates on Metals as a Form of Nanotechnology. *Chem. Rev.* **2005,** *105*, 1103-1170.

(2) Vericat, C.; Vela, M. E.; Benitez, G.; Carro, P.; Salvarezza, R. C. Self-Assembled Monolayers of Thiols and Dithiols on Gold: New Challenges for a Well-Known System. *Chem. Soc. Rev.* **2010,** *39*, 1805-1834.

(3) Claridge, S. A.; Liao, W.-S.; Thomas, J. C.; Zhao, Y.; Cao, H. H.; Cheunkar, S.; Serino, A. C.; Andrews, A. M.; Weiss, P. S. From the Bottom Up: Dimensional Control and Characterization in Molecular Monolayers. *Chem. Soc. Rev.* **2013,** *42*, 2725-2745.

(4) Goronzy, D. P.; Ebrahimi, M.; Rosei, F.; Arramel; Fang, Y.; De Feyter, S.; Tait, S. L.; Wang, C.; Beton, P. H.; Wee, A. T. S.; Weiss, P. S.; Perepichka, D. F. Supramolecular Assemblies on Surfaces: Nanopatterning, Functionality, and Reactivity. *ACS Nano* **2018,** *12*, 7445-7481.

(5) Hohman, J. N.; Claridge, S. A.; Kim, M.; Weiss, P. S. Cage Molecules for Self-Assembly. *Mater. Sci. Eng. R Rep.* **2010,** *70*, 188-208.

(6) Laibinis, P. E.; Whitesides, G. M. Ω-Terminated Alkanethiolate Monolayers on Surfaces of Copper, Silver, and Gold Have Similar Wettabilities. *J. Am. Chem. Soc.* **1992,** *114*, 1990-1995.

(7) Gershevitz, O.; Osnis, A.; Sukenik, C. N. Interfacial Chemistry on Carboxylate-Functionalized Monolayer Assemblies. *Isr. J. Chem.* **2005,** *45*, 321-336.

(8) Burris, S. C.; Zhou, Y.; Maupin, W. A.; Ebelhar, A. J.; Daugherty, M. W. The Effect of Surface Preparation on Apparent Surface pK_a's of Ω-Mercaptocarboxylic Acid Self-Assembled Monolayers on Polycrystalline Gold. *J. Phys. Chem. C* **2008,** *112*, 6811-6815.

(9) Hirata, N.; Suga, S.; Noguchi, Y.; Shibuta, M.; Tsunoyama, H.; Eguchi, T.; Nakajima, A. Highly Ordered Self-Assembled Monolayers of Carboxy- and Ester-Terminated Alkanethiols on Au(111): Infrared Absorption and Hyperthermal-Deposition Experiments with Cr(benzene)$_2$ Ions. *J. Phys. Chem. C* **2017,** *121*, 6736-6747.

(10) Ackerson, C. J.; Jadzinsky, P. D.; Kornberg, R. D. Thiolate Ligands for Synthesis of Water-Soluble Gold Clusters. *J. Am. Chem. Soc.* **2005,** *127*, 6550-6551.

(11) Thomas, J. C.; Boldog, I.; Auluck, H. S.; Bereciartua, P. J.; Dušek, M.; Macháček, J.; Bastl, Z.; Weiss, P. S.; Baše, T. Self-Assembled *p*-Carborane Analogue of *p*-Mercaptobenzoic Acid on Au{111}. *Chem. Mater.* **2015,** *27*, 5425-5435.

(12) Hohman, J. N.; Claridge, S. A.; Kim, M.; Weiss, P. S. Cage Molecules for Self-Assembly. *Mater. Sci. Eng. R Rep.* **2010,** *70*, 188-208.

(13) Hohman, J. N.; Zhang, P.; Morin, E. I.; Han, P.; Kim, M.; Kurland, A. R.; McClanahan, P. D.; Balema, V. P.; Weiss, P. S. Self-Assembly of Carboranethiol Isomers on Au{111}: Intermolecular Interactions Determined by Molecular Dipole Orientations. *ACS Nano* **2009,** *3*, 527-536.

(14) Kim, M.; Hohman, J. N.; Morin, E. I.; Daniel, T. A.; Weiss, P. S. Self-Assembled Monolayers of 2-Adamantanethiol on Au{111}: Control of Structure and Displacement. *The Journal of Physical Chemistry A* **2009,** *113*, 3895-3903.

(15) Fujii, S.; Akiba, U.; Fujihira, M. Geometry for Self-Assembling of Spherical Hydrocarbon Cages with Methane Thiolates on Au(111). *J. Am. Chem. Soc.* **2002,** *124*, 13629-13635.

(16) Dameron, A. A.; Charles, L. F.; Weiss, P. S. Structures and Displacement of 1-Adamantanethiol Self-Assembled Monolayers on Au{111}. *J. Am. Chem. Soc.* **2005,** *127*, 8697-8704.

(17) Willey, T. M.; Fabbri, J. D.; Lee, J. R. I.; Schreiner, P. R.; Fokin, A. A.; Tkachenko, B. A.; Fokina, N. A.; Dahl, J. E. P.; Carlson, R. M. K.; Vance, A. L.; Yang, W.; Terminello, L. J.; Buuren, T. v.; Melosh, N. A. Near-Edge X-Ray Absorption Fine Structure Spectroscopy of Diamondoid Thiol Monolayers on Gold. *J. Am. Chem. Soc.* **2008,** *130*, 10536-10544.

(18) Baše, T.; Bastl, Z.; Plzák, Z.; Grygar, T.; Plešek, J.; Carr, M. J.; Malina, V.; Šubrt, J.; Boháček, J.; Večerníková, E.; Kříž, O. Carboranethiol-Modified Gold Surfaces. A Study and Comparison of Modified Cluster and Flat Surfaces. *Langmuir* **2005,** *21*, 7776-7785.

(19) Grimes, R. N. Carboranes in the Chemist's Toolbox. *Dalton Trans.* **2015,** *44*, 5939-5956.

(20) Spokoyny, A. M.; Machan, C. W.; Clingerman, D. J.; Rosen, M. S.; Wiester, M. J.; Kennedy, R. D.; Stern, C. L.; Sarjeant, A. A.; Mirkin, C. A. A Coordination Chemistry Dichotomy for Icosahedral Carborane-Based Ligands. *Nat. Chem.* **2011,** *3*, 590-596.

(21) Yavuz, A.; Sohrabnia, N.; Yilmaz, A.; Danışman, M. F. Mixed Carboranethiol Self-Assembled Monolayers on Gold Surfaces. *Appl. Surf. Sci.* **2017,** *413*, 233-241.

(22) Lübben, J. F.; Baše, T.; Rupper, P.; Künniger, T.; Macháček, J.; Guimond, S. Tuning the Surface Potential of Ag Surfaces by Chemisorption of Oppositely-Oriented Thiolated Carborane Dipoles. *J. Colloid Interface Sci.* **2011,** *354*, 168-174.

(23) Thomas, J. C.; Schwartz, J. J.; Hohman, J. N.; Claridge, S. A.; Auluck, H. S.; Serino, A. C.; Spokoyny, A. M.; Tran, G.; Kelly, K. F.; Mirkin, C. A.; Gilles, J.; Osher, S. J.; Weiss, P. S. Defect-Tolerant Aligned Dipoles within Two-Dimensional Plastic Lattices. *ACS Nano* **2015,** *9*, 4734-4742.

(24) Kim, J.; Rim, Y. S.; Liu, Y.; Serino, A. C.; Thomas, J. C.; Chen, H.; Yang, Y.; Weiss, P. S. Interface Control in Organic Electronics Using Mixed Monolayers of Carboranethiol Isomers. *Nano Lett.* **2014,** *14*, 2946-2951.

(25) Vetushka, A.; Bernard, L.; Guseva, O.; Bastl, Z.; Plocek, J.; Tomandl, I.; Fejfar, A.; Baše, T.; Schmutz, P. Adsorption of Oriented Carborane Dipoles on a Silver Surface. *Phys. Status Solidi B* **2015,** *253*, 591-600.

(26) Plešek, J. The Age of Chiral Deltahedral Borane Derivatives. *Inorg. Chim. Acta* **1999,** *289*, 45-50.

(27) Gohler, B.; Hamelbeck, V.; Markus, T. Z.; Kettner, M.; Hanne, G. F.; Vager, Z.; Naaman, R.; Zacharias, H. Spin Selectivity in Electron Transmission through Self-Assembled Monolayers of Double-Stranded DNA. *Science* **2011,** *331*, 894-897.

(28) Abendroth, J. M.; Nakatsuka, N.; Ye, M.; Kim, D.; Fullerton, E. E.; Andrews, A. M.; Weiss, P. S. Analyzing Spin Selectivity in DNA-Mediated Charge Transfer *via* Fluorescence Microscopy. *ACS Nano* **2017,** *11*, 7516-7526.

(29) Abendroth, J. M.; Cheung, K. M.; Stemer, D. M.; El Hadri, M. S.; Zhao, C.; Fullerton, E. E.; Weiss, P. S. Spin-Dependent Ionization of Chiral Molecular Films. *J. Am. Chem. Soc.* **2019,** *141*, 3863-3874.

(30) Bregadze, V. I. Dicarba-*Closo*-Dodecaboranes $C_2B_{10}H_{12}$ and Their Derivatives. *Chem. Rev.* **1992,** *92*, 209-223.

(31) Plešek, J.; Heřmánek, S. Experimental Evaluation of Charge Distribution on Particular Skeletal Atoms in Icosahedral Carboranes by Means of HS-Derivatives. *Collect. Czech. Chem. Commun.* **1979,** *44*, 24-33.

(32) Plešek, J.; Heřmánek, S. Syntheses and Properties of Substituted Icosahedral Carborane Thiols. *Collect. Czech. Chem. Commun.* **1981,** *46*, 687-692.

(33) Grimes, R. N. Carboranes-3rd Edition. Elsevier: 2016.

(34) Baše, T.; Macháček, J.; Hájková, Z.; Langecker, J.; Kennedy, J. D.; Carr, M. J. Thermal Isomerizations of Monothiolated Carboranes $(HS)C_2B_{10}H_{11}$ and the Solid-State Investigation of 9-(HS)-1,2-$C_2B_{10}H_{11}$ and 9-(HS)-1,7-$C_2B_{10}H_{11}$. *J. Organomet. Chem.* **2015,** *798*, 132-140.

(35) Thomas, J. C.; Goronzy, D. P.; Dragomiretskiy, K.; Zosso, D.; Gilles, J.; Osher, S. J.; Bertozzi, A. L.; Weiss, P. S. Mapping Buried Hydrogen-Bonding Networks. *ACS Nano* **2016,** *10*, 5446-5451.

(36) Maksymovych, P.; Sorescu, D. C.; Yates, J. T. Gold-Adatom-Mediated Bonding in Self-Assembled Short-Chain Alkanethiolate Species on the Au(111) Surface. *Phys. Rev. Lett.* **2006,** *97*, 146103.

(37) Moore, A. M.; Mantooth, B. A.; Donhauser, Z. J.; Yao, Y.; Tour, J. M.; Weiss, P. S. Real-Time Measurements of Conductance Switching and Motion of Single Oligo(phenylene ethynylene) Molecules. *J. Am. Chem. Soc.* **2007,** *129*, 10352-10353.

(38) Hohman, J. N.; Kim, M.; Schüpbach, B.; Kind, M.; Thomas, J. C.; Terfort, A.; Weiss, P. S. Dynamic Double Lattice of 1-Adamantaneselenolate Self-Assembled Monolayers on Au{111}. *J. Am. Chem. Soc.* **2011,** *133*, 19422-19431.

(39) Bain, C. D.; Whitesides, G. M. A Study by Contact Angle of the Acid-Base Behavior of Monolayers Containing Ω-Mercaptocarboxylic Acids Adsorbed on Gold: An Example of Reactive Spreading. *Langmuir* **1989,** *5*, 1370-1378.

(40) Creager, S. E.; Clarke, J. Contact-Angle Titrations of Mixed Ω-Mercaptoalkanoic Acid/Alkanethiol Monolayers on Gold. Reactive Vs Nonreactive Spreading, and Chain Length Effects on Surface pK_a Values. *Langmuir* **1994,** *10*, 3675-3683.

(41) de F. Paulo, T.; Abruña, H. D.; Diógenes, I. C. N. Thermodynamic, Kinetic, Surface pK_a, and Structural Aspects of Self-Assembled Monolayers of Thio Compounds on Gold. *Langmuir* **2012,** *28*, 17825-17831.

(42) Isom, D. G.; Castañeda, C. A.; Cannon, B. R.; García-Moreno E, B. Large Shifts in pK_a Values of Lysine Residues Buried inside a Protein. *Proc. Natl. Acad. Sci. U. S. A.* **2011,** *108*, 5260.

(43) Rastogi, V. K.; Girvin, M. E. Structural Changes Linked to Proton Translocation by Subunit *C* of the ATP Synthase. *Nature* **1999,** *402*, 263-268.

(44) Guo, B.; Middha, E.; Liu, B. Solvent Magic for Organic Particles. *ACS Nano* **2019,** *13*, 2675-2680.

(45) Harms, M. J.; Castañeda, C. A.; Schlessman, J. L.; Sue, G. R.; Isom, D. G.; Cannon, B. R.; García-Moreno E, B. The pK_a Values of Acidic and Basic Residues Buried at the Same Internal Location in a Protein Are Governed by Different Factors. *J. Mol. Biol.* **2009,** *389*, 34-47.

(46) Karp, D. A.; Gittis, A. G.; Stahley, M. R.; Fitch, C. A.; Stites, W. E.; García-Moreno E, B. High Apparent Dielectric Constant inside a Protein Reflects Structural Reorganization Coupled to the Ionization of an Internal Asp. *Biophys. J.* **2007,** *92*, 2041-2053.

(47) Chen, H.; Huang, C.; Deng, Y.; Sun, Q.; Zhang, Q.-L.; Zhu, B.-X.; Ni, X.-L. Solvent-Switched Schiff-Base Macrocycles: Self-Sorting and Self-Assembly-Dependent Unconventional Organic Particles. *ACS Nano* **2019,** *13*, 2840-2848.

(48) Palatinus, L.; Chapuis, G. SUPERFLIP - A Computer Program for the Solution of Crystal Structures by Charge Flipping in Arbitrary Dimensions. *J. Appl. Crystallogr.* **2007,** *40*, 786-790.

(49) Petříček, V.; Dušek, M.; Palatinus, L. Crystallographic Computing System JANA2006: General Features. *Z. Kristallogr.* **2014,** *229*, 345-352.

(50) Valiev, M.; Bylaska, E. J.; Govind, N.; Kowalski, K.; Straatsma, T. P.; Van Dam, H. J. J.; Wang, D.; Nieplocha, J.; Apra, E.; Windus, T. L.; de Jong, W. A. NWChem: A Comprehensive and Scalable Open-Source Solution for Large Scale Molecular Simulations. *Comput. Phys. Commun.* **2010,** *181*, 1477-1489.

(51) Johnson, B. G.; Fisch, M. J. An Implementation of Analytic Second Derivatives of the Gradient-Corrected Density Functional Energy. *J. Chem. Phys.* **1994,** *100*, 7429-7442.

(52) Adamo, C.; Barone, V. Physically Motivated Density Functionals with Improved Performances: The Modified Perdew–Burke–Ernzerhof Model. *J. Chem. Phys.* **2002,** *116*, 5933-5940.

(53) Jensen, F. Unifying General and Segmented Contracted Basis Sets. Segmented Polarization Consistent Basis Sets. *J. Chem. Theory Comput.* **2014,** *10*, 1074-1085.

(54) Jensen, F. Basis Set Convergence of Nuclear Magnetic Shielding Constants Calculated by Density Functional Methods. *J. Chem. Theory Comput.* **2008,** *4*, 719-727.

(55) Ferris, J. H.; Kushmerick, J. G.; Johnson, J. A.; Yoshikawa Youngquist, M. G.; Kessinger, R. B.; Kingsbury, H. F.; Weiss, P. S. Design, Operation, and Housing of an Ultrastable, Low Temperature, Ultrahigh Vacuum Scanning Tunneling Microscope. *Rev. Sci. Instrum.* **1998,** *69*, 2691.

(56) Tersoff, J.; Hamann, D. R. Theory and Application for the Scanning Tunneling Microscope. *Phys. Rev. Lett.* **1983,** *50*, 1998-2001.

(57) Tang, W.; Sanville, E.; Henkelman, G. A Grid-Based Bader Analysis Algorithm without Lattice Bias. *J. Phys.: Condens. Matter* **2009,** *21*, 084204.

(58) Kresse, G.; Furthmüller, J. Efficient Iterative Schemes Forab Initiototal-Energy Calculations Using a Plane-Wave Basis Set. *Phys. Rev. B* **1996,** *54*, 11169-11186.

(59) Kresse, G.; Furthmüller, J. Efficiency of Ab-Initio Total Energy Calculations for Metals and Semiconductors Using a Plane-Wave Basis Set. *Comput. Mater. Sci.* **1996,** *6*, 15-50.

(60) Kresse, G.; Hafner, J. Ab Initiomolecular-Dynamics Simulation of the Liquid-Metal–Amorphous-Semiconductor Transition in Germanium. *Phys. Rev. B* **1994,** *49*, 14251-14269.

(61) Kresse, G.; Hafner, J. Ab Initiomolecular Dynamics for Liquid Metals. *Phys. Rev. B* **1993,** *47*, 558-561.

(62) Mathew, K.; Hennig, R. G. Implicit Self-Consistent Description of Electrolyte in Plane-Wave Density-Functional Theory. *arXiv* **2016,** *1601.03346*.

(63) Mathew, K.; Sundararaman, R.; Letchworth-Weaver, K.; Arias, T. A.; Hennig, R. G. Implicit Solvation Model for Density-Functional Study of Nanocrystal Surfaces and Reaction Pathways. *J. Chem. Phys.* **2014,** *140*, 084106.

(64) Liptak, M. D.; Shields, G. C. Accurate pK_a Calculations for Carboxylic Acids Using Complete Basis Set and Gaussian-N Models Combined with Cpcm Continuum Solvation Methods. *J. Am. Chem. Soc.* **2001,** *123*, 7314-7319.

(65) Frisch, M. J.; Trucks, G. W.; Schlegel, H. B.; Scuseria, G. E.; Robb, M. A.; Cheeseman, J. R.; Scalmani, G.; Barone, V.; Petersson, G. A.; Nakatsuji, H.; Li, X.; Caricato, M.; Marenich, A. V.; Bloino, J.; Janesko, B. G.; Gomperts, R.; Mennucci, B.; Hratchian, H. P.; Ortiz, J. V.; Izmaylov, A. F., *et al. Gaussian 16 Rev. C.01*, Wallingford, CT, 2016.

(66) Stephens, P. J.; Devlin, F. J.; Chabalowski, C. F.; Frisch, M. J. Ab Initio Calculation of Vibrational Absorption and Circular Dichroism Spectra Using Density Functional Force Fields. *J. Phys. Chem.* **1994,** *98*, 11623-11627.

(67) Becke, A. D. Density-Functional Thermochemistry. III. The Role of Exact Exchange. *J. Chem. Phys.* **1993,** *98*, 5648-5652.

(68) Lee, C.; Yang, W.; Parr, R. G. Development of the Colle-Salvetti Correlation-Energy Formula into a Functional of the Electron Density. *Phys. Rev. B* **1988,** *37*, 785-789.

(69) Vosko, S. H.; Wilk, L.; Nusair, M. Accurate Spin-Dependent Electron Liquid Correlation Energies for Local Spin Density Calculations: A Critical Analysis. *Can. J. Phys.* **1980,** *58*, 1200-1211.

(70) Barone, V.; Cossi, M. Quantum Calculation of Molecular Energies and Energy Gradients in Solution by a Conductor Solvent Model. *J. Phys. Chem. A* **1998,** *102*, 1995-2001.

(71) Cossi, M.; Rega, N.; Scalmani, G.; Barone, V. Energies, Structures, and Electronic Properties of Molecules in Solution with the C-PCM Solvation Model. *J. Comput. Chem.* **2003,** *24*, 669-681.

(72) van der Marel, C.; Yildirim, M.; Stapert, H. R. Multilayer Approach to the Quantitative Analysis of X-Ray Photoelectron Spectroscopy Results: Applications to Ultrathin SiO_2 on Si and to Self-Assembled Monolayers on Gold. *J. Vac. Sci. Technol., A* **2005,** *23*, 1456-1470.

(73) Powell, C. J.; Jablonski, A. NIST Electron Inelastic-Mean-Free-Path Database, Version 1.2. Gaithersburg: National Institute of Standards and Technology, 2010.

Chapter 5: Characterization of Bifunctional Boron Cluster Assemblies Modified *via* Chemical Lift-Off Lithography

5.1 Introduction

Patterning at the micro and nanoscales provides opportunities in both science and engineering for fundamental studies and device applications. We see examples in electronics,[1-3] energy applications,[4,5] biosensors,[6-8] and wearable technologies.[9,10] Conventional lithographic techniques used to achieve these length scales rely on focused beams of light, X-rays, and/or charged particles.[11-14] However, these techniques can be slow, lacking in resolution, or cost intensive. Soft lithographic techniques, such as microcontact printing, provide higher throughput and less capital-intensive methods for achieving chemical patterning of self-assembled monolayers (SAMs) at the micro and nanoscales.[15] However, conventional microcontact printing suffers from lateral diffusion of the deposited molecules outside of the desired contact area, broadening feature sizes and reducing pattern fidelity and resolution.[16,17]

One method developed in recent years, which has circumvented the traditional limits of soft lithography, is chemical lift-off lithography (CLL), a subtractive patterning technique used to pattern SAMs, typically on Au substrates.[18-20] For CLL, a SAM with a reactive interface, typically in the form of a terminal hydroxyl, carboxyl, or amine group, is brought into contact with a oxygen-plasma-activated poly(dimethylsiloxane) (PDMS) stamp, which reacts with the tail group of the SAM molecules. Upon removal of the PDMS stamp, Au-Au bonds are broken at the substrate-monolayer interface and the SAM molecules along with a monolayer of Au is lifted-off with the stamp. This technique is useful not only for creating high-fidelity patterns of monolayers but also for creating patterned Au on flexible transparent substrates, *i.e.*, PDMS. A modified form of CLL, polymer-pen chemical lift-off lithography, has increased the tunable range of feature sizes achievable *via* CLL.[21] This lithography technique has also been used for the patterning of biomolecules[22,23] and fabrication of field-effect transistors and biosensors.[24,25]

Until now, CLL has only employed SAMs where the adsorbate molecular backbone is a linear alkyl chain. However, using SAMs with stronger intermolecular interactions within the monolayer has potential benefits for increasing lift-off effectiveness and enabling patterning of domains with independent tunable properties. Recently, SAMs composed of carboranethiol molecules have garnered significant interest due to several advantages they possess over traditional *n*-alkanethiolate SAMs.[26] A carborane is an icosahedral cage molecule composed of 10 boron atoms and two carbon atoms with terminal hydrogens at the vertices. Due to the rigid, symmetric structures of the molecules, carboranethiolate monolayers tend to be more pristine and defect-free than *n*-alkanethiolate monolayers.[27]

In addition, carboranethiolate monolayers have strong dipole-dipole interactions within the assembly, where the dipole moment is determined by the positions of the carbons in the cage. These dipole-dipole interactions have been shown to overcome traditional domain boundaries.[28] Given that the dipole moment is dependent on a small structural change in the molecule, different carboranethiol isomers can be used to modify the dipole-dipole networks within the monolayers without changing other chemical and physical properties; this feature can be used to tune surface properties such as work function.[29,30] The carborane cage can act as a scaffold for multiple functional groups and the reactivity of bifunctional carboranes has been used to create monolayers with tunable surface morphology.[31-33]

In this study, we examined three isomers of bifunctional carboranes, each with a thiol group to enable surface attachment, *i.e.*, SAM formation, and a carboxylic acid group to enable lift-off with PDMS stamps. We characterized post-lifted-off surfaces with atomic force microscopy (AFM). Furthermore, these functionalized carboranethiolate monolayers can be visualized using scanning tunneling microscopy (STM) despite having hydrophilic terminal groups;[33] this property

enabled the visualization of post-lifted-off surfaces *via* STM for the *first* time. Post-CLL Au substrates and PDMS stamps were characterized using X-ray photoelectron spectroscopy (XPS), and differences in the lift-off properties based on the binding of the Au and the thiol between the various isomers were observed.

5.2 Results and Discussion

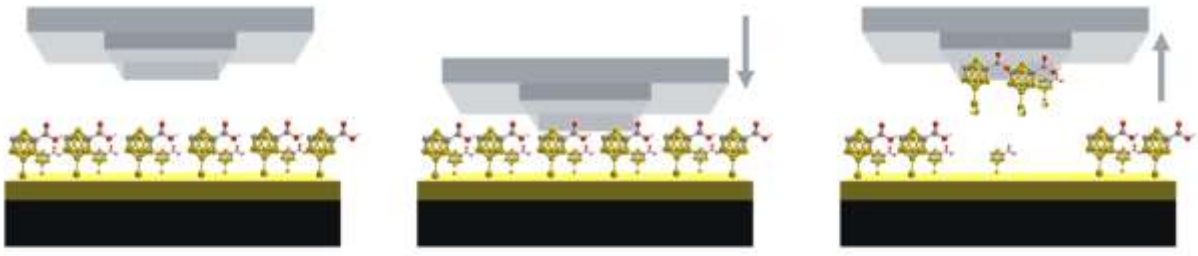

Figure 5.1 Schematic showing the chemical lift-off lithography process using bifunctional carborane self-assembled monolayers (SAMs) on Au. The thiol group enables surface attachment to Au and the carboxylic acid group reacts with the poly(dimethylsiloxane) (PDMS) stamp. Upon removal of the stamp, SAM molecules are removed from the surface along with a monolayer of Au. The yield of lift-off is fractional and molecules are left behind in contact areas.

A schematic of CLL performed on monolayers of carboxyl-carboranethiols is shown in Figure 5.1. Three bifunctional carborane species assembled on Au surfaces were explored in this paper, 1-HS-12-COOH-1,12-$C_2B_{10}H_{10}$ (P1-COOH), 1-COOH-7-SH-1,7-$C_2B_{10}H_{10}$ (M1-COOH), and *racem*-1-COOH-9-SH-1,7-$C_2B_{10}H_{10}$ (M9-COOH), see Figure 5.2 for structures. The P1-COOH isomer has the thiol group and the carboxylic acid group in a *para* configuration and thus the carboxylic acid is directly exposed to the monolayer-environment interface. In the case of M1-COOH and M9-COOH, the two functional groups are in a *meta* configuration and consequently the carboxylic acid is more laterally positioned in the monolayer and directly interacts with neighboring molecules. The critical difference between the M1-COOH and

M9-COOH isomers is that the former has the thiol attached to an electron-poor carbon vertex of the cage, while the latter has the thiol attached to an electron-rich boron vertex.

Initially, we performed CLL on SAMs composed of one of these carboranethiol isomers with patterned PDMS stamps. Subsequently, we imaged the patterned Au surfaces using peak-force AFM. The AFM images showed protruding circular features, containing carboxyl-carboranethiolates, of approximately 7.5 μm in diameter with a center-to-center spacing of approximately 10 μm (Figure 5.2). These measurements correspond exactly to the dimensions of the patterned PDMS stamp used. Patterns were observed in both AFM topography and adhesion images. Contrast in adhesion, *i.e.*, the force needed to retract an AFM tip from the surface, suggests differences in chemical composition of the patterned regions. High fidelity patterns of carboxyl-carboranethiolates could be achieved with CLL not only in the case of P1-COOH, with the exposed carboxylic acid, but also with M1-COOH and M9-COOH, with the relatively buried carboxylic acid.

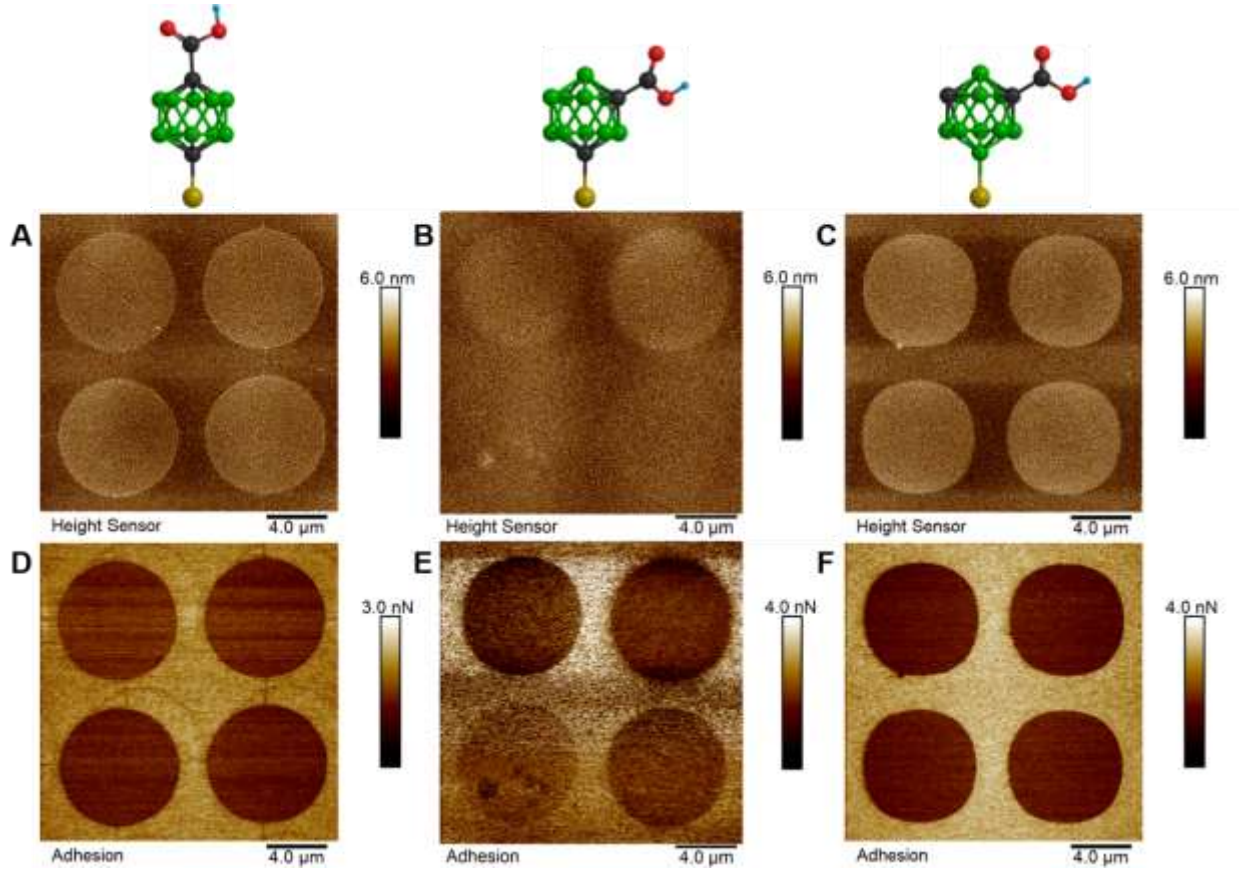

Figure 5.2 (Top) Structures of 1-HS-12-COOH-1,12-$C_2B_{10}H_{10}$ (P1-COOH), 1-COOH-7-SH-1,7-$C_2B_{10}H_{10}$ (M1-COOH), and *racem*-1-COOH-9-SH-1,7-$C_2B_{10}H_{10}$ (M9-COOH), from left to right. Boron atoms are shown in green and carbon atoms are shown in black. Terminal hydrogens on the cage are omitted for clarity. (A-C) Atomic force microscopy (AFM) height images of post-CLL Au substrates for P1-COOH, M1-COOH, and M9-COOH, respectively. (D-F) AFM adhesion images of post-CLL Au substrates for P1-COOH, M1-COOH, and M9-COOH, respectively. These images show that we can achieve chemical lift-off lithography with all three bifunctional carborane isomers and have fidelity of pattern.

Monolayers of M1-COOH and M9-COOH have been previously imaged *via* STM under ambient conditions, despite these monolayers having terminal hydrophilic groups, which can be challenging given their conformational flexibility and propensity to interact with ambient water. Thus, these molecules provided an unprecedented opportunity to visualize the morphology of the post lift-off surface using STM.[33] For samples prepared for STM studies, CLL was performed on SAMs of M9-COOH with featureless PDMS stamps in order to lift-off the entire monolayer on the surface. Scanning tunneling microscopy of the post-CLL surfaces revealed two characteristic

features. One type of such features was island domains composed of adsorbate molecules scattered non-periodically on the surface (Figure 5.3). These types of domains have not been observed previously in carboranethiolate monolayers. These islands ranged from 5 to 50 nm in diameter and appeared at a density of approximately 5-6 islands per square micron. Molecules within the island domains were better resolved under more perturbative scanning conditions (I_{tunnel} = 80 pA, V_{sample} = 0.1 V), consistent with previous STM studies of carboranethiolate monolayers.

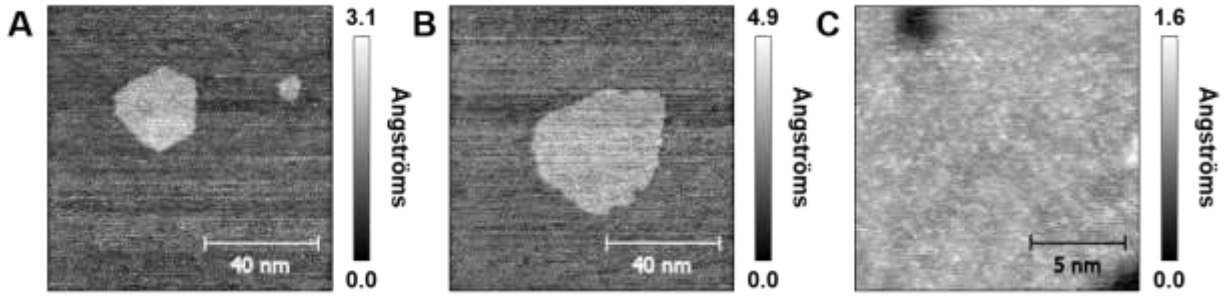

Figure 5.3 (A, B) Scanning tunneling images of *racem*-1-COOH-9-SH-1,7-$C_2B_{10}H_{10}$ (M9-COOH) monolayer after chemical lift-lithography has been performed (100 nm × 100 nm, I_{tunnel} = 3 pA, V_{sample} = 1 V). Images show molecular island domains ranging in size from 5 to 50 nm in diameter. (C) Under more perturbative conditions, molecules are resolved within the island domain, consistent with carboranethiols (15 nm × 15 nm, I_{tunnel} = 80 pA, V_{sample} = 0.1 V).

The regions surrounding the island domains were susceptible to perturbation by the STM tip. Figure 5.4 shows a 100 nm × 100 nm area before and after a 30 nm × 30 nm square at the center of the area was scanned under slightly perturbative conditions (I_{tunnel} = 20 pA, V_{sample} = 0.1 V). This behavior is indicative of low density surface coverage of highly mobile molecules. These images show that during CLL the PDMS stamp in not homogenously lifting off the entire monolayer and in most areas is leaving behind a number of individual molecules and in some cases larger aggregates of molecules. These aggregate domains may also be stabilized in part by the dipole-dipole interactions between carborane cages.

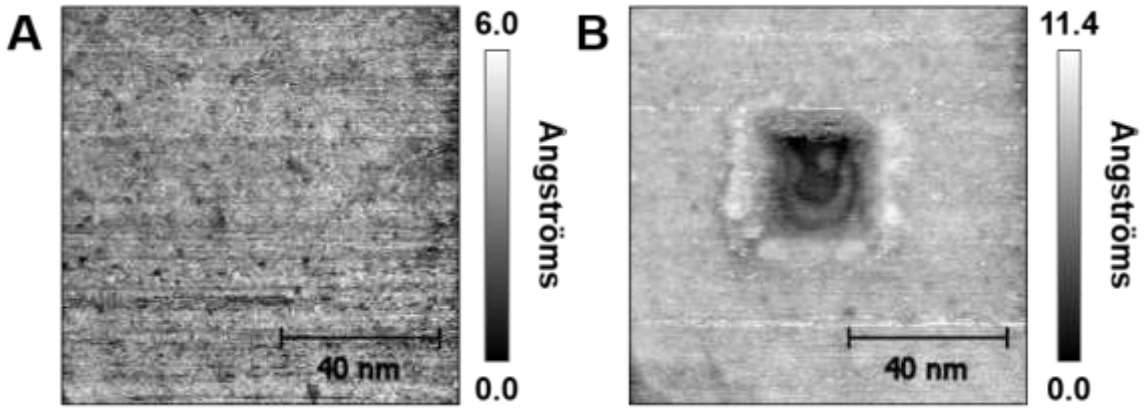

Figure 5.4 Scanning tunneling images (I_{tunnel} = 3 pA, V_{sample} = 1 V) of a 100 nm x 100 nm area (A) before and (B) after scanning a 30 nm x 30 nm area at the center under more perturbative conditions (I_{tunnel} = 20 pA, V_{sample} = 0.1 V), indicating the presence of sparse, mobile molecules on the surface.

To characterize this system and the behavior of the bifunctional carborane isomer monolayers when modified by CLL further, we performed XPS on the Au substrates and PDMS stamps after CLL. A comparison between the XPS signals of samples before and after lift-off showed that molecular coverage on the surface was decreased post-CLL. As shown in Figure 5.5, a comparison of the carbon XPS signal reveals decreases in signal intensity in the samples post-lift-off for all three isomers. While adventitious carbon is a concern for the interpretation of these peaks, this artifact is minimal as all compared samples were prepared and characterized under the same conditions in the same time frame.

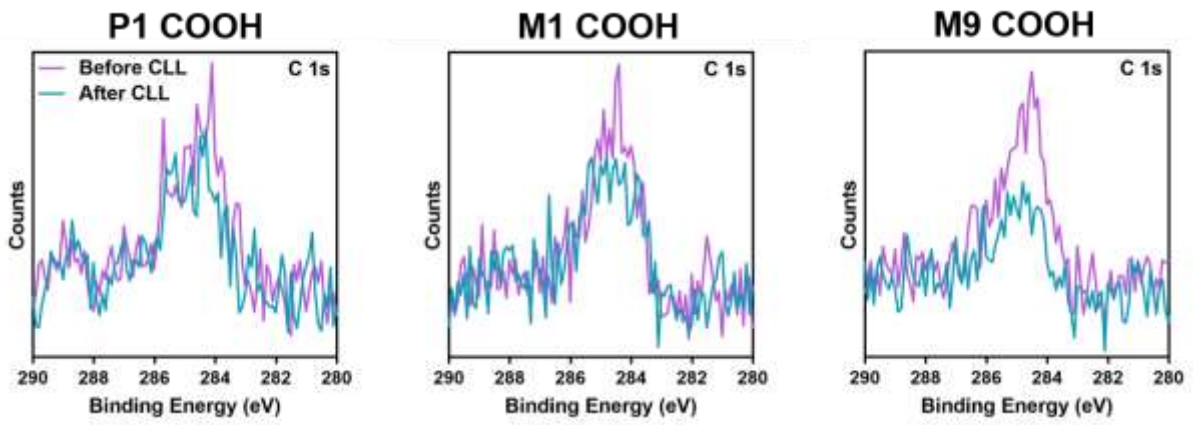

Figure 5.5 X-ray photoelectron spectra showing the C 1s peak for monolayers of 1-HS-12-COOH-1,12-$C_2B_{10}H_{10}$ (P1-COOH), 1-COOH-7-SH-1,7-$C_2B_{10}H_{10}$ (M1-COOH), and *racem*-1-COOH-9-SH-1,7-$C_2B_{10}H_{10}$ (M9-COOH) before (purple) and after (blue) chemical lift-off lithography showing a decrease in surface coverage post lift-off (N=6).

Furthermore, XPS of the PDMS stamps post-CLL demonstrated that Au atoms were also removed from the substrate during the CLL process. The XPS also revealed that the nature of the Au on the PDMS stamp varied depending on which carboranethiol isomer had been used (Figure 5.6). The Au 4f peaks were shifted to higher binding energies in the case of CLL with M9-COOH compared to that of M1-COOH. This shift indicates that the Au attached to M1-COOH molecules is more metallic whereas the Au attached to M9-COOH molecules is more Au^{1+} in character. Given that the thiol is attached to a more electropositive cage vertex in M9-COOH than in M1-COOH, these data indicate that the Au is bound more strongly to the M9-COOH molecule; this behavior is consistent with our previous findings.[33]

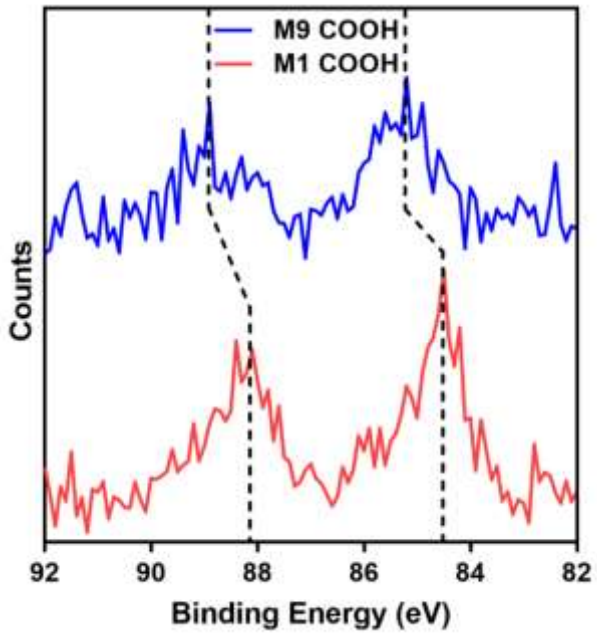

Figure 5.6 X-ray photoelectron spectra showing the Au 4f peaks for monolayers of (red) 1-COOH-7-SH-1,7-$C_2B_{10}H_{10}$ (M1-COOH) and (blue) *racem*-1-COOH-9-SH-1,7-$C_2B_{10}H_{10}$ (M9-COOH). For M9-COOH the Au peaks are shifted to higher binding energy indicating greater Au^{1+} character. This shift suggests the Au is bound more strongly to M9-COOH than M1-COOH.

5.3 Conclusions and Prospects

In this study, we examined CLL of SAMs composed of three bifunctional carboranethiol isomers, P1-COOH, M1-COOH, and M9-COOH. We characterized post-lift-off surfaces with scanning probe microscopy techniques, *i.e.*, AFM and STM. Using AFM, we confirmed that CLL was effective for creating micron-scale patterns of monolayers of all three carboxyl-carboranethiol isomers, even in the case of the *meta* isomers where the reactive carboxylic acid group is in a lateral position and interacts with neighboring monolayer molecules. Furthermore, we characterized the morphology of post-lift-off surfaces *via* STM, which revealed two characteristic features: molecular island domains and sparse coverage of highly mobile molecules, *i.e.*, adatom adsorbate complexes. X-ray photoelectron spectroscopy demonstrated that monolayer surface

coverage is decreased after CLL. Additionally, XPS revealed that the Au lifted off onto the PDMS stamp is bound more strongly to the M9-COOH isomer, where the thiol group is attached to the electron-rich boron vertex of the cage.

This study provides insight into the CLL process, both at the substrate-monolayer interface and the monolayer-stamp interface. There remain further opportunities utilizing carboranethiol-based monolayers for this technique. The amenability of the carborane cage to act as a scaffold for multiple functional groups enables multiple points of attachment to the substrate and to the PDMS stamp per molecule. This system could result in both better lift-off yields and a larger fraction of Au transferred onto the stamp. As mentioned above, another advantage of carboranethiols is the ability to tune surface properties, such as work function, independently of other chemical and physical properties, by using different isomers. This feature will enable the patterning of carboranethiol monolayers where lifted-off areas can be backfilled with another carborane isomer to create controllable domains on the micro and nanoscales with different dipole-dipole networks and properties.

5.4 Materials and Methods

Sample preparation: Bifunctional carborane isomers, P1-COOH, M1-COOH, and M9-COOH, were synthesized as previously reported.[32,33] Substrates of 100 nm Au on silicon, with a 5 nm titanium adhesion layer, were hydrogen-flame annealed with 10 passes at a rate of 0.4 Hz prior to SAM formation. Substrates were placed in 1 mM ethanolic solutions for 24 h at room temperature. Ethanol was used as received (Sigma-Aldrich, St. Louis, MO). After deposition, samples where rinsed with neat ethanol and dried under a stream of ultrahigh-purity nitrogen for

at least three cycles. For STM, Au{111}/mica substrates (Agilent Technology, Tempe, AZ) were used and prepared in an identical manner. Subsequently, chemical lift-off lithography was performed as previously reported; surfaces were contacted with patterned or featureless oxygen-plasma-activated PDMS stamps for 24 h, after which the stamps were removed.[18,20]

Atomic force microscopy: Patterned Au surfaces after chemical lift-off lithography were imaged *via* atomic force microscopy using a Dimension Icon scanning probe microscope (Bruker, Billerica, MA). Surface topographies and nanomechanical properties were measured using the PeakForce Quantitative Nanomechanical Property Mapping (PeakForce QNM) mode. ScanAsyst-Air cantilevers (Bruker, spring constant = 0.4 ± 0.1 N m^{-1}) were calibrated with a clean piece of silicon wafer before every measurement. A peak-force set-point of 400 pN and a scan rate of 1 Hz was maintained for all measurements.

Scanning tunneling microscopy: All STM measurements were performed with a custom-built Besocke-style STM with a platinum/iridium tip (80:20).[34,35] The STM image analyses were performed using MATLAB (Mathworks, Natick, MA) and Gwyddion (http://gwyddion.net/). The known lattice of the 1-dodecanethiolate SAMs on Au{111} was used for calibration.

X-ray photoelectron spectroscopy: All XPS measurements were done using an AXIS Ultra DLD photoelectron spectrometer (Kratos Analytical Inc., Chestnut Ridge, NY) and a monochromatic Al K_α X-ray source with a 200 μm circular spot size under ultrahigh vacuum (10^{-9} Torr). High-resolution spectra of C 1s and Au 4f were acquired at a pass energy of 20 eV using a 300 ms dwell time. For all scans, 15 kV was applied with an emission of 15 mA. An average of 15 scans were collected for high-resolution C 1s spectra and an average of 30 scans were collected for high-resolution Au 4f spectra. Note, all spectra were collected under charge neutralization conditions (*i.e.*, electron flood gun) to prevent charging of sample surfaces. Charge

neutralization results in shifts of binding energy values; binding energies in Figure 5.6 were calibrated to C 1s peaks.

5.5 References

(1) Carlson, A.; Bowen, A. M.; Huang, Y.; Nuzzo, R. G.; Rogers, J. A. Transfer Printing Techniques for Materials Assembly and Micro/Nanodevice Fabrication. *Adv. Mater.* **2012,** *24*, 5284-5318.

(2) Pires, D.; Hedrick, J. L.; De Silva, A.; Frommer, J.; Gotsmann, B.; Wolf, H.; Despont, M.; Duerig, U.; Knoll, A. W. Nanoscale Three-Dimensional Patterning of Molecular Resists by Scanning Probes. *Science* **2010,** *328*, 732.

(3) Priolo, F.; Gregorkiewicz, T.; Galli, M.; Krauss, T. F. Silicon Nanostructures for Photonics and Photovoltaics. *Nat. Nanotechnol.* **2014,** *9*, 19.

(4) Kung, S.-C.; van der Veer, W. E.; Yang, F.; Donavan, K. C.; Penner, R. M. 20 μs Photocurrent Response from Lithographically Patterned Nanocrystalline Cadmium Selenide Nanowires. *Nano Lett.* **2010,** *10*, 1481-1485.

(5) Fan, F.-R.; Lin, L.; Zhu, G.; Wu, W.; Zhang, R.; Wang, Z. L. Transparent Triboelectric Nanogenerators and Self-Powered Pressure Sensors Based on Micropatterned Plastic Films. *Nano Lett.* **2012,** *12*, 3109-3114.

(6) Stewart, M. E.; Anderton, C. R.; Thompson, L. B.; Maria, J.; Gray, S. K.; Rogers, J. A.; Nuzzo, R. G. Nanostructured Plasmonic Sensors. *Chem. Rev.* **2008,** *108*, 494-521.

(7) Rim, Y. S.; Bae, S.-H.; Chen, H.; Yang, J. L.; Kim, J.; Andrews, A. M.; Weiss, P. S.; Yang, Y.; Tseng, H.-R. Printable Ultrathin Metal Oxide Semiconductor-Based Conformal Biosensors. *ACS Nano* **2015,** *9*, 12174-12181.

(8) Xu, X.; Kim, K.; Li, H.; Fan, D. L. Ordered Arrays of Raman Nanosensors for Ultrasensitive and Location Predictable Biochemical Detection. *Adv. Mater.* **2012,** *24*, 5457-5463.

(9) Rogers, J. A.; Someya, T.; Huang, Y. Materials and Mechanics for Stretchable Electronics. *Science* **2010,** *327*, 1603.

(10) Windmiller, J. R.; Wang, J. Wearable Electrochemical Sensors and Biosensors: A Review. *Electroanalysis* **2013,** *25*, 29-46.

(11) Chang, S. W.; Ayothi, R.; Bratton, D.; Yang, D.; Felix, N.; Cao, H. B.; Deng, H.; Ober, C. K. Sub-50 nm Feature Sizes Using Positive Tone Molecular Glass Resists for EUV Lithography. *J. Mater. Chem.* **2006,** *16*, 1470-1474.

(12) Han, S. H.; Doherty, C. M.; Marmiroli, B.; Jo, H. J.; Buso, D.; Patelli, A.; Schiavuta, P.; Innocenzi, P.; Lee, Y. M.; Thornton, A. W.; Hill, A. J.; Falcaro, P. Simultaneous Microfabrication and Tuning of the Permselective Properties in Microporous Polymers Using X-Ray Lithography. *Small* **2013,** *9*, 2277-2282.

(13) Manfrinato, V. R.; Wen, J.; Zhang, L.; Yang, Y.; Hobbs, R. G.; Baker, B.; Su, D.; Zakharov, D.; Zaluzec, N. J.; Miller, D. J.; Stach, E. A.; Berggren, K. K. Determining the Resolution Limits of Electron-Beam Lithography: Direct Measurement of the Point-Spread Function. *Nano Lett.* **2014,** *14*, 4406-4412.

(14) Kalhor, N.; Boden, S. A.; Mizuta, H. Sub-10 nm Patterning by Focused He-Ion Beam Milling for Fabrication of Downscaled Graphene Nano Devices. *Microelectron. Eng.* **2014,** *114*, 70-77.

(15) Qin, D.; Xia, Y.; Whitesides, G. M. Soft Lithography for Micro- and Nanoscale Patterning. *Nat. Protoc.* **2010,** *5*, 491.

(16) Delamarche, E.; Schmid, H.; Bietsch, A.; Larsen, N. B.; Rothuizen, H.; Michel, B.; Biebuyck, H. Transport Mechanisms of Alkanethiols During Microcontact Printing on Gold. *J. Phys. Chem. B* **1998,** *102*, 3324-3334.

(17) Srinivasan, C.; Mullen, T. J.; Hohman, J. N.; Anderson, M. E.; Dameron, A. A.; Andrews, A. M.; Dickey, E. C.; Horn, M. W.; Weiss, P. S. Scanning Electron Microscopy of Nanoscale Chemical Patterns. *ACS Nano* **2007,** *1*, 191-201.

(18) Liao, W. S.; Cheunkar, S.; Cao, H. H.; Bednar, H. R.; Weiss, P. S.; Andrews, A. M. Subractive Patterning via Chemical Lift-Off Lithography. *Science* **2012,** *337*, 1517.

(19) Andrews, A. M.; Liao, W. S.; Weiss, P. S. Double-Sided Opportunities Using Chemical Lift-Off Lithography. *Acc. Chem. Res.* **2016,** *49*, 1449.

(20) Slaughter, L. S.; Cheung, K. M.; Kaappa, S.; Cao, H. H.; Yang, Q.; Young, T. D.; Serino, A. C.; Malola, S.; Olson, J. M.; Link, S.; Häkkinen, H.; Andrews, A. M.; Weiss, P. S. Patterning Supported Gold Monolayers via Chemical Lift-Off Lithography. *Beilstein J. Nanotechnol.* **2017,** *8*, 2648.

(21) Xu, X.; Yang, Q.; Cheung, K. M.; Zhao, C.; Wattanatorn, N.; Belling, J. N.; Abendroth, J. M.; Slaughter, L. S.; Mirkin, C. A.; Andrews, A. M.; Weiss, P. S. Polymer-Pen Chemical Lift-Off Lithography. *Nano Lett.* **2017,** *17*, 3302-3311.

(22) Cao, H. H.; Nakatsuka, N.; Liao, W.-S.; Serino, A. C.; Cheunkar, S.; Yang, H.; Weiss, P. S.; Andrews, A. M. Advancing Biocapture Substrates via Chemical Lift-Off Lithography. *Chem. Mater.* **2017,** *29*, 6829-6839.

(23) Chen, C.-Y.; Wang, C.-M.; Li, H.-H.; Chan, H.-H.; Liao, W.-S. Wafer-Scale Bioactive Substrate Patterning by Chemical Lift-Off Lithography. *Beilstein J. Nanotechnol.* **2018,** *9*, 311-320.

(24) Kim, J.; Rim, Y. S.; Chen, H.; Cao, H. H.; Nakatsuka, N.; Hinton, H. L.; Zhao, C.; Andrews, A. M.; Yang, Y.; Weiss, P. S. Fabrication of High-Performance Ultrathin In_2O_3 Film Field-Effect Transistors and Biosensors Using Chemical Lift-Off Lithography. *ACS Nano* **2015,** *9*, 4572.

(25) Zhao, C.; Xu, X.; Bae, S.-H.; Yang, Q.; Liu, W.; Belling, J. N.; Cheung, K. M.; Rim, Y. S.; Yang, Y.; Andrews, A. M.; Weiss, P. S. Large-Area, Ultrathin Metal-Oxide Semiconductor Nanoribbon Arrays Fabricated by Chemical Lift-Off Lithography. *Nano Lett.* **2018,** *18*, 5590-5595.

(26) Hohman, J. N.; Zhang, P.; Morin, E. I.; Han, P.; Kim, M.; Kurland, A. R.; McClanahan, P. D.; Balema, V. P.; Weiss, P. S. Self-Assembly of Carboranethiol Isomers on Au{111}: Intermolecular Interactions Determined by Molecular Dipole Orientations. *ACS Nano* **2009,** *3*, 527-536.

(27) Hohman, J. N.; Claridge, S. A.; Kim, M.; Weiss, P. S. Cage Molecules for Self-Assembly. *Mater. Sci. Eng. R Rep.* **2010,** *70*, 188-208.

(28) Thomas, J. C.; Schwartz, J. J.; Hohman, J. N.; Claridge, S. A.; Auluck, H. S.; Serino, A. C.; Spokoyny, A. M.; Tran, G.; Kelly, K. F.; Mirkin, C. A.; Gilles, J.; Osher, S. J.; Weiss, P. S. Defect-Tolerant Aligned Dipoles within Two-Dimensional Plastic Lattices. *ACS Nano* **2015,** *9*, 4734-4742.

(29) Kim, J.; Rim, Y. S.; Liu, Y.; Serino, A. C.; Thomas, J. C.; Chen, H.; Yang, Y.; Weiss, P. S. Interface Control in Organic Electronics Using Mixed Monolayers of Carboranethiol Isomers. *Nano Lett.* **2014,** *14*, 2946-2951.

(30) Serino, A. C.; Anderson, M. E.; Saleh, L. M. A.; Dziedzic, R. M.; Mills, H.; Heidenreich, L. K.; Spokoyny, A. M.; Weiss, P. S. Work Function Control of Germanium through Carborane-Carboxylic Acid Surface Passivation. *ACS Appl. Mater. Interfaces* **2017,** *9*, 34592-34596.

(31) Thomas, J. C.; Goronzy, D. P.; Serino, A. C.; Auluck, H. S.; Irving, O. R.; Jimenez-Izal, E.; Deirmenjian, J. M.; Macháček, J.; Sautet, P.; Alexandrova, A. N.; Baše, T.; Weiss, P. S. Acid–Base Control of Valency within Carboranedithiol Self-Assembled Monolayers: Molecules Do the Can-Can. *ACS Nano* **2018,** *12*, 2211-2221.

(32) Thomas, J. C.; Boldog, I.; Auluck, H. S.; Bereciartua, P. J.; Dušek, M.; Macháček, J.; Bastl, Z.; Weiss, P. S.; Baše, T. Self-Assembled *p*-Carborane Analogue of *p*-Mercaptobenzoic Acid on Au{111}. *Chem. Mater.* **2015,** *27*, 5425-5435.

(33) Goronzy, D. P.; Staněk, J.; Avery, E.; Kučeráková, M.; Dušek, M.; Guo, H.; Yavuz, A.; Gün, S.; Šícha, V.; Macháček, J.; Thomas, J. C.; Bastl, Z.; Danisman, F. M.; Mete, E.; Houk, K.; Alexandrova, A.; Baše, T.; Weiss, P. S. Influence of Terminal Carboxyl Group on Structure and Reactivity of Functionalized M-Carboranethiolate Self-Assembled Monolayers. Unpublished.

(34) Frohn, J.; Wolf, J. F.; Besocke, K.; Teske, M. Coarse Tip Distance Adjustment and Positioner for a Scanning Tunneling Microscope. *Rev. Sci. Instrum.* **1989,** *60*, 1200-1201.

(35) Ferris, J. H.; Kushmerick, J. G.; Johnson, J. A.; Yoshikawa Youngquist, M. G.; Kessinger, R. B.; Kingsbury, H. F.; Weiss, P. S. Design, Operation, and Housing of an Ultrastable, Low Temperature, Ultrahigh Vacuum Scanning Tunneling Microscope. *Rev. Sci. Instrum.* **1998,** *69*, 2691.

Chapter 6: Versatility of Carboranes in Self-Assembled Monolayers and Future Directions

6.1 Tuning Interfacial Interactions

Functionalized carboranes are a versatile system for fabricating self-assembled monolayers (SAMs) with a range of tunable chemical and physical properties. This versatility derives from the array of carborane isomers that can be used and the variability in how the cage can be functionalized. As such, functionalized carboranes enable modulation of the interactions and interfaces of a SAM, enabling for the precise modification of specific interactions while leaving other characteristics of the SAM unchanged. A SAM has three primary interactive interfaces that drive its assembly and determine its material properties; these are the substrate-monolayer interface, the interactions with the monolayer, and the monolayer-environment interface. Functionalized carboranes can be used to tune the interactions at all three of these interfaces. The prototypical interaction at the substrate-monolayer interface is a thiol to Au attachment, but with functionalized carboranes we have been able to modify this interface in two ways. As described in Chapter 2, carboranedithiols enable us to control the valency of surface molecules using simple acid-base chemistry. Our study of these dithiols showed that the intrinsic ratio of thiolate-thiolate binding mode to thiolate-thiol binding mode is dependent on the isomer. In the case of the thiol head groups being attached to the electron-rich boron vertices on the carborane cage the monovalent binding mode is significantly preferred. This ratio can also be tuned by performing the SAM deposition under acidic or basic conditions, which can provide intermediate tuning or induce a complete majority switch from monovalent to divalent binding. An alternative route to modifying the substrate-monolayer interface is to introduce a different group. As discussed in Chapter 3, carboraneselenolate SAMs have a surface morphology that significantly deviates from that of carboranethiolate SAMs. Selenium, while also a chalcogenide similar to sulfur, when attached to Au is much more mobile and promiscuous. This phenomenon can be seen in the

dynamic double lattice of carboraneselenolate SAMs where adsorbate molecules appear to switch between high- and low-conductance binding states. The Se-Au interface can be sensitive to substrate-mediated interactions, however the carboraneselenolate SAMs are quite stable with the monolayer morphology remaining unchanged under thermal agitation. This stability is likely a result of the prominent dipole-dipole interactions within the monolayer.

An intrinsic feature of functionalized carborane SAMs is the prominence of these dipole-dipole interactions within the monolayer. As discussed in Chapter 1, these dipole-dipole networks are long range and can modify surface properties such as the work function. One of the most versatile aspects of the carborane is how different isomers can be used to alter these dipole-dipole networks. However, as described in Chapter 4, further interactions can be present within carboranethiolate SAMs. The addition of a carboxyl group to the carboranethiol cage in the *meta* position results in changes to the monolayer in the form of a lower packing density than previously studied carboranethiolate SAMs. This decrease is a result of the increased steric demands of a laterally positioned functional group. However, the balance of these demands with the favorable interaction of the thiol with the Au surface induces a tilt in the molecule such that packing density is maximized. With this tilted configuration also comes hydrogen-bonding interactions between the carboxylic acid group and the neighboring carborane cage. It is likely that these hydrogen-bonding interactions along with the dipole-dipole interacting between carborane cages stabilize the monolayer against the defects that are typically associated with molecular tilt. These interactions within the monolayer also contribute to the dielectric of the environment that the carboxylic acid experiences. The pK_a of the surface bound carboxylic acid is increased as a result of the decreased dielectric in the monolayer, which arises due to a combination of intermolecular interactions, proximity to the Au surface, and partial desolvation.

Despite the carboxylic acid group being partially buried within the monolayers of the *meta*-functionalized carboranethiols, it remains available for interactions and reactions at the monolayer-environment interface. It can be deprotonated by treating the surface with a basic solution, but even more so, it can coordinate with metal ions. Furthermore, it appears that some metal ions, like Mg^{2+} and Ba^{2+}, coordinate *multiple* carboxyl groups on the surface simultaneously.

As described in Chapter 5, the carboxyl group can also serve as a point of attachment for a polydimethylsiloxane (PDMS) stamp and as such the monolayer can be patterned *via* chemical lift-off lithography. These carboxylic-acid-functionalized carboranethiolate monolayers further provided the opportunity to study fundamental aspects of this lithographic technique. The surface morphology of the post-lift-off Au substrates showed that the removal of the monolayer is incomplete and left behind are small molecular island domains and sparse, mobile, isolated molecules.

6.2 Future Challenges and Potential Applications

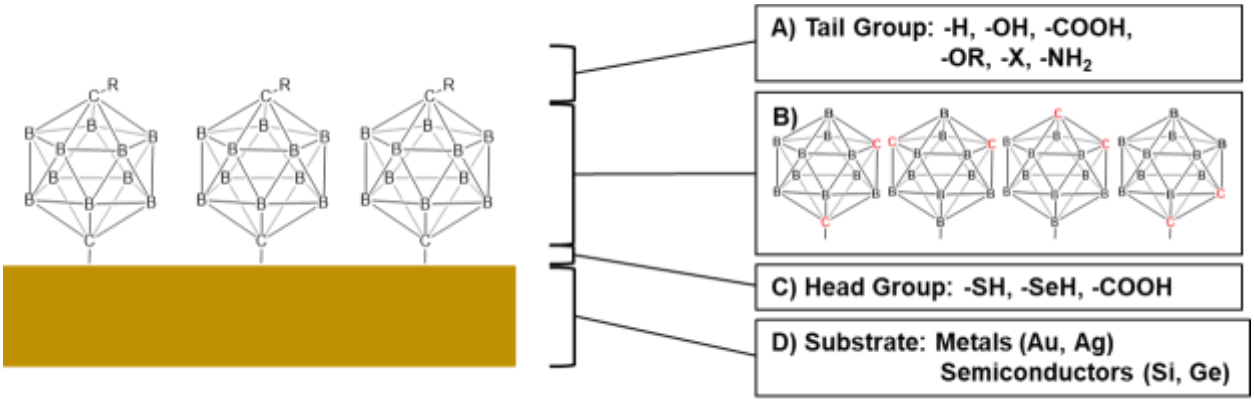

Figure 6.1 A schematic showing the versatility of functionalized carboranes at every facet of a self-assembled monolayer: (A) the tail group, (B) the backbone, (C) the head group, and (D) the substrate.

While significant characters of functionalized carborane SAMs have been elucidated, the full breadth of interactions within this system requires further characterization. The schematic in Figure 6.1 illustrates the multifaceted nature of these SAMs. The variability in head group enables assembly on both metal and semiconductor substrates and interactions between the head group and the substrate can be controllably varied to alter monolayer morphology. One of the key aspects of the cage in these system is that *para*-, *ortho*-, or *meta*-carboranes can be used in various orientations as the backbone. These different isomers not only alter the dipole-dipole interactions within the monolayer and the polarity of the exposed surface, but the chemical nature of the functional group is in part dependent on whether it is attached to an electron-rich boron vertex or an electron-poor carbon vertex. Thus far, we have looked at carboranethiol monolayers with either terminal hydrogens or carboxyls, but the cage can facilitate other functional groups including alkyl chains, alcohols, esters, ethers, amines, and halogens. These functional groups can also be varied in position such that they are exposed to the environment, interacting with neighboring molecules

within the monolayer, or participating in the interactions at the substrate and environmental interfaces.

Fundamental questions about the assembly of these SAMs remain in part unanswered. Typically, deposition is performed using ethanol as a solvent, and thus it remains unclear if there are solvent effects in the assembly process. Solvent effects have been suggested previously in SAMs composed of amide-containing alkanethiols.[1,2] As shown in Figure 6.2, the work function of a Au surface coated in a carboxyl-carboranethiolate SAM is both dependent on the isomer used and on the deposition solvent used. Whether the deposition solvent alters other characteristics of the monolayer such as lattice structure or surface pK_a remains to be seen.

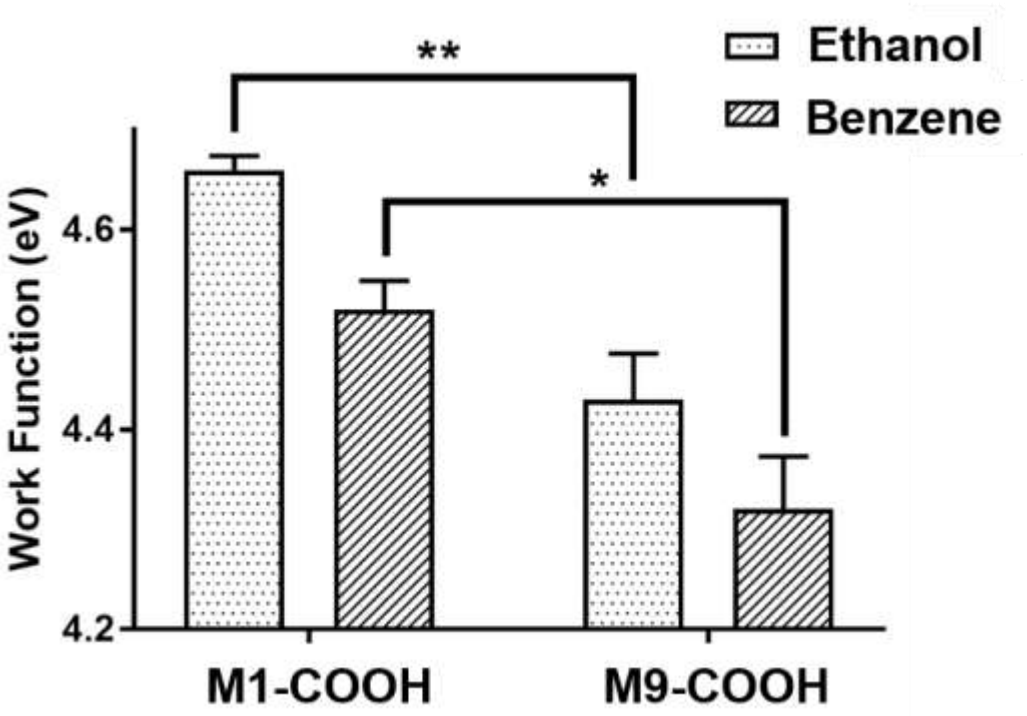

Figure 6.2 Work functions of self-assembled monolayers of 7-SH-1,7-$C_2B_{10}H_{10}$ (M1-COOH) and *racem*-1-COOH-9-SH-1,7-$C_2B_{10}H_{10}$ (M9-COOH) on Au acquired *via* ultraviolet photoelectron spectroscopy. Changes in work function are dependent both on the isomer of carboxyl-carboranethiol used and on the deposition solvent.

Another critical aspect of these carboxyl-carboranethiolate SAMs that requires further characterization is the on-surface reactivity of the carboxyl group. We have already seen that chemical lift-off lithography is possible, most likely through an ester linkage between the monolayer and the stamp. We can perform a simple *in situ* esterification by treating the monolayer with a solution of alcohol containing catalytic acid. Furthermore, given the effect that a carboranethiol monolayer has on the work function, we can use this surface property as a benchmark to track the reaction. As shown in Figure 6.3, the *in situ* esterification process does alter the work function, but much more significantly for monolayers composed of *racem*-1-COOH-9-SH-1,7-$C_2B_{10}H_{10}$ (M9-COOH) compared to monolayers composed of 7-SH-1,7-$C_2B_{10}H_{10}$ (M1-COOH). This difference can be explained by the dipole moment of M1-COOH being much more in the plane of the functional group, whereas the dipole moment of M9-COOH is closer to perpendicular to the functional group and is thus more affected by a change in that group.

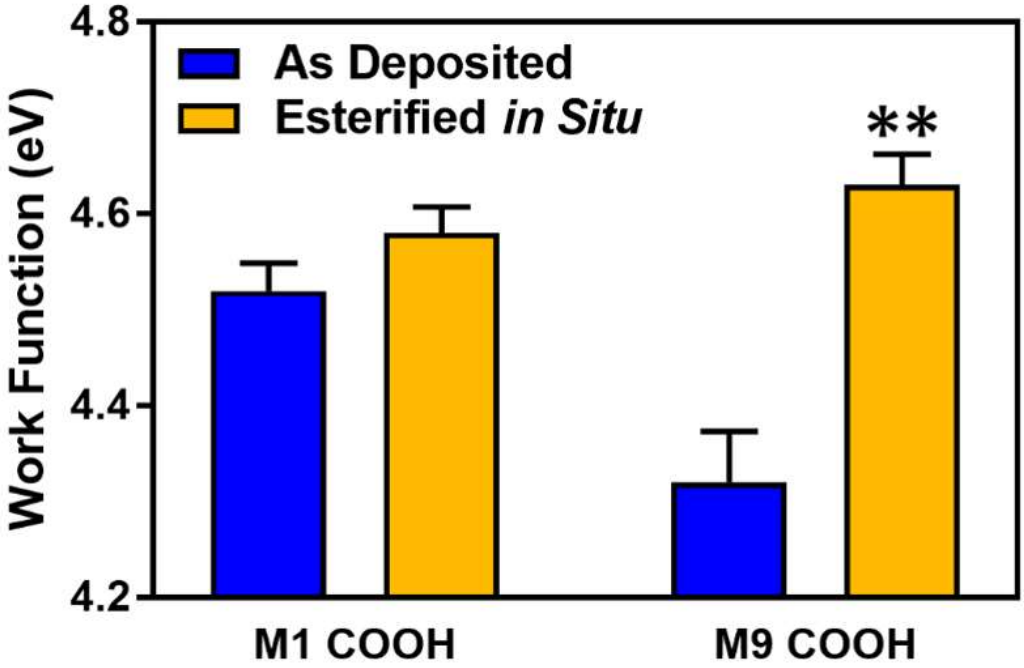

Figure 6.2 Work functions of self-assembled monolayers of 7-SH-1,7-$C_2B_{10}H_{10}$ (M1-COOH) and *racem*-1-COOH-9-SH-1,7-$C_2B_{10}H_{10}$ (M9-COOH) on Au acquired *via* ultraviolet photoelectron spectroscopy. The effect of *in situ* esterification is significantly more pronounced in the case of M9-COOH.

These preliminary data not only highlight some of the current questions surrounding functionalized carboranethiol SAMs but also show the utility of using work function to assess other characteristics of the monolayer.

Beyond exploring specific questions regarding these monolayers, they can also be used as a platform to probe broader phenomena, such as the change in chemical behavior when going from three dimensions to two dimensions. This phenomenon is particularly clear in the change in pK_a from solution to surface in the case of the carboxyl-carboranethiol molecules. If these assemblies can be modulated in such a way to mitigate factors contributing to the shift, then these effects can be examined individually. For instance, reducing intermolecular interactions by creating lower density coverages can provide information on the effects of desolvation on the pK_a shift. Changes

in pK_a due to microenvironment are not only important for chemistry and materials but also for biology,[3] where the pK_a of amino acids in proteins is critical for structure and function. Furthermore, many biological interactions occur at membranes, which are analogous to these two-dimensional monolayers in some ways.

Lastly, there is potential for the integration of functionalized carborane SAMs into organic electronics and devices, such as transistors or pH sensors. These monolayers can be used to facilitate better band alignment[4] or serve as an interfacial material to increase phonon transfer. Given that these monolayers can be patterned by chemical lift-off lithography, the fabrication of micro and nanoscale domains with individual surface properties is possible. In reality, we have only just scratched the surface of the utility of functionalized carboranes.

6.3 References

(1) Smith, R. K.; Reed, S. M.; Lewis, P. A.; Monnell, J. D.; Clegg, R. S.; Kelly, K. F.; Bumm, L. A.; Hutchison, J. E.; Weiss, P. S. Phase Separation within a Binary Self-Assembled Monolayer on Au{111} Driven by an Amide-Containing Alkanethiol. *J. Phys. Chem. B* **2001,** *105*, 1119-1122.

(2) Lewis, P. A.; Smith, R. K.; Kelly, K. F.; Bumm, L. A.; Reed, S. M.; Clegg, R. S.; Gunderson, J. D.; Hutchison, J. E.; Weiss, P. S. The Role of Buried Hydrogen Bonds in Self-Assembled Mixed Composition Thiols on Au{111}. *J. Phys. Chem. B* **2001,** *105*, 10630-10636.

(3) Guo, B.; Middha, E.; Liu, B. Solvent Magic for Organic Particles. *ACS Nano* **2019,** *13*, 2675-2680.

(4) Kim, J.; Rim, Y. S.; Liu, Y.; Serino, A. C.; Thomas, J. C.; Chen, H.; Yang, Y.; Weiss, P. S. Interface Control in Organic Electronics Using Mixed Monolayers of Carboranethiol Isomers. *Nano Lett.* **2014,** *14*, 2946-2951.